

ISSN 1997-1397 (Print)
ISSN 2313-6022 (Online)

**Журнал Сибирского
федерального университета
Математика и физика**

**Journal of Siberian
Federal University
Mathematics & Physics**

2025 18 (3)

ISSN 1997-1397
(Print)

ISSN 2313-6022
(Online)

2025 18 (3)

ЖУРНАЛ
СИБИРСКОГО
ФЕДЕРАЛЬНОГО
УНИВЕРСИТЕТА
Математика и Физика

JOURNAL
OF SIBERIAN
FEDERAL
UNIVERSITY
Mathematics & Physics

Издание индексируется Scopus (Elsevier), Emerging Sources Citation Index (WoS, Clarivate Analytics), Российским индексом научного цитирования (ИЭБ), представлено в международных и российских информационных базах: Ulrich's periodicals directory, ProQuest, EBSCO (США), Google Scholar, MathNet.ru, КиберЛенинке.

Включено в список Высшей аттестационной комиссии «Рецензируемые научные издания, входящие в международные реферативные базы данных и системы цитирования».

Все статьи представлены в открытом доступе http://journal.sfu-kras.ru/en/series/mathematics_physics.

**Журнал Сибирского федерального университета.
Математика и физика.**

Journal of Siberian Federal University. Mathematics & Physics.

Учредитель: Федеральное государственное автономное образовательное учреждение высшего образования "Сибирский федеральный университет" (СФУ)

Главный редактор: А.М. Кытманов. Редакторы: В.Е. Зализняк, А.В. Щуплев.
Компьютерная верстка: Г.В. Хрусталева

№ 3. 26.06.2025. Индекс: 42327. Тираж: 1000 экз. Свободная цена
Адрес редакции и издателя: 660041 г. Красноярск, пр. Свободный, 79,
оф. 32-03.

Отпечатано в типографии Издательства БИК СФУ
660041 г. Красноярск, пр. Свободный, 82а.

*Свидетельство о регистрации СМИ ПИ № ФС 77-28724 от 29.06.2007 г.,
выданное Федеральной службой по надзору в сфере массовых
коммуникаций, связи и охраны культурного наследия
<http://journal.sfu-kras.ru>*

Подписано в печать 15.06.25. Формат 84×108/16. Усл.печ. л. 12,0.

Уч.-изд. л. 11,8. Бумага тип. Печать офсетная.

Тираж 1000 экз. Заказ 23350

Возрастная маркировка в соответствии с Федеральным законом № 436-ФЗ:16+

Editorial Board:

Editor-in-Chief: Prof. Alexander M. Kytmanov
(Siberian Federal University, Krasnoyarsk, Russia)

Consulting Editors Mathematics & Physics:

Prof. Viktor K. Andreev (Institute Computing Modelling SB RUS, Krasnoyarsk, Russia)
Prof. Dmitry A. Balaev (Institute of Physics SB RUS, Krasnoyarsk, Russia)
Prof. Silvio Ghilardi (University of Milano, Milano, Italy)
Prof. Sergey S. Goncharov, Academician,
(Institute of Mathematics SB RUS, Novosibirsk, Russia)
Prof. Ari Laptev (KTH Royal Institute of Technology, Stockholm, Sweden)
Prof. Yury Yu. Loginov
(Reshetnev Siberian State University of Science and Technology, Krasnoyarsk, Russia)
Prof. Mikhail V. Noskov (Siberian Federal University, Krasnoyarsk, Russia)
Prof. Sergey G. Ovchinnikov (Institute of Physics SB RUS, Krasnoyarsk, Russia)
Prof. Gennady S. Patrin (Institute of Physics SB RUS, Krasnoyarsk, Russia)
Prof. Vladimir M. Sadovsky (Institute Computing Modelling SB RUS, Krasnoyarsk, Russia)
Prof. Azimbay Sadullaev, Academician
(Nathional University of Uzbekistan, Tashkent, Uzbekistan)
Prof. Vasily F. Shabanov, Academician, (Siberian Federal University, Krasnoyarsk, Russia)
Prof. Vladimir V. Shaidurov (Institute Computing delling SB RUS, Krasnoyarsk, Russia)
Prof. Avgust K. Tsikh (Siberian Federal University, Krasnoyarsk, Russia)
Prof. Eugene A.Vaganov, Academician, (Siberian Federal University, Krasnoyarsk, Russia)
Prof. Valery V. Val'kov (Institute of Physics SB RUS, Krasnoyarsk, Russia)
Prof. Alecos Vidras (Cyprus University, Nicosia, Cyprus)

CONTENTS

A. M. Kytmanov, S. G. Myslivets On One Integral Representation of the Potential Type	293
A. G. Fatyanov Sommerfeld's Method for Solving the Dynamic Rigid Stamp Indentation Problem	300
A. G. Golubovskaya, T. S. Kharlamova, V. A. Svetlichnyi Solid-phase Synthesis and Photocatalytic Properties of $\text{Bi}_2\text{SiO}_5/\text{Bi}_{12}\text{SiO}_{20}$ Heterostructures	309
I. E. Petrakov Modeling of a Sandwich Plate Cross-section with the Different Moduli of the Material under Cylindrical Loads	320
S. V. Alekseev, V. F. Losev, Ya. V. Grudtsyn, A. V. Koribut, V. I. Yalovoy Spectrum Broadening of Femtosecond Radiation Pulse at 950 nm Wavelength in Material with Cubic Nonlinearity	331
I. V. Smolekho Investigation of the Orientational Thermoelasticity Effect Using a Simplified Model of Nematic Liquid Crystal in the Acoustic Approximation	337
E. A. Izbasarova, A. R. Gazizov Near-field Interaction Effects in Colloidal Au-CeYTbF ₃ Nanoclusters in Plasmonic Immunoanalysis	347
D. A. Savelyev The Investigation of Gaussian Beams and Optical Vortices Diffraction in the Near Zone of Subwavelength Optical Elements with Variable Height	358
V. E. Prokopev, D. M. Lubenko Filamentation Process of Femtosecond Laser Pulse in Air and Associated Phenomena	371
A. K. Lappo-Danilevskaia, A. O. Ismagilov, A. A. Kalinichev, A. N. Tsyarkin Simulation of Single-Pixel Camera Method Application for mapping the Spatial Layout of Objects in LIDAR Technologies	377
A. Sadullaev, R. Sharipov, M. Ismoilov $m - cv$ measure $\omega^*(x, E, D)$ and condenser capacity $C(E, D)$ in the class m -convex functions	387
N. Fetouci, S. Radenović Some Remarks and Corrections of Recent Results from the Framework of \mathbf{S} -metric Spaces	402
E. V. Timchenko, N. A. Ryabov, O. O. Frolov, P. E. Timchenko, L. T. Volova, S. S. Ivanov Application of Optical Methods in Standardization of Collagen-containing Hydrogen for 3D Bioprinting of Supporting and Connective Tissues	412
S. V. Ludkowski Measures on Smashed Products of Quasigroups and their Algebras	420

СОДЕРЖАНИЕ

А. М. Кытманов, С. Г. Мысливец	293
Об одном интегральном представлении типа потенциала	
А. Г. Фатьянов	300
Метод Зоммерфельда решения динамической задачи о вдавлении жесткого штампа	
А. Г. Голубовская, Т. С. Харламова, В. А. Светличный	309
Твердофазный синтез и фотокаталитические свойства гетероструктур $\text{Bi}_2\text{SiO}_5/\text{Bi}_{12}\text{SiO}_{20}$	
И. Е. Петраков	320
Моделирование сечения сэндвич-пластины при цилиндрических нагрузках с учетом разномодульности материала	
С. В. Алексеев, В. Ф. Лосев, Я. В. Грудцын, А. В. Корибут, В. И. Яловой	331
Уширение спектра фемтосекундного импульса излучения на длине волны 950 нм в материале с кубической нелинейностью	
И. В. Смолехо	337
Исследование эффекта ориентационной термоупругости с помощью упрощенной модели нематического жидкого кристалла в акустическом приближении	
Э. А. Избасарова, А. Р. Газизов	347
Эффекты ближнеполевого взаимодействия в коллоидных нанокластерах Au-CeYbF_3 при плазмонном иммуноанализе	
Д. А. Савельев	358
Исследование дифракции гауссовых пучков и оптических вихрей в ближней зоне субволновых оптических элементов переменной высоты	
В. Е. Прокопьев, Д. М. Лубенко	371
Процесс филаментации фемтосекундного излучения в воздухе и явления ее сопровождающие	
А. К. Лаппо-Данилевская, А. О. Исмагилов, А. А. Калинин, А. Н. Цыпки	377
Моделирование метода однопиксельной визуализации для получения пространственного распределения объектов в ЛИДАР технологиях	
А. Садуллаев, Р. Шарипов, М. Исмоилов	387
$m - cv$ мера $\omega^*(x, E, D)$ и емкость конденсатора $C(E, D)$ в классе m -выпуклых функций	
Н. Фетуси, С. Раденович	402
Некоторые замечания и исправления недавних результатов из теории \mathbf{S} -метрических пространств	
Е. В. Тимченко, Н. А. Рябов, О. О. Фролов, П. Е. Тимченко, Л. Т. Волова, С. С. Иванов	412
Применение оптических методов в стандартизации коллагенсодержащего гидрогеля для 3D-биопечати опорных и соединительных тканей	
С. В. Людковский	420
Меры на сокрушающих произведениях квазигрупп и их алгебры	

EDN: ISZQFR
 УДК 517.55

On One Integral Representation of the Potential Type

Alexander M. Kytmanov*

Simona G. Myslivets†

Siberian Federal University
 Krasnoyarsk, Russian Federation

Received 15.11.2024, received in revised form 18.01.2025, accepted 24.02.2025

Abstract. In this article, we consider some integral representation of the potential type (Cauchy–Fantappiè) for a smooth function defined on the boundary of a bounded multidimensional domain. Derivatives of this integral representation are found and their boundary behavior is studied. An analogue of the Bochner–Martinelli formula for smooth functions is proved.

Keywords: Bochner–Martinelli integral, bounded domain, boundary behavior.

Citation: A.M. Kytmanov, S.G. Myslivets, On One Integral Representation of the Potential Type, *J. Sib. Fed. Univ. Math. Phys.*, 2025, 18(3), 293–299. EDN: ISZQFR.



The method of integral representations is one of the main constructive methods in the study of holomorphic functions of several complex variables (see, for example, [1–4]). One such representation is the classical Bochner–Martinelli representation. Although it does not have a holomorphic kernel, its versatility has allowed it to be used in matters of analytical continuation of functions and other analytic objects. It has been studied in detail in the monograph [5].

The integral representation considered in the paper is close to the Bochner–Martinelli representation. The aim of the work is to study the properties of this integral representation for holomorphic functions (Cauchy–Fantappiè type), the kernel of which consists of derivatives of the fundamental solution of the Laplace equation.

We consider n -dimensional complex space \mathbb{C}^n , $n > 1$ with variables $z = (z_1, \dots, z_n)$. Let us introduce the vector module $|z| = \sqrt{z_1^2 + \dots + z_n^2}$ and the differential forms $dz = dz_1 \wedge \dots \wedge dz_n$ and $d\bar{z} = d\bar{z}_1 \wedge \dots \wedge d\bar{z}_n$ and also $dz[k] = dz_1 \wedge \dots \wedge dz_{k-1} \wedge dz_{k+1} \wedge \dots \wedge dz_n$.

We shall consider bounded domains $D \subset \mathbb{C}^n$ with a smooth boundary ∂D of class \mathcal{C}^1 , that is $D = \{z \in \mathbb{C}^n : \rho(z) < 0\}$, where ρ is real-valued function of class \mathcal{C}^1 on some neighborhood of the closure of domain D , and the differential $d\rho \neq 0$ on ∂D . Let us denote the "complex" guiding cosines

$$\rho_k = \frac{1}{|\text{grad } \rho|} \frac{\partial \rho}{\partial z_k}, \quad \rho_{\bar{k}} = \frac{1}{|\text{grad } \rho|} \frac{\partial \rho}{\partial \bar{z}_k}, \quad k = 1, \dots, n.$$

Consider the Bochner–Martinelli kernel, which is an exterior differential form $U(\zeta, z)$ of type $(n, n-1)$ (see, for example, [5, Ch. 1]), given by

$$U(\zeta, z) = \frac{(n-1)!}{(2\pi i)^n} \sum_{k=1}^n (-1)^{k-1} \frac{\bar{\zeta}_k - \bar{z}_k}{|\zeta - z|^{2n}} d\bar{\zeta}[k] \wedge d\zeta.$$

This kernel plays an important role in multidimensional complex analysis (see, for example, [1–6]). It is a closed differential form of type $(n, n-1)$. For $n = 1$ this kernel turns into a Cauchy kernel.

*akytmanov@sfu-kras.ru <https://orcid.org/0000-0002-7394-1480>

†asmyslivets@sfu-kras.ru

© Siberian Federal University. All rights reserved

Let $g(\zeta, z)$ be the fundamental solution to the Laplace equation:

$$g(\zeta, z) = -\frac{(n-2)!}{(2\pi i)^n} \frac{1}{|\zeta - z|^{2n-2}}, \quad n > 1,$$

then

$$U(\zeta, z) = \sum_{k=1}^n (-1)^{k-1} \frac{\partial g}{\partial \zeta_k} d\bar{\zeta}[k] \wedge d\zeta.$$

For the function $f \in \mathcal{C}^1(\partial D)$ we introduce the Bochner-Martinelli integral (integral operator)

$$M[f](z) = \int_{\partial D} f(\zeta) U(\zeta, z), \quad z \notin \partial D,$$

and also the single-layer potential (integral operator)

$$\Phi[f](z) = -i^n 2^{n-1} \int_{\partial D} f(\zeta) g(\zeta, z) d\sigma(\zeta) = \frac{(n-2)!}{2\pi^n} \int_{\partial D} f(\zeta) \frac{d\sigma}{|\zeta - z|^{2n-2}}, \quad z \notin \partial D,$$

where $d\sigma$ is the Lebesgue surface measure on ∂D .

Let us define the differential form μ_f for the function $f \in \mathcal{C}^1(\partial D)$ as follows [5, Ch. 1]:

$$\mu_f = \sum_{k=1}^n (-1)^{n+k-1} \frac{\partial f}{\partial \bar{\zeta}_k} d\zeta[k] \wedge d\bar{\zeta}.$$

In the monograph [5], the problem of holomorphicity of the harmonic function $f \in \mathcal{C}^1(\bar{D})$ satisfying condition (23.5) in [5] of the following form is posed

$$\mu_f|_{\partial D} = \sum_{k>l} a_{k,l}(z) df \wedge d\bar{z}[k, l] \wedge dz|_{\partial D}, \quad (1)$$

where $a_{k,l}$ are some smooth functions on ∂D . Here, the differential form $d\bar{z}[k, l]$ is obtained from the differential form $d\bar{z} = d\bar{z}_1 \wedge \cdots \wedge d\bar{z}_n$ by removing the differentials $d\bar{z}_k, d\bar{z}_l$.

This is related to the problem of holomorphicity of functions represented by the Bochner-Martinelli integral (see [5, Ch. 15]) (in this case, all functions $a_{kl} = 0$). Some special cases of this problem are considered in [5, Ch. 23]. In [5, Ch. 23], the problem 1 is rewritten in integral form.

Recall Green's formula (in complex form) for the function f (corollary 1.2 of [5]).

Theorem 1 (Green's formula). *Let D be a bounded domain with a piecewise smooth boundary, the function f is harmonic in D and $f \in \mathcal{C}^1(\bar{D})$, then*

$$\int_{\partial D} f(\zeta) U(\zeta, z) - \int_{\partial D} g(\zeta, z) \mu_f = \begin{cases} f(z), & z \in D, \\ 0, & z \notin \bar{D}. \end{cases} \quad (2)$$

From the equality of (1) and Green's formula (2), we obtain that

$$f(z) = \int_{\partial D} f(\zeta) U(\zeta, z) - \int_{\partial D} g(\zeta, z) \sum_{k>l} a_{k,l}(\zeta) df \wedge d\bar{\zeta}[k, l] \wedge d\zeta, \quad z \in D. \quad (3)$$

Applying the Stokes and the Green's formula (2), in [5, Ch. 23] it is shown that the equality (3) for functions $f \in \mathcal{C}^1(\bar{D})$ and harmonic in D is equivalent to the condition

$$f(z) = \int_{\partial D} f(\zeta) U(\zeta, z) + \int_{\partial D} f(\zeta) \sum_{k>l} d(a_{k,l}(\zeta) g(\zeta, z)) \wedge d\bar{\zeta}[k, l] \wedge d\zeta, \quad z \in D. \quad (4)$$

The first integral is a Bochner–Martinelli integral (integral operator) of the function f , i.e.

$$M[f](z) = \int_{\partial D} f(\zeta) U(\zeta, z), \quad z \notin \partial D,$$

and the second integral (integral operator) is denoted by

$$G[f](z) = \int_{\partial D} f(\zeta) \sum_{k>l} d(a_{k,l}(\zeta) g(\zeta, z)) \wedge d\bar{\zeta}[k, l] \wedge d\zeta, \quad z \notin \partial D.$$

For $n = 1$ this integral disappears.

Let us introduce the kernel of the second integral operator

$$W(\zeta, z) = \sum_{k>l} d(a_{k,l}(\zeta) g(\zeta, z)) \wedge d\bar{\zeta}[k, l] \wedge d\zeta,$$

we obtain that for holomorphic functions f an integral representation of the Cauchy–Fantappiè type is valid (see, for example, [4, Ch. 26])

$$f(z) = \int_{\partial D} f(\zeta) (U(\zeta, z) + W(\zeta, z)), \quad z \in D. \quad (5)$$

Thus, the problem (1) transforms into the problem of holomorphicity of the harmonic function f satisfying the equality (5) in the domain D (see [5, Ch. 23]).

Let us denote the operator $M + G$ by

$$Q[f](z) = M[f](z) + G[f](z) = \int_{\partial D} f(\zeta) (U(\zeta, z) + W(\zeta, z)), \quad z \notin \partial D. \quad (6)$$

In this paper, we will study the properties of this integral with the kernel $U(\zeta, z) + W(\zeta, z)$, calculate its derivatives and their boundary behavior.

1. Derivatives of the integral operator

Let the domain D have a boundary of the class \mathcal{C}^2 (i.e., the function ρ is twice smooth in a neighborhood of the closure of the domain D). The function $f \in \mathcal{C}^2(\partial D)$, and the functions $a_{k,l} \in \mathcal{C}^2(\partial D)$, $k, l = 1, \dots, n$.

We introduce, as in the article [8], the following differential operators

$$L_m(f) = \frac{\partial f}{\partial \zeta_m} - \rho_m \sum_{k=1}^n \rho_k \frac{\partial f}{\partial \bar{\zeta}_k},$$

$$K_m(f) = i^n 2^{n-1} \sum_{s,k=1}^n \left[\rho_k \frac{\partial}{\partial \zeta_s} \left(\rho_m \rho_{\bar{k}} \frac{\partial f}{\partial \bar{\zeta}_s} \right) - \rho_m \frac{\partial}{\partial \zeta_k} \left(\rho_m \rho_{\bar{k}} \frac{\partial f}{\partial \bar{\zeta}_s} \right) \right],$$

accordingly,

$$L_{\bar{m}}(f) = \frac{\partial f}{\partial \bar{\zeta}_m} - \rho_{\bar{m}} \sum_{k=1}^n \rho_k \frac{\partial f}{\partial \zeta_k},$$

$$K_{\bar{m}}(f) = i^n 2^{n-1} \sum_{s,k=1}^n \left[\rho_k \frac{\partial}{\partial \zeta_s} \left(\rho_{\bar{m}} \rho_{\bar{k}} \frac{\partial f}{\partial \zeta_s} \right) - \rho_{\bar{m}} \frac{\partial}{\partial \zeta_k} \left(\rho_{\bar{m}} \rho_{\bar{k}} \frac{\partial f}{\partial \zeta_s} \right) \right].$$

Then, according to Corollary 1 of [8], we get

$$\frac{\partial M[f]}{\partial z_m} = M[L_m(f)] - \Phi[K_m(f)], \quad (7)$$

$$\frac{\partial M[f]}{\partial \bar{z}_m} = M[L_{\bar{m}}(f)] - \Phi[K_{\bar{m}}(f)]. \quad (8)$$

These formulas are derived from the formulas of the classical potential theory [7] and formulas from [5, Ch.1].

Similarly, we introduce the operators

$$\begin{aligned} \tilde{L}_m(f) &= -f\rho_m, \\ \tilde{K}_m(f) &= +i^n 2^{n-1} \sum_{k=1}^n \left[\rho_k \frac{\partial}{\partial \zeta_m} (f\rho_{\bar{k}}) - \rho_m \frac{\partial}{\partial \zeta_k} (f\rho_{\bar{k}}) \right], \end{aligned}$$

accordingly,

$$\begin{aligned} \tilde{L}_{\bar{m}}(f) &= -f\rho_{\bar{m}}, \\ \tilde{K}_{\bar{m}}(f) &= i^n 2^{n-1} \sum_{k=1}^n \left[\rho_k \frac{\partial}{\partial \zeta_{\bar{m}}} (f\rho_{\bar{k}}) - \rho_{\bar{m}} \frac{\partial}{\partial \zeta_k} (f\rho_{\bar{k}}) \right]. \end{aligned}$$

Then, according to Corollary 1 of [8], we get

$$\frac{\partial \Phi[f]}{\partial z_m} = M[\tilde{L}_m(f)] - \Phi[\tilde{K}_m(f)], \quad (9)$$

$$\frac{\partial \Phi[f]}{\partial \bar{z}_m} = M[\tilde{L}_{\bar{m}}(f)] - \Phi[\tilde{K}_{\bar{m}}(f)]. \quad (10)$$

Lemma 1. *Let D be a bounded domain with a boundary of the class \mathcal{C}^2 , a function f is harmonic in D and $f \in \mathcal{C}^2(\bar{D})$, and $a_{k,l} \in \mathcal{C}^2(\partial D)$, $k, l = 1, \dots, n$, then $G[f] = -\Phi[h]$, where*

$$h(\zeta) = \sum_{k>l} (-1)^{k+l} a_{k,l}(\zeta) \left(\frac{\partial f}{\partial \zeta_k} \rho_{\bar{l}} - \frac{\partial f}{\partial \zeta_l} \rho_{\bar{k}} \right).$$

Proof. It follows from formulas (3) and (4) that

$$\int_{\partial D} f(\zeta) \sum_{k>l} d(a_{k,l}(\zeta)g(\zeta, z)) \wedge d\bar{\zeta}[k, l] \wedge d\zeta = - \int_{\partial D} g(\zeta, z) \sum_{k>l} a_{k,l}(\zeta) df \wedge d\bar{\zeta}[k, l] \wedge d\zeta.$$

Therefore, transforming the differential form $df \wedge d\bar{\zeta}[k, l] \wedge d\zeta$, we get

$$\begin{aligned} df \wedge d\bar{\zeta}[k, l] \wedge d\zeta &= \left((-1)^{l-1} \frac{\partial f}{\partial \zeta_l} d\bar{\zeta}[k] + (-1)^k \frac{\partial f}{\partial \zeta_k} d\bar{\zeta}[l] \right) \wedge d\zeta = \\ &= (-1)^{l-1} \frac{\partial f}{\partial \zeta_l} 2^{n-1} i^n (-1)^{k-1} \rho_{\bar{k}} d\sigma + (-1)^k \frac{\partial f}{\partial \zeta_k} 2^{n-1} i^n (-1)^{l-1} \rho_{\bar{l}} d\sigma = \\ &= 2^{n-1} i^n \left((-1)^{l+k} \frac{\partial f}{\partial \zeta_l} \rho_{\bar{k}} + (-1)^{k+l-1} \frac{\partial f}{\partial \zeta_k} \rho_{\bar{l}} \right) d\sigma = 2^{n-1} i^n (-1)^{k+l-1} \left(\frac{\partial f}{\partial \zeta_k} \rho_{\bar{l}} - \frac{\partial f}{\partial \zeta_l} \rho_{\bar{k}} \right) d\sigma, \end{aligned}$$

where $d\sigma$ is the Lebesgue surface measure on ∂D . Then

$$G[f] = 2^{n-1} i^n \int_{\partial D} \sum_{k>l} (-1)^{k+l} a_{k,l}(\zeta) \left(\frac{\partial f}{\partial \zeta_k} \rho_{\bar{l}} - \frac{\partial f}{\partial \zeta_l} \rho_{\bar{k}} \right) g(\zeta, z) d\sigma(\zeta).$$

Therefore, from the form of the integral operator Φ , we get that $G[f] = -\Phi[h]$. \square

We formulate a theorem on the form of partial derivatives of the function f .

Theorem 2. *Let D be a bounded domain with a twice smooth boundary and a function f is harmonic in D and $f \in \mathcal{C}^1(\bar{D})$ and $a_{k,l} \in \mathcal{C}^1(\partial D)$, $k, l = 1, \dots, n$, then*

$$\begin{aligned} \frac{\partial f}{\partial z_m} &= \frac{\partial Q[f]}{\partial z_m} = M[L_m(f) + \tilde{L}_m(h)] - \Phi[K_m(f) + \tilde{K}_m(h)], \\ \frac{\partial f}{\partial \bar{z}_m} &= \frac{\partial Q[f]}{\partial \bar{z}_m} = M[L_{\bar{m}}(f) + \tilde{L}_{\bar{m}}(h)] - \Phi[K_{\bar{m}}(f) + \tilde{K}_{\bar{m}}(h)]. \end{aligned}$$

Proof. From Lemma 1 and formula (6) we get that

$$Q[f] = M[f] + G[f] = M[f] - \Phi[h].$$

Now, using formulas (7)–(10), we obtain expressions for partial derivatives of the function f , and hence the operator $Q[f]$. Then

$$\begin{aligned} \frac{\partial f}{\partial z_m} &= \frac{\partial Q[f]}{\partial z_m} = \frac{\partial M[f]}{\partial z_m} - \frac{\partial \Phi[h]}{\partial z_m} = \\ &= M[L_m(f)] + \Phi[K_m(f)] + M[\tilde{L}_m(h)] - \Phi[\tilde{K}_m(h)] = \\ &= M[L_m(f) + \tilde{L}_m(h)] - \Phi[K_m(f) + \tilde{K}_m(h)]. \end{aligned}$$

Similarly

$$\begin{aligned} \frac{\partial f}{\partial \bar{z}_m} &= \frac{\partial Q[f]}{\partial \bar{z}_m} = \frac{\partial M[f]}{\partial \bar{z}_m} - \frac{\partial \Phi[h]}{\partial \bar{z}_m} = \\ &= M[L_{\bar{m}}(f)] - \Phi[K_{\bar{m}}(f)] + M[\tilde{L}_{\bar{m}}(h)] - \Phi[\tilde{K}_{\bar{m}}(h)] = \\ &= M[L_{\bar{m}}(f) + \tilde{L}_{\bar{m}}(h)] - \Phi[K_{\bar{m}}(f) + \tilde{K}_{\bar{m}}(h)]. \end{aligned}$$

\square

The boundary behavior of the potential of a simple layer and the Bochner–Martinelli integral operator is well known (see, for example, [7], [5, Ch. 1], [6, Ch. 1]). Therefore, from these properties of potentials, we obtain the statement

Theorem 3. *If $\partial D \in \mathcal{C}^\infty$ and $f \in \mathcal{C}^\infty(\partial D)$, $a_{k,l} \in \mathcal{C}^\infty(\partial D)$, $k, l = 1, \dots, n$, then the integral $Q[f](z)$ ($z \in D$, $z \in \mathbb{C}^n \setminus \bar{D}$) continues on \bar{D} and on $\mathbb{C}^n \setminus D$, respectively, as an infinitely differentiable function.*

For the Bochner–Martinelli integral, this property is noted in [8].

2. Integral representation for smooth functions

For the integral representation of (5), an analogue of the Bochner–Martinelli formula for smooth functions is valid (see, for example, [5, Ch. 1]).

Theorem 4. *Let D be a bounded domain with a smooth boundary and a function f of class $\mathcal{C}^1(\bar{D})$, then*

$$f(z) = \int_{\partial D} f(\zeta)U(\zeta, z) - \int_D \bar{\partial}f(\zeta) \wedge U(\zeta, z), \quad z \in D, \quad (11)$$

where the operator $\bar{\partial} = \sum_{k=1}^n \frac{\partial}{\partial \bar{\zeta}_k} d\bar{\zeta}_k$, and the integral of the domain in (11) converges absolutely.

We will now prove an analogue of this formula for our operator Q .

Theorem 5. *Let D be a bounded domain with a smooth boundary and a function f of class $\mathcal{C}^1(\bar{D})$ and $a_{k,l} \in \mathcal{C}^1(\bar{D}), k, l = 1, \dots, n$, then*

$$f(z) = \int_{\partial D} f(\zeta)(U(\zeta, z) + W(\zeta, z)) - \int_D \bar{\partial}f(\zeta) \wedge (U(\zeta, z) + W(\zeta, z)), \quad z \in D, \quad (12)$$

and the integral of the domain in (12) converges absolutely.

Proof. Since the theorem is true for the operator $U(\zeta, z)$ (Theorem 1.3 in [5]), it remains to show that

$$\int_{\partial D} f(\zeta)W(\zeta, z) - \int_D \bar{\partial}f(\zeta) \wedge W(\zeta, z) = 0, \quad z \in D.$$

Let $z \in D$, by $B(z, \varepsilon)$ denote a ball of radius $\varepsilon > 0$ centered at z , and its boundary by $S(z, \varepsilon)$. For sufficiently small ε , using the Stokes formula, we obtain

$$\begin{aligned} \int_D \bar{\partial}f(\zeta) \wedge W(\zeta, z) &= \int_{D \setminus B(z, \varepsilon)} \bar{\partial}f(\zeta) \wedge W(\zeta, z) + \int_{B(z, \varepsilon)} \bar{\partial}f(\zeta) \wedge W(\zeta, z) = \\ &= \int_{\partial D} f(\zeta)W(\zeta, z) - \int_{S(z, \varepsilon)} f(\zeta)W(\zeta, z) + \int_{B(z, \varepsilon)} \bar{\partial}f(\zeta) \wedge W(\zeta, z). \end{aligned}$$

According to Green's formula (2), for the modulus of the integral, we get

$$\left| \int_{S(z, \varepsilon)} f(\zeta)W(\zeta, z) \right| = \left| \int_{S(z, \varepsilon)} g(\zeta, z)\mu_f \right| \leq \frac{(n-2)!}{(2\pi)^n \varepsilon^{2n-2}} \int_{S(z, \varepsilon)} |\mu_f| \leq C\varepsilon,$$

then $\lim_{\varepsilon \rightarrow +0} \int_{S(z, \varepsilon)} f(\zeta)W(\zeta, z) = 0$.

Since the singularity of the integral $\int_{B(z, \varepsilon)} \bar{\partial}f(\zeta) \wedge W(\zeta, z)$ is equal to $(2n-1) < 2n$, then

$$\lim_{\varepsilon \rightarrow +0} \int_{B(z, \varepsilon)} \bar{\partial}f(\zeta) \wedge W(\zeta, z) = 0. \text{ From here we get the necessary equality.}$$

□

This work is supported by the Krasnoyarsk Mathematical Center and financed by the Ministry of Science and Higher Education of the Russian Federation in the framework of the establishment and development of regional Centers for Mathematics Research and Education (Agreement No. 075-02-2025-1606) and by the fundamental project IL-5421101746 of the Uzbek National University.

References

- [1] V.S.Vladimirov, Methods of the theory of functions of many complex variables, MIT Press, Cambridge, MA, 1966.
- [2] B.V.Shabat, Introduction to complex analysis. Part 2. Function of several variables, Amer. Math. Soc., Providence, 1992.

- [3] R.M.Range, Holomorphic functions and integral representations in several complex variables, Springer Verlag, 1986.
- [4] L.A.Aizenberg, A.P.Yuzhakov, Integral Representations and Residues in Multidimensional Complex Analysis, Amer. Nath. Soc., Providence, RI, 1983.
- [5] A.M.Kytmanov, The Bochner-Martinelli integral and its applications. Basel, Boston, Berlin: Birkhäuser, 1995.
- [6] A.M.Kytmanov, S.G.Myslivets, Multidimensional Integral Representations. Problems of Analytic Continuation. Springer Verlag, Basel, Boston, 2015.
- [7] N.M.Günter, Potential theory and its applications to basic problems of mathematical physics, Ungar, New York. 1967.
- [8] S.G.Myslivets, Integral Operator of Potential Type for Infinitely Differentiable Functions *Journal of Siberian Federal University, Mathematics and Physics*, 17(2024), no. 4, 464–469. EDN: GIMRFC

Об одном интегральном представлении типа потенциала

Александр М. Кытманов

Симона Г. Мысливец

Сибирский федеральный университет
Красноярск, Российская Федерация

Аннотация. Цель работы состоит в исследовании свойств одного интегрального представления для голоморфных функций (типа Коши–Фанташье), ядро которого состоит из производных фундаментального решения уравнения Лапласа.

Ключевые слова: интеграл Бохнера-Мартинелли, ограниченная область, граничное поведение.

EDN: AFWNXZ
УДК 550.344, 517.9

Sommerfeld's Method for Solving the Dynamic Rigid Stamp Indentation Problem

Alexey G. Fatyanov*

Institute of Computational Mathematics and Mathematical Geophysics SB RAS
Novosibirsk, Russian Federation

Received 10.08.2024, received in revised form 15.09.2024, accepted 24.10.2024

Abstract. The work is based on Sommerfeld's ideas in solving the diffraction problem on a mirror segment. On this basis, a new method for solving the dynamic problem for a vibrating rigid stamp is developed. The solution is sought by minimizing a functional. Sommerfeld's method is used to select the only physically correct solution. Namely, the expressions in the minimized functional are reduced to dimensionless form. This allowed us to create a method for calculating wave acoustic fields for arbitrary radius of a rigid stamp. Applied to vibration problems, the solution for a small rigid stamp is obtained in explicit form. This allows stable calculation of vibrating wave fields for teleseismic distances. The program created on this basis allows carrying out calculations even on personal computers with OpenMP parallelization. A result of analytical calculations the distinction of wave fields for a stamp and a distributed source of small dimensions are shown.

Keywords: Sommerfeld method, mixed problem, hard stamp, functional minimization, dimensionality equalization, acoustic waves.

Citation: A.G. Fatyanov, Sommerfeld's Method for Solving the Dynamic Rigid Stamp Indentation Problem, J. Sib. Fed. Univ. Math. Phys., 2025, 18(3), 300–308. EDN: AFWNXZ.



Introduction

A considerable number of works are devoted to methods of solving mixed problems. Let us note the works [1–6]. In the paper, based on the solution of the diffraction problem [1], a new method for solving the dynamic problem for a vibrating rigid die is developed. This method for solving the dynamic problem for a vibrating rigid stamp, which allows to carry out calculations for teleseismic distances. The acoustic case for an arbitrary layered medium is considered. Following [2, 3, 4, 6] in a cylindrical coordinate system on one part of the daytime surface ($z=0$) is given a displacement different from zero; on the other — stress equal to zero. Following [1], the solution is sought by minimising the functional. This method of solution construction admits an infinite number of mathematically correct solutions. And only one of them will give physically correct solution. To choose the only solution, the behaviour of the solution in the vicinity of the point of discontinuity of the of boundary conditions (condition on an rib) [3, 4, 5]. But other methods are also known. In [2], it is assumed that the force applied to the stamp is known. On this basis of the only solution is found. In this paper, in order to select the only physically correct solution, Sommerfeld's method [1] is used. Namely, in the minimised functional, the expressions are reduced to dimensionless form (dimensionalities is equalised). As a result, the problem is

*agfat@mail.ru <https://orcid.org/0000-0001-6038-6505>

© Siberian Federal University. All rights reserved

reduced to the solution of a system of linear algebraic equations (SLAE). This allowed us to create a method of calculation of wave acoustic fields for arbitrary radius of rigid stamp. SLAE is solved on the basis of the open package of linear algebra, developed at Moscow State University. In this case, the solution of SLAE for significant spatial and temporal scales requires the use of technology of high-performance computing. That is, for calculations it is necessary to use supercomputer. For vibration problems, the size of the seismic source (stamp) is always much smaller than the length of the wavelength. In this case, an explicit received formula for the solution in the spectral domain. For it it is no longer necessary to solve SLAE. And it allows to stably calculate vibrating wave fields for teleseismic distances. The programme created on this basis allows to carry out calculations even on personal computers with OpenMP parallelisation. A result of analytical calculations, the distinction between the wave fields for a stamp and a distributed source of small sizes.

1. Statement of the task

The mathematical statement of the task of modelling P waves is formulated in a cylindrical coordinate system ($0 \leq r < \infty$, $0 \leq z < \infty$) in the axisymmetric case as follows. Determine the function $u(z, r, t)$ from the equation:

$$\frac{\partial^2 u}{\partial z^2} + \frac{1}{r} \frac{\partial u}{\partial r} + \frac{\partial^2 u}{\partial r^2} = \frac{1}{V^2(z)} \frac{\partial^2 u}{\partial t^2}. \quad (1)$$

In this paper, the problem of wave propagation from a vibrating rigid stamp. Statements of the task for a rigid stamp are given in many works [2, 3, 4, 6]. Of these, the boundary conditions in the axisymmetric case for the wave displacement u in the cylindrical coordinate system (r, z) are set as follows:

$$u|_{z=0} = f(t), \quad r \leq r_0, \quad (2)$$

$$\frac{\partial u}{\partial z}|_{z=0} = 0, \quad r > r_0. \quad (3)$$

The initial conditions are added to the (1)–(3) formulas

$$u = \frac{\partial u}{\partial t}|_{t=0} = 0. \quad (4)$$

In (1)–(3) r_0 is the radius of the stamp, the velocity $V(z) > 0$ is an arbitrary piecewise function (layered medium). The input impulse $f(t)$ is chosen as a Gaussian function $e^{-(\pi f_0 t/2)^2} \sin(2\pi f_0 t)$, f_0 is its carrier frequency.

In addition, we still need a condition for the isolation of a single physically correct solution, which will be discussed below.

2. Analytical method of solution

The solution (1)–(4) is constructed by using finite integral transformations in terms of of time t and lateral variable r :

$$u(z, r, t) = \frac{1}{2T} \sum_{j=-\infty}^{\infty} u(z, r, \omega_j) \exp(-\omega_j \cdot t). \quad (5)$$

$$u(z, r, \omega_j) = \frac{2}{a^2} \sum_{n=1}^{\infty} u(z, k_n \omega_j) J_0(k_n r) / J_1^2(k_n a). \quad (6)$$

In (5) and (6) $\omega_j = j \cdot \pi / T$, $k_n = x_n / a$. Where x_n are the roots of the equation $J_0(x) = 0$. T and a are the boundaries of the computational domain.

In the following, irrelevant indices will be omitted to shorten the notation. Also, for the sake of clarity, we first consider the case of a homogeneous half-space. In this case, the equation (1) using (5)–(6) will turn into an ordinary differential equation:

$$\frac{d^2 u(z, k_n, \omega)}{dz^2} = (k_n^2 - \omega^2 / V^2) u(z, k_n, \omega). \quad (7)$$

From (7) we elementarily obtain

$$u(z, k_n, \omega) = u(0, k_n, \omega) \exp(-\nu_n z) = C_n \exp(-\nu_n z), \quad (8)$$

$$\frac{du(z, k_n, \omega)}{dz} = -\nu_n C_n \exp(-\nu_n z). \quad (9)$$

The formulas (8) and (9) give expressions for the displacement u and "stress" $\frac{du}{dz}$ as a function of the as yet unknown coefficients C_n , $\nu_n = \sqrt{k_n^2 - \omega^2 / V^2}$. In the following, for the sake of clarity, "stress" will not be taken in quotes. To satisfy the conditions at infinity in (8)–(9), the principle of limiting absorption is used. For this purpose instead of ω^2 we take $\omega^2 + i \cdot \varepsilon \cdot \omega$, where ε is a small value [7].

Given (8)–(9), the boundary conditions (2)–(3) in the spectral region (k, ω) will look as follows:

$$\sum_{m=1}^{\infty} C_m \beta_m J_0(k_m r) = F(\omega), \quad r \leq r_0, \quad (10)$$

$$-\sum_{m=1}^{\infty} \nu_m C_m \beta_m J_0(k_m r) = 0, \quad r > r_0. \quad (11)$$

In (10)–(11) $F(\omega)$ is the spectrum of the function $f(t)$ and the abbreviation is introduced: $\beta_m = 2 / \langle a^2 J_1^2(k_m a) \rangle$.

To find the unknown coefficients of C_m , following Sommerfeld [1] we consider the quadratic errors corresponding to (10) and (11):

$$\int_0^{r_0} \left| F - \sum_m C_m \beta_m J_0(k_m r) \right|^2 r dr \quad \text{and} \quad \int_{r_0}^a \left| \sum_m \nu_m C_m \beta_m J_0(k_m r) \right|^2 r dr. \quad (12)$$

The sum of both errors in (12) should reach a minimum at the appropriate choice of C_m . Differentiating over C_n^* we obtain a system of linear algebraic equations (SLAE):

$$\sum_m (a_{n,m} + \nu_n^* \nu_m b_{n,m}) \beta_m C_m = F(\omega) \int_0^{r_0} r J_0(k_n r) dr = F(\omega) g_n. \quad (13)$$

In (13) and hereafter, an asterisk denotes a complex-conjugate quantity. The matrices $a_{n,m}$ and $b_{n,m}$ using Green's formula [1] are calculated exactly by explicit formulas.

$$a_{nn} = \int_0^{r_0} r J_0(k_n r) J_0(k_n r) r dr = \frac{r_0^2}{2} [J_0^2(k_n r_0) + J_1^2(k_n r_0)],$$

$$a_{nm} = r_0 \frac{k_m J_0(k_n r_0) J_1(k_m r_0) - k_n J_0(k_m r_0) J_1(k_n r_0)}{k_m^2 - k_n^2}, \quad n \neq m. \quad (14)$$

Similarly for $b_{n,m}$.

In this case, the time frequency ω is included as a parameter in the SLAE (13).

$$g_n = \int_0^{r_0} r J_0(k_n r) dr = r_0 J_1(k_n r_0) / k_n. \quad (15)$$

The equality (11) can be multiplied by any real number X different from zero. In this case, when minimising the functional, instead of the SLAE (13) we obtain:

$$\sum_m (a_{n,m}/X^2 + \nu_n^* \nu_m b_{n,m}) \beta_m C_m = F(\omega) g_n / X^2 = F(\omega) f_n. \quad (16)$$

SLAE (16) has an infinite number of mathematically correct solutions for different X . And only one will give a physically correct solution [5]. At present, the only physically correct solution is chosen on the basis of the asymptotics of the solution in the vicinity of the stamp edge (rib) [3, 4, 5].

However, other methods are also known. In [2], it is assumed that the force applied to the stamp is known. Based on this, a correct solution is received. In this paper, the single solution is determined based on the method of Sommerfeld's method [1]. At the consideration of diffraction on a part of a mirror, he brings the corresponding quantities to a dimensionless form. Since ν_n has a dimension inverse to the metre, then X must have a dimension in metres. From (15) and (16), consider the expression g_n/X^2 . Require, that at $r_0 \rightarrow 0$ $g_n/X^2 \rightarrow 1$. That is, so that at the point stamp ($r_0 = 0$) there is a concentrated impact. Since $J_1(\alpha) \approx \alpha/2$ when α is small, we obtain that $X = r_0/\sqrt{2}$. The value X will have the dimension in metres. Thus the dimensions in (10) and (11) will coincide. In this case

$$f_n = g_n/X^2 = 2J_1(k_n r_0)/k_n r_0. \quad (17)$$

The expression (17) coincides with the source of the normal force uniformly distributed over the area of the circle on a flat day surface [8].

For a stamp of arbitrary sizes, the SLAE (16) is solved using the software open source software developed at Moscow State University.

For vibration problems, the size of the seismic source (stamp) is always much smaller than the wavelength. In this case, following [1], an approximate explicit formula for the solution in the spectral region is obtained. Let $r_0 \ll \lambda$. Here λ is the wavelength. This condition is known to be fulfilled for the radiating platform of the vibrator.

It is known, for example, from [1] that at small ρ

$$J_0(\rho) \sim 1, \quad J_1(\rho) \sim \rho/2. \quad (18)$$

In (18), terms above the first order of smallness are discarded.

Consider the SLAE (16) at small r_0 . Using (18) we obtain

$$a_{nn}/X^2 = \frac{2}{r_0^2} \frac{r_0^2}{2} [J_0^2(k_n r_0) + J_1^2(k_n r_0)] \sim 1, \quad a_{nm}/X^2 \sim 1. \quad (19)$$

Given (19), the SLAE of (16) will take the form:

$$\sum_m \beta_m C_m + \nu_n^* \nu_n C_n = F(\omega) f_n. \quad (20)$$

After the transformation $\beta_m C_m = x_m$ (20) will take the elementary form:

$$\frac{\nu_n \nu_n^*}{\beta_n} x_n + \sum_m x_m = F(\omega) f_n. \quad (21)$$

We find the solution to (21) as follows. Assume

$$x_m = c(F(\omega) f_m \beta_m / \nu_m \nu_m^*). \quad (22)$$

Substituting (22) into (21) we determine c .

$$c = \frac{f_n}{f_n + s} = \frac{1}{1 + \frac{1}{f_n} s}. \quad (23)$$

In (23)

$$s = \sum_m \frac{\beta_m}{\nu_m \nu_m^*} f_m. \quad (24)$$

Since from (17) and (18)

$$\frac{1}{f_n} = \frac{k_n r_0}{2} \frac{1}{J_1(k_n r_0)} \sim 1. \quad (25)$$

In (25), terms above the first order of smallness are also discarded.

Taking into account (25) we obtain

$$c = c(\omega) = \frac{1}{1 + s}. \quad (26)$$

Since $C_m = x_m / \beta_m$ then from (22–26) taking into account (8) we obtain the the solution for a stamp of small dimensions. On the day surface $z = 0$ the solution looks as follows:

$$u(0, k_n, \omega) = c \frac{F(\omega)}{\nu_n \nu_n^*} f_n. \quad (27)$$

Verification of the accuracy of the formula (27) was performed by comparing it with the solution of the SLAE (16) in the physical domain. For transition to the physical domain formulas (5) and (6) were used. The result was a match with an accuracy of three digits.

At present, the formulations often used for vibration problems are, when the stress distribution on the day surface is given. In [9] it is stated that such a problem is solved much easier than the mixed problem. If there is no need to solve the mixed problem at small sizes of the source.

Let us set a uniform stress distribution on the day surface at $0 < r \leq r_0$:

$$\frac{\partial u}{\partial z} /_{z=0} = \frac{2}{r_0^2} f(t), \quad r \leq r_0; \quad \frac{\partial u}{\partial z} /_{z=0} = 0, \quad r > r_0. \quad (28)$$

The solution of the problem (1), (28), (4) is well known [8]. In the notation of this paper, it is as follows:

$$u(0, k_n, \omega) = \frac{F(\omega)}{\nu_n} f_n. \quad (29)$$

Thus, the solution for a rigid stamp (27) is fundamentally different from the solution for a radiation source in the form of a distributed force (29).

In this approach it is quite simple to take into account the layering of the medium. For this purpose second-order ordinary differential equation (7) by introducing a auxiliary function $\alpha(z)$ such that $\frac{du}{dz} = -\alpha(z)u$ in each layer reduces to a first order equation [10].

$$\frac{d\alpha}{dz} - \alpha^2 = -\nu^2. \quad (30)$$

The nonlinear equation (30) has an explicit solution. Let the medium consists of N layers. And all of them are located on a half-space. In this case, the recalculation of the auxiliary function α_p from the layer with index p to the layer with index $p - 1$. Index $p - 1$ is made by the formula:

$$\alpha_{p-1} = \nu_p \frac{\alpha_p + \nu_p \operatorname{th}(\nu_p(h_p - h_{p-1}))}{\nu_p + \alpha_p \operatorname{th}(\nu_p(h_p - h_{p-1}))}. \quad (31)$$

In (31) $h_p - h_{p-1}$ is the power of the layer with index k .

The process starts with the layer with index N. In this case, $\alpha_N = \sqrt{k_n^2 - \omega^2/V_{N+1}^2}$, where V_{N+1} is the velocity in the half-space. Finally, using the differential sweep method (31). α_0 is found [10]. And then the solution for a rigid stamp of small size will be given by the formula (27), in which ν is replaced by α_0 .

3. Results of the analytical solution

Fig. 1 gives the wavefield for the rigid stamp at $z=0$. On the vertical axis is the time, milliseconds (increases down); on the horizontal axis is the distance, kilometres. The initial distance is 1 kilometre and the final distance is 5 kilometre. The radius of the rigid stamp $r_0=1$ metre. A homogeneous half-space is considered. The velocity in the half-space $V=1$ km/sec. The pulse $f(t)$ in the source is taken as a Gaussian function with a carrier frequency of 50 hertz. Fig. 1 (A) shows the displacement, and Fig. 1 (B) — stress. It can be seen from Fig. 1 that the displacement occurs and the stress is zero. Thus it is numerically shown that the condition (3) is fulfilled.

Next, the wave fields for a stamp and a distributed source are given. Moreover, the rigid stamp and the distributed source have small sizes. For the simplest model of a layer on a half-space is taken for comparison. Fig. 2 is given the wave field with a distributed source. A layer on a half-space is taken. The velocity in the layer is 1 km/sec and in the half-space is 2 km/sec. The thickness of the layer is 1 km. The distributed source has a size of 1 metre. In Fig. 3 shows the wave field in the case for a 1 metre size rigid stamp. The other parameters are the same as in Fig. 2. In Figs. 2 and 3, P — direct wave, PP — reflected wave, PPP — multiple wave. It can be seen from Fig. 2 that in the case of supercritical reflection, for example, the reflected wave becomes larger than the direct wave. This is consistent with wave theory [11]. In the case of the rigid stamp in Figure 3, the wave dynamics strongly changes. Thus, the wave fields are different for a rigid stamp and a distributed source of small sizes.

Conclusions

In this paper, based on Sommerfeld's ideas, a new method of solving the dynamic problem for a rigid stamp. It allows to carry out calculations of acoustic waves for teleseismic distances.

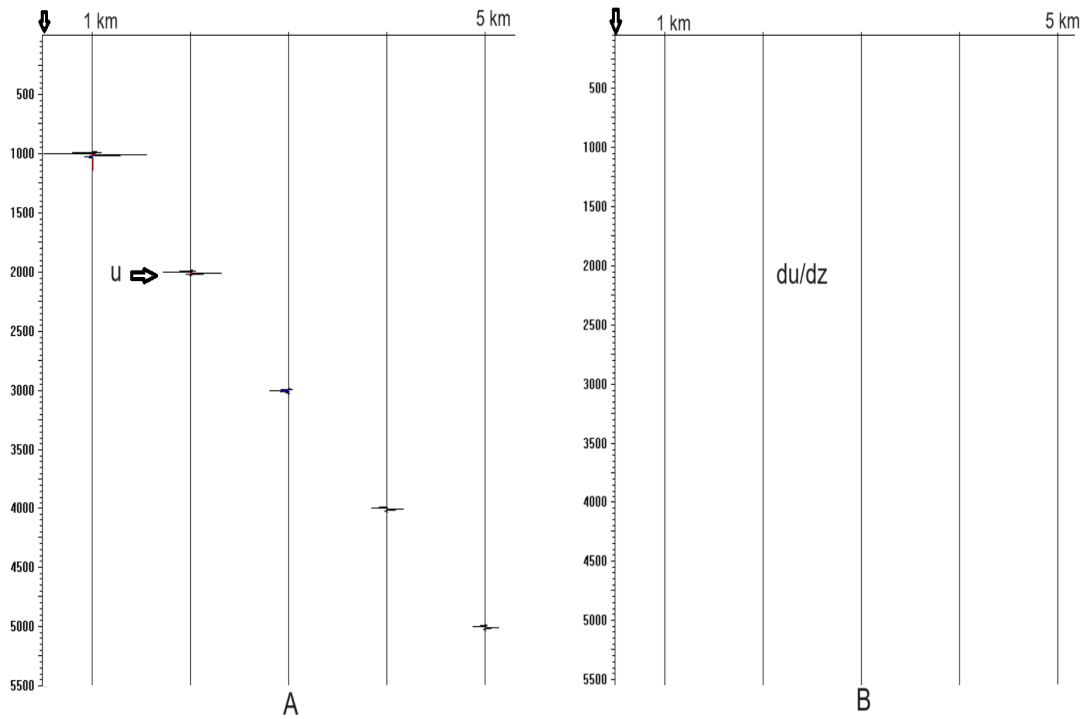


Fig. 1. Wave fields for a rigid stamp. Half-space. The radius of the stamp is 1 metre. Displacement field (A). Stress field (B)

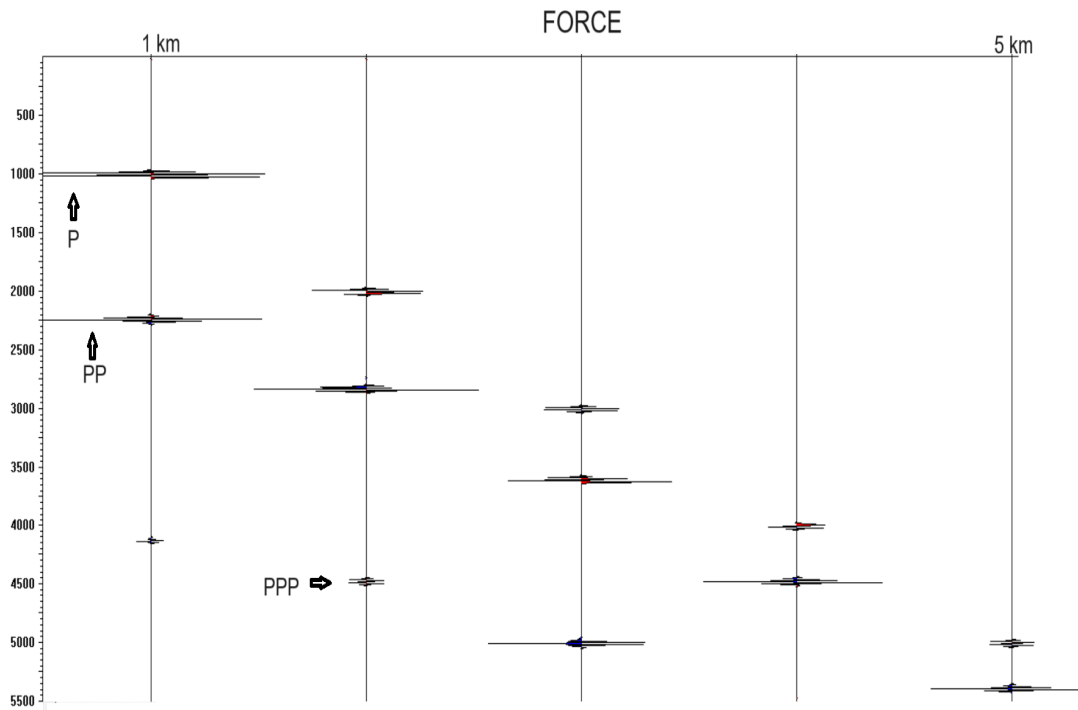


Fig. 2. Wave field for a distributed source of 1 metre. The layer on a half-space

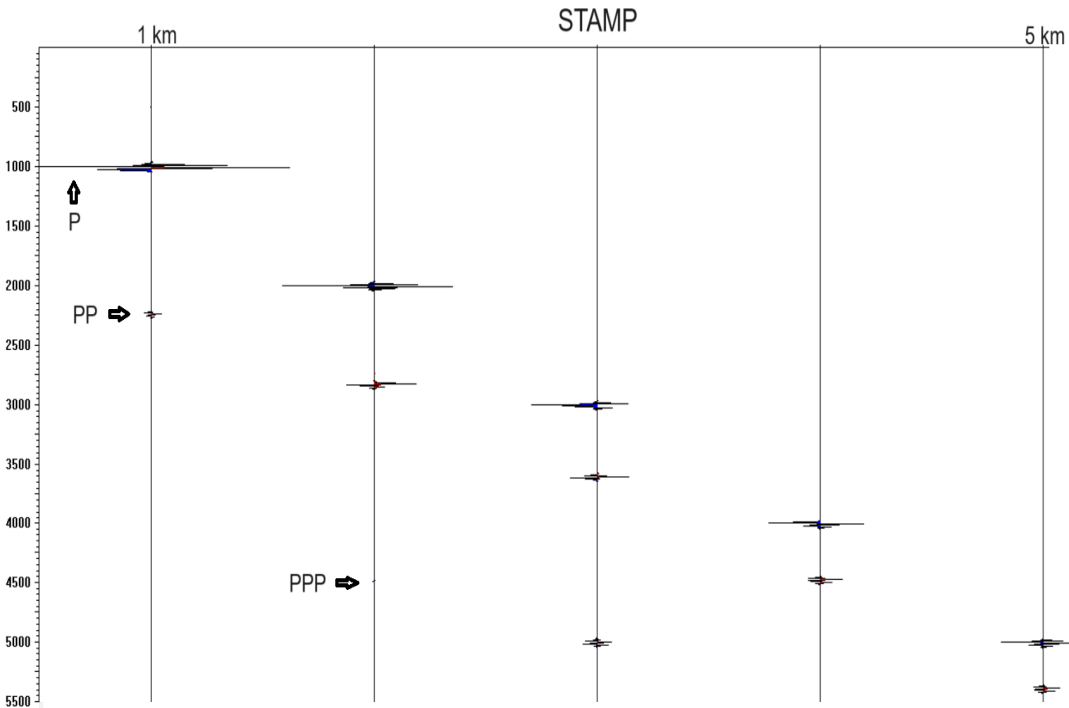


Fig. 3. Wavefield for a 1 metre rigid stamp. The layer on a half-space

The method is based on minimisation of a functional. The functional includes the displacement at the foot of the stamp and the stress outside the stamp. Knowing the law of stress distribution under the plate of the seismic source is not necessary for this method. In order to choose the only physically correct solution of this diffraction problem, the Sommerfeld method is used. Namely, in the minimised functional, the expressions are reduced to a dimensionless form (dimensionality is equalised). From the minimisation of the functional in the standard way, a system of linear algebraic equations (SLAE) is obtained. For its solution is used open source software developed at the MSU.

Applied to vibration problems, when the size of the stamp is much smaller than the wavelength, an explicit formula for the solution is obtained. In this case, there is no need to solve SLAE. Therefore, the created programme allows to calculate vibration wave fields for teleseismic distances even on personal computers with OpenMP parallelisation. As a result of analytical calculations, a distinction was found between the wave fields for a rigid stamp and a distributed source in the case of their small sizes.

This work was conducted within the framework of State Assignments of the Institute of Computational Mathematics and Mathematical Geophysics SB RAS, project No. FWNM-2025-0004.

References

- [1] A.Sommerfeld, Partielle differentialgleichungen der physik, Leipzig, 1948.
- [2] S.G.Mikhlin, Application of integral equations, Moscow, 1947 (in Russian).

- [3] W.Z.Parton, P.I.Perlin, Methods of mathematical theory of elasticity, Moscow, 1981 (in Russian).
- [4] V.A.Babeshko, The method of generalised factorisation in spatial dynamic mixed problems of elasticity theory, Moscow, 1984 (in Russian).
- [5] R.Mittra, S.Lee, Analytical techniques in the theory of guided waves, New York, 1971.
- [6] A.V.Razin, A.L.Sobisevich, Geoacoustics of layered media, Moscow, 2012 (in Russian).
- [7] V.A.Babeshko, I.S.Chichinin, Problems of vibrational research of the Earth, Moscow, 1977, 53–61, (in Russian).
- [8] V.V.Gushchin, V.P.Dokuchaev, Y.M.Zaslavsky, V.D.Konyukhova, Earth exploration by non-explosive seismic sources, Moscow, 1981, 113–126 (in Russian).
- [9] I.S.Chichinin, Vibratory radiation of seismic waves, Moscow, 1984 (in Russian).
- [10] A.G.Fatyanov, A semi-analytic method for solving direct dynamical problems in layered media, *Dokl. AN SSSR*, **310**(1990), no. 2, 323–327.
- [11] K.Aki, P.G.Richards, Quantitative seismology, San Francisco, 1983.

Метод Зоммерфельда решения динамической задачи о вдавливании жесткого штампа

Алексей Г. Фатьянов

Институт вычислительной математики и математической геофизики СО РАН
Новосибирск, Российская Федерация

Аннотация. Работа основана на идеях Зоммерфельда при решении задачи дифракции на сегменте зеркала. На этой основе развит новый метод решения динамической задачи для вибрирующего жесткого штампа. Решение ищется с помощью минимизации функционала. Для выбора единственного физически верного решения используется метод Зоммерфельда. А именно, в минимизируемом функционале выражения приводятся к безразмерному виду. Это позволило создать метод расчета волновых акустических полей для произвольного радиуса жесткого штампа. Применительно к вибрационным задачам получено решение для малого жесткого штампа в явном виде. Это позволяет устойчиво вычислять вибрационные волновые поля на телесеismicкие расстояния. Созданная на этой основе программа позволяет проводить расчеты даже на персональных компьютерах с распараллеливанием OpenMP. В результате аналитических расчетов показано отличие волновых полей для штампа и распределенного источника малых размеров.

Ключевые слова: метод Зоммерфельда, смешанная задача, жесткий штамп, минимизация функционала, выравнивание размерностей, акустические волны.

EDN: EFCEHY
УДК 535.34; 544.47

Solid-phase Synthesis and Photocatalytic Properties of $\text{Bi}_2\text{SiO}_5/\text{Bi}_{12}\text{SiO}_{20}$ Heterostructures

Aleksandra G. Golubovskaya*

Tamara S. Kharlamova†

Valery A. Svetlichnyi‡

Tomsk State University
Tomsk, Russian Federation

Received 29.10.2024, received in revised form 13.12.2024, accepted 24.01.2025

Abstract. In this work, a new approach to the preparation of heterostructured nanoparticles (NPs) based on bismuth silicates $\text{Bi}_2\text{SiO}_5/\text{Bi}_{12}\text{SiO}_{20}$ is proposed and implemented. This approach is based on solid-phase synthesis by annealing of a pre-homogenized mixture of $\beta\text{-Bi}_2\text{O}_3$ and SiO_2 powders in different ratios. For this purpose, industrial silica nanopowder and β -bismuth oxide NPs powder obtained by pulsed laser ablation (PLA) in air are used. The morphology, phase composition and optical properties of the obtained materials are studied. By changing the ratio of precursors, the powders similar in structure to single-phase bismuth silicates Bi_2SiO_5 and $\text{Bi}_{12}\text{SiO}_{20}$ as well as heterostructured NPs on their basis are obtained. The activity of the photocatalysts in the reactions of Rhodamine B (Rh B) decomposition and selective oxidation of 5-hydroxymethylfurfural (5-HMF) is estimated. The best photocatalytic activity is demonstrated by powders with a similar $\text{Bi}_2\text{SiO}_5/\text{Bi}_{12}\text{SiO}_{20}$ (or 4Bi: 1Si) phase ratio. As a result of the analysis of the data obtained, the formation of a type II heterojunction is proposed.

Keywords: solid-phase synthesis, bismuth silicates, heterostructured nanoparticles, pulsed laser ablation, photocatalysis, heterojunction II type, rhodamine B, 5-hydroxymethylfurfural.

Citation: A.G. Golubovskaya, T.S. Kharlamova, V.A. Svetlichnyi, Solid-phase Synthesis and Photocatalytic Properties of $\text{Bi}_2\text{SiO}_5/\text{Bi}_{12}\text{SiO}_{20}$ Heterostructures, J. Sib. Fed. Univ. Math. Phys., 2025, 18(3), 309–319. EDN: EFCEHY.



Introduction

In recent years, photocatalytic (PC) technologies have attracted increasing interest due to their great potential for solving challenges in green energy, bioresource processing, and ecology [1–3]. Photocatalysis is effective for cleaning the industrial wastewater from synthetic dyes, phenols, and antibiotics [4]. Another promising area of photocatalysis is the production of valuable materials with high added value by oxidizing intermediate products of processing of biomass, the most accessible raw material on Earth [5]. For instance, selective photooxidation of 5-hydroxymethylfurfural (5-HMF) can produce 5-formyl-2-furancarboxylic acid (FFCA) and subsequently 2,5-furandicarboxylic acid (FDCA) [6]. The FFCA and FDCA are an alternative substitute for phthalic acid and furan polymers, which are obtained from fossil resources and are

*aleksandra.golubovskaya@mail.ru <https://orcid.org/0000-0002-9273-1825>

†kharlamova83@gmail.com <https://orcid.org/0000-0002-6463-3582>

‡v_svetlichnyi@bk.ru <https://orcid.org/0000-0002-3935-0871>

© Siberian Federal University. All rights reserved

widely used in industry. The ability to use sunlight as a radiation source and non-toxic, low-cost materials as catalysts makes photocatalysis a safe and environmentally friendly method.

The effectiveness of PC technologies primarily depends on the catalyst characteristics. Currently, the most successful and promising photocatalysts are materials based on semiconductor nanoparticles (NPs). Due to a wide choice of semiconductor materials, it is possible to select a photocatalyst with the desired value of the band gap (E_g) for optimal light absorption. The use of NPs as photocatalysts is due to their unique physical-chemical properties, including size, morphology, surface charge, large specific surface area, spectroscopic characteristics, and the presence of defects. Among the wide variety of photocatalysts, bismuth-based materials are distinguished [7, 8], in particular bismuth silicates (Bi_2SiO_5 , $\text{Bi}_{12}\text{SiO}_{20}$) [9, 10], which feature suitable physical-chemical properties. However, as in the majority of single-phase semiconductors, a relatively rapid charge recombination occurs in bismuth silicates, which reduces their PC activity [11]. The best solution to this problem is currently considered to be the creation of heterostructured NPs consisting of two or more semiconductors with different band gaps. If the heterojunction is of the so-called type II, then spatial charge separation occurs better in such a composite particle. If the Z-scheme of operation is implemented in NPs based on such a heterojunction, then it is also possible to increase the oxidation-reduction capacity of the photocatalyst [12, 13].

An important task in the development of the PC technologies is the elaboration of methods to synthesize new photocatalysts. It is possible to increase the variability and effectively control the structure and properties of materials by combining different synthesis methods. This approach also allows one to avoid the limitations inherent in any single method. For instance, along with traditional chemical synthesis approaches, the laser methods to synthesize the nanomaterials for photocatalysis have recently been actively developed [14, 15]. Thus, by combining procedures such as pulsed laser ablation (PLA), laser treatment (LT) of colloids, coprecipitation, drying and annealing, various single-phase and composite particles based on bismuth oxides and silicates were obtained [16, 17].

In this work, a new approach to prepare the heterostructured NPs of bismuth silicates $\text{Bi}_2\text{SiO}_5/\text{Bi}_{12}\text{SiO}_{20}$ was proposed. The approach was based on solid-phase synthesis by annealing a pre-homogenized mixture of $\beta\text{-Bi}_2\text{O}_3$ and SiO_2 powders in different ratios by grinding. In this case, β -bismuth oxide powder obtained by PLA in air was used as one of the precursors. The structure and properties of the obtained powders as well as their PC activity in the reactions of Rhodamine B (Rh B) decomposition and selective oxidation of 5-HMF were studied and analyzed.

1. Materials and methods

The samples were obtained by the solid-phase synthesis from precursors, namely, SiO_2 and $\beta\text{-Bi}_2\text{O}_3$ nanopowders. The $\beta\text{-Bi}_2\text{O}_3$ powder was obtained by PLA of metallic bismuth (99.5 % purity) in atmospheric air. Ablation was carried out by focusing radiation of the LS2131-20 Nd:YAG laser (LOTIS TII, Belarus) (1064 nm, 7 ns, 150 mJ, 20 Hz) onto the target. The laser power density on the target surface was 1200 MW/cm². The nanopowder obtained as a result of the PLA consisted predominantly of the β -bismuth oxide phase (~ 94 %, with an admixture of non-stoichiometric bismuth oxide) with an average particle size of 20 nm and a specific surface area of 44 m²/g. The experimental technique and powder characteristics are described in detail in Ref. [18]. Silica of the Polysorb MP brand (JSC "Polysorb", Russia) had a particle size of less

than 10 nm and a specific surface area of 300 m²/g.

Bismuth and silicon oxides were mixed at atomic ratios Bi:Si = 2:1, 4:1, 6:1, 8:1, 12:1. The extreme ratios in this series correspond to stoichiometric Bi₂SiO₅ and Bi₁₂SiO₂₀ bismuth silicates. The mixtures were then thoroughly ground in an agate mortar for 15 min. The resulting series of samples was calcined at 600 °C in a muffle furnace for 4 h.

The size and shape of the NPs were analyzed using the CM12 transmission electron microscope (Philips, Netherlands). The crystal structure of the powders was studied by X-ray diffraction using the XRD 6000 diffractometer (Shimadzu, Japan). The phase content was analyzed using the Powder Diffraction Database PDF-4 (ICDD, USA) and PowderCell 2.4 software. The optical properties of the powders were studied by diffuse reflectance spectroscopy (DRS) in the UV-Vis range using the Cary 100SCAN spectrophotometer (Varian, Australia) with the DRA-CA-30I add-on (Labsphere, USA). The band gap (E_g) was estimated using two methods. The widely used Tauc method involved estimating the E_g by the edge of the absorption band using the following equation:

$$(\alpha h\nu)^{1/n} = A(h\nu - E_g), \quad (1)$$

where α is the absorption coefficient, $h\nu$ is the photon energy, A is a constant independent of energy, n is a parameter depending on the type of transition ($n = 2$ for indirect transition, $n = 1/2$ for direct transition).

As an alternative, the DASf (Derivation of Absorption Spectrum Fitting) method [19] was used. This method is not sensitive to the transition type and is particularly effective in assessing multiphase composite semiconductor particles. The E_g is estimated according to the equation:

$$\partial [\ln(\alpha/\lambda)] / \partial [1/\lambda] = m / (h\nu - E_g), \quad (2)$$

where m is constant, λ is a wavelength.

The PC activity of the samples was studied in the reactions of Rh B decomposition and selective oxidation of 5-HMF under LED irradiation with a wavelength of $\lambda = 375$ nm.

During the Rh B decomposition in water, the total optical power of the LEDs was $W_{rad} = 50$ mW, the solution volume was 30 ml, the photocatalyst mass was 15 mg, and the dye concentration was 5×10^{-6} M. Before the irradiation, the dispersion was stirred in the dark for 1 h to establish the adsorption-desorption equilibrium. After irradiation, the absorption spectra of the Rh B were recorded at regular intervals on the SF-56 spectrophotometer (LLC "SDB SPEKTR", Russia). Based on the change in the Rh B concentration at the absorption maximum at $\lambda = 553$ nm, the rate constant of the first-order reaction was calculated according to the equation:

$$\ln(C_0/C) = K_N t, \quad (3)$$

where C_0 is the concentration of Rh B at the initial moment of time, C is the current concentration value, t is the time of the PC reaction.

During selective photooxidation of 5-HMF, the total optical power of the LEDs was $W_{rad} = 2$ W. The reactor was loaded with 100 mg of the photocatalyst under study and 100 ml of the HMF aqueous solution with a concentration of 0.01 M. Na₂CO₃ was added as an alkaline agent at a concentration of 0.04 M. The dispersion was stirred in the dark for 1 h, similar to the experiment with Rh B. During the photocatalysis, the reactor with the dispersion was purged with atmospheric air. Photoproducts were analyzed by a high-performance liquid chromatography (HPLC) using the Prominence-i LC-2030C chromatograph (Shimadzu, Japan). The Rezex ROA-Organic Acid H+ (8 %) LC column and 0.025 M H₂SO₄ eluent as well as PDA detector

were used for separation and registration of the components. The 5-HMF, 5-hydroxymethyl-2-furancarboxylic acid (HMFCA), 2,5-furandicarboxylic acid (FDCA), 2,5-diformylfuran (DFF), and 5-formyl-2-furancarboxylic acid (FFCA) reference solutions were used to calibrate the detector, with the compound concentrations being determined from the peak areas. The analysis was carried out at the eluent flow rate of 0.8 mL/min, and the injection volume was 10 μ L. Prior to the analysis, 50 μ L aliquot taken was diluted with 1 mL of 0.0125 M H_2SO_4 . The HMF conversion $X(\text{HMF})$, product yield $Y(i)$, and selectivity $S(i)$, were calculated based on the concentrations determined by HPLC:

$$X(\text{HMF}) = \frac{C(\text{HMF})_0 - C(\text{HMF})}{C(\text{HMF})_0} \cdot 100\%, \quad (4)$$

$$S(i) = \frac{C(i)}{C(\text{HMF})_0 - C(\text{HMF})} \cdot 100\%, \quad (5)$$

where $C(\text{HMF})_0$ and $C(\text{HMF})$ are initial and current HMF concentrations, mol/l; $C(i)$ is current concentration of the i^{th} product, mol/l; $i = \text{HFCa, FDCA, DFF, and FFCA}$.

2. Results and discussion

Fig. 1 shows the diffraction patterns, and Tab. 1 presents the phase composition of the obtained samples. The samples synthesized at the 2Bi:1Si and 12Bi:1Si ratios are predominantly represented by the phases of the orthorhombic bismuth metasilicate Bi_2SiO_5 (PDF-4 #00-036-0287) with the space group $Cmc2_1$ and the lattice constants $a = 15.22 \text{ \AA}$, $b = 5.47 \text{ \AA}$, $c = 5.33 \text{ \AA}$ and cubic sillenite $\text{Bi}_{12}\text{SiO}_{20}$ (PDF-4 #04-007-2767) with the space group $I23$ and the lattice constant $a = 10.11 \text{ \AA}$, respectively. At intermediate non-stoichiometric Bi:Si ratios, two phases of bismuth silicates Bi_2SiO_5 and $\text{Bi}_{12}\text{SiO}_{20}$ are formed in the samples after calcination. Their content correlates with the bismuth oxide and silicon oxide ratios selected during the synthesis. Tab. 1 shows the data on the phase content in the samples and crystallite sizes (based on the calculation of coherent scattering regions (CSR)). According to the XRD analysis, with varying Bi-to-Si ratio, the CSR size changes in the range and does not exceed 56–90 nm.

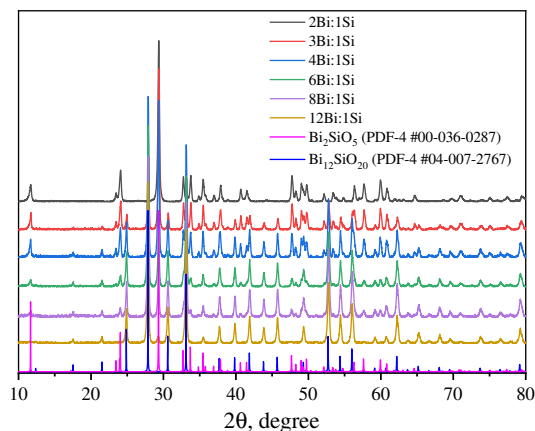


Fig. 1. XRD patterns for synthesized powders

Table 1. Phase content, CSR size, and E_g values for studied samples

Sample	Phase content, mass. %		CSR size, nm		E_g , eV	
	Bi_2SiO_5	$\text{Bi}_{12}\text{SiO}_{20}$	Bi_2SiO_5	$\text{Bi}_{12}\text{SiO}_{20}$	Tauc method	DASF method
2Bi:1Si	99.8	0.2	57	—	3.9	3.8
3Bi:1Si	66	36	87	90	3.3 / 3.9	3.3 / 3.8
4Bi:1Si	47	53	75	90	3.3 / 3.9	3.3 / 3.8
6Bi:1Si	21	79	56	77	3.2	3.0–3.3
8Bi:1Si	19	81	62	82	3.2	3.0–3.3
12Bi:1Si	3	97	—	82	3.1	3.0

In solid-phase synthesis, as a result of calcination, a homogenized mixture of powders of NPs of amorphous silica and highly active particles of the quasi-stable phase of the β -bismuth oxide, their effective chemical interaction with the formation of bismuth silicate phases, sintering and coarsening occur. Fig. 2 shows the morphology of the obtained particles. The NPs feature an irregular shape with rounded edges, some of the particles are fused together, forming spatial structures, which is typical for such materials [16]. In addition, at high magnification, small (~ 5 nm) spherical NPs are observed in the samples, which are located on the surface of large particles. Depending on the Bi-to-Si ratio, these particles can be attributed to either bismuth metasilicate or silica [16]. Due to the complex shape and sintering, we did not evaluate the particle size, but from Fig. 2, it is evident that with an increase in the Bi fraction in the samples in relation to Si, an increase in the average particle size can also be observed. The largest particles are characteristic of the sample obtained with a ratio of 12Bi:1Si and represented predominantly by the metasilicate phase. Fig. 2d shows a single composite particle of the 4Bi:1Si sample and the corresponding selected area electron diffraction (SAED) (Fig. 2e). The SAED data (Fig. 2e) show the presence of reflections belonging to two the Bi_2SiO_5 and $\text{Bi}_{12}\text{SiO}_{20}$ silicate phases, which is consistent with the XRD data and confirms the presence of the composite particles in the sample.

Fig. 3a shows the UV-vis spectra of the samples characterizing the absorption. They were obtained by transforming the reflectance spectra using the Kubelka-Munk function $F(R)$. For the nearly monophase 2Bi:1Si sample consisting of Bi_2SiO_5 , the absorption band edge lies in the spectral region of 300–340 nm. With an increase in the Bi concentration, the absorption band edge shifts towards the long-wavelength region of the spectrum to 380–420 nm for the 12Bi:1Si sample consisting of the $\text{Bi}_{12}\text{SiO}_{20}$ phase. For the 3Bi:1Si and 4Bi:1Si samples, two absorption bands can be observed in the spectra, which is consistent with the XRD analysis data on the presence of several phases in the sample.

Tab. 1 and in Fig. 3b (an example for the DASF method) show the results of the E_g estimation. According to the literature data [20, 21], both Bi_2SiO_5 and $\text{Bi}_{12}\text{SiO}_{20}$ are direct-gap semiconductors, the E_g values for them are 3.9–3.5 eV and 2.9–3.3 eV, respectively, and can vary depending on the particle size and a number of other factors. In our case, for single-phase bismuth metasilicate Bi_2SiO_5 (sample 2Bi:1Si), the E_g value is estimated by both Tauc and DASF methods as 3.8–3.9 eV, for sillenite $\text{Bi}_{12}\text{SiO}_{20}$ (sample 12Bi:1Si), the E_g value is 3.0–3.1 eV.

In heterostructured NPs, the absorption of the short-wave semiconductor can be observed up to the 4Bi:1Si ratio. The optical width of its band gap remains unchanged (the position of the short-wave peak in Fig. 3b). The long-wave band related to $\text{Bi}_{12}\text{SiO}_{20}$ and the corresponding band gap with an increase in the content of this phase in the heterostructure is shifted towards

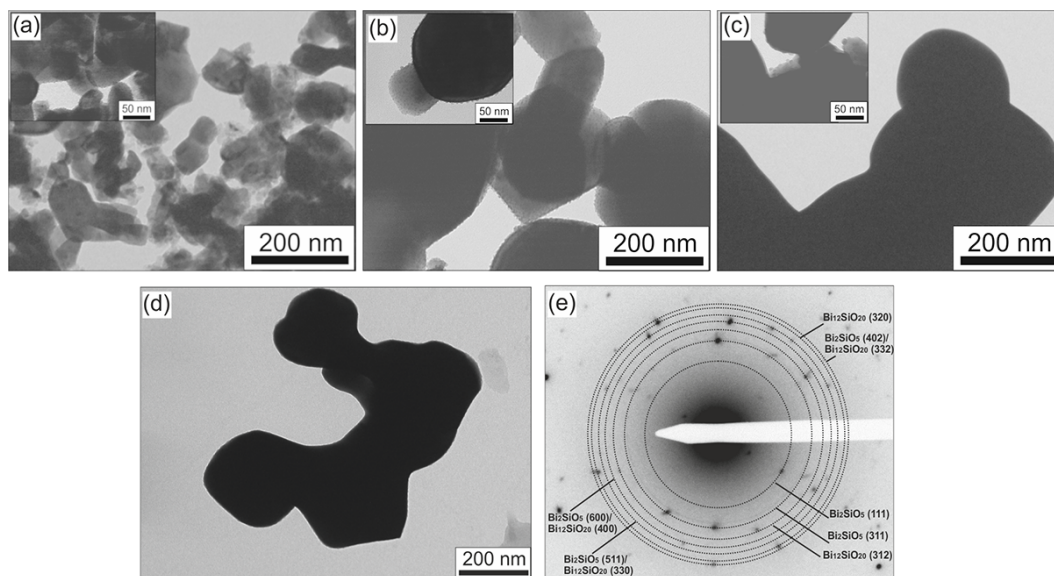


Fig. 2. TEM images of 2Bi:1Si (a), 4Bi:1Si (b, d), 12Bi:1Si (c) samples and SAED of 4Bi:1Si sample (e)

the long-wave region from 3.3 to 3.0 eV. A broad band with the redistributed maxima can indicate the presence of particles with different ratios of bismuth metasilicate and sillenite in such samples.

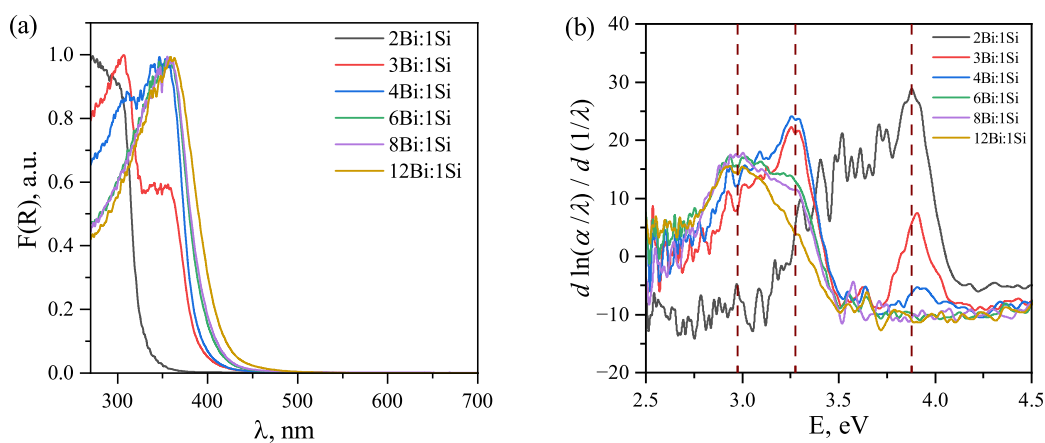


Fig. 3. UV-Vis spectra (a) and DASf plots (b) of $\text{Bi}_2\text{SiO}_5/\text{Bi}_{12}\text{SiO}_{20}$ samples

Fig. 4 shows the results of the study of the PC decomposition of Rh B in the presence of the obtained photocatalysts. Without a catalyst, no decomposition of the dye occurs during the experiment under soft UV irradiation (Fig. 4b). As a result of the Rh B destruction in the presence of the photocatalyst, a decrease in its intensity occurs in the entire spectrum range, and a shift in the absorption maximum from 553 nm towards the short-wave region of the spectrum is observed (Fig. 4a), which indicates the occurrence of the process of Rh B N-deethylation with the formation of the intermediate product Rhodamine 110 [22]. Calculation of the reaction rate

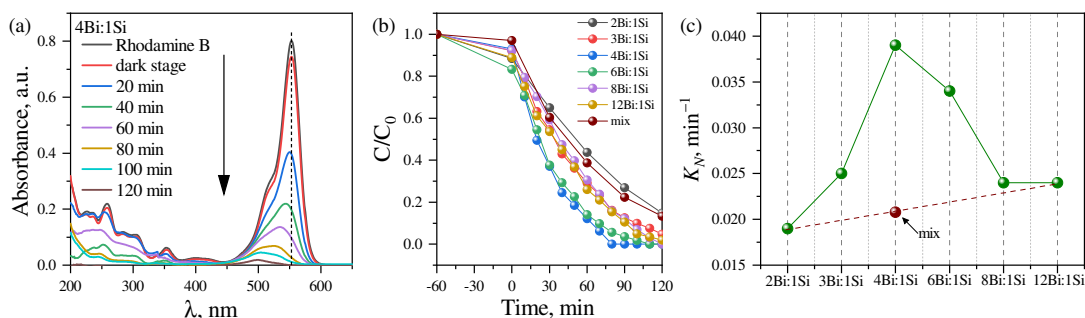


Fig. 4. Rh B spectra during PC decomposition (a), kinetic curves (b), and deethylation rate constant K_N for different samples (c)

constant K_N (Fig. 4c) shows that at a non-stoichiometric Bi:Si ratio, the samples work more efficiently than the monophasic samples 2Bi:1Si (Bi_2SiO_5) and 12Bi:1Si ($\text{Bi}_{12}\text{SiO}_{20}$). The highest efficiency is demonstrated by the 4Bi:1Si sample, in which the phase ratio is 47 % Bi_2SiO_5 and 53 % $\text{Bi}_{12}\text{SiO}_{20}$. For comparison, the catalytic activity of a simple mixture of 2Bi:1Si and 12Bi:1Si monophasic powders in a 50/50 ratio, corresponding in composition to the 4Bi:1Si composite, was also investigated. The data in Fig. 4 show that the powder mixture works significantly worse than the 4Bi:1Si sample obtained by the solid-phase synthesis. The reaction rate constant K_N for the mixture lies between those for the monophasic samples indicating the independent operation of the two phases in the powder mixture during photocatalysis. Based on the data obtained, it can be concluded that in the composite samples consisting of two phases of bismuth silicates, there is a better separation of the photogenerated charges. Thus, it can be assumed that a type II heterojunction is formed between two semiconductors Bi_2SiO_5 and $\text{Bi}_{12}\text{SiO}_{20}$.

Fig. 5 shows the histograms of 5-HMF conversion and product yield in the selective PC oxidation of 5-HMF. It is evident from Fig. 5 that the oxidation of 5-HMF occurs both through the formation of DFF and HMFCA. Then, the subsequent oxidation of the semi-products to FFCA and even to FDCA occurs. The lowest 5-HMF conversion (~ 11 %) and selectivity are demonstrated by the 2Bi:1Si sample, which consists of the Bi_2SiO_5 phase (Fig. 5a). As in the case of the Rh B decomposition, the best efficiency is demonstrated by the sample obtained at the 4Bi:1Si ratio with a similar contents of bismuth metasilicate and sillenite. The 5-HMF conversion for this sample for 8 h of irradiation reached 35.1 %, while the yields of the products FFCA and FDCA are 10.0 and 2.1 %, respectively (Fig. 5c). It is noteworthy that the samples synthesized in this work by the solid-phase synthesis method show better PC characteristics in the 5-HMF oxidation under the same conditions compared to the composite NPs $\beta\text{-Bi}_2\text{O}_3/\text{Bi}_{12}\text{SiO}_{20}$ (conversion is 20.6 %, selectivity towards FFCA is 9.4 % and the one to FDCA is 1.3 %), which we obtained earlier using the PLA in liquid [17].

Using the optical band gap estimated from the spectra, the energy band positions were calculated and the energy state diagram was constructed (Fig. 6). The calculation was based on the technique described in Refs. [23, 24]. In the literature, Bi_2SiO_5 is defined as the n-type semiconductor [25], and $\text{Bi}_{12}\text{SiO}_{20}$ is defined as the p-type semiconductor [26]. After contact, these semiconductors form a type II heterojunction. In addition, sillenite $\text{Bi}_{12}\text{SiO}_{20}$ has a unique feature: upon photoexcitation, the long-lived electron-donor center $\text{Bi}_{\text{Si}}^{3+} + h^+$, which is 1 eV above the valence band [27], is populated; this leads to a decrease in the band gap and an additional shift of the Fermi level. In this case, the conductivity type also changes from p-type to n-type

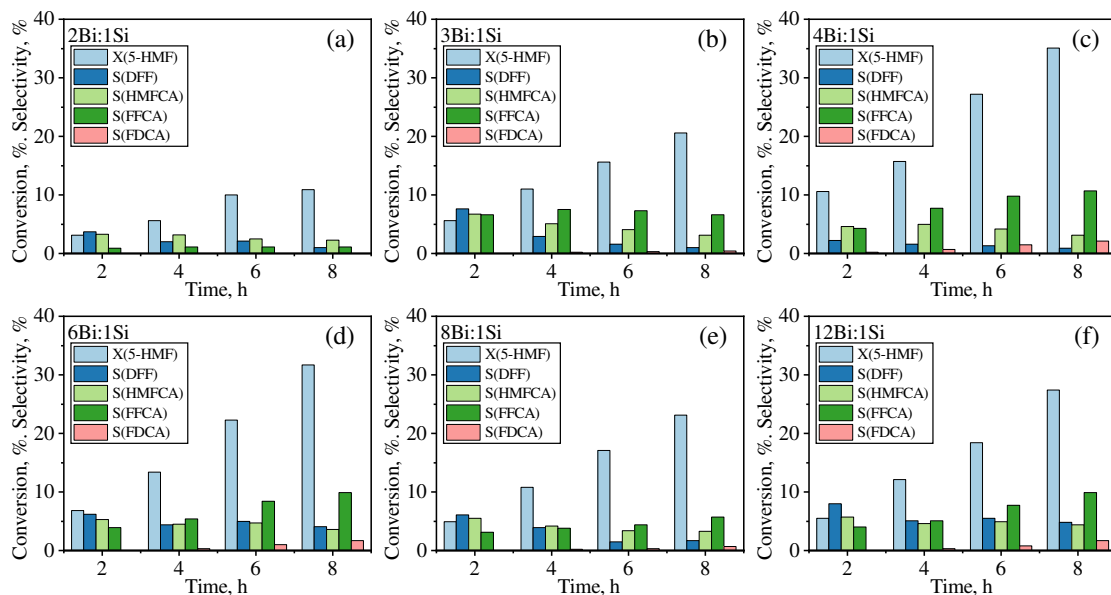


Fig. 5. Photocatalytic oxidation of 5-HMF in the presence of Na_2CO_3 over 2Bi:1Si (a), 3Bi:1Si (b), 4Bi:1Si (c), 6Bi:1Si (d), 8Bi:1Si (e), and 12Bi:1Si (f) samples

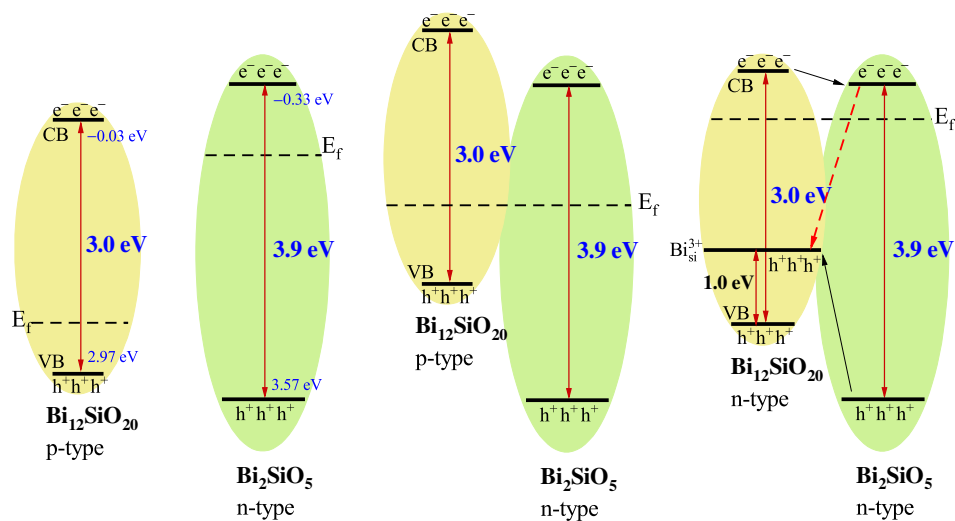


Fig. 6. Scheme of energy states in individual semiconductor NPs (left) the $\text{Bi}_2\text{SiO}_5/\text{Bi}_{12}\text{SiO}_{20}$ heterostructure in the dark (middle) and under the influence of light (right)

(Fig. 6, left). It can be assumed that during the operation of such a heterojunction, the Z-scheme (dotted arrow) is implemented, however, this assumption requires additional studies.

Conclusion

In the present work, heterostructures based on bismuth silicates $\text{Bi}_2\text{SiO}_5/\text{Bi}_{12}\text{SiO}_{20}$ were obtained by the solid-phase synthesis from a mixture of bismuth and silicon oxides, their

phase composition, morphology and optical properties were studied. Photocatalytic activity of powders was tested in reactions of Rhodamine B decomposition and selective oxidation of 5-hydroxymethylfurfural. Successful synthesis was ensured by both high dispersions of both precursors and high activity of the powder of unstable β - Bi_2O_3 phase obtained by pulsed laser ablation of metallic bismuth in air. It was shown that at stoichiometric ratios Bi:Si = 2:1 and 12:1, Bi_2SiO_5 and $\text{Bi}_{12}\text{SiO}_{20}$ powders similar to single-phase composition were formed, respectively. At the Bi:Si ratios of 3:1, 4:1, 6:1, and 8:1, the samples consisted of two phases of bismuth silicates, thus forming a heterojunction. Formation of composite particles was confirmed by the SAED data. Analysis of the optical characteristics of the obtained $\text{Bi}_2\text{SiO}_5/\text{Bi}_{12}\text{SiO}_{20}$ nanoparticles showed that the heterojunction belonged to the second type. This explained the increase in the PC activity of the composite nanoparticles, which was maximum for the sample with a similar content of bismuth metasilicate and sillenite obtained at the Bi:Si ratio of 4:1.

This work was supported by the Russian Science Foundation, grant no. 19-73-30026-P.

References

- [1] B.Abhishek, A.Jayarama, et. all., Challenges in photocatalytic hydrogen evolution: Importance of photocatalysts and photocatalytic reactors, *Int. J. Hydrogen Energy.*, **81**(2024), 1442–1466. DOI: 10.1016/j.ijhydene.2024.07.262
- [2] Z.Lin, R.C.Shao, K.Y.Xin, L.Teck-Peng, From biomass to fuel: Advancing biomass upcycling through photocatalytic innovation, *Mater. Today Chem.*, **38**(2024), 102091. DOI: 10.1016/j.mtchem.2024.102091
- [3] P.Qiangsheng, W.Yuanfeng, et. all., A review on the recent development of bismuth-based catalysts for CO_2 photoreduction, *J. Mol. Struct.*, **1294**(2023), 136404. DOI 10.1016/j.molstruc.2023.136404
- [4] A.Krishnan, A.Swarnalal, D.Das, M.Krishnan, V.S. Saji, S.M.A. Shibli, A review on transition metal oxides based photocatalysts for degradation of synthetic organic pollutants, *J. Environ. Sci.*, **139**(2024), 389–417. DOI: 10.1016/j.jes.2023.02.051
- [5] T.Butburee, P.Chakthranont, C.Phawa, K.Faungnawakij, Beyond Artificial Photosynthesis: Prospects on Photobiorefinery, *ChemCatChem*, **12**(2020), 1873-1890. DOI: 10.1002/cctc.201901856
- [6] Y.Meng, S.Yang, H.Li, Electro- and Photocatalytic Oxidative Upgrading of Biobased 5-Hydroxymethylfurfural, *ChemSusChem*, **15**(2022), e202102581. DOI: 10.1002/cssc.202102581
- [7] H.Li, B.Cheng, et. all., Recent advances in the application of bismuth-based catalysts for degrading environmental emerging organic contaminants through photocatalysis: A review, *J. Environ. Chem. Eng.*, **11**(2023), 110371. DOI: 10.1016/j.jece.2023.110371
- [8] J.Sharma, P.Dhiman, et. all., Advances in photocatalytic environmental and clean energy applications of bismuth-rich oxy halides-based heterojunctions:a review, *Materials Today Sustainability*, **21**(2023), 100327. DOI: 10.1016/j.mtsust.2023.100327

- [9] L.Dou, J.Zhong, J.Li, J.Luo, Y.Zeng, Fabrication of Bi_2SiO_5 hierarchical microspheres with an efficient photocatalytic performance for rhodamine B and phenol removal, *Mater. Res. Bull.*, **116**(2019), 50–58. DOI: 10.1016/j.materresbull.2019.03.031
- [10] Y.Wu, X.Chang, M.Li, X.Hei, C.Liu, X.Zhang, Studying the preparation of pure $\text{Bi}_{12}\text{SiO}_{20}$ by Pechini method with high photocatalytic performance, *J. Solgel Sci. Technol.*, **97**(2021), 311–319. DOI: 10.1007/s10971-020-05447-0
- [11] Q.Guo, C.Zhou, Z.Ma, X.Yang, Fundamentals of TiO_2 Photocatalysis: Concepts, Mechanisms, and Challenges, *Adv. Mater.*, **31**(2019), 1901997. DOI: 10.1002/adma.201901997
- [12] J.Low, J.Yu, M.Jaroniec, S.Wageh, A.A.Al-Ghamdi, Heterojunction Photocatalysts, *Adv. Mater.*, **29**(2017), 1601694. DOI: 10.1002/adma.201601694
- [13] A.V.Emeline, A.V.Rudakova, V.K.Ryabchuk, N.Serpone, Recent advances in composite and heterostructured photoactive materials for the photochemical conversion of solar energy, *Curr. Opin. Green Sustain. Chem.*, **34**(2022), 100588. DOI: 10.1016/j.cogsc.2021.100588
- [14] S.Reichenberger, G.Marzun, M.Muhler, S.Barcikowski, Perspective of Surfactant-free Colloidal Nanoparticles in Heterogeneous Catalysis, *ChemCatChem*, **11**(2019), 1–31. DOI: 10.1002/cctc.201900666
- [15] A.A.Manshina, I.I.Tumkin, et. all., The Second Laser Revolution in Chemistry: Emerging Laser Technologies for Precise Fabrication of Multifunctional Nanomaterials and Nanostructures, *Adv. Funct. Mater.*, (2024), 2405457. DOI: 10.1002/adfm.202405457
- [16] A.V.Shabalina, A.G.Golubovskaya, et. all., Phase and structural thermal evolution of Bi-Si-O catalysts obtained via laser ablation, *Nanomaterials*, **12**(2022), 4101. DOI: 10.3390/nano12224101
- [17] A.G.Golubovskaya, T.S.Kharlamova, et. all., Photocatalytic Decomposition of Rhodamine B and Selective Oxidation of 5-Hydroxymethylfurfural by $\beta\text{-Bi}_2\text{O}_3/\text{Bi}_{12}\text{SiO}_{20}$ Nanocomposites Produced by Laser, *J. Compos. Sci.*, **8**(2024), 42. DOI: 10.3390/jcs8020042
- [18] E.S.Savelyev, A.G.Golubovskaya, D.A.Goncharova, T.S.Kharlamova, V.A.Svetlichnyi, Effect of laser power density on formation of oxide particles during ablation of metallic bismuth in atmospheric air, *Optics and Laser Technology*, **181**(2025), 111676. DOI: 10.1016/j.optlastec.2024.111676
- [19] D.Souri, Z.E.Tahan, A new method for the determination of optical band gap and the nature of optical transitions in semiconductors, *Appl. Phys. B*, **119**(2015), 273–279. DOI: 10.1007/s00340-015-6053-9
- [20] L.Dou, X.Jin, J.Chen, J.Zhong, J.Z.Li, Y.Zeng, R.Duan, One-pot solvothermal fabrication of S-scheme $\text{OVs-Bi}_2\text{O}_3/\text{Bi}_2\text{SiO}_5$ microsphere heterojunctions with enhanced photocatalytic performance toward decontamination of organic pollutants, *Appl. Surf. Sci.*, **527**(2020), 146775. DOI: 10.1016/j.apsusc.2020.146775
- [21] D.Hou, X.Hu, Y.Wen, et. all., Electrospun sillenite $\text{Bi}_{12}\text{MO}_{20}$ (M = Ti, Ge, Si) nanofibers: General synthesis, band structure, and photocatalytic activity, *Phys. Chem. Chem. Phys.*, **15**(2013), 20698. DOI: 10.1039/c3cp53945h

- [22] A.A.Isari, A.Payan, M.Fattahi, S.Jorfi, B.Kakavandi, Photocatalytic degradation of rhodamine B and real textile wastewater using Fe-doped TiO₂ anchored on reduced graphene oxide (Fe-TiO₂/rGO): Characterization and feasibility, mechanism and pathway studies, *Appl. Surf. Sci.*, **462**(2018), 549–564.
- [23] M.A.Butler, D.S.Ginley, Prediction of Flatband Potentials at Semiconductor-Electrolyte Interfaces from Atomic Electronegativities, *Journal of The Electrochemical Society*, **125**(1978), 228–232. DOI: 10.1149/1.2131419
- [24] W.Q.Li, Z.H.Wen, S.H. Tian, L.J.Shan, Y.Xiong, Citric acid-assisted hydrothermal synthesis of a self-modified Bi₂SiO₅/Bi₁₂SiO₂₀ heterojunction for efficient photocatalytic degradation of aqueous pollutants, *Catal. Sci. Technol.*, **8**(2018), 1051–1061. DOI: 10.1039/C7CY02272G
- [25] L.Dou, J.Li, N.Long, C.Lai, J.Zhong, J.Li, S.Huang, Fabrication of 3D flower-like OVs-Bi₂SiO₅ hierarchical microstructures for visible light-driven removal of tetracycline, *Surf. Interfaces*, **29**(2022), 101787.
- [26] M.Isik, G.Surucu, A.Gencer, N.M.Gasanly, Electronic, optical and thermodynamic characteristics of Bi₁₂SiO₂₀ sillenite: First principle calculations, *Mater. Chem. Phys.*, **267**(2021), 124711. DOI:10.1016/j.matchemphys.2021.124711
- [27] J.Frejlich, Photorefractive Materials: Fundamental Concepts, Holographic Recording and Materials Characterization, John Wiley & Sons, 2007, 19-43.

Твердофазный синтез и фотокаталитические свойства гетероструктур Bi₂SiO₅/Bi₁₂SiO₂₀

Александра Г. Голубовская
Тамара С. Харламова
Валерий А. Светличный
Томский государственный университет
Томск, Российская Федерация

Аннотация. В работе предложен и реализован новый подход к созданию гетероструктурных наночастиц (НЧ) на основе силикатов висмута Bi₂SiO₅/Bi₁₂SiO₂₀. В основе данного подхода лежит твердофазный синтез путем отжига предварительно гомогенизированной перетиранием смеси порошков β-Bi₂O₃ и SiO₂ в различном соотношении. Для этого использовались промышленный нанопорошок диоксида кремния и порошок наночастиц β-оксида висмута, полученный импульсной лазерной абляцией (ИЛА) в воздухе. Исследованы морфология, фазовый состав и оптические свойства полученных материалов. Изменяя соотношение прекурсоров, были получены порошки, близкие по структуре к монофазным силикатам висмута Bi₂SiO₅ и Bi₁₂SiO₂₀, так и гетероструктурные НЧ на их основе. Оценена активность фотокатализаторов в реакциях разложения Родамина Б и селективного окисления 5-гидроксиметилфурфуrolа (5-НМФ). Лучшую фотокаталитическую активность демонстрируют порошки с близким соотношением фаз Bi₂SiO₅/Bi₁₂SiO₂₀ (или 4Bi:1Si). В результате анализа полученных результатов было предположено формирование гетероперехода II типа.

Ключевые слова: твердофазный синтез, силикаты висмута, гетероструктурные наночастицы, импульсная лазерная абляция, фотокатализ, гетеропереход II типа, 5-гидроксиметилфурфуrol, родамин В.

EDN: KOZBCF

УДК 539.378

Modelling of a Sandwich Plate Cross-section with Different Moduli of the Material under Cylindrical Loads

Igor E. Petrakov*

Institute of Computational Modelling SB RAS
Krasnoyarsk, Russian Federation

Received 10.08.2024, received in revised form 15.09.2024, accepted 24.11.2024

Abstract. A model of three-layer sandwich plate consisting of two layers of composite material connected by an elastic isotropic layer is considered in the paper. Composite layers with different tensile and compression moduli of elasticity are described as an orthotropic material reinforced with parallel carbon fibres. Constitutive equations of the model are based on the generalized rheological method. The energy functional is constructed with the use of the Lagrange variational method which is minimized using the initial stress method and the finite element method. The results of a series of computational experiments are presented wherein the stress-strain state of a vertical section of a plate under the action of cylindrical load is calculated.

Keywords: composite material, multi-modular theory of elasticity, generalized rheological method, composite plate, finite element method.

Citation: I.E. Petrakov, Modelling of a Sandwich Plate Cross-section with Different Moduli of the Material under Cylindrical Loads, J. Sib. Fed. Univ. Math. Phys., 2025, 18(3), 320–330. EDN: KOZBCF.



Composite materials are materials consisting of two or more distinct components and they have properties different from the properties of the original materials. In addition, the composition and distribution of individual components are known in advance, the proportion of each component is not lower than a certain value, and there are clear boundaries separating the starting materials [1,2]. Despite the heterogeneity of composites on micro-scale they can be considered as homogeneous materials on macro-scale. The components of a composite material are divided into a continuous phase, which is called the matrix, and a reinforcing phase. Moreover, the same material can play the role of a matrix or be a reinforcing material in various composites [3].

Various industries such as automotive industry, mechanical engineering, aircraft manufacturing and space industry widely use composite materials. The use of composite materials is growing in aerospace industry. The share of composites ranges from 15% to 30% of the total weight in modern aircraft, and in rocket engines reaches 90% [4, 5].

One of the composite materials is sandwich structures consisting of a filler and a shell. Polymers reinforced with glass fibre, carbon fibre or biofilter [6] can be used as shell material. Sandwich structures are increasingly used in industry, building structures and transportation due to their light weight and strength under heavy loads. A sandwich structure in which the shell is a fibrous composite reinforced with long parallel fibres, and the filler is an elastic isotropic material is considered in this paper. Since such shell material has different moduli of elasticity and different strengths it is necessary to take this into account when calculating structures made of such material [7].

*petigr@icm.krasn.ru

One of the approaches that allows one to construct model that takes into account different moduli of elasticity of a composite under tension and compression is the generalized rheological method [8]. The method provides thermodynamically correct governing equations for fibre composites. The method is based on the construction of rheological schemes using basic elements (elastic spring, viscous damper and plastic hinge) and a new element — hard contact that simulates the behaviour of ideal granular medium with absolutely solid particles. The rheological method has proven itself well in modelling the dynamics and statics of granular and porous materials with a threshold change in rigidity during the collapse of pores. A similar change in stiffness occurs in fibre composite when the sign of deformation changes.

1. Generalized rheological method

Let us construct the scheme describing a three-layer structure that consists of two layers of a multi-modulus composite and one layer of isotropic filler. Fig. 1 shows rheological scheme consisting of five elastic elements and two rigid contact elements, where σ is the actual stress tensor, a_i is the tensor of elastic moduli in compression for i -th layer, b_i is the tensor of additional moduli under tension for the i -th layer.

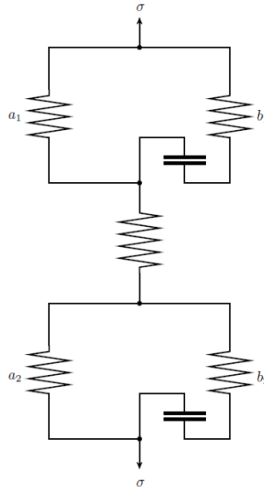


Fig. 1. Scheme of three-layer sandwich plate

Derivation of the rigid contact equations used to describe heteromodularity is presented in [9,10]. Two equivalent variational inequalities for the reverse rigid contact are

$$\sigma(\varepsilon - \tilde{\varepsilon}) \geq 0, \quad \varepsilon, \tilde{\varepsilon} \leq 0; \quad (\sigma - \tilde{\sigma})\varepsilon \geq 0, \quad \sigma, \tilde{\sigma} \geq 0. \quad (1)$$

Let us consider layer of composite material separately.

Layer of a material with different moduli is described by the diagram shown in Fig. 2, where ε is the strain tensor, σ is the actual stress tensor, σ' is the additional stress tensor, a is the tensor of elastic moduli in compression, b is the tensor of additional moduli in tension. The governing equations of the stress-strain state of elastic composites for finite linear or non-linear relations between stress tensors σ and strain tensors ε admit the potential representation

$$\sigma = \frac{\partial \Phi(\varepsilon)}{\partial \varepsilon}, \quad \varepsilon = \frac{\partial \Psi(\sigma)}{\partial \sigma}. \quad (2)$$

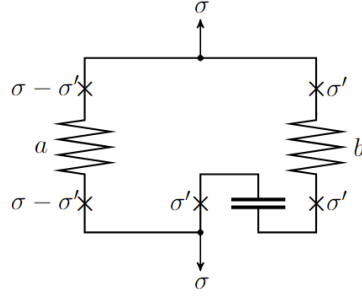


Fig. 2. Scheme of layer of composite material

Here Φ and Ψ are elastic potentials of stress and strain related to each other through the Young transformation:

$$\Psi(\sigma) = \sup_{\varepsilon} (\sigma : \varepsilon - \Phi(\varepsilon)), \quad (3)$$

$$\Phi(\varepsilon) = \sup_{\sigma} (\sigma : \varepsilon - \Psi(\sigma)), \quad (4)$$

where the colon denotes double convolution of tensors.

According to [11, 12] such scheme corresponds to the following governing equation

$$\sigma = a : \varepsilon + b : (\varepsilon - \Pi(\varepsilon)), \quad (5)$$

where $\Pi(\varepsilon)$ is the projection of tensor ε onto the cone C according to the norm $|\varepsilon| = \sqrt{\varepsilon : b : \varepsilon}$ and stress and strain potentials

$$\Phi(\varepsilon) = \frac{1}{2} \varepsilon : a : \varepsilon + \frac{1}{2} (\varepsilon - \Pi(\varepsilon))^2, \quad (6)$$

$$\Psi(\sigma) = \frac{1}{2} \sigma : a^{-1} : \sigma - \frac{1}{2} \|\pi(\bar{\sigma})\|^2, \quad (7)$$

where $\pi(\bar{\sigma})$ is the projection of stress tensor $\bar{\sigma}$ onto the cone that is conjugate to the cone C according to the norm $\|\sigma\|^2 = \sigma : (a^{-1} + b^{-1}) : \sigma$. The equivalent form of equation (9) are two equations for the actual stress tensor σ , the additional stress tensor σ' and the intrinsic strain tensor of the rigid contact ε' :

$$\sigma - \sigma' = a : \varepsilon, \quad \sigma' = b : (\varepsilon - \varepsilon'). \quad (8)$$

Let us assume that governing equation at each point of composite layers of the plate has the form

$$\sigma = a(x_1, x_2, x_3) : \varepsilon + b(x_1, x_2, x_3) : (\varepsilon - \Pi(\varepsilon)), \quad (9)$$

where $a(x_1, x_2, x_3)$ and $b(x_1, x_2, x_3)$ take constant values a_1, b_1 and a_2, b_2 for each layer, respectively, cones C_i are half-spaces associated with direction of reinforcement. In the filler layer, potentials and the governing equation take the form

$$\Phi(\varepsilon) = \frac{1}{2} \varepsilon : a_m : \varepsilon, \quad \Psi(\sigma) = \frac{1}{2} \sigma : a_m^{-1} : \sigma, \quad \sigma = a_m : \varepsilon. \quad (10)$$

2. Sandwich plate section

Let us consider the stress-strain state of the sandwich plate section. Let the x_1 axis of the Cartesian coordinate system Ox_1x_2 be located in the direction of fibre. Let us assume that during compression the plate material is described by the Hooke law for transversally isotropic body. Then the first equation of system (8) can be written in the following matrix form

$$\begin{pmatrix} \varepsilon_{11} \\ \varepsilon_{22} \\ \varepsilon_{12} \end{pmatrix} = \begin{pmatrix} \frac{1}{E_1} & -\frac{\nu_2}{E_2} & 0 \\ -\frac{\nu_1}{E_1} & \frac{1}{E_2} & 0 \\ 0 & 0 & \frac{1}{2G} \end{pmatrix} \begin{pmatrix} \sigma_{11} - \sigma'_{11} \\ \sigma_{22} - \sigma'_{22} \\ \sigma_{12} - \sigma'_{12} \end{pmatrix}, \quad (11)$$

where E_1 and E_2 are the Young moduli along the fibre and perpendicular to the fibre, respectively, ν_1 and ν_2 are the corresponding Poisson's ratios, and G is the shear modulus. When the strain of fibres is positive additional stress is

$$\sigma'_{11} = b_{11}\varepsilon_{11},$$

which is introduced using tensor b . In the case under consideration it has only one non-zero component b_{11} . To ensure that introduced tensor is non-degenerate and positive definite small positive components β and γ are introduced, and they subsequently tend to zero. Let us write the second equation of system (8)

$$\begin{pmatrix} \varepsilon_{11} - \varepsilon'_{11} \\ \varepsilon_{22} - \varepsilon'_{22} \\ \varepsilon_{12} - \varepsilon'_{12} \end{pmatrix} = \begin{pmatrix} \frac{1}{b_{11}} & 0 & 0 \\ 0 & \frac{1}{\beta} & 0 \\ 0 & 0 & \frac{1}{2\gamma} \end{pmatrix} \begin{pmatrix} \sigma'_{11} \\ \sigma'_{22} \\ \sigma'_{12} \end{pmatrix}. \quad (12)$$

Substituting the resulting expressions into (9), governing equations for the plane stress state are obtained:

$$\begin{cases} \sigma_{11} = \frac{E_1(\varepsilon_{11} + \nu_2\varepsilon_{22})}{1 - \nu_1\nu_2} + b_{11}(\varepsilon_{11} - \Pi_{11}), \\ \sigma_{22} = \frac{E_2(\varepsilon_{22} + \nu_1\varepsilon_{11})}{1 - \nu_1\nu_2}, \\ \sigma_{12} = 2G\varepsilon_{12}. \end{cases} \quad (13)$$

Let us write out tensor $a^{-1} + b^{-1}$ and represent it in matrix form

$$\begin{pmatrix} \frac{1}{E_1} + \frac{1}{b_{11}} & -\frac{\nu_2}{E_2} & 0 \\ -\frac{\nu_1}{E_1} & \frac{1}{E_2} + \frac{1}{\beta} & 0 \\ 0 & 0 & \frac{1}{2G} + \frac{1}{2\gamma} \end{pmatrix}. \quad (14)$$

Consider the minor of size 2×2 of the matrix $(a^{-1} + b^{-1})^{-1}$:

$$\frac{1}{(b_{11} + E_1)(\beta + E_2) - \nu_1\nu_2b\beta} \begin{pmatrix} b_{11}(\beta + E_2)E_1 & \nu_1b\beta E_2 \\ \nu_1b_{11}\beta E_2 & \beta(b_{11} + E_1)E_2 \end{pmatrix}. \quad (15)$$

Taking the limit $\beta, \gamma \rightarrow 0$, matrix with single non-zero element $bE_1/(b + E_1)$ is obtained. Thus, components of the conditional stress tensor $\bar{\sigma}$ are

$$\bar{\sigma}_{11} = \frac{E_1b_{11}}{b_{11} + E_1} \left(\frac{\sigma_{11}}{E_1} - \nu_2 \frac{\sigma_{22}}{E_2} \right), \quad \bar{\sigma}_{22} = \bar{\sigma}_{12} = 0. \quad (16)$$

Let us assume that each layer of the shell is reinforced with parallel fibres in the plane of the plate at an angle R_i to the x axis. Let us write down the governing equations for this case. Since the rotation occurs in the plane of the plate, components σ_{22} and σ_{12} remain unchanged:

$$\begin{cases} \sigma_{11} = \left(\frac{(E_1 \cos R_i + E_2 \sin R_i)(\varepsilon_{11} + \nu_2 \varepsilon_{22})}{1 - \nu_1 \nu_2} + b_{11} \cos R_i (\varepsilon_{11} - \Pi_{11}) \right), \\ \sigma_{22} = \frac{E_2(\varepsilon_{22} + \nu_1 \varepsilon_{11})}{1 - \nu_1 \nu_2}, \\ \sigma_{12} = 2G\varepsilon_{12}. \end{cases} \quad (17)$$

Let us consider the following problem. Region Ω with boundary Γ coincide with the vertical section of the sandwich plate. Boundary Γ consists of a part Γ_u on which there are no movements and part Γ_σ that does not intersect with it, and distributed load is specified on part Γ_σ :

$$\begin{cases} u = 0 & \text{на } \Gamma_u, \\ \sigma n = q & \text{на } \Gamma_\sigma. \end{cases} \quad (18)$$

It is required to determine the vector displacement field u and the tensor field σ that satisfy the differential equations

$$\nabla \cdot \sigma = 0, \quad 2\varepsilon(u) = \nabla u + (\nabla u)^*,$$

and boundary conditions (18), and for which the following variational equations are satisfied in Ω

$$\sigma_i = a_i : \varepsilon_i + b_i : (\varepsilon_i - \Pi_i(\varepsilon_i)), \quad \sigma_m = a_m : \varepsilon_m. \quad (19)$$

Components of the small strain tensor are related to displacements as follows

$$\varepsilon_{11} = \frac{\partial u_x}{\partial x}, \quad \varepsilon_{22} = \frac{\partial u_y}{\partial y}, \quad \varepsilon_{12} = \frac{1}{2} \left(\frac{\partial u_x}{\partial y} + \frac{\partial u_y}{\partial x} \right).$$

Let us formulate variational principles that are equivalent to the differential formulation of the problem under consideration. The required displacement field minimizes the integral

$$J(u) = \int_{\Omega} (\Phi(\varepsilon(u))) d\Omega - \int_{\Gamma_\sigma} q u d\Gamma \quad (20)$$

on the linear space U of generalized functions $u \in H^1(\Omega)$.

To obtain the equation of the stress-strain state, the Lagrange variational principle is used. The actual distribution of plate displacements is minimized on a set of variations consistent with the main boundary conditions by the elastic energy functional:

$$\begin{aligned} \sum_{i=1,2} \left(\int_{\Omega_i} \left(\frac{1}{2} \nabla u : (a_i + b_i) : \nabla u - b_i : \Pi_i(\varepsilon) \sigma : \nabla u \right) d\Omega_i - \int_{\Gamma_i} \vec{q} \cdot u d\Gamma_i \right) + \\ + \int_{\Omega_m} \left(\frac{1}{2} \nabla u : a_m : \nabla u \right) d\Omega_m - \int_{\Gamma_m} \vec{q} \cdot u d\Gamma_m = 0, \end{aligned}$$

where index i denotes the layer number, u is the vector field of displacements in Ω , ∇ is the Hamilton operator, \vec{q} is the stress vector at the boundary of the plate Γ_σ , a_i is the tensor of elastic moduli under compression, b_i is the tensor of additional moduli under tension, a_m is the tensor of elastic moduli of the interlayer.

Let us apply the obtained constitutive equations to the analysis of the plane stress state of the section of a sandwich plate loaded along the edge with static self-balanced stress system, using the initial stress method. To do this, defining equation of the fibre composite in form (19) is replaced with the following iterative formula

$$\sigma^k = \sum_{i=1,2} ((a_i + b_i) : \varepsilon^k - \Delta\sigma_i^{k-1}) + a_m : \varepsilon^k, \quad \Delta\sigma_i^{k-1} = b_i : \Pi_i(\varepsilon^{k-1}).$$

At the first step, the problem for unstressed plate is solved when initial stress tensor $\Delta\sigma^0$ is identically equal to zero. In this case, the elastic modulus tensor is $a + b$. For the next steps, tensor $\Delta\sigma^{k-1}$ is determined, using the projection of tensor ε^{k-1} . Taking into account the iterative formula, the elastic energy functional takes the following form

$$\sum_{i=1,2} \left(\int_{\Omega_i} \left(\frac{1}{2} \nabla u : (a_i + b_i) : \nabla u - \Delta\sigma^{k-1} : \nabla u \right) d\Omega_i - \int_{\Gamma_i} \vec{q} \cdot u d\Gamma_i \right) + \int_{\Omega_m} \left(\frac{1}{2} \nabla u : a_m : \nabla u \right) d\Omega_m - \int_{\Gamma_m} \vec{q} \cdot u d\Gamma_m = 0. \quad (21)$$

To ensure the uniqueness of the solution any point on the plate is fixed, and rotation around this point is excluded. By minimizing functional (21) at each step of the algorithm, the required displacement vector u is obtained.

3. Numerical results

The finite element method is used for the numerical solution. The triangular Lagrange element with three nodes is used, and displacements u_x, u_y are specified at the nodes. An irregular triangular mesh is constructed in domain Ω . Vector of generalized coordinates U of dimension $2n$ is introduced, where n is the number of grid nodes. The functional is represented as a sum of integrals over all triangles of the mesh

$$J(U) = \sum_{l=1}^m \iint_{\Omega_l} ((U_l)^T S^T K(x_1, x_2) S U_l - b \Pi(S U_l^{k-1}) S U_l - q_l U_l) dx_1 dx_2, \quad (22)$$

where Ω_l is the domain of the l th finite element, U_l is the local vector of generalized coordinates, S_l is the local matrix of displacements and deformations, K is the matrix of elastic constants, q is a global vector of generalized forces, the superscript T means transpose. When conducting computational experiments, sandwich plates with different layer thicknesses were considered. Loading schemes are presented in Fig. 3. The shell parameters corresponded to carbon fibre plastic are $E_1^+ = 114$, $E_1^- = 57$, $E_2 = 14$, $G = 3.5$ GPa, $\nu_1 = 0.19$. The filler is isotropic epoxy resin with parameters $E = 4$, $G = 1.54$ GPa, $\nu = 0.3$. In the first series of computational experiments, tension-compression along fibres is considered. The figures show axial displacements for the plate with shell layer thickness of 1 mm and filler of 3 mm. The force of 50 kN (tension, Fig. 5) and -50 kN (compression, Fig. 6) is applied to the right side of the plate.

Similar calculations are carried out for the transverse direction. The deformation is calculated under the action of distributed load applied to the upper boundary of the plate. Displacements for tension and compression are shown in Fig. 7.

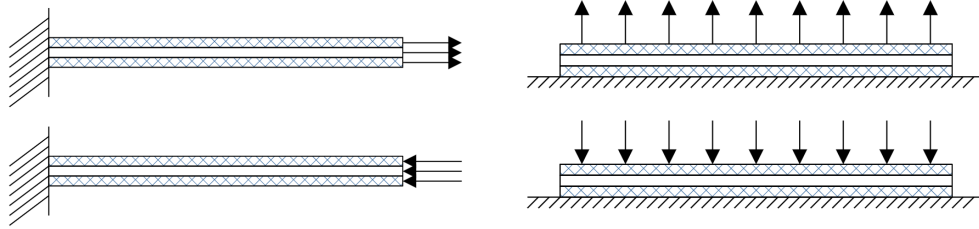


Fig. 3. Schemes of sandwich plate loading under tension-compression along and across fibres

As a result of calculations for the described material, the following values of effective elastic moduli for the sandwich structure are obtained

$$E_1^+ = 41\Gamma\Pi a, \quad E_1^- = 23\Gamma\Pi a, \quad E_2^+ = 5.88\Gamma\Pi a, \quad E_2^- = 5.93\Gamma\Pi a.$$

A series of computational experiments on bending of the sandwich plate under the action of concentrated force (diagram is shown in Fig. 4) is carried out.

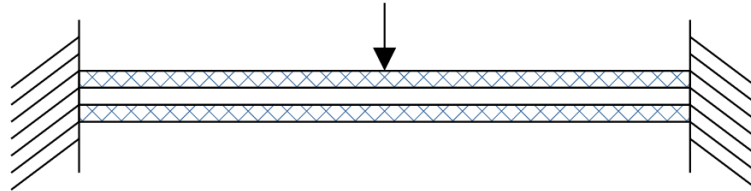


Fig. 4. Loading diagram for cylindrical bending

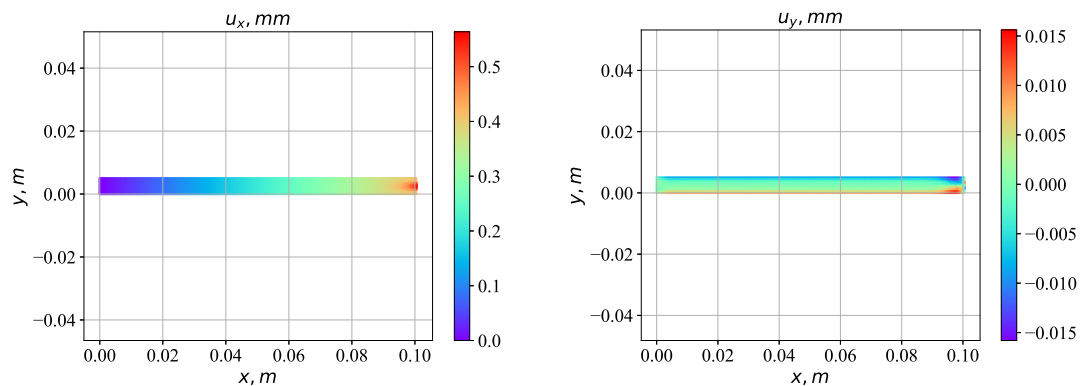


Fig. 5. Displacement of sandwich plate under tension with force applied along the shell reinforcement

Displacements and strains ε_{11} during bending for sandwich plate with shell layer thickness of 4 mm and filler layer of 4 mm are shown in Fig. 8. One can observe the distribution of tension and compression zones near edges and the centre of the plate.

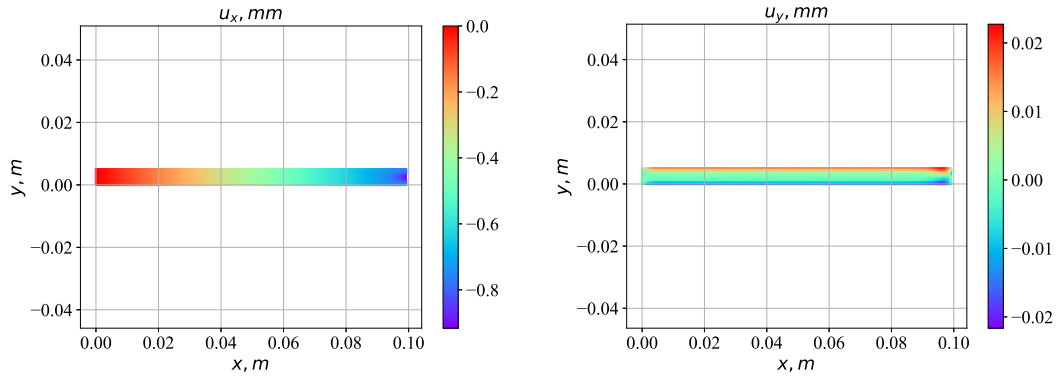


Fig. 6. Displacement of sandwich plate under compression with force applied along the shell reinforcement

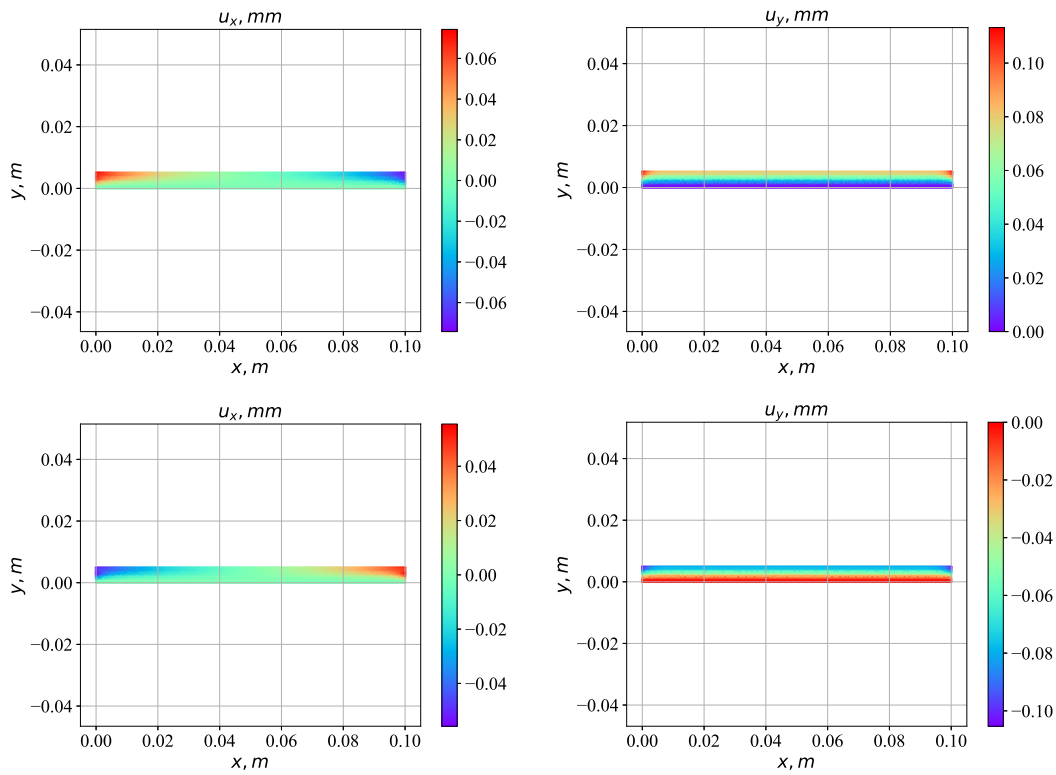


Fig. 7. Displacement of sandwich plate under tensile (top pictures) and compressive (bottom pictures) with force applied across the shell reinforcement

Tab. 1 shows values of deflections for various ratios of shell and filler thicknesses, where T_i is the thickness of the interlayer, T_a is the thickness of the reinforcement, w_d is the deflection when difference in modularity is taken into account, w is the deflection when difference in modularity is not taken into account. As thickness of the shell layers increases the influence of different moduli on the value of deflection is also increased. When difference in moduli is not taken into account different moduli the error of calculation of deflection can reach 10%.

Table 1. Deflection of sandwich plate under the action of concentrated force

T_i , mm	T_a , mm	w_d , mm	w , mm	δw , %
0.24	0.96	1.88	1.66	11%
0.48	0.72	1.99	1.78	10%
0.72	0.48	2.11	1.9	10%
0.96	0.24	2.24	2.08	7%

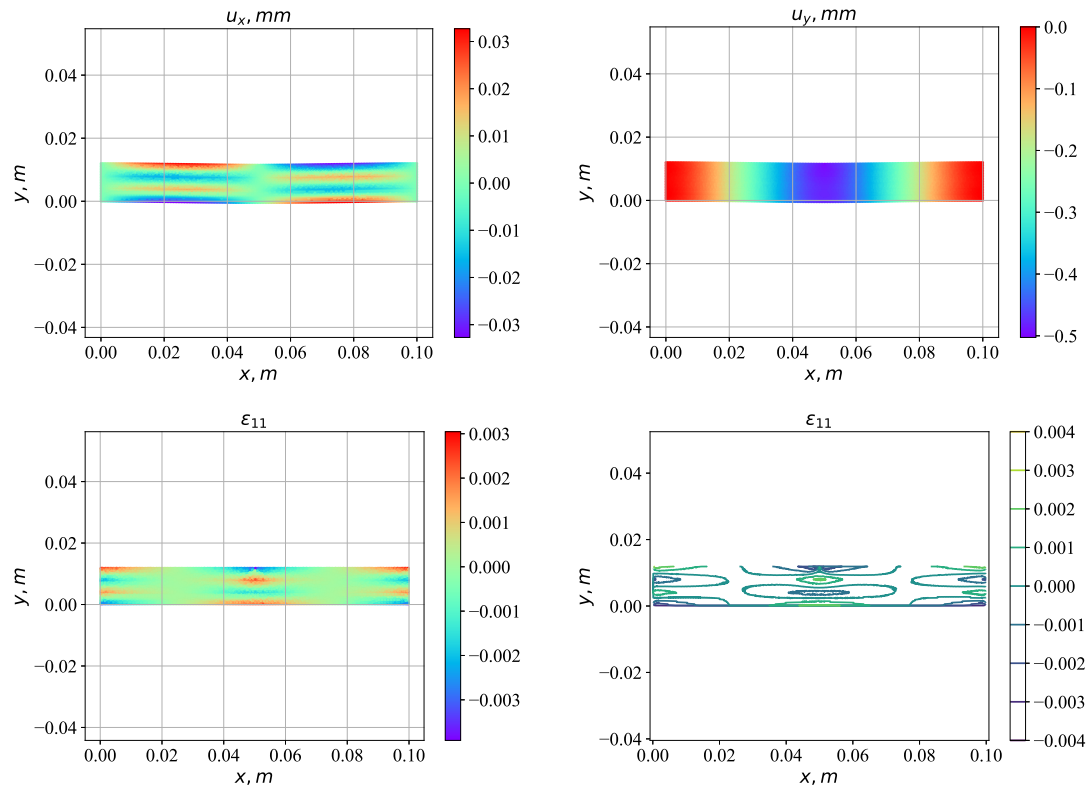


Fig. 8. Strain and displacement of sandwich plate with equal thickness of layers under the action of concentrated force

Conclusion

Model of sandwich plate that takes into account the different resistance of the material to tension and compression was considered. Computational algorithm for solving the problem of calculating the stress-strain state of sandwich plate section under the influence of cylindrical load has been developed. The developed model allows one to determine tension-compression zones of the sandwich plate section. Analysis of the results of numerical calculations showed the influence of different moduli on the deformed state of sandwich plate under cylindrical bending.

This work is supported by the Krasnoyarsk Mathematical Center and financed by the Ministry of Science and Higher Education of the Russian Federation in the framework of the establishment and development of regional Centers for Mathematics Research and Education (Agreement No. 075-02-2024-1378).

References

- [1] T.Fujii, M.Zako, Fracture mechanics of composite materials, Moscow, Mir, 1982 (in Russian).
- [2] D.Lubin, Handbook of Composite Materials, Moscow: Mashinostroenie, 1988 (in Russian).
- [3] F.L.Matthews, R.D.Rawlings, Composite materials: Engineering and science, Cambridge: CRC Press, Woodhead Publishing, 1999.
- [4] A.A.Bataev, V.A.Bataev, Composite materials: structure, production, application, Novosibirsk: NGTU, 2002 (in Russian).
- [5] I.M.Bulanov, V.V.Vorobej, Technology of rocket and aerospace structures made of composite materials, Moscow: MGTU, 1998 (in Russian).
- [6] B.Vijaya Ramnath, K.Alagarraja, C.Elanchezhian, Review on Sandwich Composite and their Applications, *Materials Today: Proceedings*, **16**(2)(2019), 859-864.
DOI: 10.1016/j.matpr.2019.05.169
- [7] S.A.Ambartsumyan, Heteromodular Elasticity Theory, Moscow: Nauka, 1982 (in Russian).
- [8] O.Sadovskaya, V.Sadovskii, Mathematical modeling in problems of mechanics of granular media, Moscow: Fizmatlit (in Russian).
- [9] O.Sadovskaya, V.Sadovskii, Mathematical Modeling in Mechanics of Granular Materials, Heidelberg – New York – Dordrecht – London: Springer, 2012.
- [10] V.M.Sadovskii, Thermodynamic Consistency and Mathematical Well-Posedness in the Theory of Elastoplastic, Granular, and Porous Materials, *Computational Mathematics and Mathematical Physics*, **60**(4), (2020), 738-751. DOI: 10.1134/S0965542520040156
- [11] B.D.Annin, V.M.Sadovskii, I.E.Petrakov, A.Yu.Vlasov, Strong Bending of a Beam from a Fibrous Composite, Differently Resistant to Tension and Compression, *Journal of Siberian Federal Universit. Mathematics and Physics*, **12**(5)(2019), 533-542.
DOI: 10.17516/1997-1397-2019-12-5-533-542
- [12] V.M.Sadovskii, O.V.Sadovskaya, I.E.Petrakov, On the theory of constitutive equations for composites with different resistance in compression and tension, *Composite Structures*, **268**(2021), 113921. DOI: 10.1016/j.compstruct.2021.113921

Моделирование сечения сэндвич-пластины при цилиндрических нагрузках с учетом разномодульности материала

Игорь Е. Петраков

Институт вычислительного моделирования СО РАН

Красноярск, Российская Федерация

Аннотация. В работе рассматривается модель трехслойной сэндвич-пластины, состоящей из двух слоев композитного материала, связанного упругой изотропной прослойкой. Слои композитного материала моделируются с учетом различных модулей упругости при растяжении и сжатии и представляют собой ортотропный материал, армированный параллельными углеродными волокнами. Представлена модель на основе обобщенного реологического метода, с помощью которого получены определяющие уравнения. С помощью вариационного метода Лагранжа построен функционал энергии, минимизация которого проведена с использованием метода начальных напряжений и метода конечных элементов. Представлены результаты серии вычислительных экспериментов по расчету напряженно-деформированного состояния вертикального сечения пластины под действием цилиндрической нагрузки.

Ключевые слова: композитный материал, разномодульная теория упругости, обобщенный реологический метод, сэндвич-пластина, метод конечных элементов.

EDN: JOFSFJ

УДК 535-15

Spectrum Broadening of Femtosecond Radiation Pulse at 950 nm Wavelength in Material with Cubic Nonlinearity

Sergey V. Alekseev*

Valery F. Losev†

Institute of High Current Electronics SB RAS

Tomsk, Russian Federation

Yakov V. Grudtsyn‡

Andrey V. Koribut§

Valery I. Yalovoy¶

Lebedev Physical Institute of RAS

Moscow, Russian Federation

Received 11.09.2024, received in revised form 24.10.2024, accepted 25.01.2025

Abstract. The conditions for spectrum broadening of 60 fs radiation pulse at a central wavelength 950 nm in fused quartz plates due to phase self-modulation are studied experimentally and theoretically. The studies are conducted at radiation intensities from 50 to 400 GW/cm^2 and plates thicknesses from 1 to 10 cm. The experimental conditions and a calculation model based on solving a system of nonlinear Schrödinger equations in the approximation of a slowly changing wave are described. The possibility of compressing radiation pulse with a broadened spectrum in case of quadratic nonlinear phase compensation is estimated. It is shown that in case spectrum broadening it is possible to reduce the spectrally limited duration by no more than two times.

Keywords: femtosecond pulse, spectrum width, self-phase modulation, fused quartz.

Citation: S.V. Alekseev, V.F. Losev, Ya.V. Grudtsyn, A.V. Koribut, V.I. Yalovoy, Spectrum Broadening of Femtosecond Radiation Pulse at 950 nm Wavelength in Material with Cubic Nonlinearity, *J. Sib. Fed. Univ. Math. Phys.*, 2025, 18(3), 331–336.

EDN: JOFSFJ.



Introduction

Currently, powerful infrared ($0.8 - 1 \mu\text{m}$) laser systems are usually used to obtain powerful radiation pulses in the visible spectrum, the radiation pulses of which are converted into the second harmonic (SH) in nonlinear crystals. In Tomsk (IHCE SB RAS) together with Moscow group (FIAN), the alternative way of obtaining such pulses in visible region (475 nm) is being developed based on the THL-100 hybrid laser system. This way is associated with the initial production of femtosecond SH pulse in visible region with low energies (1 – 5 mJ) and subsequent increase in energy in a gas amplifier on XeF(C-A) molecules to the Joule level. The THL-100

*alekseev10100@gmail.com <https://orcid.org/0000-0003-2940-7157>

†losev@ogl.hcei.tsc.ru

‡grudcynyv@lebedev.ru

§koributav@lebedev.ru

¶yalovoyvi@lebedev.ru

laser system, operating on this principle, is currently one of the most powerful systems in visible spectrum [1, 2]. The general interest in powerful pulses of radiation in visible spectrum is connected with the higher quantum energy, which allows to increase the efficiency of interaction of laser beam with various materials and environments. Powerful pulses also help to develop new applications, which include the creation of an X-ray laser in transparency window of water and the generation of powerful terahertz radiation [3–5].

One of the ways to increase the power of THL-100 laser system is to reduce the duration of output radiation pulse while maintaining the radiation energy. To do this, it is necessary to increase the spectral width of SH radiation pulse in the Ti:Sa complex and amplify it in active medium on XeF(C-A) molecules, which has a wide gain contour corresponding to a spectrally limited duration of 10 fs [6]. Since the femtosecond complex operates at the gain contour edge (950 nm) to match the SH wavelength with gas amplifier, it does not allow forming a radiation pulse shorter than 60 fs at the fundamental harmonic. To reduce the spectrally limited duration of radiation pulse, it is necessary to increase the width of its spectral contour by some artificial method. At present, the most common method of spectrum broadening for reducing the spectrally limited pulse duration is self-phase modulation in a medium with cubic nonlinearity.

This approach was proposed for high-power laser systems [7] and demonstrated at the PEARL facility (central wavelength 910 nm, pulse duration 65 – 75 fs, pulse energy up to 17 J, beam diameter 18 cm) [8]. The pulse spectrum at the laser output was broadened due to self-phase modulation in fused silica and then the pulse was compressed by chirped mirrors. It was demonstrated that with optimal choice of mirror dispersion a pulse with energy of 17 J can be compressed from 70 to 14 fs. This compression has undoubted merits: simplicity, low cost, negligible pulse energy losses, and applicability to any high-power laser.

This paper presents theoretical and experimental results of studies aimed at studying the possibility of broadening the radiation spectrum with a central wavelength of 950 nm depending on the glass block thickness and radiation intensity.

1. The equipment and methods

In the experiments, the femtosecond Ti:Sa laser complex operating at the gain contour edge (central wavelength is 950 nm) and serving as master oscillator (front end) for multiterawatt THL-100 laser system was used. The laser complex consists of master oscillator, stretcher, regenerative and two multi-pass amplifiers, and compressor on diffraction gratings. The output pulse at the fundamental harmonic has duration of 60 fs, beam diameter of 15 mm with intensity decay of e^2 times and energy of up to 10 mJ. The beam was directed without focusing onto polished fused quartz plates of different thickness (from 1 to 10 cm), where the spectrum was broadened due to self-phase modulation. After that, the radiation was recorded with an Ocean Optics HR4000 spectrometer (200 – 1100 nm, 0.7 nm). The laser radiation energy in the experiments was measured by Gentec-e maestro energy meter.

The model that takes into account the influence of phase self-modulation, group velocity dispersion and nonlinear response, nonlinear absorption, plasma formation and spatial effects associated with self-focusing was used in simulations. The model is based on solving the system of nonlinear Schrödinger equations in approximation of slowly varying wave [9] in cylindrical coordinate system and it has the following form:

$$\frac{\partial A}{\partial z} + iD \frac{\partial^2 A}{\partial \eta^2} + iD_{\perp} \Delta_{\perp} A + i \frac{ik_0^2 n_2}{n_0} \left(1 + \frac{i}{\omega_0} \frac{\partial}{\partial \eta} \right) \left(\int_0^{\infty} R(t') |A(\eta - t')|^2 dt' \right) = 0 \quad (1)$$

where η is the dimensionless time in the traveling coordinate system, z is the longitudinal coordinate, D is the coefficient characterizing the second-order dispersion, ω_0 is the average pulse frequency, k_0 is the wave number, $A(n, r, z)$ is the complex envelope of the electric field (the initial distribution was Gaussian), $R(t)$ is the nonlinear response function, including the fast and slow part, n_0 and n_2 are linear and nonlinear refractive coefficients. For numerical solution of nonlinear Schrödinger equations the conservative difference scheme with second order approximation was used both in the spatial coordinate and in time [10]. The simulations were carried out for laser beam intensity from 50 to 400 GW/cm^2 . The thickness of fused quartz was varied in the same range as in experiments.

2. Results and discussion

The experimental study of spectrum broadening of first harmonic radiation was carried out at laser pulse energy of 8 mJ and radiation intensity at entrance to the material of 76 GW/cm^2 . The initial width of laser radiation spectrum at half-maximum (FWHM) was 28 nm (Fig. 1).

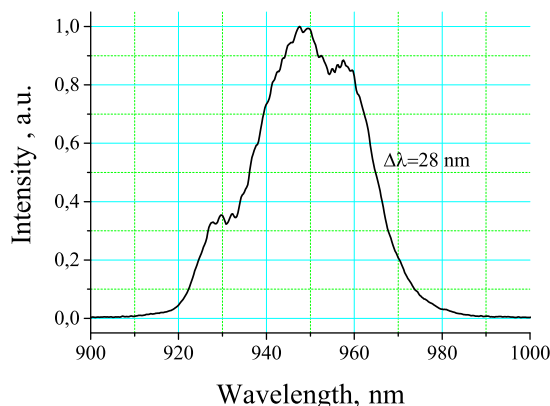


Fig. 1. Spectral contour of the fundamental harmonic radiation

The beam was passed through plates of fused quartz starting from 1 cm thickness and up to 10 cm. At the same time with thickness increase of the plates to 6 cm the spectrum width was increased, and with its further increase the spectrum width began to decrease due to Kerr nonlinearity. Here we present the spectrum only for the optimal regions. Thus, the spectrum width increased to 41.8 nm when using a 4 cm thick plate (Fig. 2a). When using a 6 cm plate, the spectrum width increased to 53.3 nm (Fig. 2b). That is, for these conditions, the spectrum width increased by 1.5 and 2 times, respectively. It is clear that, in general, the spectrum shifts to the short-wave side. Most likely, this is due to the fact that the temporal shape of laser radiation pulse is not Gaussian and the trailing edge is significantly steeper than the leading edge. Deep amplitude modulation of the radiation intensity is typical for spectral form behavior in phase self-modulation. In this case the duration of spectrally limited pulse is usually determined by the spectrum envelope at half amplitude. That is, we can hope that in our case the duration will be reduced by about two times.

Simulations close to the experiment showed that at intensity of 100 GW/cm^2 and 4 and 6 cm thick plates the spectrum width increases to 38.9 and 42.6 nm, respectively (Fig. 3a). In

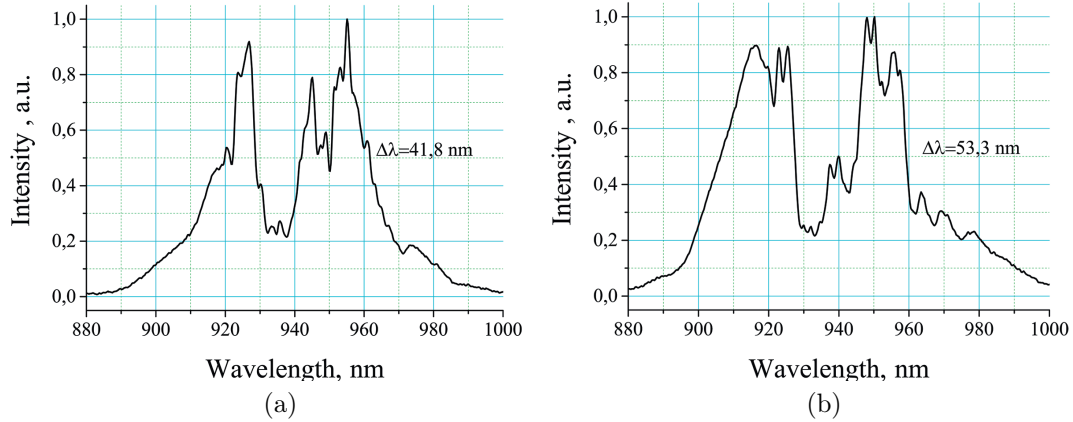


Fig. 2. Experimental spectral contours of broadened radiation obtained after passing through 4 m (a) and 6 cm (b) of fused quartz

this case, the broadening occurs symmetrically on both sides of the central wavelength. With increasing of intensity to 400 GW/cm^2 the spectrum width increased to 72 nm (Fig. 3b). In this case a significant width increase at the spectrum base was observed. Simulations showed that the spectrum broadening occurs mainly due to phase self-modulation. The simplified model did not allow obtaining a real picture of the spectrum with modulation.

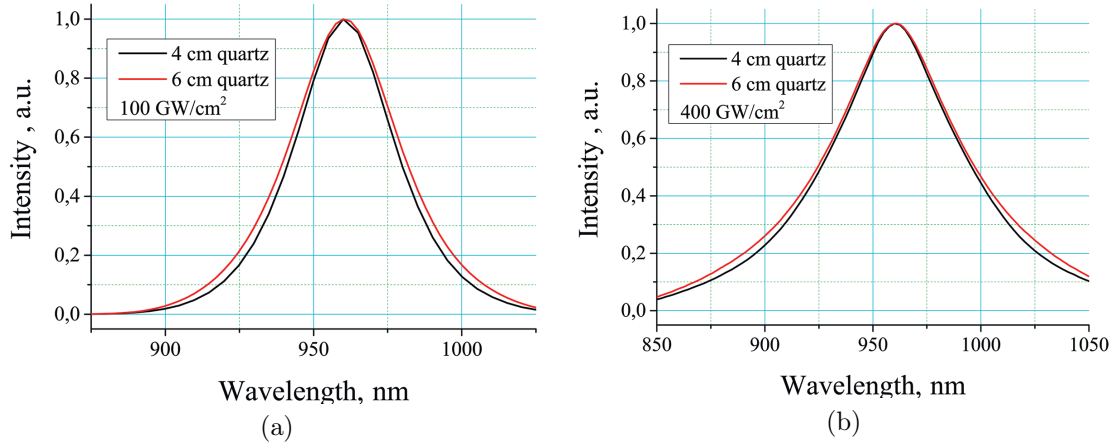


Fig. 3. Theoretical spectral contours of broadened radiation obtained after passing 4 (black) and 6 (red) cm of fused quartz at laser beam intensity of 100 (a) and 400 (b) GW/cm^2

To calculate the pulse duration of radiation with a broadened spectrum the beam was propagated in medium with negative dispersion. It was shown that pulse duration was reduced no more than twice. That is compensation for only the second-order dispersion is sufficient for Gaussian beam profile.

Conclusion

Thus experimental and theoretical studies of the broadening possibility of radiation spectral contour of the fundamental harmonic at a central wavelength of 950 nm in fused quartz have

been carried out and the possibility of compression of the radiation pulse with a broadened spectrum when compensating for the quadratic nonlinear phase was evaluated. It was shown that with increase of the material thickness from 1 to 6 cm in experiment and simulations the spectrum widens up to two times. However, the calculated shape of broadened spectral contour does not coincide with the experiment. To reconcile these data, both further refinement of the computational model (accounting for absorption and scattering) and greater approximation of the calculation conditions to the experiments (non-Gaussian pulse, the presence of cubic phase, etc.) are required. This is planned in our further research. Actually, in calculations, it is possible to reduce the spectrally limited duration up to two times. A similar pattern is expected in the experiment when compensating for the positive dispersion.

The work was supported by the Ministry of Science and Higher Education of the Russian Federation (FWRM-2021-0014).

References

- [1] S.V.Alekseev, A.I.Aristov, N.G.Ivanov, et. all., Multiterawatt femtosecond laser system in the visible with photochemically driven XeF(C-A) boosting amplifier, *Laser and Particle Beams*, **31**(2013), no. 1, 17–21. DOI: 10.1017/S0263034612000870
- [2] S.V.Alekseev, N.G.Ivanov, V.F.Losev, et. all., Attainment of a 40 TW peak output power with a visible-range hybrid femtosecond laser system, *Quantum Electronics*, **49**(2019), no. 10, 901–904. DOI: 10.1070/QEL17050
- [3] T.Ozaki, J.-C.Kieffer, R.Toth, et al., Experimental prospects at the Canadian advanced laser light source facility, *Laser and particle beams*, **24**(2006), no. 01, 101–106. DOI: 10.1017/S0263034606060150
- [4] L.D.Mikheev, V.I.Tcheremiskine, O.P.Uteza, M.L.Sentis, Photochemical gas lasers and hybrid (solid/gas) blue-green femtosecond systems, *Progress in Quantum Electronics*, **36**(2012), no. 01, 98–142. DOI: 10.1016/j.pquantelec.2012.03.004
- [5] L.D.Mikheev, V.F.Losev, Multiterawatt Hybrid (Solid/Gas) Femtosecond Systems in the Visible, In: High Energy and Short Pulse Lasers, ed. R. Viskup (Croatia: InTech), chapter 6, 2016, 131–161. DOI: 10.5772/63972
- [6] S.V.Alekseev, V.F.Losev, V.I.Trunov, S.A.Frolov, Shortening of femtosecond pulse duration during second harmonic generation, *J. Sib. Fed. Univ. Math. Phys.*, **15**(2022), no. 6, 703–709. DOI: 10.17516/1997-1397-2022-15-6-703-709
- [7] E.A.Khazanov, S.Yu.Mironov, G.Mourou, Nonlinear compression of high-power laser pulses: compression after compressor approach, *Physics–Uspekhi*, **62**(2019), no. 11, 1096–1124. DOI: 10.3367/UFNe.2019.05.038564
- [8] V.Ginzburg, I.Yakovlev, et. all., Fivefold compression of 250-TW laser pulses, *Physical Review A*, **101**(2020), 013829. DOI: 10.1103/physreva.101.013829
- [9] T.Brabec, F.Krausz, Nonlinear optical pulse propagation in the single-cycle regime, *Physical Review Letters*, **78**(1997), no. 17, 3282–3285. DOI: 10.1103/PhysRevLett.78.3282

- [10] V.A.Trofimov, Invariants of nonlinear propagation of femtosecond pulses, *News of higher educational institutions. Radiophysics*, **42**(1999), no. 4, 369–372. DOI: 10.1007/BF02677576

Уширение спектра фемтосекундного импульса излучения на длине волны 950 нм в материале с кубической нелинейностью

Сергей В. Алексеев

Валерий Ф. Лосев

Институт сильноточной электроники СО РАН
Томск, Российская Федерация

Яков В. Грудцын

Андрей В. Корибут

Валерий И. Яловой

Физический институт им. П.Н. Лебедева РАН
Москва, Российская Федерация

Аннотация. Экспериментально и теоретически исследуются условия уширения спектра 60 фс импульса излучения на центральной длине волны 950 нм в пластинах из плавленного кварца за счет фазовой самомодуляции. Исследования проводятся при интенсивности излучения от 50 до 400 ГВт/см² и толщине пластин от 1 до 10 см. Описываются условия экспериментов и расчетная модель, основанная на решении системы нелинейных уравнений Шредингера в приближении медленно меняющейся волны. Оценивается возможность сжатия импульса излучения с уширенным спектром при компенсации квадратичной нелинейной фазы. Показывается, что при уширении спектра удается сократить спектрально ограниченную длительность не более двух раз.

Ключевые слова: фемтосекундный импульс, ширина спектра, плавленный кварц.

EDN: FDPGQX
УДК 519.688

Investigation of the Orientational Thermoelasticity Effect Using a Simplified Model of Nematic Liquid Crystal in the Acoustic Approximation

Irina V. Smolekho*

Institute of Computational Modelling SB RAS
Krasnoyarsk, Russian Federation

Received 10.08.2024, received in revised form 15.09.2024, accepted 24.10.2024

Abstract. Analysis of the orientational thermoelasticity effect using a two-dimensional simplified dynamic model of liquid crystal in the acoustic approximation is presented in the paper. It is assumed that effect occurs when one of the boundaries of a rectangular liquid crystal layer is heated. To solve the system of model equations, the method of two-cycle splitting with respect to spatial variables is used in combination with the finite-difference Godunov scheme for the acoustic equations and the Ivanov scheme with controlled energy dissipation for the heat conduction equation. This combination of finite-difference methods allows one to calculate related thermomechanical processes using the same time and space steps that satisfy the Courant-Friedrichs-Levy criterion. The numerical algorithm was implemented as a parallel program written in C++. Parallelization of computations was performed with NVIDIA graphic accelerators using CUDA technology. Simulations demonstrate that it is impossible to observe the effect of reorientation of liquid crystal molecules under the influence of temperature for the presented simplified model in the acoustic approximation. It was concluded that when surface tension forces are taken into account this effect will be observed for the model used in this work.

Keywords: liquid crystal, thermal conductivity, dynamics, CUDA technology.

Citation: I.V. Smolekho, Investigation of the Orientational Thermoelasticity Effect Using a Simplified Model of Nematic Liquid Crystal in the Acoustic Approximation, J. Sib. Fed. Univ. Math. Phys., 2025, 18(3), 337–346. EDN: FDPGQX.



Introduction

Liquid crystals are substances combining the optical anisotropy of crystals and the molecular mobility of liquids in some temperature range. This is the most important property of such systems [1, 2]. Liquid crystal molecules have a specific shape but they also have the property of fluidity. Depending on the initial orientation, liquid crystals are divided into nematic, smectic and cholesteric. The most common type of liquid crystals, namely, nematic crystal is considered in present which best reflects the dual nature of these substances. This type has a wide range of applications, ranging from information display technologies to optical devices and sensors. It helps to regulate the brightness of the screen in LCDs by changing the strength of the electric field acting on the crystal. In addition, orientation of liquid crystals is sensitive to temperature change. If liquid crystals are heated they take a more ordered state which can be used, for example, for data storage. If such liquid crystals are cooled they return to their original state. It means that data can be erased and rewritten. Liquid crystal sensors are used for temperature

*ismol@icm.krasn.ru <https://orcid.org/0000-0002-9852-9310>

© Siberian Federal University. All rights reserved

measurement and biochemical analysis, they continue to be of interest due to their controllable optical and electro-optical properties. Studies in this field are progressing, and new applications are being developed so liquid crystals play an important role in modern constantly evolving technologies. By now, dynamic model of Ericksen and Leslie [3, 4] has been developed on the basis of conservation laws. It takes into account all types of movements as well as the flow of liquid crystals. However, it turned out to be too complex to solve using numerical methods because it includes a large number of equations and parameters that must be determined experimentally which is not always possible. Then, there was a need to develop simpler models allowing for a detailed description of the processes occurring in liquid crystals that would significantly facilitate their study.

This paper presents analysis of the orientational thermoelasticity effect using a simplified two-dimensional model in the acoustic approximation. It takes into account mechanical, temperature and electrical effects in liquid crystals [5]. The effect occurs when the boundary of a horizontal liquid crystal layer is heated. The effect of temperature on the orientation of liquid crystal molecules was studied experimentally [6]. It was concluded that susceptibility to heat flows is similar to the interaction with electromagnetic fields. However, a plate with significantly different coefficient of volumetric expansion was used in experiments. It is likely that the effect of molecular reorientation is associated with the thermal expansion of the plate but not with the effect of the heat flow.

1. Mathematical model of liquid crystal in acoustic approximation

The equations of the model that describe behaviour of liquid crystals under thermomechanical and electrical perturbations are derived from the integral conservation laws of energy, momentum, and angular momentum on the basis of the Cosserat continuum theory [7] using the Clausius–Duhem inequality. In the planar case, the model includes the following equations

$$\text{translational motion} \quad \rho \frac{\partial v_1}{\partial t} = -\frac{\partial p}{\partial x_1} - \frac{\partial q}{\partial x_2} + f_1, \quad \rho \frac{\partial v_2}{\partial t} = \frac{\partial q}{\partial x_1} - \frac{\partial p}{\partial x_2} + f_2, \quad (1)$$

$$\text{rotational motion} \quad J \frac{\partial \omega}{\partial t} = 2q + \frac{\partial \mu_1}{\partial x_1} + \frac{\partial \mu_2}{\partial x_2} + m, \quad (2)$$

$$\text{couple stresses} \quad \frac{\partial \mu_1}{\partial t} = \gamma \frac{\partial \omega}{\partial x_1}, \quad \frac{\partial \mu_2}{\partial t} = \gamma \frac{\partial \omega}{\partial x_2}, \quad (3)$$

$$\text{angle of rotation} \quad \frac{\partial \theta}{\partial t} = \omega, \quad (4)$$

state for pressure and tangential stress

$$\frac{\partial p}{\partial t} = -\kappa \left(\frac{\partial v_1}{\partial x_1} + \frac{\partial v_2}{\partial x_2} \right) + \beta \frac{\partial T}{\partial t}, \quad \frac{\partial q}{\partial t} = \alpha \left(\frac{\partial v_2}{\partial x_1} - \frac{\partial v_1}{\partial x_2} \right) - 2\alpha \left(\omega + \frac{q}{\eta} \right), \quad (5)$$

anisotropic heat conduction

$$\rho c \frac{\partial T}{\partial t} = \frac{\partial}{\partial x_1} \left(\mathfrak{a}_{11} \frac{\partial T}{\partial x_1} + \mathfrak{a}_{12} \frac{\partial T}{\partial x_2} \right) + \frac{\partial}{\partial x_2} \left(\mathfrak{a}_{12} \frac{\partial T}{\partial x_1} + \mathfrak{a}_{22} \frac{\partial T}{\partial x_2} \right) - \quad (6)$$

$$-\beta T \left(\frac{\partial v_1}{\partial x_1} + \frac{\partial v_2}{\partial x_2} \right) + \frac{2q^2}{\eta} + H,$$

$$\mathfrak{a}_{11} = \mathfrak{a}_{\parallel} \cos^2 \theta + \mathfrak{a}_{\perp} \sin^2 \theta, \quad \mathfrak{a}_{12} = (\mathfrak{a}_{\parallel} - \mathfrak{a}_{\perp}) \sin \theta \cos \theta, \quad \mathfrak{a}_{22} = \mathfrak{a}_{\parallel} \sin^2 \theta + \mathfrak{a}_{\perp} \cos^2 \theta,$$

where v_1 and v_2 are the components of the velocity vector, ω is the angular velocity, θ is the rotation angle of molecules, p is the pressure, q is the tangential stress, μ_1 and μ_2 are the couple stresses, T is the temperature, ρ is the density, J is the moment of inertia, κ is the bulk compression modulus, α is the modulus of elastic resistance to rotation, β is the coefficient of thermal expansion, γ is the modulus of elastic resistance to curvature change, η is the viscosity coefficient, H is the intensity of heat sources, c is the specific heat capacity, \mathfrak{a}_{\parallel} and \mathfrak{a}_{\perp} are the thermal conductivity coefficients of a liquid crystal in the direction of molecular orientation and in the transverse direction, f_1 , f_2 and m are the bulk forces and couple force caused by the electric field. Here, they are not taken into account when studying the thermodynamic effect since they do not affect the temperature change. The algorithm of the electric effect is presented, for example, in [8].

2. Computational algorithm

A rectangular region of liquid crystal is considered with dimensions l_{x_1} and l_{x_2} in the directions x_1 and x_2 , respectively. The finite-difference grid is

$$R_{i_1 i_2}^i = \{(t_i, x_{1i_1}, x_{2i_2}) : t_i = i \Delta t, \quad x_{1i_1} = i_1 \Delta x_1, \quad x_{2i_2} = i_2 \Delta x_2, \\ i = 0, \dots, Nt, \quad i_1 = 0, \dots, Nx_1, \quad i_2 = 0, \dots, Nx_2\},$$

where Δx_1 and Δx_2 are space steps in the directions x_1 and x_2 such that $x_{1i_1} \in (0, l_{x_1})$, $x_{2i_2} \in (0, l_{x_2})$, Δt is the time step, Nt is the number of time steps, Nx_1 and Nx_2 are the arbitrary numbers of cells of the finite difference grid in the directions x_1 and x_2 . At the initial moment of time, zero values are set in this region for all quantities except $\theta = \theta_0$ and $T = T_0$. The boundary conditions are presented in terms of pressure, velocity, stress and temperature. The load on the boundary can act continuously or for a given number of time steps.

System of equations (1)–(6) is hyperbolic in the sense of Friedrichs so the formulation of the Cauchy problem is correct. The system is solved using the method of two-cycle splitting by spatial variables, and it is assumed that five consecutive stages occur at each time step. At the 1st and 5th stages, one-dimensional equations that depend on x_1 are solved at different half-steps in time:

$$\left\{ \begin{array}{l} \rho \frac{\partial v_1}{\partial t} = -\frac{\partial p}{\partial x_1} \\ \frac{\partial p}{\partial t} = -\kappa \frac{\partial v_1}{\partial x_1} \end{array} \right\}, \quad \left\{ \begin{array}{l} \rho \frac{\partial v_2}{\partial t} = \frac{\partial q}{\partial x_1} \\ \frac{\partial q}{\partial t} = \alpha \frac{\partial v_2}{\partial x_1} \end{array} \right\}, \quad \left\{ \begin{array}{l} J \frac{\partial \omega}{\partial t} = \frac{\partial \mu_1}{\partial x_1} \\ \frac{\partial \mu_1}{\partial t} = \gamma \frac{\partial \omega}{\partial x_1} \end{array} \right\}, \quad (7)$$

$$\rho c \frac{\partial T}{\partial t} = \frac{\partial h_1}{\partial x_1} - \beta T \frac{\partial v_1}{\partial x_1}, \quad h_1 = \mathfrak{a}_{11} \frac{\partial T}{\partial x_1} + \mathfrak{a}_{12} \frac{\partial T}{\partial x_2}. \quad (8)$$

To solve equations (7), the finite-difference Godunov scheme [9] of the "predictor-corrector" type is used. At the "predictor" step, the following equations on characteristics obtained from

(7) are used

$$\begin{aligned}
dx_1 = \mp \sqrt{\kappa/\rho} dt : \quad dI_1^\pm &= 0, \quad I_1^\pm = p \pm v_1 \sqrt{\kappa\rho} \\
dx_1 = \pm \sqrt{\alpha/\rho} dt : \quad dI_2^\pm &= 0, \quad I_2^\pm = q \pm v_2 \sqrt{\alpha\rho} \\
dx_1 = \pm \sqrt{\gamma/J} dt : \quad dI_3^\pm &= 0, \quad I_3^\pm = \mu_1 \pm \omega \sqrt{\gamma J}.
\end{aligned} \tag{9}$$

These equations allow one to determine the values with fractional indices on the lateral faces of the cells of the finite difference grid in the plane x_1 and t :

$$\begin{aligned}
v_{1_{i_1-1/2}} &= \frac{I_{1,i_1-1}^+ - I_{1,i_1}^-}{2\sqrt{\rho\kappa}}, \quad p_{i_1-1/2} = \frac{I_{1,i_1-1}^+ + I_{1,i_1}^-}{2}, \quad v_{2_{i_1-1/2}} = \frac{I_{2,i_1}^+ - I_{2,i_1-1}^-}{2\sqrt{\rho\alpha}}, \\
q_{i_1-1/2} &= \frac{I_{2,i_1}^+ + I_{2,i_1-1}^-}{2}, \quad \omega_{i_1-1/2} = \frac{I_{3,i_1}^+ - I_{3,i_1-1}^-}{2\sqrt{\gamma J}}, \quad \mu_{1_{i_1-1/2}} = \frac{I_{3,i_1}^+ + I_{3,i_1-1}^-}{2},
\end{aligned} \tag{10}$$

where integer indices refer to the internal nodes of the grid $i_1 = 2, \dots, Nx_1$. At the boundary nodes, these values are found from the boundary conditions. Then heat conduction equation (7) is solved with the help of the Ivanov finite-difference scheme [10] that is used to solve problems of the dynamics of solids, plates and shells. The idea of the method is to implement the law of conservation of energy at discrete level. Let us consider the extended system in the x_1 direction

$$\rho c \frac{\partial T}{\partial t} = \frac{\partial \bar{h}}{\partial x_1}, \quad h = \varkappa_{11} \frac{\partial \bar{T}}{\partial x_1} + g,$$

where the unknown functions are $\bar{T} \neq T$ and $\bar{h} \neq h$. For this system, the energy balance equation

$$\frac{\rho c}{2} \frac{\partial T^2}{\partial t} + \varkappa_{11} \left(\frac{\partial \bar{T}}{\partial x_1} \right)^2 = \frac{\partial \bar{h}}{\partial x_1} (T - \bar{T}) + \frac{\partial \bar{T}}{\partial x_1} (h - \bar{h}) + \frac{\partial(\bar{T}\bar{h})}{\partial x_1} - g \frac{\partial \bar{T}}{\partial x_1}. \tag{11}$$

is satisfied. It is transformed into a dissipative inequality

$$\frac{\rho c}{2} \frac{\partial T^2}{\partial t} + \varkappa_{11} \left(\frac{\partial \bar{T}}{\partial x_1} \right)^2 \leq \frac{\partial(\bar{T}\bar{h})}{\partial x_1} - g \frac{\partial \bar{T}}{\partial x_1}.$$

The closing equations of the extended system take the form

$$\begin{bmatrix} T - \bar{T} \\ h - \bar{h} \end{bmatrix} = -D \begin{bmatrix} \frac{\partial \bar{h}}{\partial x_1} \\ \frac{\partial \bar{T}}{\partial x_1} \end{bmatrix}, \quad D = \begin{bmatrix} D_{11} & D_{12} \\ D_{21} & D_{22} \end{bmatrix},$$

where D is a positive definite matrix. The discrete analogue of the extended system is the ‘‘corrector’’ step of the finite difference scheme:

$$\rho c \frac{T^{i_1} - T_{i_1}}{\Delta t/2} = \frac{h_{i_1+\frac{1}{2}} - h_{i_1-\frac{1}{2}}}{\Delta x_1}, \quad h_{i_1} = \varkappa_{11,i_1} \frac{T_{i_1+\frac{1}{2}} - T_{i_1-\frac{1}{2}}}{\Delta x_1} + g_{i_1}. \tag{12}$$

For a more brief notation, there are no indices of the second direction, the upper indices correspond to the current time step, the lower indices correspond to the previous one, Δx_1 , h_i and \varkappa_{11} are the spatial step, fluxes with mixed derivatives and the thermal conductivity

coefficient in the x_1 direction. The quantities g_i are calculated explicitly using the values from the previous time step, and they include mixed derivatives with the coefficient \mathfrak{a}_{12} . The solution is constructed with the time step $\Delta t/2$ as required for the splitting stages. The discrete analogue of equation (11) is

$$\rho c \frac{(T^{i_1})^2 - (T_{i_1})^2}{\Delta t} + \mathfrak{a}_{11,i} \left(\frac{T_{i_1+\frac{1}{2}} - T_{i_1-\frac{1}{2}}}{\Delta x_1} \right)^2 = \frac{h_{i_1+\frac{1}{2}} - h_{i_1-\frac{1}{2}}}{\Delta x_1} \left(\frac{T^{i_1} + T_{i_1}}{2} - \frac{T_{i_1+\frac{1}{2}} + T_{i_1-\frac{1}{2}}}{2} \right) + \frac{T_{i_1+\frac{1}{2}} - T_{i_1-\frac{1}{2}}}{\Delta x_1} \left(h_{i_1} - \frac{h_{i_1+\frac{1}{2}} + h_{i_1-\frac{1}{2}}}{2} \right) + \frac{(Th)_{i_1+\frac{1}{2}} - (Th)_{i_1-\frac{1}{2}}}{\Delta x_1} - g_{i_1} \frac{T_{i_1+\frac{1}{2}} - T_{i_1-\frac{1}{2}}}{\Delta x_1}.$$

The closing equations take the form

$$\begin{bmatrix} T^{i_1} + T_{i_1} - T_{i_1+\frac{1}{2}} - T_{i_1-\frac{1}{2}} \\ 2h_{i_1} - h_{i_1+\frac{1}{2}} - h_{i_1-\frac{1}{2}} \end{bmatrix} = \frac{-2D}{\Delta x_1} \begin{bmatrix} h_{i_1+\frac{1}{2}} - h_{i_1-\frac{1}{2}} \\ T_{i_1+\frac{1}{2}} - T_{i_1-\frac{1}{2}} \end{bmatrix}.$$

For simplicity, matrix D with one non-zero element with free parameter d is used: $D_{11} = d - \Delta t/c \Delta x_1 \geq 0$ since the scheme approximates the heat conduction equation only with small elements of this matrix. The closing equations take the form

$$T_i - \frac{T_{i_1+\frac{1}{2}} + T_{i_1-\frac{1}{2}}}{2} = -d \frac{h_{i_1+\frac{1}{2}} - h_{i_1-\frac{1}{2}}}{2}, \quad g_{i_1} + \mathfrak{a}_{11,i_1} \frac{T_{i_1+\frac{1}{2}} - T_{i_1-\frac{1}{2}}}{\Delta x_1} = \frac{h_{i_1+\frac{1}{2}} + h_{i_1-\frac{1}{2}}}{2}.$$

The equations for heat fluxes are obtained by adding and subtracting the closing equations:

$$dh_{i_1 \pm \frac{1}{2}} = d \mathfrak{a}_{11,i_1} \frac{T_{i_1+\frac{1}{2}} - T_{i_1-\frac{1}{2}}}{\Delta x_1} \pm \frac{T_{i_1+\frac{1}{2}} + T_{i_1-\frac{1}{2}}}{2} \pm T_{i_1} + dg_{i_1}.$$

The step "predictor" for temperature is calculated using three-point sweep method in each direction:

$$\begin{aligned} - \left(\frac{d \mathfrak{a}_{11,i_1}}{\Delta x_1} - \frac{1}{2} \right) T_{i_1+\frac{1}{2}} + \left(1 + \frac{d(\mathfrak{a}_{11,i_1} + \mathfrak{a}_{11,i_1-1})}{\Delta x_1} \right) T_{i_1-\frac{1}{2}} - \left(\frac{d \mathfrak{a}_{11,i_1-1}}{\Delta x_1} - \frac{1}{2} \right) T_{i_1-\frac{3}{2}} = \\ = T_{i_1} + T_{i_1-1} + d(g_{i_1} - g_{i_1-1}). \end{aligned}$$

The final step of the splitting stage is the "corrector" step of the Godunov scheme. Taking into account that temperature in the right part is already found, the unknown quantities are determined as follows

$$\begin{aligned} \rho \frac{\bar{v}_1 - v_1}{\Delta t} = \frac{p_{i_1} - p_{i_1-1}}{2\Delta x_1}, \quad \rho \frac{\bar{v}_2 - v_2}{\Delta t} = \frac{q_{i_1} - q_{i_1-1}}{2\Delta x_1}, \quad \frac{\bar{p} - p}{\Delta t} = -\kappa \frac{v_{1_{i_1}} - v_{1_{i_1-1}}}{2\Delta x_1} + \beta \frac{\bar{T} - T}{\Delta t}, \\ \frac{\bar{q} - q}{\Delta t} = \alpha \frac{v_{2_{i_1}} - v_{2_{i_1-1}}}{2\Delta x_1}, \quad J \frac{\bar{\omega} - \omega}{\Delta t} = \frac{\mu_{1_{i_1}} - \mu_{1_{i_1-1}}}{2\Delta x_1}, \quad \frac{\bar{\mu}_1 - \mu_1}{\Delta t} = \gamma \frac{\omega_{i_1} - \omega_{i_1-1}}{2\Delta x_1}. \end{aligned}$$

The values with a bar denote the values at the current time step, without a bar - at the previous time step. The indices for the second direction $i_2 - 1/2$ are omitted for brevity. In the finite differences in time, the indices $i_1 - 1/2$, $i_2 - 1/2$ are also omitted. At the 2nd and 4th stages, system of acoustic equations (13) and heat conduction equation (14) for the direction x_2 are solved in a similar way:

$$\left\{ \begin{array}{l} \rho \frac{\partial v_1}{\partial t} = -\frac{\partial q}{\partial x_2} \\ \frac{\partial q}{\partial t} = -\alpha \frac{\partial v_1}{\partial x_2} \end{array} \right\}, \quad \left\{ \begin{array}{l} \rho \frac{\partial v_2}{\partial t} = -\frac{\partial p}{\partial x_2} \\ \frac{\partial p}{\partial t} = -\kappa \frac{\partial v_2}{\partial x_2} \end{array} \right\}, \quad \left\{ \begin{array}{l} J \frac{\partial \omega}{\partial t} = \frac{\partial \mu_2}{\partial x_2} \\ \frac{\partial \mu_2}{\partial t} = \gamma \frac{\partial \omega}{\partial x_2} \end{array} \right\}. \quad (13)$$

$$\rho c \frac{\partial T}{\partial t} = \frac{\partial h_2}{\partial x_2} - \beta T \frac{\partial v_2}{\partial x_2}, \quad h_2 = \varkappa_{12} \frac{\partial T}{\partial x_1} + \varkappa_{22} \frac{\partial T}{\partial x_2}. \quad (14)$$

At the 3rd stage the equations

$$J \frac{\partial \omega}{\partial t} = 2q, \quad \frac{\partial \theta}{\partial t} = \omega, \quad \frac{\partial q}{\partial t} = -2\alpha \left(\omega + \frac{q}{\eta} \right), \quad \rho c \frac{\partial T}{\partial t} = \frac{2q^2}{\eta}.$$

are solved in accordance with the Crank–Nicholson scheme:

$$J \frac{\bar{\omega} - \omega}{\Delta t} = 2 \frac{\bar{q} + q}{2}, \quad \frac{\bar{\theta} - \theta}{\Delta t} = \frac{\bar{\omega} + \omega}{2}, \quad \frac{\bar{q} - q}{\Delta t} = -2\alpha \left(\frac{\bar{\omega} + \omega}{2} + \frac{\bar{q} + q}{2\eta} \right), \quad \rho c \frac{\bar{T} - T}{\Delta t} = \frac{(\bar{q} + q)^2}{2\eta}.$$

The indices $i_1 - 1/2$, $i_2 - 1/2$ for the values at the previous time step q , ω , θ and T as well as at the current time step \bar{q} , $\bar{\omega}$, $\bar{\theta}$ and \bar{T} are omitted for brevity. Calculations are performed using the following formulas

$$\bar{q} = \frac{J\eta - \Delta t\alpha(\Delta t\eta + J)}{J\eta + \Delta t\alpha(\Delta t\eta + J)} q - \frac{2\Delta t\alpha J\eta}{J\eta + \Delta t\alpha(\Delta t\eta + J)} \omega,$$

$$\bar{\omega} = \omega + \frac{\Delta t}{J}(\bar{q} + q), \quad \bar{\theta} = \theta + \frac{\Delta t}{2}(\bar{\omega} + \omega), \quad \bar{T} = T + \frac{\Delta t}{2\rho c\eta}(\bar{q} + q)^2.$$

3. Results of computations

The described algorithm was implemented using the CUDA parallel programming technology [11]. Numerical calculations were performed for the 5CB liquid crystal. Parameters of the liquid crystal are [12, 13] $\rho = 1022 \text{ kg/m}^3$, $j = 0.03 \cdot 10^{-12} \text{ kg/m}$, $\kappa = 11.1 \text{ GPa}$, $\alpha = 360 \text{ Pa}$, $\beta = 0.3 \cdot 10^{-6} \text{ K}^{-1}$, $\gamma = 6 \cdot 10^{-12} \text{ N}$, $\eta = 0.036 \text{ Pa} \cdot \text{c}$, $c = 100 \text{ J}/(\text{kg} \cdot \text{K})$, $\varkappa_{\parallel} = 0.226 \text{ W}/(\text{m} \cdot \text{K})$, $\varkappa_{\perp} = 0.135 \text{ W}/(\text{m} \cdot \text{K})$.

A rectangular LC layer with dimensions of $200 \times 80 \mu\text{m}$ was considered. The finite difference grid contains 640×256 cells. At the initial moment of time $T_0 = 297 \text{ K}$ and $\theta = \pi/2$. At the upper border the temperature is set as follows $T = T_0 + T' e^{-4(x_{i_1} - x_c)^2/x_r^2}$, where T' is some constant, x_c is the centre of load application, x_r is the radius of the load.

Fig. 1 shows the results of the action of four heat sources with the radius of $20 \mu\text{m}$ on the lower boundary. In this case, $x_c = (i - 0.5)lx_1/n$, where $n = 4$ is the number of heat sources, $i = 1, 2, 3, 4$. Fig. 2 demonstrates the propagation and reflection of pressure waves initiated in the heating region. Fig. 3 shows the vector field of velocities. Fig. 4 shows the results of the action of one heat source in the middle of the right boundary. The other parameters are similar to the previous case. Fig. 5 and Fig. 6 show the propagation of pressure waves and the vector field of velocities, respectively. In both cases, velocities change in accordance with the change in pressure. Tangential stress, angular velocity and moment stresses in this case are equal to zero. The rotation angle remains unchanged due to the absence of tangential stresses. Thus, within the framework of the described model it is impossible to change the orientation of nematic liquid crystal molecules by varying only temperature field.

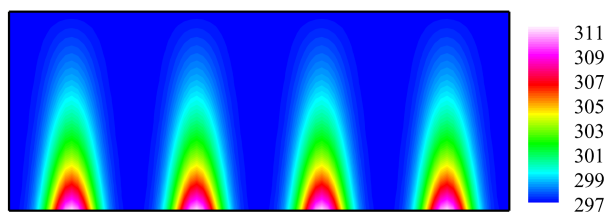


Fig. 1. Heating of the lower boundary: temperature level lines T , [K]

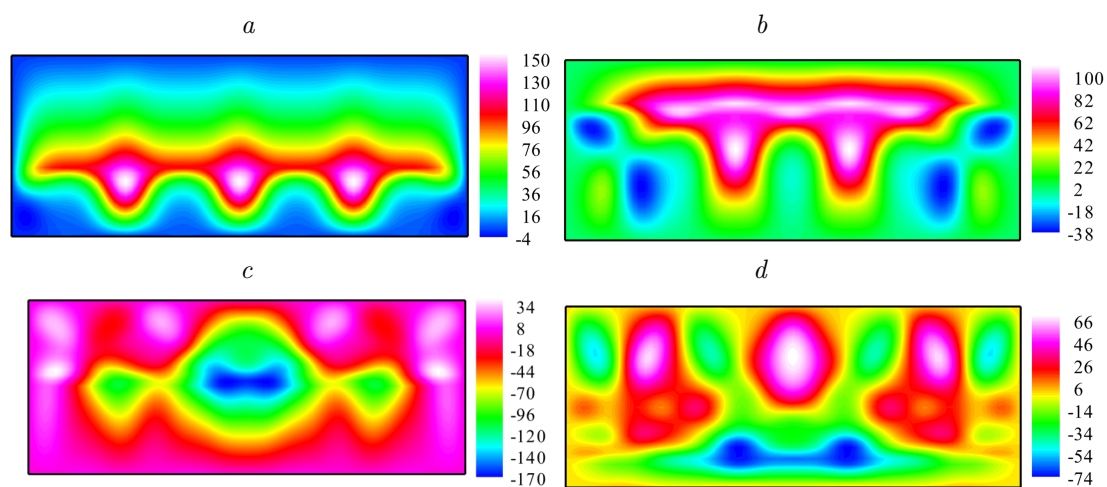


Fig. 2. Heating of part of the lower boundary: pressure level lines p , [nPa] (a – 9 ps, b – 18 ps, c – 36 ps, d – 45 ps)

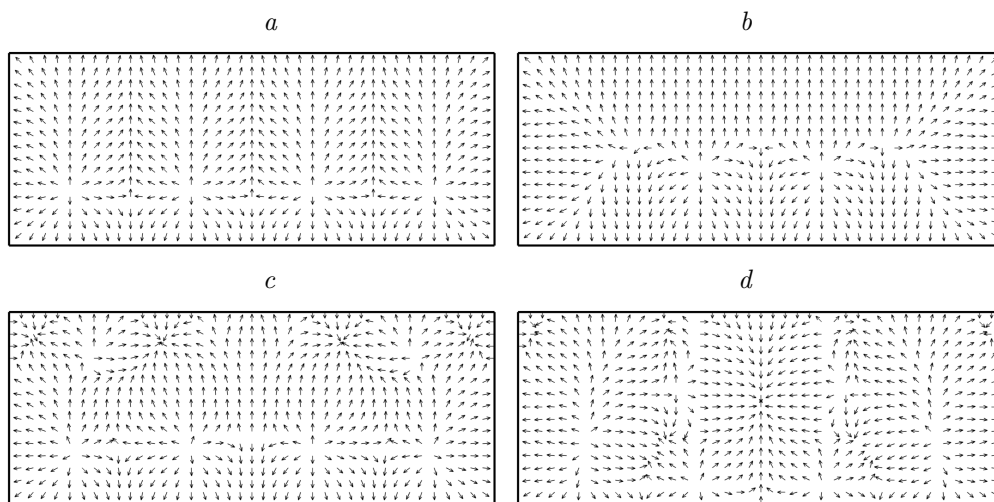


Fig. 3. Heating of part of the lower boundary: vector velocity field (a – 9 ps, b – 18 ps, c – 36 ps, d – 45 ps)

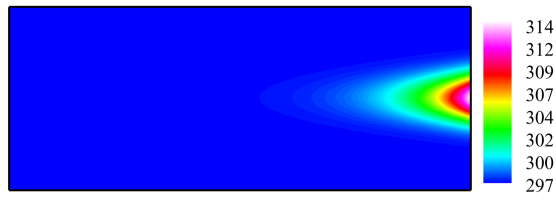


Fig. 4. Heating in the middle of the right boundary: temperature level lines T , [K]

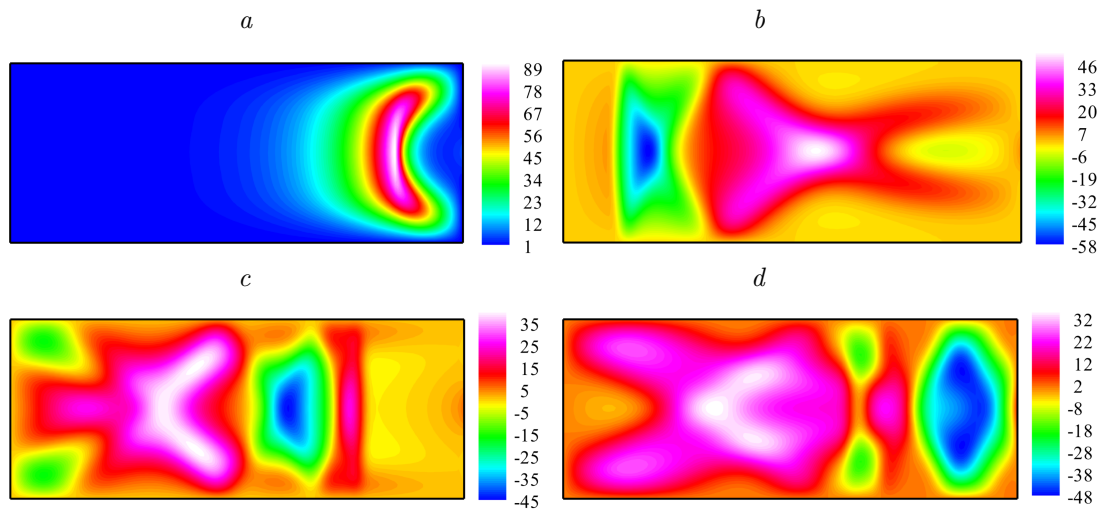


Fig. 5. Heating in the middle of the right boundary: pressure level lines p , [nPa] (a — 9 ps, b — 54 ps, c — 108 ps, d — 162 ps)

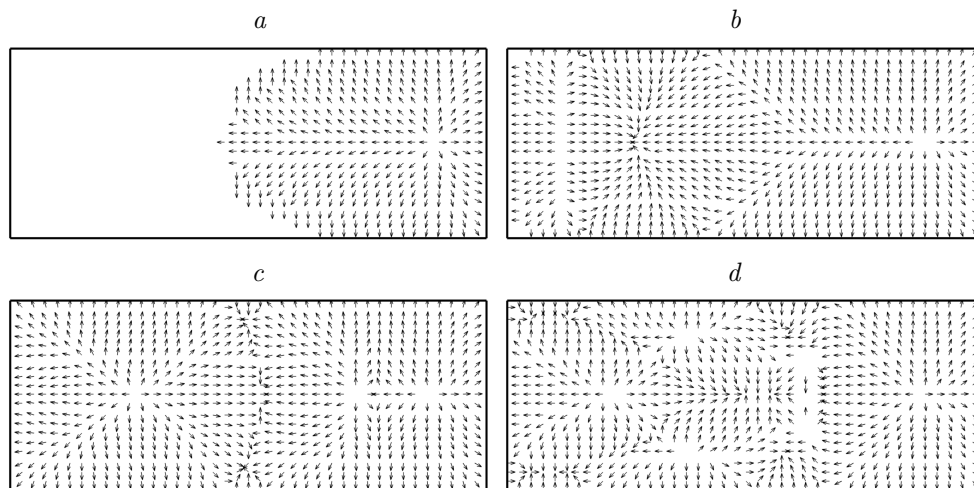


Fig. 6. Heating in the middle of the right boundary: vector velocity field (a — 9 ps, b — 54 ps, c — 108 ps, d — 162 ps)

Conclusion

The paper presents: a simplified model of thermomechanical and electrical effects in the acoustic approximation; an algorithm for numerical solution of the model equations; implementation of the algorithm as a parallel program in the C++ language with the help of the CUDA technology; a series of simulations that demonstrate that it is impossible to observe the effect of orientational thermoelasticity using the presented dynamic model. It is assumed that if the surface tension forces will be taken into account then orientation of the molecules would change when one of the boundaries of the liquid crystal layer is heated.

This work is supported by the Krasnoyarsk Mathematical Center and financed by the Ministry of Science and Higher Education of the Russian Federation in the framework of the establishment and development of regional Centers for Mathematics Research and Education (Agreement No. 075-02-2024-1378).

References

- [1] L.M.Blinov, Structure and Properties of Liquid Crystals, Springer, Dordrecht, 2011.
DOI: 10.1007/978-90-481-8829-1.
- [2] P.G.de Gennes, J.Prost, The Physics of Liquid Crystals, New York: Oxford University Press, 1993.
- [3] J.L.Ericksen, Conservation laws for liquid crystals, *Trans. Soc. Rheol.*, **5**(1961), no. 1, 23–34.
DOI: 10.1122/1.548883.
- [4] F.M.Leslie, Some constitutive equations for liquid crystals, *Arch. Ration. Mech. Anal.*, **28**(1968), no. 4, 265–283.
- [5] V.M.Sadovskii, O.V.Sadovskaya, I.V.Smolekho, Modeling of the dynamics of a liquid crystal under the action of weak perturbations, *J. Appl. Mech. Tech. Phys.*, **62**(2021), no. 1, 193–206. DOI:10.1134/S0021894421010211
- [6] S.I.Trashkeev, A.V.Britvin, Thermal orientation effect in a nematic liquid crystal, *Tech. Phys.*, **56**(2011), 747–753. DOI: 10.1134/S1063784211060247.
- [7] E.Cosseratm, F.Cosserat, Théorie des Corps Déformables, Chwolson’s *Traité Physique*, 1909, 2nd ed., 953–1173.
- [8] V.M.Sadovskii, O.V.Sadovskaya, I.V.Smolekho, Parallel implementation of the algorithm describing the behavior of liquid crystals under the action of electric field, *AIP Conf. Proc.*, **2025**(2018), art. 070005. DOI: 10.1063/1.5064917.
- [9] S.K.Godunov, A.V.Zabrodin, M.Ya.Ivanov, A.N.Kraiko, G.P.Prokopov, Numerical Solving Many-Dimensional Problems of Gas Dynamics, Nauka, Moscow, 1976 (in Russian).
- [10] G.V.Ivanov, Yu.M.Volchkov, I.O.Bogulskii, S.A.Anisimov, V.D.Kurguzov, Numerical Solution of Dynamic Elastic-Plastic Problems of Deformable Solids, Sib. Univ. Izd., Novosibirsk, 2002 (in Russian).

- [11] R.Farber, *CUDA Application Design and Development*, Amsterdam – Boston – London – New York – Oxford – Paris – San Francisco – Singapore – Sydney – Tokyo: Elsevier, 2011.
- [12] K.Skarp, S.T.Lagerwall, B.Stebler, Measurements of hydrodynamic parameters for nematic 5CB, *Mol. Cryst. Liq. Cryst.*, **60**(1980), no. 3, 215–236. DOI: 10.1080/00268948008072401.
- [13] B.A.Belyaev, N.A.Drokin, V.F.Shabanov, V.N.Shepov, Dielectric anisotropy of 5CB liquid crystal in a decimeter wavelenght range, *Phys. Solid State*, **42**(2000), no. 3, 577–579. DOI: 10.1134/1.1131251.

Исследование эффекта ориентационной термоупругости с помощью упрощенной модели нематического жидкого кристалла в акустическом приближении

Ирина В. Смолехо

Институт вычислительного моделирования СО РАН
Красноярск, Российская Федерация

Аннотация. В работе представлен анализ эффекта ориентационной термоупругости с применением двумерной упрощенной динамической модели жидкого кристалла в акустическом приближении. Предполагается, что эффект возникает при нагревании одной из границ прямоугольного жидкокристаллического слоя. При решении системы уравнений модели применяется метод двучиклического расщепления по пространственным переменным в сочетании с конечно-разностной схемой распада разрыва Годунова для уравнений акустики и схемы Иванова с контролируемой диссипацией энергии для уравнения теплопроводности. Использование такой комбинации конечно-разностных схем позволяет проводить расчеты связанных термомеханических процессов с одинаковыми шагами по времени и по пространству, удовлетворяющими условию Куранта-Фридрихса-Леви. Численный алгоритм реализован в виде параллельной программы, написанной на языке C++. Распараллеливание вычислений выполнено для компьютеров с графическими ускорителями NVIDIA по технологии CUDA. Проведены расчеты, демонстрирующие невозможность наблюдения эффекта переориентации молекул жидкого кристалла под действием температуры для представленной упрощенной модели в акустическом приближении. Однако воздействие температуры существенно влияет на давление и скорости. Сделано заключение, что при учете сил поверхностного натяжения этот эффект будет наблюдаться для используемой в работе модели.

Ключевые слова: жидкий кристалл, теплопроводность, динамика, технология CUDA.

EDN: LPTQXH
УДК 535.211:536.331

Near-field Interaction Effects in Colloidal Au-CeYbF₃ Nanoclusters in Plasmonic Immunoanalysis

Elina A. Izbasarova*

Almaz R. Gazizov†

Institute of Physics
Kazan Federal University
Kazan, Russian Federation

Received 13.11.2024, received in revised form 29.12.2024, accepted 04.02.2025

Abstract. In this paper, we study the effects of plasmonic enhancement of spontaneous emission in colloidal nanoclusters consisting of Au nanoparticles and CeYbF₃ phosphor. Based on numerical simulation of various configurations of Au nanoparticles coated with polyethyleneimine, we analyzed the dependence of plasmonic resonances position on their number and distribution. The results showed that optimal nanoparticle configurations significantly enhance luminescence in the desired region of the visible spectrum, which opens up new possibilities for the development of highly sensitive nanosensors. At the same time, nanoclusters located on a Au substrate demonstrate a lower luminescence enhancement coefficient, while having a more inhomogeneous distribution of the optical near field. The results obtained reveal the dependence of the luminescence enhancement coefficient on the spatial distribution and coordination number of plasmonic nanoparticles in a nanocluster. This study contributes to the understanding of plasmonic interaction mechanisms and its applications in optical immunoassay and biomedical technologies.

Keywords: plasmonic nanoparticles, Purcell effect, Förster effect, FDTD modeling, luminescent nanoparticles.

Citation: E.A. Izbasarova, A.R. Gazizov, Near-field Interaction Effects in Colloidal Au-CeYbF₃ Nanoclusters in Plasmonic Immunoanalysis, J. Sib. Fed. Univ. Math. Phys., 2025, 18(3), 347–357. EDN: LPTQXH.



Introduction

The scale of quantitative and dynamic analysis, which allows determining the state and behavioral characteristics of chemical and biological objects, is steadily growing [1]. Over the past decades, a number of electronic methods and devices have been developed for the detection of biomolecules. On the other hand, analysis based on the detection of photons rather than electrons is of growing interest to researchers due to the simplification of analytical instruments and their low cost. Moreover, optical analysis methods are more suitable for studying biological samples, are non-invasive and allow the sample to be examined under normal conditions. One such method is immunoassay based on the use of luminescent labels, the emission of which changes when an antigen with this label (referred to as probe when combined) is attached to the analyte [2]. Organic molecules are primarily used as labels in many areas of biomedicine. Nevertheless, despite the significant amount of research devoted to optical sensor systems using

*Izbasarova.E.A@mail.ru <https://orcid.org/0000-0001-8300-4725>

†equus.meteores@gmail.com <https://orcid.org/0000-0002-9542-8856>

© Siberian Federal University. All rights reserved

organic probes, the difficulties associated with the preparation and production of such systems, as well as the photonic instability of organic materials, to some extent limit their practical application, especially in the context of long-term monitoring. In this regard, it seems advisable to develop stable optical systems based on new materials.

In the context dynamic progress in various fields of medicine, nanomaterials with a high specific surface area and unique optoelectronic properties are widely used for adsorption, in catalysis and analyte detection [3–5]. In particular, optical analysis based on plasmonic nanoparticles is applied to study various target objects, including chemical compounds, biomolecules, as well as physical characteristics such as temperature and viscosity to name a few [6–8]. Localized surface plasmon resonance (LSPR) in noble metal nanoparticles, associated with collective oscillations of free electrons, not only determines the color of the nanoparticles, but also leads to a change in the luminescence of nearby emitters due to interaction with their near-field. In this regard, optical analysis based on plasmonic nanoparticles can be carried out both through absorption and through fluorescence. The high stability of LSPR allows for long-term tracking of individual plasmonic nanoparticles, which facilitates the detection of transient processes and detailed study of chemical and biological reactions [9].

LSPRs significantly increase the efficiency of photon absorption and scattering. As a result, plasmonic nanoparticles, unlike traditional organic dyes, demonstrate a significantly higher extinction coefficient, which often exceeds that of dyes by several orders of magnitude. LSPRs enhance electric fields near the surface of nanoparticles, with the magnitude of the enhancement depends on the inverse of the distance to the surface. In addition, the LSPR characteristics of nanoparticles can be tuned by varying parameters such as size, morphology, distance between nanoparticles, and properties of the environment [10, 11]. In particular, the aggregation of colloidal plasmonic nanoparticles into clusters can significantly modify the fields on their surface. Recent studies have demonstrated that excited conduction electrons located on the surface of plasmonic nanoparticles are also capable of interacting with the dipoles of nearby luminescent nanoparticles (LNPs) used to detect a specific target molecule, changing their luminescent properties [11, 12]. This interaction can lead to two opposite results: luminescence quenching and enhancement. In particular, the degree of quenching or enhancement caused by LSPR is affected by the LNP characteristics and the distance between the LNP and plasmonic nanoparticles in addition to the LSPR parameters. An increase in the signal level is usually achieved when the LSPR frequency of the metal nanostructure coincides with the LNP excitation frequency. This contributes to an increase in the excitation intensity due to the localization of the electromagnetic field near the metal nanostructure. An increase in the luminescence intensity can also be realized by increasing the rate of radiative transition of emitters, which is known as the Purcell effect [13]. This effect is observed when the LSPR frequency of the metal nanostructure coincides with the radiation frequency of the LNP.

In addition to enhancing luminescence, this condition can lead to non-radiative resonant energy transfer (RET) from the donor ion to the metal nanostructure through their near fields. This interaction can cause luminescence quenching, known as the Förster effect [14, 15]. Most studies indicate that the luminescence of LNPs is enhanced by interaction with various types of plasmonic metal nanostructures, such as silver periodic nanogratings [16], gold pyramids, nanoholes, nanorods and planar triangular nanoantennas [17–20]. A 20–30-fold enhancement of the fluorescence of labeled biomarkers on cells was also demonstrated using plasmonic gold nanoisland films [9]. A significant Purcell factor (~ 100) and a limiting detection concentration of 3.1 pmol/L were demonstrated using a system consisting of an organic label and an Au/Ag

oligomer [21]. In the work [22], the influence of the geometry and number of NPs in Au oligomers on the luminescence of organic label was studied, but the authors did not distinguish Purcell effect from other causes of decay rate increasing. However, luminescence quenching has also been observed in other studies. For example, Zhang et al. [23] reported a decrease in the luminescence brightness of 120 nm diameter LNPs with a 20 nm thick silica shell when interacting with 9.4 nm diameter gold nanoparticles. Luminescence quenching due to non-radiative RET in LNPs has also been demonstrated when interacting with gold nanoparticles of similar or smaller size [24, 25].

In the context of the above, plasmon-enhanced luminescence is the result of the influence of many factors. In particular, the sensitivity of LSPR to the surrounding analyte molecules can be used. In our work, nanoclusters are considered, the cores of which are LNPs of CeYTbF₃ surrounded by gold nanoparticles (AuNP). The luminescence of these LNPs occurs due to transitions from the ⁵D₄ level to the sublevels of the ⁷F state [26]. The wavelengths of the four observed transitions are approximately 490 nm, 540 nm, 590 nm and 620 nm. These lines are partially or completely overlapped by the LSPR band of AuNP, which enables Purcell effect. This system can be synthesized in a colloidal solution and then deposited on a substrate. An idea arises to use such structures as labels for immunoassay of biologically significant analytes both in liquid and in the form of special substrates for analysis. Radachlorin, which has absorption bands in the violet and red-orange regions of the visible spectrum, is considered as a test analyte in the work. Among the extensive set of experimental data on the control of particle luminescence using plasmonic nanostructures, two main aspects are distinguished that determine the unique properties of hybrid systems: the size and shape of the subsystems, as well as the distance between them. Our main goal is to characterize from a fundamental perspective the possibility of plasmonic enhancement of luminescence as the number of plasmonic nanoparticles and their configuration change. This will allow us to predict the average Purcell factor and to determine the configurations that contribute most to the luminescence enhancement for different concentrations of AuNPs and their ratio to the concentration of LNPs. This will be a significant step in the development of nanosensors based on luminescence quenching or enhancement.

1. Simulation parameters and conditions

Simulation of plasmonic enhancement of spontaneous emission (Purcell effect) in a nanocluster was carried out, consisting of a core – a dielectric particle of CeYTbF₃ phosphor with a radius of 10 nm and ligands surrounding the core – plasmonic AuNP with a radius of 47 nm, coated with a polyethyleneimine (PEI) shell with a thickness of 4 nm. The polymer shell was used as a linker between the core and ligands, as well as to reduce the influence of near-field energy transfer (Förster effect). Radachlorin was considered as a possible analyte near the examined system. The finite-difference time-domain (FDTD) method was used. The size of the simulation region was 600x600x650 nm, the cell size of the computational grid was 4 nm, and a denser grid with a cell size of 1 nm was set on the objects. The refractive index of the surrounding space was chosen to be constant and equal to 1.33 (water). The boundary conditions chosen were perfectly matched layers (PML) with a total of 8 layers with a standard profile in the stretched-coordinate formulation. To mitigate the consequences of the staircasing approximation of non-flat surfaces on a Cartesian computational grid, a conformal sub-pixel smoothing algorithm was applied. The dielectric permittivity of the phosphor was specified using the Lorentz model:

$$\varepsilon = \varepsilon_d + \frac{Ne^2}{m\varepsilon_0} \frac{f_{osc}}{\omega_0^2 - \omega^2 - i\omega\gamma} \quad (1)$$

where $\varepsilon_d = 2$ is the dielectric permittivity of the crystalline matrix, $N = 10^{21} \text{ cm}^{-3}$ is the concentration of Tb ions, $f_{osc} = 6 \cdot 10^{-8}$ is the oscillator strength of the transition from the ground state to the 5D_4 level [27, 28], ω_0 and γ are the cyclic frequency and linewidth, taken from the experimental spectrum [26], m, e are the mass and charge of the electron. The dielectric permittivity of gold was taken from the CRC Handbook [29]. Tabulated values are approximated by built-in models of the simulation software (Ansys Lumerical FDTD). The refractive index of the polymer linker shell (PEI) was assumed constant and equal to 1.52 [30].

The Purcell factor was calculated as the ratio of local densities of electromagnetic states in the presence and absence of plasmonic nanoparticles. The power emitted by a unit point light source was calculated for this. The local density of states is defined by the formula:

$$\rho_\mu(\mathbf{r}, \omega) = \frac{6\omega}{\pi c^2} \left\{ \mathbf{n}_\mu \cdot \text{Im} \left[\hat{G}(\mathbf{r}, \mathbf{r}, \omega) \right] \cdot \mathbf{n}_\mu \right\} \quad (2)$$

where c is the speed of light in vacuum, \mathbf{n}_μ is the unit vector in the direction of the dipole moment, \hat{G} is the total dyadic Green's function for the electric field. The light source was a point dipole located at the center of the LNP. The range of emitted wavelengths was 300–800 nm. As follows from the Eq. (2), the Purcell effect depends on the Green's function, which means the enhancement of luminescence is influenced by the environment. For the sensor to be most sensitive to the presence of a specific analyte, the absorption bands of the analyte should fall within the band of the LSPR. In this case, the influence of the analyte on the Purcell effect will be greatest, potentially shifting the peak of luminescence enhancement.

2. Modeling of different configurations of Au ligands surrounding a CeYTbF₃ nanoparticle on an Au substrate

In order to achieve a significant change in the Purcell effect in the presence of one or more analyte molecules near a nanoparticle or nanocluster, it is necessary to use structures with LSPR in the analyte absorption region. To find structures with such properties, we simulated the plasmonic enhancement of spontaneous emission in a system consisting of one dielectric particle of the CeTbF₃ phosphor and a different number (from 1 to 5) of AuNPs coated with a PEI shell and lying on an Au substrate.

The number of all simulated configurations of the ligand arrangement around the LNP was 7: there were 1 configuration with one AuNP, 1 with two AuNPs, 2 with three AuNPs, 2 with four AuNPs, and 1 with five AuNPs.

In the first configuration, one AuNP and a LNP were positioned vertically one above the other relative to the Au substrate, with the AuNP being closer to the substrate surface. The dipole moment of the source was directed along the vertical axis of the nanocluster, perpendicular to the substrate surface (Fig. 1(a)). In this configuration, the plasmon resonance was in the green region of the visible spectrum. In the second configuration, two AuNPs and a LNP lay on the surface of an Au substrate on one straight line, the dipole moment of the source was directed parallel to the substrate surface (Fig. 1(b)). The main peak of the plasmon resonance was also in the green region of the visible spectrum, but, in addition, there were also bands in the red-orange region.

In the configuration with three AuNPs, the ligands were arranged on the substrate surface in such a way that they formed an isosceles triangle, with the LNP located at its center. The dipole moment was oriented parallel to the substrate surface and parallel (blue curve) or perpendicular

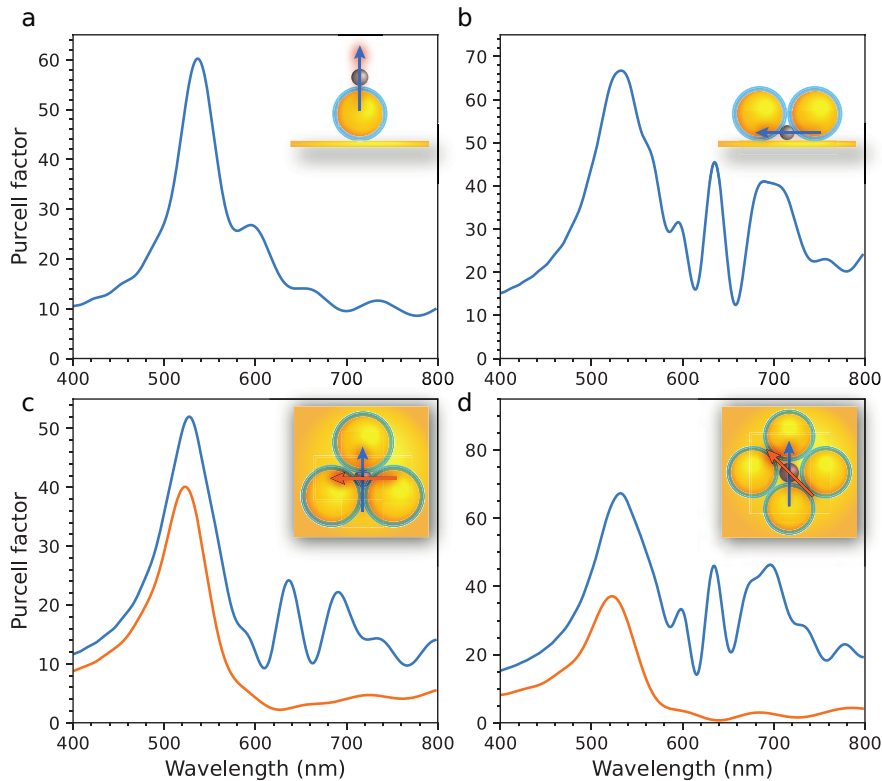


Fig. 1. The Purcell factor: (a) in the presence of one ligand on the Au substrate with the source dipole moment oriented along the vertical axis of the nanocluster, perpendicular to the substrate surface, (b) in a linear configuration of 2 ligands on the Au substrate with the source dipole moment oriented parallel to the line of connection of AuNPs, (c) in a triangular configuration of 3 ligands on the Au substrate with the source dipole moment oriented along the height (blue curve) and perpendicular to the height (orange curve) of the triangle, (d) in a square configuration of 4 ligands on the Au substrate with the source dipole moment oriented along the side (blue curve) and the diagonal (orange curve) of the square. The insets show the nanocluster geometry (side view for (a-b) and top view for (c-d))

(orange curve) to the height of the triangle. The Purcell factor for this configuration are presented in Fig. 1(c).

In the configuration with four AuNPs, the ligands were arranged on the surface of the Au substrate to form a square, with the LNP at its center. The dipole moment was oriented parallel to the substrate surface along the side (blue curve) or the diagonal (orange curve) of the square. Fig. 1(d) shows the Purcell factor in this configuration.

In the configuration with five AuNPs, the ligands were located on the surface of the Au substrate, forming a regular quadrangular pyramid, the LNP was in the center of the pyramid. The dipole moment was oriented parallel to the surface of the substrate along the diagonal of the pyramid base. A schematic representation of this configuration (side view) is shown in Fig. 2. It should be noted that the spectrum contains additional plasmon resonance peaks at other wavelengths, which is due to the fact that the geometry of this cluster supports several

plasmon resonance modes. When using radachlorin as an analyte, configurations with four and five AuNPs on a substrate are optimal, since they exhibit a plasmonic enhancement peak that coincides with the long-wavelength absorption region of radachlorin.

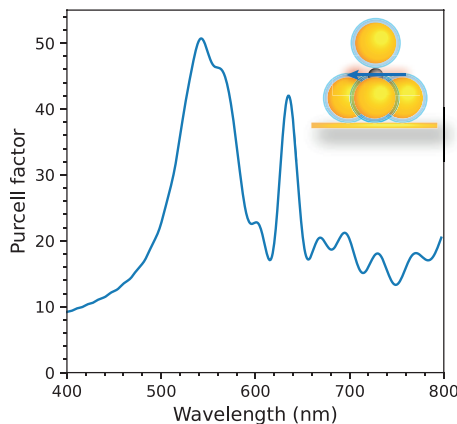


Fig. 2. Purcell factor in a configuration with 5 AuNPs forming a regular quadrangular pyramid with the LNP in the center, on an Au substrate. The dipole moment was oriented parallel to the substrate surface along the diagonal of the pyramid base. The inset shows a schematic representation of the system configuration (side view)

3. Modeling of different configurations of Au ligands surrounding a CeTbF_3 nanoparticle in a colloidal solution

In order to clarify the overall picture of luminescence enhancement in a colloidal solution, the simulations of plasmonic enhancement of spontaneous emission were performed in a system consisting of one dielectric particle of the CeTbF_3 phosphor and a different number (from 1 to 4) of Au ligands in nonequivalent configurations. The number of all simulated configurations of the arrangement of AuNPs around the phosphor was 19, of which there were 1 configuration with one nanoparticle, 4 with two AuNPs, 7 with three AuNPs, and 7 with four AuNPs. In the case of two AuNPs, we simulated the local density of states in the following configurations:

2.1. Two AuNPs are adjacent to the LNP along the diameter, the source dipole moment vector is parallel to the system axis;

2.2. Two AuNPs are adjacent to the LNP and touch each other, forming a dimer, the dipole moment is directed towards the center of one of the AuNP of the dimer;

2.3. Two AuNPs are adjacent to the LNP and are in contact with each other, forming a dimer, the dipole moment is directed perpendicular to the direction of the center of one of the AuNPs;

2.4. Two AuNPs are adjacent to the LNP and are in contact with each other, forming a dimer, the dipole moment is parallel to the dimer axis.

In the case of three gold particles, we performed numerical simulation of the local density of states in the following configurations:

3.1. The third AuNP is added to the configuration 2.1 adjacent with one of the AuNPs along the diameter;

3.2. Three AuNP are adjacent each to the LNP and placed at the vertices of the isosceles triangle, which lateral sides are formed by contacting AuNP, the source dipole moment is oriented along the height of the isosceles triangle;

3.3. Similar to the configuration 3.2, but the source dipole moment is oriented parallel the base of the isosceles triangle formed by the centers of AuNPs;

3.4. Similar to the configuration 3.2, but the source dipole moment is oriented parallel the leg of the isosceles triangle formed by the centers of AuNPs;

3.5. Three AuNPs are in contact and are located at the vertices of the square, in the center of which is the LNP, leaving one corner of the square free; the dipole moment is directed along the diagonal of the square;

3.6. The third AuNP is added to the configuration 2.1 adjacent with both of the AuNPs, but no touching LNP, the source dipole moment is oriented along the base of the acute-angled isosceles triangle formed by the centers of AuNPs;

3.7. Three AuNPs are in contact and are located at the vertices of obtuse-angled isosceles triangle, the LNP occupies the base center, contacting only the middle AuNP (at the obtuse angle), the source dipole moment is oriented along the base of the triangle;

In the case of four AuNPs, we modeled the local density of states in the following configurations:

4.1. Two dimers of AuNPs are arranged along the diameter of the LNP, touching it so that the centers of all five nanoparticles lie on the same line; the dipole moment of the source is parallel to the axis of the system;

4.2. The fourth AuNP is added at the free corner of the square in the configuration 3.5, the dipole moment of the source is directed parallel to the side of the square;

4.3. Similar to the configuration 4.2, but the source dipole moment is directed parallel to the diagonal of the square;

4.4. The four contacting AuNPs are located at the corners of a rhombus and the LNP occupies the center, touching two AuNPs and forming the minor diagonal of the rhombus; the dipole moment of the source is directed parallel to the major diagonal of the rhombus;

4.5. Similar to the configuration 4.4, but the dipole moment of the source is directed parallel to the minor diagonal of the rhombus;

4.6. Two dimers are each contacting the LNP by all their AuNPs so that the axes of the dimers are mutually perpendicular, and they themselves form two of the six edges of a tetrahedron with the LNP in the center; the dipole moment of the source is oriented orthogonally to the axes of both dimers;

4.7. Similar to the configuration 4.6, but the source dipole moment is oriented parallel to the axis of one dimer and perpendicular to the axis of the other dimer.

Several plasmon resonance modes were observed in clusters of plasmonic nanoparticles. For each configuration, the positions and values of the Purcell factor function were found in no more than two most intense maxima of the spectrum. The results are shown in Fig. 3(a). In most configurations, the plasmon resonance peak is in the green part of the visible spectrum. Due to the large inhomogeneity of the field near the contacts of AuNPs, plasmon resonance peaks at other wavelengths are also observed in the spectrum. For example, in the configurations 2.4, 4.2 and 4.4, the main plasmon resonance peak is located in the orange part of the spectrum, and in the configuration 4.5, both plasmon resonance peaks (green and orange) have approximately the same intensity. For instance, the Purcell factor for different configurations of two AuNPs are given in Fig. 3(b).

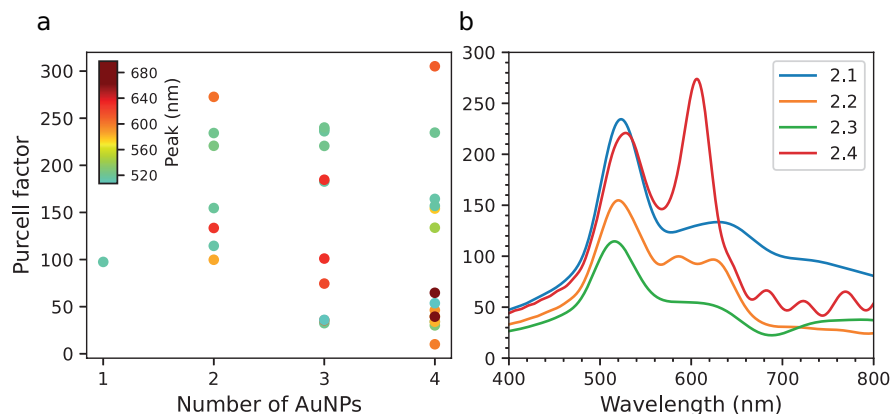


Fig. 3. (a) Purcell enhancement factor as a function of the number of AuNPs for different configurations of their arrangement. The wavelength of the plasmon resonance peaks is shown in color. (b) Purcell enhancement factor for different configurations of two AuNP as a function of wavelength

Conclusion

The study yielded interesting results concerning plasmonic enhancement of spontaneous emission in Au-CeYbF₃ colloidal nanoclusters. Modeling of various AuNP configurations showed that the number and spatial arrangement of nanoparticles relative to each other significantly affect plasmonic resonances and, accordingly, the luminescence efficiency. The Purcell factor at the peak of plasmonic resonance in the most nanocluster configurations reaches about a hundred.

In the studied configurations, the main peaks of plasmon resonance were observed, which were mainly located in the green part of the visible spectrum. This peak is associated with the main dipole mode of plasmon resonance of nanoparticles. However, depending on the geometry of the nanoclusters, peaks were also recorded at other wavelengths, which indicates a complex nature of interactions between nanoparticles. There are configurations where plasmon resonance is observed in the red-orange region of the visible spectrum. This is also a dipole resonance, but not in individual particles, but in the cluster as a whole. In this case, the remaining peaks are associated with the excitation of a higher order multipolar resonances. As a consequence, the optical near-field of these modes decays in space much faster.

Numerical simulation of clusters on the Au substrate showed that there also can be excited several plasmon resonance modes. The substrate acts as a mirror, as if doubling the number of particles, thereby leading to greater inhomogeneity in the space of the exciting field, and this in turn leads to the excitation of modes of greater multipolarity, while the field has a greater localization in the space between the particles. If it is necessary to control the symmetry of individual configurations, the system of clusters on a substrate looks preferable. In addition, a nanocluster located on a substrate leads to the excitation of surface plasmons on its surface, thereby part of the energy leaks away. Therefore, for these systems, a smaller value of the Purcell factor is observed than in colloidal nanoclusters.

The best results in terms of plasmonic enhancement were obtained for configurations with four and five AuNPs, where the plasmonic enhancement peaks coincided with the long-wavelength absorption region of radachlorin.

The study allows us to determine the number of particles in a cluster that is required for a given analyte to produce plasmonic resonance in the desired region. Specific configurations can be controlled in the case of a nanocluster on a substrate, but cannot be controlled in a colloidal solution. Thus, by changing the particle size and changing the concentration of plasmonic particles, it is possible to tune the sensor for a specific desired substance. Given the importance of the spatial distribution and orientation of nanoparticles, further research can focus on optimizing the configurations and studying the effect of the ligand material on the plasmonic resonance of the nanoparticle cluster, which will improve the performance of future sensor systems.

This paper has been supported by the Kazan Federal University Strategic Academic Leadership Program "Priority 2030".

References

- [1] K.P.Carter, Fluorescent sensors for measuring metal ions in living systems, *Chem. Rev.*, **114**(2014), 4564–4601. DOI: 10.1021/cr400546e
- [2] Y.Han, Inorganic nanoparticles as donors in resonance energy transfer for solid-phase bioassays and biosensors, *Langmuir*, **33**(2017), no. 45, 12839–12858. DOI: 10.1021/acs.langmuir.7b01483
- [3] J.Beik, Gold nanoparticles in combinatorial cancer therapy strategies, *Coord. Chem. Rev.*, **387**(2019), 299–324. DOI: 10.1016/j.ccr.2019.02.025
- [4] Y.-W.Lin, Gold nanoparticle probes for the detection of mercury, lead and copper ions, *Analyst*, **136**(2011), no. 5, 863–871. DOI: 10.1039/c0an00652a
- [5] X.Huang, Gold nanoparticle based platforms for circulating cancer marker detection, *Nanotheranostics*, **1**(2017), no. 1, 80. DOI: 10.7150/ntno.18216
- [6] K.Saha, Gold nanoparticles in chemical and biological sensing, *Chem. Rev.*, **112**(2012), no. 5, 2739–2779. DOI: 10.1021/cr2001178
- [7] W.Zhou, Gold nanoparticles for in vitro diagnostics, *Chem. Rev.*, **115**(2015), no. 19, 10575–10636. DOI: 10.1021/acs.chemrev.5b00100
- [8] M.Tian, Recent advances of plasmonic nanoparticle-based optical analysis in homogeneous solution and at the single-nanoparticle level, *Analyst*, **145**(2020), no. 14, 4737–4752. DOI: 10.1039/D0AN00609B
- [9] S.Lee, Plasmonic nanostructure-based bioimaging and detection techniques at the single-cell level, *Trends Analyt. Chem.*, **117**(2019), 58–68. DOI: 10.1016/j.trac.2019.05.006
- [10] I.S.Che Sulaiman, A review on colorimetric methods for determination of organophosphate pesticides using gold and silver nanoparticles, *Mikrochim. Acta.*, **187**(2020), 1–22. DOI: 10.1007/s00604-019-3893-8
- [11] D.Mendez-Gonzalez, Control of upconversion luminescence by gold nanoparticle size: from quenching to enhancement, *Nanoscale*, **11**(2019), no. 29, 13832–13844. DOI: 10.1039/c9nr02039j

- [12] M.Kushlyk, Enhancement of the YAG:Ce,Yb down-conversion emission by plasmon resonance in Ag nanoparticles, *J. Alloys Compd.*, **804**(2019), 202–212. DOI:10.1016/j.jallcom.2019.06.382
- [13] E.M.Purcell, Spontaneous emission probabilities at radio frequencies, Springer, (1995), 839.
- [14] T.Förster, Zwischenmolekulare energiewanderung und fluoereszenz, *Ann. Phys.*, **437**(1948), no. 1-2, 55–75. DOI: 10.1002/ANDP.19484370105
- [15] J.Fan, Energy transfer cassettes based on organic fluorophores: construction and applications in ratiometric sensing, *Chem. Soc. Rev.*, **42**(2013), no. 1, 29–43. DOI: 10.1039/c2cs35273g
- [16] D.Lu, Plasmon enhancement mechanism for the upconversion processes in NaYF₄:Yb³⁺,Er³⁺ nanoparticles: Maxwell versus Förster, *ACS Nano*, **8**(2014), no. 8, 7780–7792. DOI: 10.1021/nn5011254
- [17] Q.C.Sun, Plasmon-enhanced energy transfer for improved upconversion of infrared radiation in doped-lanthanide nanocrystals, *Nano Lett.*, **14**(2014), no. 1, 101–106. DOI: 10.1021/nl403383w
- [18] M.Saboktakin, Plasmonic enhancement of nanophosphor upconversion luminescence in Au nanohole arrays, *ACS Nano*, **7**(2013), no. 8, 7186–7192. DOI: 10.1021/nn402598e
- [19] N.J.Greybush, Plasmon-enhanced upconversion luminescence in single nanophosphor–nanorod heterodimers formed through template-assisted self-assembly, *ACS Nano*, **8**(2014), no. 9, 9482–9491. DOI: 10.1021/nn503675a
- [20] G.Yi, Systematic investigation of the wavelength-dependent upconversion enhancement induced by single plasmonic nanoparticles, *J. Phys. Chem. C*, **122**(2018), no. 24, 13047–13053. DOI:10.1021/acs.jpcc.8b02437
- [21] Z.Zhu, Plasmon-enhanced fluorescence in coupled nanostructures and applications in DNA detection, *ACS Appl. Bio Mater.*, **1**(2018), no. 1, 118–124. DOI: 10.1021/acsabm.8b00032
- [22] P.Moutet, Surface-enhanced spectroscopy on plasmonic oligomers assembled by AFM nanoxerography, *Nanoscale*, **7**(2015), no. 5, 2009–2022. DOI: 10.1039/c4nr05092d
- [23] S.Z.Zhang, Reversible luminescence switching of NaYF₄:Yb,Er nanoparticles with controlled assembly of gold nanoparticles, *Chem. Comm.*, **18**(2009), no. 18, 2547–2549. DOI: 10.1039/b823453a
- [24] Q.Wu, An upconversion fluorescence resonance energy transfer nanosensor for one step detection of melamine in raw milk, *Talanta*, **136**(2015), 47–53. DOI: 10.1016/j.talanta.2015.01.005
- [25] K.Saha, Modification of NaYF₄:Yb,Er@SiO₂ nanoparticles with gold nanocrystals for tunable green-to-red upconversion emissions, *J. Phys. Chem. C*, **115**(2011), no. 8, 3291–3296. DOI:10.1021/jp110603r
- [26] M.S.Pudovkin, CeF₃-TbF₃-YF₃ nanoparticles for ratiometric temperature sensing, *Opt. Mater.*, **148**(2024), 114831. DOI: 10.1016/j.optmat.2024.114831

- [27] E.A.Seregina, Spectral and luminescent characteristics of trivalent lanthanide ions in a $\text{POCl}_3\text{-SnCl}_4$ inorganic solvent, *Opt. Spectrosc.*, **116**(2014), no. 3, 438–453.
DOI: 10.1134/S0030400X14020209
- [28] I.A.Terra, Judd-Ofelt analysis of Tb^{3+} and upconversion study in $\text{Yb}^{3+}\text{-Tb}^{3+}$ co-doped calibo glasses, *Chem. Rev.*, **43**(2020), 188–193. DOI: 10.21577/0100-4042.20170465
- [29] J.R.Ramble, Handbook of Chemistry and Physics, CRC Press ed,(2021).
- [30] L.R.Ip, Loss of INPP4B causes a DNA repair defect through loss of BRCA1, ATM and ATR and can be targeted with PARP inhibitor treatment, *Oncotarget*, **6**(2015), no. 12, 10548.
DOI: 10.18632/oncotarget.3307

Эффекты ближнеполевого взаимодействия в коллоидных нанокластерах Au-CeYbF_3 при плазмонном иммуноанализе

Элина А. Избасарова

Алмаз Р. Газизов

Институт физики

Казанский федеральный университет

Казань, Российская Федерация

Аннотация. В данной статье исследуются эффекты плазмонного усиления спонтанного излучения в коллоидных нанокластерах, состоящих из золотых наночастиц и люминофора CeYbF_3 . С помощью моделирования различных конфигураций наночастиц, покрытых полиэтиленгликолем, была проанализирована зависимость положения плазмонных резонансов от их количества и расположения. Результаты показали, что оптимальные конфигурации наночастиц значительно усиливают люминесценцию в требуемой области видимого света, что открывает новые возможности для разработки высокочувствительных наносенсоров. В то же время нанокластеры, расположенные на золотой подложке, демонстрируют меньший коэффициент усиления люминесценции, обладая при этом более неоднородным распределением ближнего оптического поля. Полученные результаты раскрывают зависимость коэффициента усиления люминесценции от пространственного распределения и координационного числа плазмонных наночастиц в нанокластере. Данное исследование вносит вклад в понимание механизмов плазмонного взаимодействия и его применения в области оптического иммуноанализа и биомедицинских технологий.

Ключевые слова: плазмонные наночастицы, эффект Парселла, эффект Ферстера, моделирование методом FDTD, люминесцентные наночастицы.

EDN: NXGRGO

УДК 535.42

The Investigation of Gaussian Beams and Optical Vortices Diffraction in the Near Zone of Subwavelength Optical Elements with Variable Height

Dmitry A. Savelyev*

Samara National Research University

Samara, Russian Federation

Received 27.10.2024, received in revised form 12.12.2024, accepted 14.02.2025

Abstract. The finite difference time domain method was used to simulate the propagation of Gaussian beams and optical vortices with circular, radial, azimuthal polarization on subwavelength ring gratings with standard and GRIN substrates in this paper. The height of individual zones of the optical elements relief was varied. It was shown that it is possible to select the beam type and element parameters in such a way that a long light needle (up to 8.2λ) and a narrow focal spot are formed on the optical axis (up to 0.33λ).

Keywords: Gaussian beams, optical vortices, FDTD, GRIN, subwavelength ring gratings, Meep.

Citation: D.A. Savelyev, The Investigation of Gaussian Beams and Optical Vortices Diffraction in the Near Zone of Subwavelength Optical Elements with Variable Height, J. Sib. Fed. Univ. Math. Phys., 2025, 18(3), 358–370. EDN: NXGRGO.



Introduction

The materials and media with gradient refractive index (GRIN) have found wide application in many areas of human activity [1–13]. The use of GRIN materials for light collimation [8, 14], solving optical communication problems [15], light propagation control [5, 16], and in biology [6, 12] is well known. One of the main features of gradient refractive index media is the non-uniform distribution of the refractive index in space [2, 4, 9, 17]. Such media can be classified depending on the shape of the surfaces, for which the refractive index is constant [9], often distinguishing symmetrical GRIN media with respect to a given coordinate [9] and arbitrary GRIN media (F-GRIN), where an arbitrary three-dimensional distribution of the refractive index is observed [4]. Also, neural networks are known to be used for designing such media [18].

The vortex and Gaussian beams have been actively used to solve problems in optics and photonics [19–36] in recent years. In particular, such laser beams are used for tight focusing [16, 30, 25, 37], optical information transmission [22, 38], optical manipulation [20, 24, 35, 39–41], and probing [42]. To generate such beams, it is known to use such optical structures as metalenses and metasurfaces [8, 20, 43], spiral phase plates [20, 44, 45], and ring gratings [46–48]. It should be noted that ring gratings and diffraction axicons in various combinations are also used to obtain optical needles with a large focal depth [30, 34, 49–51].

The diffraction of Laguerre–Gaussian modes $(0, 0)$ and $(0, 1)$ (Gaussian beams and first-order optical vortices with the azimuthal index is equal to one were considered) with circular, radial,

*dmitrey.savelyev@yandex.ru <https://orcid.org/0000-0003-2282-3895>

© Siberian Federal University. All rights reserved

azimuthal polarization in the near zone of subwavelength ring gratings with a standard substrate and a GRIN substrate was studied in this paper. The height of individual zones of the element relief was varied. Numerical 3D-modeling was performed by the finite difference time domain (FDTD) method using the Meep software package [52].

1. The Gaussian beams diffraction on different substrates with varying relief height

The FDTD simulation was performed with the following simulation parameters: the wavelength λ of the input radiation was $0.532 \mu\text{m}$, the spatial simulation step was $\lambda/30$, and the time step was $\lambda/(60c)$, where c is the speed of light.

The three-dimensional computational domain with $8.4 \mu\text{m}$ in size was considered in paper, which was surrounded on all sides by a $0.6 \mu\text{m}$ thick PML absorbing layer.

The effect of three different types of substrates was analyzed in the paper: a standard substrate with a refractive index of $n = 1.47$, and two types of GRIN substrates with different directions of refractive index change. The case when the refractive index changes from a maximum value in the center to a minimum value at the edges will be called a direct GRIN substrate, the opposite case, when the minimum refractive index is in the center and its uniform increase occurs toward the edges of the substrate, will be called a reverse GRIN substrate.

The minimum refractive index size in the case of GRIN substrates was $n = 1.47$ (similar to the standard substrate), the maximum refractive index was 2.7 . The refractive index change step was 0.123 . It should be noted that the GRIN substrates were rings of the same width with different radii, uniformly inscribed into each other on a square substrate measuring $16.5\lambda \times 16.5\lambda \times \lambda$. The height of all substrates was fixed and was λ .

The propagation of Laguerre–Gauss modes in free space can be described by the expression (1) [53–55]:

$$GL_{nm}(r, \phi, z) = \left(\frac{\sqrt{2}r}{\sigma(z)} \right)^{|m|} \exp(ikz) \exp[-i(2n + |m| + 1)\eta(z)] \times \\ \times \exp \left[\frac{i\pi r^2}{\lambda R(z)} \right] \exp \left[-\frac{r^2}{\sigma^2(z)} \right] L_n^{|m|} \left(\frac{2r^2}{\sigma^2(z)} \right) \exp(im\phi), \quad (1)$$

where $r^2 = x^2 + y^2$, $\phi = \arctg(y/x)$, $\eta = \arctg(z/z_0)$, $R(z) = z(1 + z_0^2/z^2)$ – radius of curvature of the light field parabolic front, $\sigma(z) = \sigma_0\sqrt{1 + z^2/z_0^2}$ – the effective beam radius, $z_0 = \pi\sigma_0^2/\lambda$ – confocal parameter, $L_n^m(x)$ – generalized Laguerre polynomial.

The input beams were first-order optical vortices (Laguerre-Gaussian modes $(0, 1)$) and Gaussian beams with $\sigma = 1.5 \mu\text{m}$ with circular, radial and azimuthal polarizations. It should be noted that the circular polarization, in which the sign of the circular polarization is opposite to the sign of the introduced vortex phase singularity, was considered in this paper. In this case the maximum intensity value is formed on the optical axis for the Laguerre–Gaussian modes $(0, 1)$ [21].

The optical elements were considered: a diffraction axicon with a height of $h = 1.06\lambda$ (the relief height was chosen based on the phase jump of π radians), a direct ring grating (the height of the relief rings changed from a maximum in the center $h_{\text{max}} = 4.79\lambda$ to a minimum at the edge $h_{\text{min}} = 1.06\lambda$ with a step of 0.53λ), and an inverse ring grating (similar maximum height and step of its change), in the case of which the height changed from a minimum in the center $h_{\text{min}} = 1.06\lambda$ to a maximum value $h_{\text{max}} = 4.79\lambda$ at the edge of the element. The period of all

optical elements considered was 1.05λ .

The longitudinal and transverse dimensions of the light segments obtained on the optical axis were estimated in the paper. The focal spot size was estimated by the standard full width at half maximum (FWHM) at the point of maximum intensity on the optical axis outside the element, and the length of the light needle along the radiation propagation axis (depth of focus – DOF) was estimated in a similar manner.

It should be noted that a direct GRIN substrate allows for additional focusing of radiation and, accordingly, a smaller focal spot size, while in the case of a reverse GRIN substrate, which in this case acts as a diffusing lens, an extension of the light segment size is observed.

Fig. 1 shows the passage of a Gaussian beam through a diffraction axicon with a standard

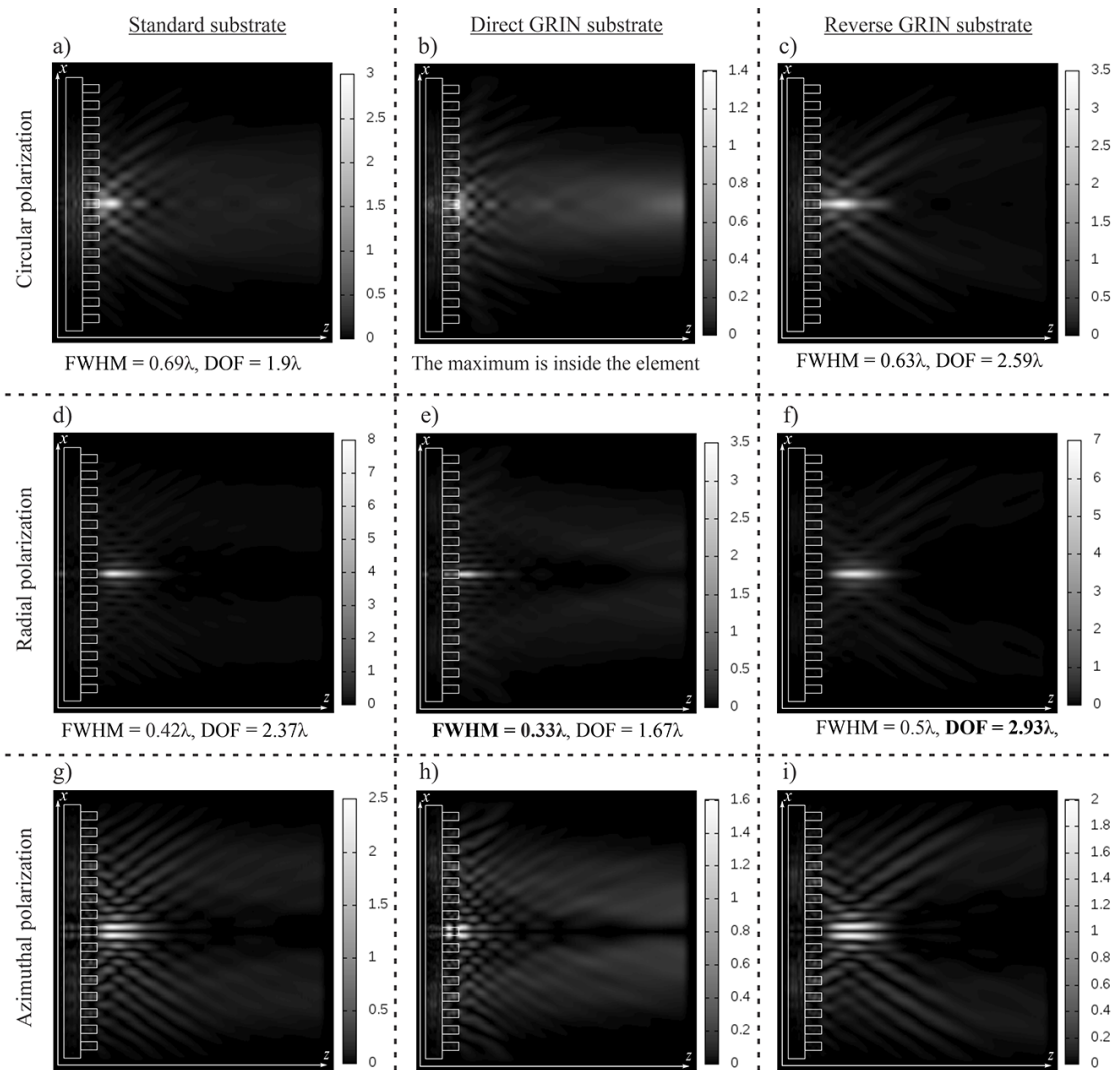


Fig. 1. Longitudinal cross-section (xz) of Gaussian beam propagation (intensity), diffraction axicon for different types of substrate, circular polarization (a, b, c), radial polarization (d, e, f), azimuthal polarization (g, h, i)

substrate and GRIN substrates for different polarizations of laser radiation; the element relief

height was $h = 1.06\lambda$, and the numerical aperture was $NA = 0.95$. Focusing on the optical axis is observed for circular and radial polarizations of laser radiation.

The minimum focal spot size was obtained for radial polarization with a direct GRIN substrate $FWHM = 0.33\lambda$, which is 21.4% smaller than the focal spot size obtained with the same type of polarization for a standard substrate.

The maximum size of the light needle was also obtained for radial polarization, but for a reverse GRIN substrate $DOF = 2.93\lambda$, which is 23.6% longer than the light needle obtained in the case of a standard substrate. It also should be noted that for circular polarization, the use of a direct GRIN substrate led to focusing of the beam inside the element.

Let us now consider the diffraction of Gaussian beams on the direct and inverse ring gratings described above (Fig. 2 and Fig. 3, respectively). We will also monitor the longitudinal and transverse sizes of the light segment on the optical axis. Accordingly, we will now consider circular and radial polarization of laser radiation.

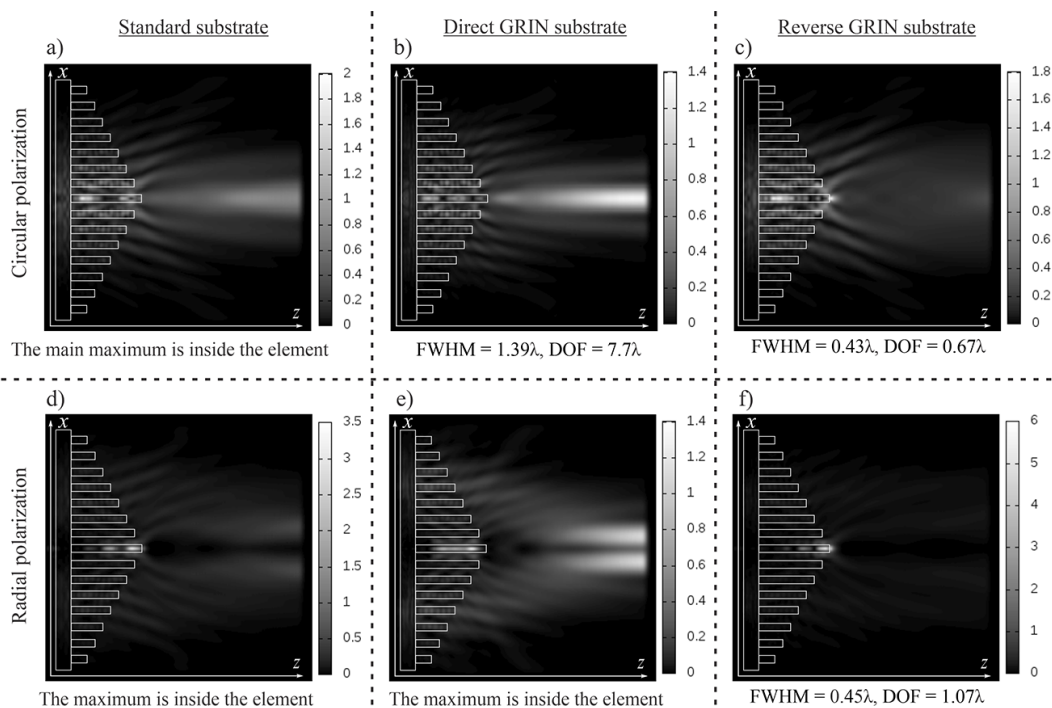


Fig. 2. Longitudinal cross-section (xz) of Gaussian beam propagation (intensity), direct ring grating for different types of substrate, circular polarization (a, b, c), radial polarization (d, e, f)

So, as can be seen from Fig. 2, the formation of intensity peaks on the optical axis inside the element is observed for the standard substrate, as well as for the direct GRIN substrate with radial polarization. The smallest focal spot size was obtained for the reverse GRIN substrate with circular polarization $FWHM = 0.43\lambda$. The maximum size of the light needle was also obtained for circular polarization with the direct GRIN substrate ($DOF = 7.7\lambda$).

It should be noted that in the case of the direct GRIN substrate for radial polarization a redistribution of intensity from the optical axis and the formation of a ring are observed at a distance of over 4λ from the element relief.

In the case of the inverse ring grating (Fig. 3) the main intensity peak is formed inside

the element for circular polarization and the standard and direct GRIN substrates, but then the formation of maxima of comparable intensity values was observed outside the element. The minimum focal spot size was obtained for the direct GRIN substrate with radial polarization (FWHM = 0.54λ). In this case, the maximum size of the light needle also was obtained: $\text{DOF} = 8.2\lambda$.

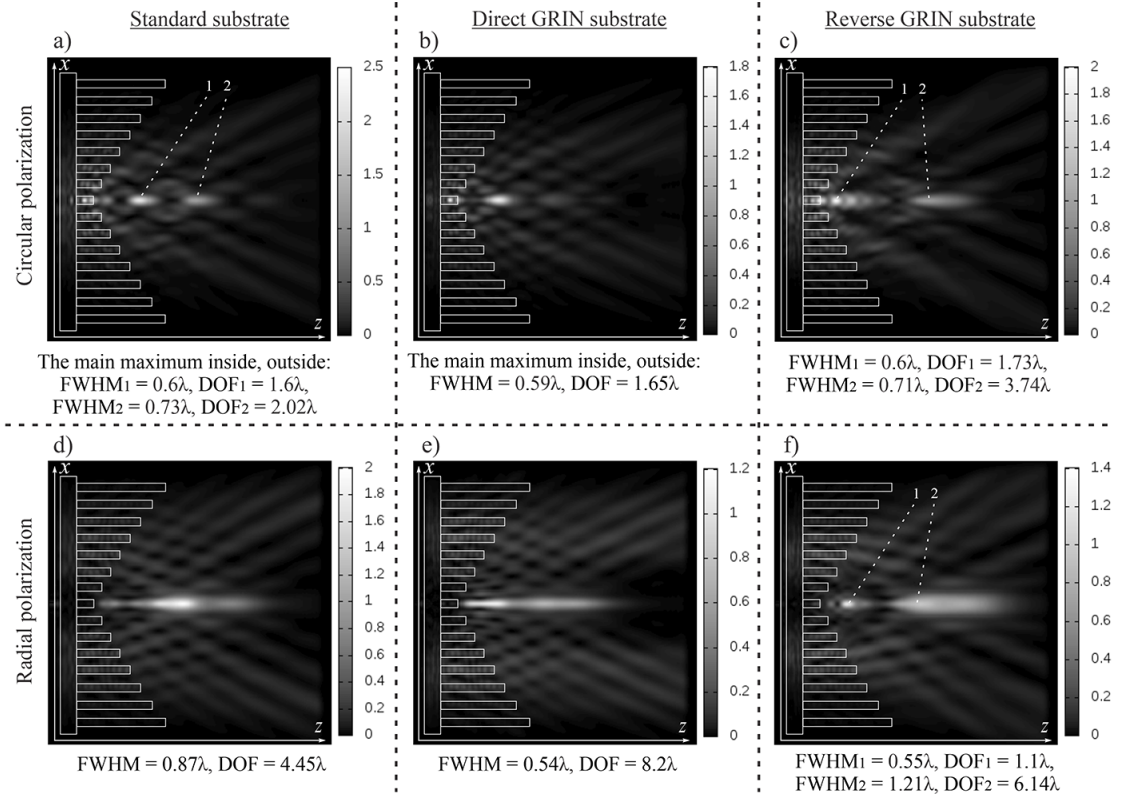


Fig. 3. Longitudinal cross-section (xz) of Gaussian beam propagation (intensity), inverse ring grating for different types of substrate, circular polarization (a, b, c), radial polarization (d, e, f)

Thus, the direct GRIN substrate with radial polarization of laser radiation demonstrated its efficiency for Gaussian beams: the minimum focal spot size (FWHM = 0.33λ) was obtained for the usual relief of the diffraction axicon, the maximum size of the light needle was obtained for the relief of the inverse ring grating ($\text{DOF} = 8.2\lambda$).

Let us further consider similar optical elements with a different type of input laser radiation — the Laguerre–Gauss mode (0, 1).

2. The Laguerre-Gauss mode (0, 1) diffraction on different substrates with varying relief height

This section presents studies on the influence of changes in the height of individual relief zones, the type of substrates, and the polarization of the input laser radiation for Laguerre–Gaussian modes (0, 1) on the diffraction pattern in the near zone.

Fig. 4 shows the passage of first-order optical vortices through a standard substrate and GRIN substrates for different laser radiation polarizations (the element relief height was $h = 1.06\lambda$). The

focusing on the optical axis is observed for circular and azimuthal laser radiation polarizations as expected [21].

The minimum focal spot size was obtained for the direct GRIN substrate for azimuthal polarization of laser radiation ($\text{FWHM} = 0.42\lambda$). However, it should be noted that the decrease in the focal spot size is insignificant. The maximum size of the light needle was also obtained for azimuthal polarization in the case of the reverse GRIN substrate ($\text{DOF} = 3.07\lambda$).

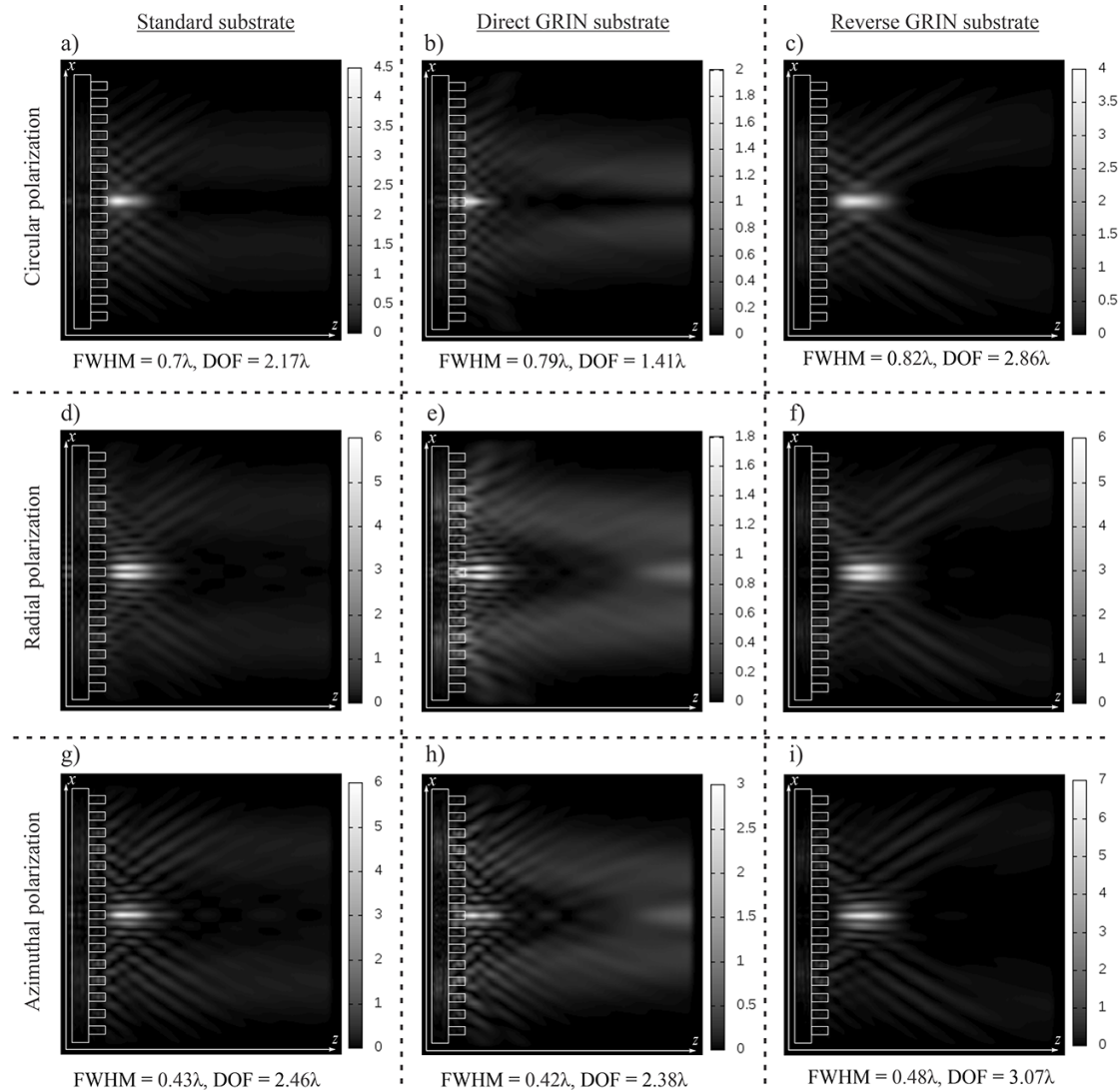


Fig. 4. Longitudinal cross-section (xz) of the propagation of first-order optical vortices (intensity), diffraction axicon for different types of substrate, circular polarization (a, b, c), radial polarization (d, e, f), azimuthal polarization (g, h, i)

Let us consider further, as before, the direct and inverse ring gratings (Fig. 5 and 6, respectively), with circular and azimuthal polarization of laser radiation.

As can be seen from Fig. 5, the focusing is observed inside the element for a standard substrate, as in the case of a Gaussian beam. It should be noted that the focusing on the optical axis is

observed for a direct ring substrate only in two cases: for a reverse GRIN substrate with circular polarization (with a focal spot size of $\text{FWHM} = 0.52 \lambda$) and for a direct GRIN substrate in the case of azimuthal polarization ($\text{DOF} = 4.91 \lambda$).

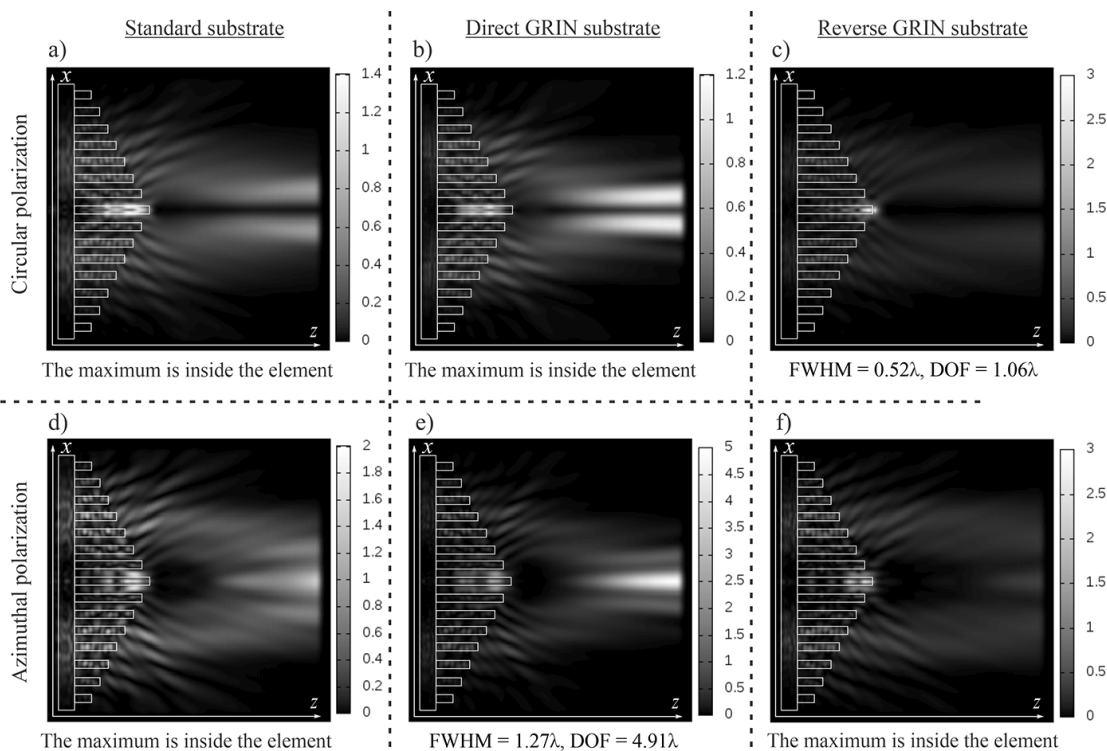


Fig. 5. Longitudinal cross-section (xz) of the propagation of first-order optical vortices (intensity), direct ring grating for different types of substrate, circular polarization (a, b, c), azimuthal polarization (d, e, f)

For a direct GRIN substrate a ring is formed in the case of circular polarization. But a light needle was formed on the optical axis for a similar type of element and polarization for a Gaussian beam.

In the case of a reverse ring grating (Fig. 6), for the considered types of polarization, intensity oscillations are observed on the optical axis. Moreover, for circular polarization, with distance from the element, a redistribution of intensity from the optical axis is observed and intensity ring with a minimum intensity value on the optical axis is formed.

The minimum focal spot size was obtained for a direct GRIN substrate with azimuthal polarization of laser radiation ($\text{FWHM} = 0.43 \lambda$) in the first maximum outside the element.

The maximum size of the light needle is also obtained for this case, i.e. in the case of the reverse GRIN substrate ($\text{DOF} = 5.99 \lambda$). However, it should also be noted that a powerful light needle is formed for the case of the reverse GRIN substrate with azimuthal polarization ($\text{DOF} = 5.58 \lambda$).

Thus, the use of both the direct and reverse GRIN substrates also allows one to obtain longer focal segments for the Laguerre-Gaussian modes $(0, 1)$ than when using a standard substrate.

In particular, the use of the reverse GRIN substrate for circular polarization allowed one to achieve an increase in the focal light segment size by 31.8% ($\text{DOF} = 2.86 \lambda$) than when using a

standard substrate in the case of a diffractive axicon. And both the direct and reverse GRIN substrates in the case of a reverse ring grating for azimuthal polarization allow one to obtain an extended light segment.

Moreover, the formation of a light needle 2.43 times longer than the light needle formed by a standard diffractive axicon ($\text{DOF} = 5.99\lambda$) is observed in the case of the direct GRIN substrate.

It should be noted that for a Gaussian beam, the maximum light tip size was also obtained for the inverse ring grating relief ($\text{DOF} = 8.2\lambda$) and the direct GRIN substrate.

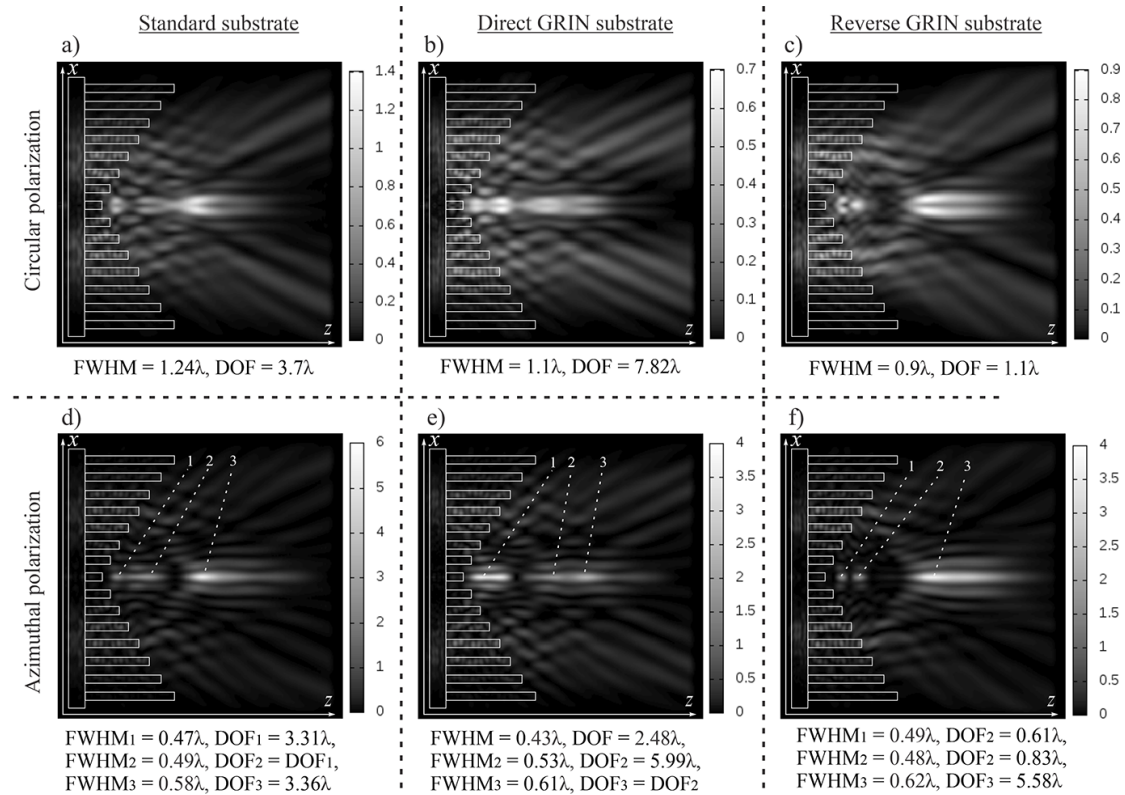


Fig. 6. Longitudinal cross-section (xz) of the propagation of first-order optical vortices (intensity), inverse ring grating for different types of substrate, circular polarization (a, b, c), azimuthal polarization (d, e, f)

Conclusion

The FDTD method was used to simulate the diffraction of Gaussian beams and Laguerre–Gauss modes (0, 1) with circular, radial, azimuthal polarization on subwavelength ring gratings with standard and GRIN substrates in this paper. The height of individual zones of the element relief was varied.

It should be noted that the use of a direct GRIN substrate resulted in a decrease in the focal spot size for both the Gaussian beam ($\text{FWHM} = 0.33\lambda$) and the Laguerre–Gaussian mode (0, 1), $\text{FWHM} = 0.42\lambda$, compared to the action of a diffractive axicon with a conventional substrate.

The influence of the direct GRIN substrate for individual cases also manifested itself in the formation of long light segments. In particular, for Gaussian beams, the maximum size of the

light needle was obtained for the relief of the inverse ring grating ($\text{DOF} = 8.2\lambda$) with radial polarization. In the case of an optical vortex, this type of element also made it possible to form an extended light segment with azimuthal polarization ($\text{DOF} = 5.99\lambda$).

The use of the inverse GRIN substrate also resulted in the formation of extended light segments, in particular, for the inverse ring grating in the case of the Laguerre-Gaussian mode $(0, 1)$, a powerful light needle with $\text{DOF} = 5.58\lambda$ was obtained. The same type of element, when illuminated by a conventional Gaussian beam, allowed the formation of a focal light segment with an extension of $\text{DOF} = 6.14\lambda$.

This research was funded by the Russian Science Foundation (project No. 24-22-00044), <https://rscf.ru/en/project/24-22-00044/>.

References

- [1] Y.Kang, J.Wang, Y.Zhao, X.Zhao, H.Tao, Y.Xu, High refractive index GRIN lens for IR optics, *Materials*, **16**(2023), no. 7, 2566. DOI: 10.3390/ma16072566.
- [2] K.A.Richardson et al., Advances in infrared gradient refractive index (GRIN) materials: a review, *Optical Engineering*, **59**(2020), no. 11, 112602. DOI: 10.1117/1.OE.59.11.112602.
- [3] Z.Zhang et al., Refractive index measurement deflectometry for measuring gradient refractive index lens, *Optics Express*, **32**(2024), no. 7, 12620–12635. DOI: 10.1364/OE.518670.
- [4] D.H.Lippman et al., Freeform gradient-index media: a new frontier in freeform optics, *Optics Express*, **29**(2021), no. 22, 36997–37012. DOI: 10.1364/OE.443427.
- [5] J.M.Luque-Gonzalez et al., An ultracompact GRIN-lens-based spot size converter using sub-wavelength grating metamaterials, *Laser & Photonics Reviews*, **13**(2019), no. 11, 1900172. DOI: 10.1002/lpor.201900172.
- [6] C.Guo, T.Urner, S.Jia, 3D light-field endoscopic imaging using a GRIN lens array, *Applied Physics Letters*, **116**(2020), no. 10, 101105. DOI: 10.1063/1.5143113.
- [7] G.I.Greisukh, I.Y.Levin, E.G.Ezhov, Ultra-high-aperture infrared triplet with a GRIN lens: modeling stages of composite gradient-index material and potential possibilities of the optical system, *Journal of Optical Technology*, **91**(2024), no. 3, 137–141. DOI: 10.1364/JOT.91.000137.
- [8] P.Lalanne, P.Chavel, Metalenses at visible wavelengths: past, present, perspectives, *Laser & Photonics Reviews*, **11**(2017), no. 3, 1600295. DOI: 10.1002/lpor.201600295.
- [9] J.E.Gomez-Correa et al., Symmetric gradient-index media reconstruction, *Optics Express*, **31**(2023), no. 18, 29196–29212. DOI: 10.1364/OE.498649.
- [10] J.E.Gomez-Correa, Geometrical-light-propagation in non-normalized symmetric gradient-index media, *Optics Express*, **30**(2022), no. 19, 33896–33910. DOI: 10.1364/OE.465957.
- [11] L.Wei, G.Li, M.Song, C.H.Wang, W.Zhang, Determination of gradient index based on laser beam deflection by stochastic particle swarm optimization, *Applied Physics B*, **127**(2021), no. 9, 131. DOI: 10.1007/s00340-021-07676-9.

-
- [12] Y.F.Chien et al., Dual GRIN lens two-photon endoscopy for high-speed volumetric and deep brain imaging, *Biomedical Optics Express*, **12**(2021), no. 1, 162–172. DOI: 10.1364/BOE.405738.
- [13] G.M.Williams, J. Paul Harmon, Dispersion controlled nanocomposite gradient index lenses, *Optics Continuum*, **2**(2023), no. 2, 456–472. DOI: 10.1364/OPTCON.481205.
- [14] D.A.Savelyev, A.V.Ustinov, S.N.Khonina, N.L.Kazanskiy, Layered lens with a linear dependence of the refractive index change, *Proceedings of SPIE*, **9807**(2016), 203–209. DOI: 10.1117/12.2234404.
- [15] A.K.Baghel, S.S.Kulkarni, S.K.Nayak, Far-field wireless power transfer using GRIN lens metamaterial at GHz frequency, *IEEE Microwave and Wireless Components Letters*, **29**(2019), no. 6, 424–426. DOI: 10.1109/LMWC.2019.2912056.
- [16] D.A.Savelyev, S.V.Karpeev, Development of 3D Microstructures for the Formation of a Set of Optical Traps on the Optical Axis, *Photonics*, **10**(2023), no. 2, 117. DOI: 10.3390/photonics10020117.
- [17] H.Ohno, Symplectic ray tracing based on Hamiltonian optics in gradient-index media, *JOSA A*, **37**(2020), no. 3, 411–416. DOI: 10.1364/JOSAA.378829.
- [18] H.Ohno, T.Usui, Neural network gradient-index mapping, *OSA Continuum*, **4**(2021), no. 10, 2543–2551. DOI: 10.1364/OSAC.437395.
- [19] R.Azizkhani, D.Hebri, S.Rasouli, Gaussian beam diffraction from radial structures: detailed study on the diffraction from sinusoidal amplitude radial gratings, *Optics Express*, **31**(2023), no. 13, 20665–20682. DOI: 10.1364/OE.489659.
- [20] A.P.Porfiev et al., Phase singularities and optical vortices in photonics, *Phys. Usp.*, **192**(2022), no. 8, 841–866. DOI: 10.3367/UFNe.2021.07.039028.
- [21] D.Savelyev, N.Kazanskiy, Near-Field Vortex Beams Diffraction on Surface Micro-Defects and Diffractive Axicons for Polarization State Recognition, *Sensors*, **21**(2021), no. 6, 1973. DOI: 10.3390/s21061973.
- [22] S.N.Khonina, S.V.Karpeev, M.A.Butt, Spatial-light-modulator-based multichannel data transmission by vortex beams of various orders, *Sensors*, **21**(2021), no. 9, 2988. DOI: 10.3390/s21092988.
- [23] Y.Lian et al., OAM beam generation in space and its applications: A review, *Optics and Lasers in Engineering*, **151**(2022), 106923. DOI: 10.1016/j.optlaseng.2021.106923.
- [24] D.A.Savelyev, Features of a Gaussian beam near-field diffraction upon variations in the relief height of subwavelength silicon optical elements, *Computer Optics*, **47**(2023), no. 6, 938–947 (in Russian). DOI: 10.18287/2412-6179-CO-1402.
- [25] V.V.Kotlyar et al., Spin–Orbital Transformation in a Tight Focus of an Optical Vortex with Circular Polarization, *Applied Sciences*, **13**(2023), no. 14, 8361. DOI: 10.3390/app13148361.

-
- [26] S.N.Khonina, A.V.Ustinov, S.G.Volotovskiy, N.A.Ivliev, V.V.Podlipnov, Influence of optical forces induced by paraxial vortex Gaussian beams on the formation of a microrelief on carbazole-containing azopolymer films, *Applied Optics*, **59**(2020), no. 29, 9185-9194. DOI: 10.1364/AO.398620.
- [27] J.Baltrukonis, O.Ulcinas, S.Orlov, V.Jukna, High-order vector bessel-gauss beams for laser micromachining of transparent materials, *Physical Review Applied*, **16**(2021), no. 3, 034001. DOI: 10.1103/PhysRevApplied.16.034001.
- [28] B.Wang et al., Generating optical vortex beams by momentum-space polarization vortices centred at bound states in the continuum, *Nature Photonics*, **14**(2020), no. 10, 623-628. DOI: 10.1038/s41566-020-0658-1.
- [29] A.Brimis, K.G.Makris, D.G.Papazoglou, Optical vortices shape optical tornados, *Optics Express*, **31**(2023), no. 17, 27582-27593. DOI: 10.1364/OE.495836.
- [30] D.A.Savelyev, The investigation of the features of focusing vortex super-Gaussian beams with a variable-height diffractive axicon, *Computer Optics*, **45**(2021), no. 2, 214-221 (in Russian). DOI: 10.18287/2412-6179-CO-862.
- [31] J.Adams, I.Agha, A.Chong, Spatiotemporal optical vortex reconnections of multi-vortices, *Scientific Reports*, **14**(2024), no. 1, 5483. DOI: 10.1038/s41598-024-54216-4.
- [32] D.Savelyev, S.Degtyarev, Features of the Optical Vortices Diffraction on Silicon Ring Gratings, *Optical Memory and Neural Networks*, **31**(2022), no. 1, 55-66. DOI: 10.3103/S1060992X22050095.
- [33] K.Zhang, Y.Wang, Y.Yuan, S.N.Burokur, A review of orbital angular momentum vortex beams generation: from traditional methods to metasurfaces, *Applied Sciences*, **10**(2020), no. 3, 1015. DOI: 10.3390/app10031015.
- [34] D.A.Savelyev, Peculiarities of focusing circularly and radially polarized super-Gaussian beams using ring gratings with varying relief height, *Computer Optics*, **46**(2022), no. 4, 537-546 (Russian). DOI: 10.18287/2412-6179-CO-1131.
- [35] M.Dong, C.Zhao, Y.Cai, Y.Yang, Partially coherent vortex beams: Fundamentals and applications, *Science China Physics, Mechanics & Astronomy*, **64**(2021), no. 2, 224201. DOI: 10.1007/s11433-020-1579-9.
- [36] D.L.Andrews, Symmetry and quantum features in optical vortices, *Symmetry*, **13**(2021), no. 8, 1368. DOI: 10.3390/sym13081368.
- [37] N.Jimenez, V.Romero-Garcia, L.M.Garcia-Raffi, F.Camarena, K.Staliunas, Sharp acoustic vortex focusing by Fresnel-spiral zone plates, *Applied Physics Letters*, **112**(2018), no. 20, 204101. DOI: 10.1063/1.5029424.
- [38] E.V.Barshak et al., Robust higher-order optical vortices for information transmission in twisted anisotropic optical fibers, *Journal of Optics*, **23**(2021), no. 3, 035603. DOI: 10.1088/2040-8986/abda85.

- [39] Y. Shen et al., Optical vortices 30 years on: OAM manipulation from topological charge to multiple singularities, *Light: Science & Applications*, **8**(2019), no. 1, 1–29. DOI: 10.1038/s41377-019-0194-2.
- [40] D.A. Savelyev, The Features of the Optical Traps Formation Using Silicon Ring Gratings with Variable Height, *Photonics*, **10**(2023), no. 11, 1264. DOI: 10.3390/photonics10111264.
- [41] J. Bayat, F. Hajizadeh, A.M. Khazaei, S. Rasouli, Gear-like rotatable optical trapping with radial carpet beams, *Sci. Rep.*, **10**(2020), no. 1, 11721. DOI: 10.1038/s41598-020-68695-8.
- [42] A.A. Sirenko et al., Terahertz vortex beam as a spectroscopic probe of magnetic excitations, *Physical Review Letters*, **122**(2019), no. 23, 237401. DOI: 10.1103/PhysRevLett.122.237401.
- [43] S.N. Khonina, M.A. Butt, N.L. Kazanskiy, A Review on Reconfigurable Metalenses Revolutionizing Flat Optics, *Adv. Optical Mater.*, **12**(2024), no. 4, 2302794. DOI: 10.1002/adom.202302794.
- [44] S. Lightman, G. Hurvitz, R. Gvishi, A. Arie, Miniature wide-spectrum mode sorter for vortex beams produced by 3D laser printing, *Optica*, **4**(2017), no. 6, 605–610. DOI: 10.1364/OPTICA.4.000605.
- [45] S. Yu, Potentials and challenges of using orbital angular momentum communications in optical interconnects, *Optics Express*, **23**(2015), no. 3, 3075–3087. DOI: 10.1364/OE.23.003075.
- [46] S.N. Khonina, N.L. Kazanskiy, P.A. Khorin, M.A. Butt, Modern types of axicons: new functions and applications, *Sensors*, **21**(2021), no. 19, 6690. DOI: 10.3390/s21196690.
- [47] Z. Yang et al., Design of bottle beam based on dual-beam for trapping particles in air, *Applied Optics*, **58**(2019), no. 10, 2471. DOI: 10.1364/AO.58.002471.
- [48] D.A. Savelyev, S.N. Khonina, Characteristics of sharp focusing of vortex Laguerre-Gaussian beams, *Computer Optics*, **39**(2015), no. 5, 654–662 (in Russian). DOI: 10.18287/0134-2452-2015-39-5-654-662.
- [49] C. Shi et al., Sub-wavelength longitudinally polarized optical needle arrays generated with tightly focused radially polarized Gaussian beam, *Optics Communications*, **505**(2022), 127506. DOI: 10.1016/j.optcom.2021.127506.
- [50] D.A. Savelyev, The Comparison of Laser Radiation Focusing by Diffractive Axicons and Annular Gratings with Variable Height Using High-performance Computer Systems, Proceedings of IEEE – 2021 Photonics & Electromagnetics Research Symposium (PIERS), 2021, 2709–2716. DOI: 10.1109/PIERS53385.2021.9694860.
- [51] N.L. Kazanskiy, S.N. Khonina, Nonparaxial effects in lensacon optical systems, *Optoelectronics, Instrumentation and Data Processing*, **53**(2017), no. 5, 484–493. DOI: 10.3103/S8756699017050089.
- [52] M. Rani, J. Kashyap, U. Singh, A. Kapoor, Optimisation of dielectric spacer layer thickness in Ag nanospheres/ITO/c-Si structure for plasmonic solar cells using FDTD simulation, *Materials Technology*, **37**(2022), no. 10, 1320–1328. DOI: 10.1080/10667857.2021.1940046.
- [53] M.S. Soskin, M.V. Vasnetsov, Singular optics, *Progress in optics*, **42**(2001), 219–276. DOI: 10.1016/S0079-6638(01)80018-4.

- [54] A.V.Chernykh, N.V.Petrov, Optical vortex trajectory of the edge-diffracted single-charged Laguerre-Gaussian beam, *Optics and Lasers in Engineering*, **139**(2021), 106504.
DOI: 10.1016/j.optlaseng.2020.106504.
- [55] V.A.Soifer et al., Computer Design of Diffractive Optics, *Woodhead Publishing Series in Electronic and Optical Materials*, **50**(2013). DOI: 10.1533/9780857093745.

Исследование дифракции гауссовых пучков и оптических вихрей в ближней зоне субволновых оптических элементов переменной высоты

Дмитрий А. Савельев

Самарский национальный исследовательский университет
Самара, Российская Федерация

Аннотация. В работе методом конечных разностей во временной области было проведено моделирование распространения гауссовых пучков и оптических вихрей первого порядка с круговой, радиальной, азимутальной поляризацией на субволновых кольцевых решетках со стандартной и GRIN-подложками. Изменялась высота отдельных зон оптических элементов. Показано, что можно подобрать тип пучка и параметры элемента таким образом, чтобы на оптической оси формировалась длинная световая игла (до 8.2λ), а также узкое фокальное пятно (до 0.33λ).

Ключевые слова: гауссовы пучки, оптические вихри, FDTD, GRIN, субволновые кольцевые решетки, Меер.

EDN: OXWQIY
УДК 535.232.233

Filamentation Process of Femtosecond Laser Pulse in Air and Associated Phenomena

Vladimir E. Prokopev*

Dmitrii M. Lubenko[†]

Tomsk State University

Tomsk Polytechnic University

Institute of High Current Electronics SB RAS

Tomsk, Russian Federation

Received 29.10.2024, received in revised form 25.12.2024, accepted 04.02.2025

Abstract. The paper presents experimental studies of physical processes and conditions for generate high-directional white-light supercontinuum in visible range. It was shown that it occurs in filamentation area and postfilamentation channel under different spectral broadening mechanisms step by step. Experimentally shown that these phenomena can be realized under aberration focusing.

Keywords: femtosecond laser, laser filament, white-light supercontinuum, simulated Raman scattering, coherent anti-stokes Raman scattering, Four-wave mixing.

Citation: V.E. Prokopev, D.M. Lubenko, Filamentation Process of Femtosecond Laser Pulse in Air and Associated Phenomena, *J. Sib. Fed. Univ. Math. Phys.*, 2025, 18(3), 371–376. EDN: OXWQIY.



Introduction

One of the most interesting phenomena of modern nonlinear physical optics is the effect of supercontinuum (SC) generation. A significant broadening of laser pulse spectrum during the propagation in transparent media, including air, under self-focusing, channeling and filamentation conditions leads to generation of white-light SC. Studies of SC generation present not only fundamental interest, but also a practical one. The first is associated with the diversity of nonlinear optical mechanisms involved in the formation of wide SC spectra and determining the set of its properties, which can change both when using different optical media and when varying the parameters of pump. Interest in the use of SC in various applications arose and increased not only due to transportation of light energy over long distances, but also due to fundamental possibility of remote monitoring of the environment and study of ultrafast processes. In this case, not only the spectrum width, but also the directionality of the SC is important from both scientific and practical points of view.

The listed parameters depend on the physical characteristics of the laser radiation such as, for example: central wavelength, power and intensity, pulse duration and steepness of its leading and trailing edges, width and shape of the pulse envelope, distribution of radiation in the beam, etc., as well as environmental parameters: media composition and concentration of elements, nonlinear responsibility, external influences. In addition, the spectral parameters of the SC depend not

*prokop@ogl.hcei.tsc.ru <https://orcid.org/0000-0002-9426-7755>

[†]lubenkodm@gmail.com <https://orcid.org/0000-0002-3009-762X>

© Siberian Federal University. All rights reserved

only on the propagation medium parameters, but also on the conditions and mechanisms of interaction of the electromagnetic field with the external environment. Moreover, environment conditions strongly depend on the beam parameters in the case of high-intensity beams.

SC generation in air has a particular interest, which is accompanied by the filamentation phenomenon during propagation of a powerful ultrashort laser pulse. This effect was first described by Brown in [1]. Studies of various scientific groups were devoted to the investigation of processes occurring during filamentation. Thus, the filament structure was studied by the teams of MSU and Quebec Laval University [2–6], the same groups considered the process of broadening of SC conical spectrum arising from self-phase modulation (SPM) during filamentation of collimated beams [7, 8]. The groups of National Research Institute of Quebec and Laval University investigated the broadening of axial SC arising from focusing a beam in air [9, 10]. In this case, using dual-frequency pumping, the four-wave Raman mixing (FWRM) process with broadening of the spectrum into the anti-Stokes region was realized. The generation of separate anti-Stokes lines is also caused by the rotational SRS processes described in [11, 12].

The filamentation process under fs pulse focusing in gases (air and nitrogen under pressure) is considered in this paper. It is shown that under these conditions axial broadband SC is generated by the alternate implementation of various spectrum broadening mechanisms which is promoted by aberration focusing.

1. Results and discussion

The experiments were carried out on the laser complex 'Start-480M' (Avesta project, Russia) with the following parameters: central wavelength of 940 nm, pulse energy up to 10 mJ, pulse duration of 60 ± 10 fs. Radiation focusing was performed both by lenses with a focal length of 400 to 1000 mm and by mirror with same foci. Laser beam was focused in a cell filled with air at atmospheric pressure or with nitrogen of 1–3 atm. The tilt angle of the lens (mirror) and the gas pressure were selected such that the laser pulse was transformed into an axial white supercontinuum. The supercontinuum spectrum was recorded using an Ocean Optics HR4000 spectrometer (200–1100 nm): reflected beam sent directly to the spectrometer. The duration of the pump pulse was measured using an autocorrelator ASF-20 (Avesta Project, Russia). The energy parameters were recorded by a power and energy meter Gentec Maestro. The experimental setup is shown in Fig. 1.

The experimental spectra, which are obtained from experiments with producing 2 beams, are shown in Fig. 2. Results were similar for experiment with 1 beam. Spectral measurements were made both in the middle of filamentation area (Fig. 2a) and at a distance of 10 meters from it (Fig. 2b). To obtain stable generation of white light, the tilt angle of the lens (to obtain one white-light beam) or the mirror (to obtain two white-light beams) was adjusted in each experiment; in both cases, the tilt angle was about 15° . When focusing with a mirror, two beams of white light arise due to diffraction on the plasma near the first geometric focus of the system [13]. All presented spectra were recorded in atmospheric air.

In our investigations [14, 15] it was shown that when focusing a high intensity fs pulse in air medium, SRS on rotational transitions of nitrogen occurs. At the same time, coherent anti-Stokes Raman scattering (CARS) is observed, producing a peak in the blue wing of the spectrum (Fig. 2a). The presence of the resulting triplet triggers a cascade FWRM process in the anti-Stokes region up to 300–500 nm (Fig. 2b). The evidence that it is precisely these processes lead to spectrum broadening, versus, for example SPM [7] are: high conversion efficiency; dependence

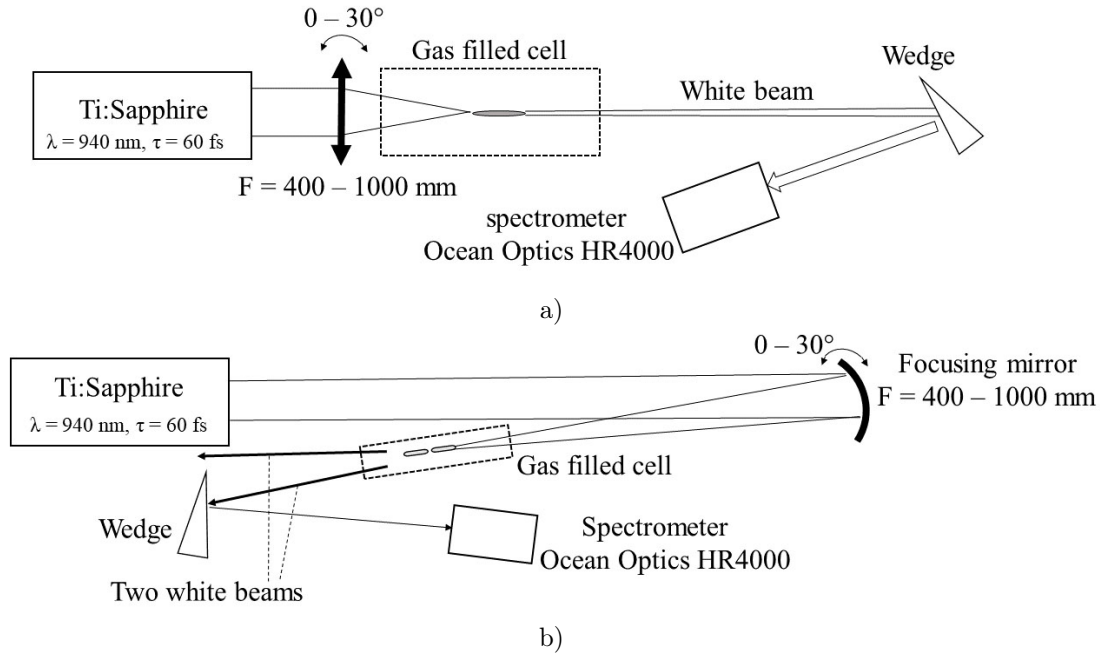


Fig. 1. Experimental setup: a) with focusing lens, b) with focusing mirror

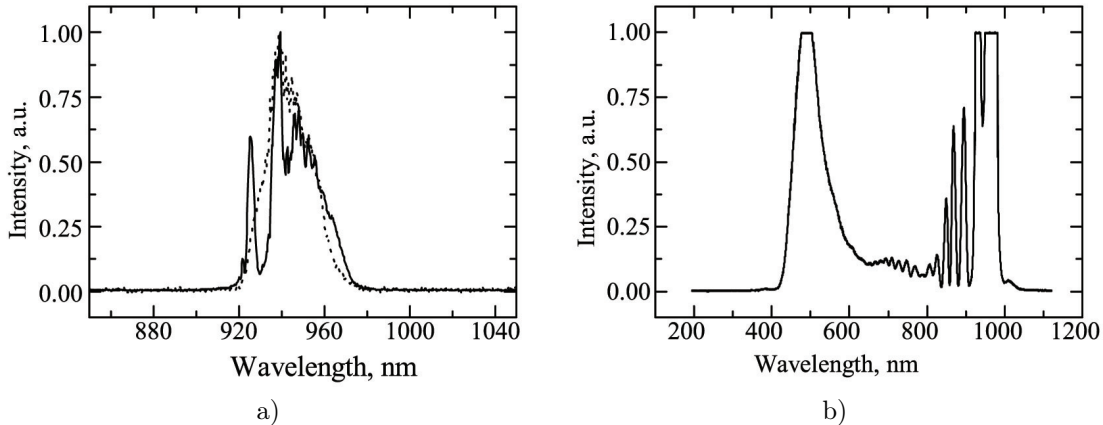


Fig. 2. Spectral measurements: a) in filamentation area (dotted line is spectra from output laser); b) at distance of 10 m from filamentation area

of the threshold value of the pump energy required to generate a white-light beam on the pump wavelength (in [16] the conditions of a same experiment to produce white-light with pumping at 800 nm are described, but no explanation of the conversion mechanisms is given). Also, the dependence of intensity of white-light beam on the gas pressure in the cell was obtained in experiments. When the spectrum is broadened due to the SPM process such phenomena should not be observed.

However, the fact of need to use aberration focusing to produce white light has previously remained unnoticed. A number of experiments to determine the optimal lens (mirror) tilt angle have shown that the optimal angle is $15 \pm 5^\circ$. At this tilt angle, stable generation of a narrow-

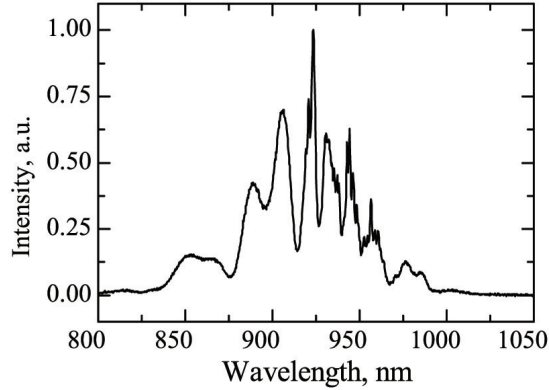


Fig. 3. Four-wave Raman mixing near the central wavelength spectral region

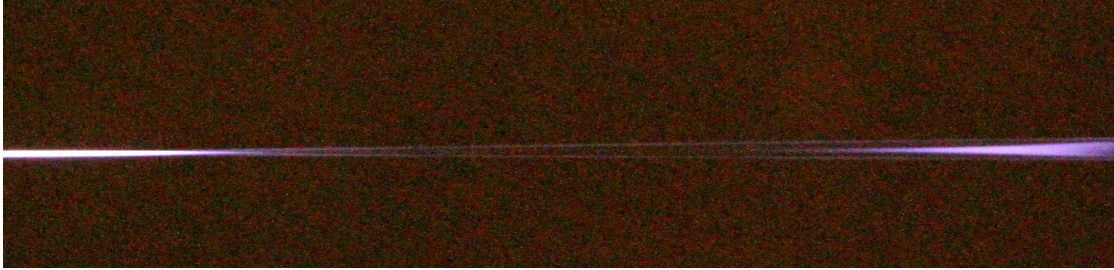


Fig. 4. Photo of filamentation area under aberration focusing by mirror. Light propagation from left to right. Bright regions are geometrical foci. Plasma formation between two thick beams in second foci region is an energetic reservoir

beam white-light supercontinuum is observed. A study of the spectral component of the white supercontinuum in the 600–1000 nm region at different lens (mirror) tilt angles has shown that at non-optimal angles, a process of FWRM to the anti-Stokes region containing only a few peaks is observed (Fig. 3), whereas in the optimal mode, a cascade process is observed (Fig. 2b). An analysis of different sources [17, 18] shows the contribution of the energy reservoir to the formation of a stable beam. The same energy reservoir in the region of the second geometric focus of the system (Fig. 4) contributes to the processes of radiation amplification, which leads to cascade generation of spectral lines.

Conclusions

The presented results allow us to state that aberration focusing of femtosecond radiation causes a number of physical processes that lead to ultra-wideband broadening of the pump pulse and formation of a beam with a divergence close to the diffraction limit. In the prefilament area, stimulated Raman scattering on nitrogen molecules occurs, leading to the generation of first- and second-order Stokes lines. Further, in the filamentation area, as a result of the process of CARS an anti-Stokes component is generated. In the filament and post-filamentation channels, a cascade process of FWRM is started, the seed components of which are the pump pulse and the anti-Stokes line. Aberration focusing provides the cascade process, supplement energy from

the paraxial energy reservoir. High intensity of white-light beam promotes self-channeling in the post-filamentation area, providing a divergence close to the diffraction limit.

The work supported by the Ministry of Science and Higher Education of the Russian Federation (FWRM-2021-0014).

References

- [1] A.Braun, G.Korn, X.Liu, et al., Self-channeling of high-peak-power femtosecond laser pulses in air, *Optics Letters*, **20**(1995), no. 1, 73–75. DOI: 10.1364/ol.20.000073
- [2] W.Liu, S.L.Chin, Abnormal wavelength dependence of the self-cleaning phenomenon during femtosecond-laser-pulse filamentation, *Physical Review A*, **76**(2007), no. 1, 013826. DOI: 10.1103/PhysRevA.76.013826
- [3] S.L.Chin, Y.Chen, O.Kosareva, et al., What is a filament? *Laser Physics*, **18**(2008), no. 8, 962–964. DOI: 10.1134/S1054660X08080070
- [4] J.-F.Daigle, T.J.Wang, S.Hosseini, et al., Dynamic behavior of postfilamentation Raman pulses, *Applied Optics*, **50**(2011), no. 33, 6234–6238. DOI: 10.1364/AO.50.006234
- [5] O.Kosareva, N.Panov, D.Shipilo, et al., Postfilament supercontinuum on 100 m path in air, *Optics Letters*, **46**(2021), no. 5, 1125–1128. DOI: 10.1364/OL.416224
- [6] V.P.Kandidov, E.D.Zaloznaya, A.E.Dormidonov, et al., Light bullets in transparent dielectrics, *Quantum Electronics*, **52**(2022), no. 3, 233–246. DOI: 10.1070/QEL18000
- [7] V.P.Kandidov, I.S.Golubtsov, O.G.Kosareva, Supercontinuum sources in a high-power femtosecond laser pulse propagating in liquids and gases, *Quantum Electronics*, **34**(2004), no.4, 348–354. DOI: 10.1070/QE2004v034n04ABEH002679
- [8] J.-F.Daigle, O.Kosareva, N.Panov, et al., Formation and evolution of intense, post-filamentation, ionization-free low divergence beams, *Optics Communications*, **284**(2011), 3601–3606. DOI: 10.1016/j.optcom.2011.03.077
- [9] F.Théberge, N.Aközbek, W.Liu, et al., Tunable Ultrashort Laser Pulses Generated through Filamentation in Gases, *Physical Review Letters*, **97**(2006), 023904. DOI: 10.1103/PhysRevLett.97.023904
- [10] F.Théberge, P.Lassonde, S.Payeur, et al., Efficient spectral-step expansion of a filamenting laser pulse, *Optics Letters*, **38**(2013), no. 9, 1576–1578. DOI: 10.1364/OL.38.001576
- [11] J.R.Péñano, P.Sprangle, P.Serafim, et al., Stimulated Raman scattering of intense laser pulses in air, *Physical Review E*, **68**(2003), 056502. DOI: 10.1103/PhysRevE.68.056502
- [12] H.Kawano, Y.Hirakawa, T.Imasaka, Generation of High-Order Rotational Lines in Hydrogen by Four-Wave Raman Mixing in Femtosecond Regime, *IEEE Journal of quantum electronics*, **34**(1998), no. 2, 260–268. DOI: 10.1109/3.658704
- [13] V.E.Prokop'ev, D.M.Lubenko, V.F.Losev, Investigation of the filament spatial structure by aberration focusing in air of a femtosecond radiation pulse, *Results in Optics*, **1**(2020), 100029. DOI: 10.1016/j.rio.2020.100029

- [14] D.M.Lubenko, V.E.Prokopev, Generation of Broadband Radiation During Filamentation of a Femtosecond Laser Pulse in the Atmosphere, *Journal of Siberian Federal University. Mathematics & Physics*, **15**(2022), no. 6, 718–723.
DOI: 10.17516/1997-1397-2022-15-6-718-723
- [15] V.E.Prokopev, D.M.Lubenko, Transformation of the spectrum of a femtosecond laser pulse during propagation in the atmosphere, *Atmospheric and Oceanic Optics*, **37**(2024), no. 8, 648–652 (Russian). DOI: 10.15372/AOO20240804
- [16] Femtosecond Atmospheric Optics, ed. S. N. Bagaev and G. G. Matvienko, Novosibirsk Publishing House SB RAS, 2010, 110–112 (in Russian).
- [17] W.Liu, F.Théberge, E.Arévalo, et al., Experiment and simulations on the energy reservoir effect in femtosecond light filaments, *Optics Letters*, **30**(2005), no. 19, 2602–2604.
DOI: 10.1364/OL.30.002602
- [18] J.Wang, Y.Guo, X.Song, et al., Multi-dimensional control of femtosecond laser filaments by inserting a wedge plate in the forced focusing region, *Physics of Plasmas*, **29**(2022), 012301.
DOI: 10.1063/5.0073278

Процесс филаментации фемтосекундного излучения в воздухе и явления ее сопровождающие

Владимир Е. Прокопьев

Дмитрий М. Лубенко

Томский государственный университет

Томский политехнический университет

Институт сильноточной электроники СО РАН

Томск, Российская Федерация

Аннотация. В работе приводятся экспериментальные результаты исследований условий и механизмов формирования высоконаправленного широкополосного суперконтинуума в видимой области спектра. Показано, что формирование такого излучения происходит в области филамента и постфиламентационном канале путем последовательной реализации различных механизмов уширения спектра. Экспериментально подтверждается, что данное излучение наиболее устойчиво формируется при создании aberrаций на волновом фронте излучения накачки.

Ключевые слова: фемтосекундный лазер, лазерный филамент, суперконтинуум, вынужденное комбинационное излучение, когерентное антистоксово рассеяние света, четырехволновое взаимодействие.

EDN: RULPRP
УДК 535.8

Simulation of Single-Pixel Camera Method Application for mapping the Spatial Layout of Objects in LIDAR Technologies

Anastasiia K. Lappo-Danilevskaia*

Azat O. Ismagilov[†]

ITMO University
Saint-Petersburg, Russian Federation

Aleksei A. Kalinichev[‡]

Saint-Petersburg State University
Saint-Petersburg, Russian Federation

Anton N. Tsytkin[§]

ITMO University
Saint-Petersburg, Russian Federation

Received 27.10.2024, received in revised form 13.12.2024, accepted 14.01.2025

Abstract. This work presents the simulation results demonstrating the successful application of single-pixel imaging for the reconstruction of three-dimensional object images, in combination with LIDAR technologies. Specifically, the integration of pulsed radiation-based Time of Flight (ToF) and Frequency Modulated Continuous Wave (FMCW) LIDAR methods is explored. In the case of ToF, the simulations reveal enhanced accuracy in distinguishing distances between objects that are smaller than the distance light travels in half the duration of the scanning pulse. These findings highlight the potential of single-pixel imaging in advanced 3D visualization and distance measurement applications.

Keywords: Single pixel camera, 3D visualisation, Time of flight LIDAR, Frequency-modulated continuous wave LIDAR

Citation: A.K. Lappo-Danilevskaia, A.O. Ismagilov, A.A. Kalinichev, A.N. Tsytkin, Simulation of Single-Pixel Camera Method Application for mapping the Spatial Layout of Objects in LIDAR Technologies, J. Sib. Fed. Univ. Math. Phys., 2025, 18(3), 377–386. EDN: RULPRP.



With the active development of autonomous vehicles, robotics, digitalization of the urban environment, and the spread of smart home technology, object recognition, visualization, and location detection systems are becoming key elements to ensure more advanced, secure, high-precision implementations that can adapt to changing conditions. One of the popular methods currently in use is LIDAR — a technology that stands for "Light Detection and Ranging". LIDAR technologies are actively used for autonomous navigation [1], environmental monitoring [2], for autonomous and safe precision landing on solar system bodies [3], service robots [4], odometry and geospatial mapping [5]. Despite significant progress in remote 3D visualization, current methods are limited by either detection range or application mode limitations.

The principle of distance measurement in LIDARs can be classified based on the type of the source. Pulsed illumination is used in the Time of Flight (TOF) technique, where the distance is calculated by measuring the time it takes for light to return from the object. Continuous frequency-modulated signal is used in Frequency Modulated Continuous Wave (FMCW)

*ankonstld@itmo.ru <https://orcid.org/0000-0002-1762-2688>

[†] <https://orcid.org/0000-0002-5844-2966>

[‡] <https://orcid.org/0000-0001-8242-9457>

[§] <https://orcid.org/0000-0002-9254-1116>

© Siberian Federal University. All rights reserved

LIDAR systems, where the distance is determined using the beat frequency between the initial and reflected from the object signals. Such techniques can be combined with different imaging principles.

One of them is raster scanning. For example, advantages of TOF-systems with raster scanning are a high resolution and long detection range due to the use of short pulses with high peak power. Notably, the reconstruction of a scene consisting of $n \times n \times n$ pixels takes n^2 measurements. Accordingly, there is a task of reducing the number of measurements while maintaining quality, as, for example, increasing the image speed is important for visualizing moving targets. Another implementation is a Flash camera that illuminates the entire field of view. Flash cameras utilize a matrix of detectors, raising concerns related to increasing quality and distance range. The cost associated with resolution enhancements can prove to be exorbitant when employing detector matrices.

As an alternative can be considered single-pixel imaging (SPI) techniques. Single pixel imaging has found applications in various fields, showcasing its versatility and potential impact. Some notable applications are Terahertz imaging [7, 8], X-ray imaging [9], where is a lack of detectors with spatial resolution, remote sensing [10], microscopy [11], imaging in low light [12] and noisy environments [13]. Instead of capturing the entire image at once, SPI relies on illuminating the object with a series of known, structured light patterns. For each pattern, the light transmitted or reflected by the object is collected by a single-pixel detector (sometimes called a "bucket detector"), which measures the total intensity of light, without any spatial information. The modulator position in the setup determines the setup configuration. In the case when the modulator stays between the object and illumination source, the technique names as a ghost imaging (GI) [14]. Currently from single-pixel technologies, the use of ghost imaging to improve LIDAR technology has been investigated and has shown both distance improvement and reconstruction speed increase [15–17].

Another approach is a single pixel camera method (SPC) that is based on structured detection [18]. This method achieves higher quality of the reconstructed image with an increased distance compared to the Ghost Imaging (GI) methods. This difference in quality can be attributed to the contributions of the optical setup elements [19]. This shows the possibility of obtaining better results when using the SPC method in lidar technologies compared to the GI.

In this work, SPC approach as a a method for obtaining information about the spatial distribution of objects was studied in combination with Time-of-Flight and Frequency modulated continuous wave LIDAR technologies for three-dimensional Objects Image Reconstruction.

1. Methods

The simulation was conducted in a Matlab Software Package. The propagation of the spatial distribution of radiation is considered using the example of the TOF configuration presented in the Fig. 1a. Simulation of the spatial profile of radiation includes calculating the field in the plane in front of the object $E_0(x, y, t)$, its interaction with objects $T(x, y, t)$, propagation of the interacted radiation to the DMD and its modulation by patterns.

The distribution of the field in the cross-section was given in the Gauss form according to [20]. The time distribution of pulses also took the form of a Gaussian distribution. The interaction of the spatial profile with the objects with transfer function $T(x, y, t)$ is calculated as follows: $E(x, y, t) = E_0(x, y, t) \times T(x, y, t)$. Propagation of whole reflected light to the DMD and all transmitted light to the next objects were made via angular spectrum approach [21].

The pulse $E_{beforeDMD}(x, y, t)$, which came to the spatial light modulator, is modulated by the mask $P_i(x, y)$ at each moment of time. After that, the integral intensity of the modulated radiation coming to the detector is calculated:

$$B_i(t) = \sum_{n=1}^{N_T} \iint E_{beforeDMDn}(x, y, t) \cdot P_i \cdot \cos(\varphi(x, y)) dx dy, \quad (1)$$

$$\varphi(x, y) = \arctan\left(\frac{\sqrt{x^2 + y^2}}{R_n}\right), \quad (2)$$

where $\varphi(x, y)$ is the solid angle between the target points and detector.

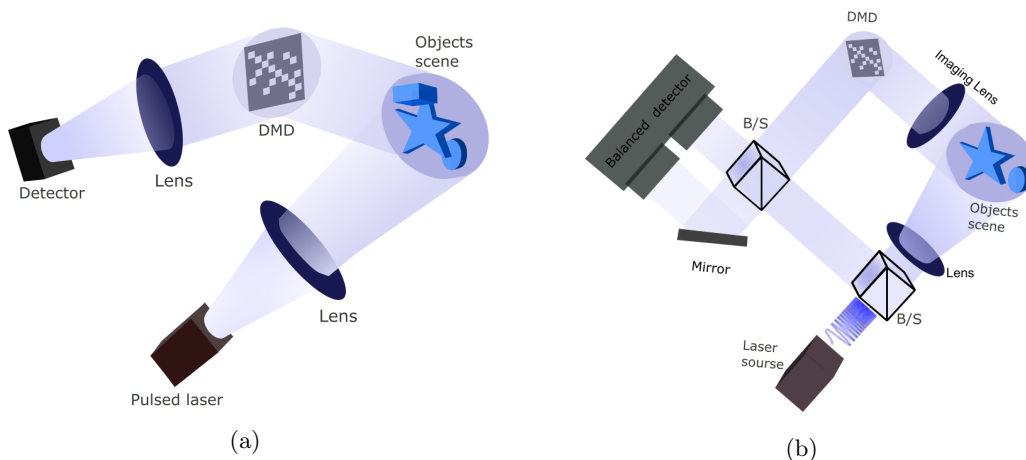


Fig. 1. A schematic diagram of (a) SPC TOF LIDAR. A pulsed radiation source illuminates the scene with the object, the light from the target reflects and goes to a DMD. Modulated radiation is collected on a single-pixel detector, (b) SPC FMCW LIDAR. Frequency chirped radiation passes through a beamsplitter. The small fraction acts as a local oscillator, another one goes to the target, reflects and passes to the DMD. After DMD object beam is combined with the LO signal on the beamsplitter and combined radiation is detected by a balanced detector

The selection of patterns plays a crucial role in SPI, as there are various options available. One approach is to utilize random patterns, which are particularly advantageous in image recognition tasks where the full set of patterns is unnecessary. This approach can significantly reduce the number of measurements, making the process faster and more efficient. However, achievement of high-precision image restoration still requires a large number of measurements [22]. Another option is to use Fourier patterns, although they involve gray-scale values, which adds complexity to their generation and projection when compared to binary Hadamard patterns [23]. At the same time, in order to obtain a correct image, there is no need to use the entire set of masks. There are proposed techniques that help to reduce the required number of patterns based on sorting the columns of the Hadamard matrix, vivid examples are cake-cutting basis sort [24] and russian dolls [25]. In simulation the Hadamard patterns were used, the P_i modulation pattern is a 256×256 pixel matrix. To reduce the computational complexity, the generated mask was 64×64 and was expanded in 4 times. Hadamard patterns were formed from the Hadamard matrix H_{2^n} of order $n = 6$. Initially, the elements of the matrix contain values $(-1, 1)$, however, only positive Hadamard patterns are used to restore the images, therefore the -1 value is changed to 0. The Single pixel image were reconstructed with the use of Hadamard patterns by the following formula for SPC approach:

$$G(x, y) = \frac{1}{N} \sum_{i=1}^N B_i P_{i,(x,y)}. \quad (3)$$

The quality assessment can be performed using the structural similarity index (SSIM), which

takes into account parameters such as luminance $l(x, y)$, contrast $c(x, y)$ and structure $s(x, y)$

$$SSIM(x, y) = [l(x, y)]^\alpha \cdot [c(x, y)]^\beta \cdot [s(x, y)]^\gamma, \quad (4)$$

where $\alpha = \beta = \gamma = 1$.

The Fig. 1b shows a schematic diagram on which the simulation of the implementation of FMCW SPC LIDAR based on heterodyne detection [26] was performed. Electric field of the initial laser radiation $E_{\text{modulated}}$ has a linear frequency chirp with the start frequency f_0 and the final f_{max} [27]:

$$E_{\text{modulated}}(t) = A \exp \left(2\pi i \left[f_0 + \frac{f_{\text{max}} - f_0}{2T} t \right] t \right), \quad (5)$$

where A is an amplitude, T is a period of modulation.

Signal splits on a beamsplitter, one part acts as a local oscillator $E_{LO} = E_{\text{modulated}}$ and another fraction goes to the object, reflects and acquires time delay τ . The object signal is modulated by spatial masks on the DMD. The spatial profile of radiation and its interaction with the DMD is simulated as in the TOF case.

On the second beam splitter, E_{sig} is combined with E_{LO} and then the combined signal is sent to the balanced photodetector. The signal on the balanced photodetector after filtering sum-frequency signal components looks like this [27]:

$$\begin{aligned} P_{\text{Scope}}(t) &= \frac{\epsilon_0 c}{2} \left(\left| \frac{E_{LO}(t) + i \sum_j E_{\text{Sig}}(t - \tau_j) * P_R(t)}{\sqrt{2}} \right|^2 - \right. \\ &\quad \left. - \left| \frac{i E_{LO}(t) + \sum_j E_{\text{Sig}}(t - \tau_j) * P_R(t)}{\sqrt{2}} \right|^2 \right) = \\ &= \epsilon_0 c \sum_j A_{LO} A_j P_R(t) \sin \left(2\pi \frac{\Delta \nu \tau_j}{T} t + v_0 \tau_j - \frac{\Delta \nu}{2T} \tau_j^2 \right). \end{aligned} \quad (6)$$

The received signal is amplified by the signal of the local oscillator, which is 2 orders of magnitude more intense and at the same time contains only the following frequencies, which are visible as peaks in the frequency spectrum after the Fourier transform $P_{\text{Scope}}(t)$:

$$v_j = \frac{v_0 \tau_j}{2T}. \quad (7)$$

They are used to calculate the distance

$$d_j = \frac{v_j T c}{2\Delta \nu} \quad (8)$$

the value of the peak is used to reconstruct an image of the object via SPI method.

2. Simulation results

The following parameters were used: $w_0 = 15\text{mm}$ is the waist radius of a laser beam, $\lambda = 1550\text{ nm}$ — laser wavelength. The spatial distribution of objects is shown in the Fig. 2a. The size of the reconstructed images is 256×256 pixels or 0.04×0.04 m.

The single-pixel camera approach reconstructs the image that directly passed on the spatial modulator, that is the diffracted one. When the Hadamard patterns are used for image reconstruction due to the high accuracy and quality on reconstructed image the diffraction artefacts are clearly visible (Fig. 2b). This necessitates the back propagation by the angular spectrum

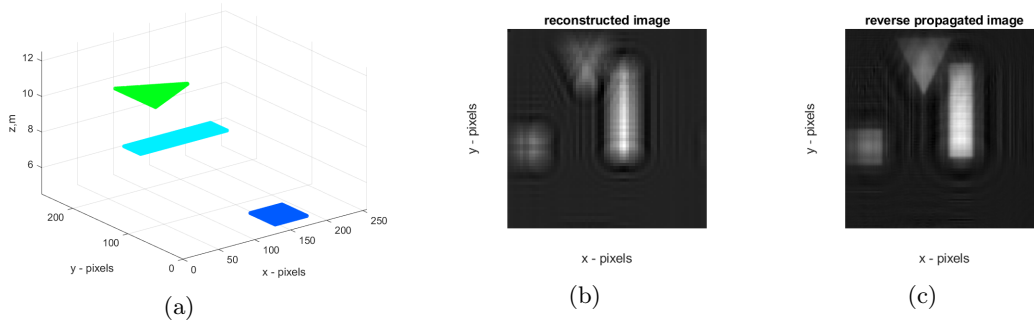


Fig. 2. (a) Object's spatial profile, (b) reconstructed image, (c) reverse propagated reconstructed image

method over a distance of $d_1 = \frac{t_1 c}{2}$, obtained using LIDAR technology. In the image obtained with its help, objects become clearly visible (Fig. 2c).

The temporal profile of the radiation was simulated with the following parameters: standard deviation $\sigma = 1.2 \times 10^{-9}$ and $FWHM = 2.8$ ns. This parameter determines the distance that can be distinguished using the TOF technique and it is determined by the response time of the detector. The time resolution of detected signal is controlled by an oscilloscope. On the market are presented oscilloscopes with following sampling rate: 2,5 GSa/s (Rohde Schwarz RTM3004), 8 GSa/s (RIGOL MSO5104), up to the 4 GSa/s (GW Instek GDS-73504A). 4 GSa/s was selected which corresponds to the time step 1 ps. The sampling rate F_s directly affects the resolution of the distance $\delta R = \frac{c}{2F_s}$.

Globally, the time profiles of reflected signals can be divided into two cases: objects are too close and the signals overlap into one indistinguishable peak (Fig. 3a) and objects are at a sufficient distance for the reflected signals to be resolved by the detection system (Fig. 4a). Using single-pixel imaging, it is possible to restore the image of objects at each discretized point, build depth maps of objects using them, take the average distance at which the object is distinguishable and thereby improve the quality of distance determination.

As an illustration of the construction of three-dimensional depth maps, two-dimensional reconstructed images were taken, restored at each discretized time point with a signal intensity above 20 %. After isolating objects from noise, the objects were built at a certain distance FROM LIDAR technology, forming a three-dimensional map of the objects.

To evaluate the determination of distances using TOF LIDAR technology and using reconstructed depth maps, error functions were constructed, calculated as a relative measurement error:

$$error = \frac{d_{measured} - d_{real}}{d_{real}} \quad (9)$$

where $d_{measured}$ is a calculated distance d_{real} is a real distance.

For comparison, the distance determination with using only the peak intensity (Fig. 5b) is presented. It increases linearly for all objects except the central one until the peaks of the pulses are distinguishable at a distance of about 60 centimeters between the objects. However, when peaks are distinguishable, the technology produces a minimal error, which indicates that there is no need to improve it and single-pixel imaging can be used only at peak points for visualization. When determining the distance from depth maps (Fig. 5a) the advantage of the technology is visible at distances less than 60 centimeters, since the error does not exceed 2.5% against 10% for the case of classical determination.

During simulation of FMCW LIDAR were used following parameters of radiation: $T \approx 3ms$ — modulation time of each signal, $f_0 = 0.5GHz$ — initial frequency, $B = 4.3GHz$ — chirp

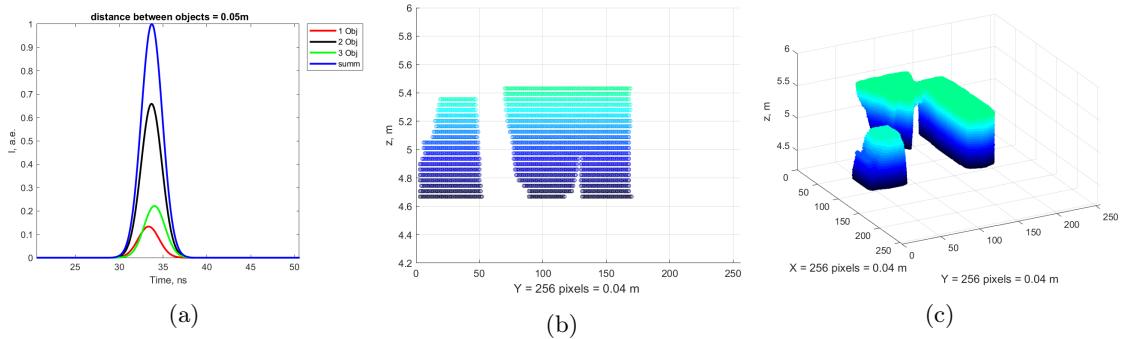


Fig. 3. The SPC TOF realisation based depth maps of three objects located at the distances 5m – square, 5.05m – rectangle, 5.1 m – triangle, (a) Temporal profile of the reflected signals, isometric (b) and side (c) view of depth maps constructed with single pixel images reconstructed using Hadamard patterns

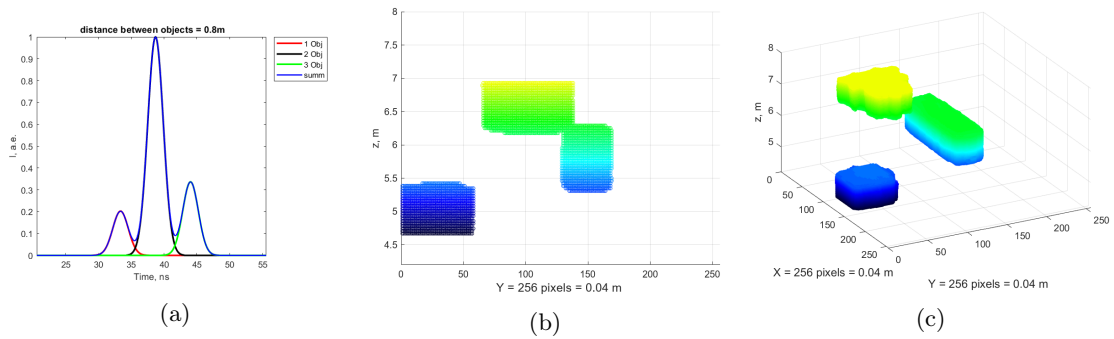


Fig. 4. The SPC TOF realisation based depth maps of three objects located at the distances 5m – square, 5.85m – rectangle, 6.6 m – triangle, (a) Temporal profile of the reflected signals, isometric (b) and side (c) view of depth maps constructed with single pixel images reconstructed using Hadamard patterns

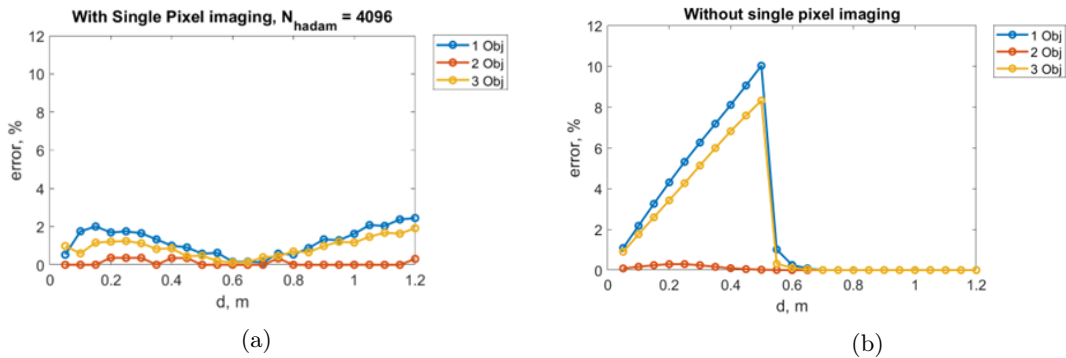


Fig. 5. Relative error in distance determination via simulated TOF LIDAR, (a), with SPC and Hadamard patterns, (b) without SPC

bandwidth. Range resolution of FMCW LIDAR system can be calculated as: $\delta R = \frac{c}{2B}$. After the Fourier transform, just B determines the position and width of the frequency peak, which directly affects the ability to recognize distances. The step between the frequencies is

approximately 0.03 MHz, which, when converted to a distance using $B = 4300$ MHz 0.07 m. To demonstrate the application of the single-pixel camera method using $B = 4300$ MHz frequency peak intensities marked with red dots correlate with information about objects located at a distance of 5 centimeters (Fig. 6). It indicates the possibility of improving the quality of distance determination, as in the case of TOF LIDAR, Despite the proximity of the frequency peaks, the single-pixel visualization method does not produce noise in the form of residual information about neighboring objects.

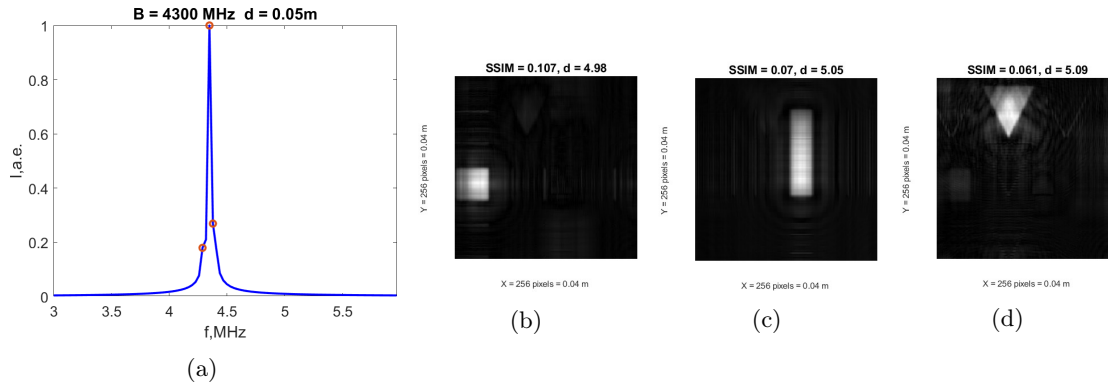


Fig. 6. The SPC FMCW realisation ($B = 4300$ MHz) with three objects at the distances 5m — square, 5.05m — rectangle, 5.1m — triangle: (a) Frequency spectrum of the reflected signals, (b), (c), (d) reconstructed images using Hadamard patterns

Conclusion

In this work, we explored the feasibility of integrating Time-of-Flight (TOF) and Frequency-Modulated Continuous-Wave (FMCW) LIDAR technologies with the single-pixel camera approach to enhance systems for generating three-dimensional depth maps of objects. The successful combination of LIDAR techniques with ghost imaging and the application of methods like compressive sensing to accelerate image acquisition has inspired further research into developing single-pixel LIDAR systems. While the use of single-pixel cameras for LIDAR applications has received limited attention, it shows promise for improving object image reconstruction at longer distances compared to ghost imaging.

The key result of this study is the simulation of the successful application of the single-pixel camera method to both FMCW and TOF LIDAR technologies to restore three-dimensional object maps. One important finding is the complementarity of these technologies: distance information obtained from LIDAR systems is crucial for image reconstruction through backward propagation. This confirms that three-dimensional single-pixel camera imaging relies on this data, highlighting avenues for the continued development of 3D single-pixel visualization.

Additionally, single-pixel imaging demonstrates improvements in LIDAR systems, particularly in visualizing objects that would otherwise be indistinguishable due to proximity. This is especially relevant in cases where frequency peaks merge in FMCW systems. In the simulations of SPC TOF and SPC FMCW systems, images of objects were successfully reconstructed even when the distance between them was small enough that the reflected signals became indistinguishable. For TOF LIDAR, this distance was less than 65 centimeters, demonstrating the system's ability to accurately locate objects based on compiled three-dimensional maps.

The successful integration of SPC TOF and SPC FMCW technologies demonstrated in this research opens new possibilities for enhancing remote sensing systems. It enables the visualization

of objects at greater distances than conventional TOF and FMCW LIDARs can achieve with similar technical performance. For FMCW LIDAR, SPC presents an appealing alternative to raster scanning, allowing for faster imaging. For TOF LIDAR, SPC offers an opportunity to improve accuracy without increasing the response time or cost of the receiver

Funding

Ministry of Education and Science of the Russian Federation (2019-0903).

References

- [1] N.Jonnavithula, Y.Lyu, Z.Zhang, LiDAR Odometry Methodologies for Autonomous Driving: A Survey, 2021, arXiv preprint arXiv:2109.06120.
- [2] G.Zhao, M.Lian, Y.Li, Z.Duan, S.Zhu, L.Mei, S.Svanberg, Mobile Lidar System for Environmental Monitoring, *Applied Optics*, **56**(2017), no. 5, 1506–1516. DOI: 10.1364/AO.56.001506
- [3] F.Amzajerjian, V.E.Roback, A.Bulyshev, P.F.Brewster, G.D.Hines, Imaging Flash Lidar for Autonomous Safe Landing and Spacecraft Proximity Operation, in *AIAA SPACE 2016*, 2016, 5591. DOI: 10.2514/6.2016-5591
- [4] T.Olvera Hale, Mapping and Navigation in an Unknown Environment Using LiDAR for Mobile Service Robots, 2020.
- [5] D.Lee, M.Jung, W.Yang, A.Kim, LiDAR Odometry Survey: Recent Advancements and Remaining Challenges, *Intelligent Service Robotics*, **17**(2024), 1-24. DOI: 10.1007/s11370-024-00515-8
- [6] B Behroozpour, P.A.Sandborn, M.C.Wu, B.E.Boser, Lidar system architectures and circuits, *IEEE Commun. Mag.*, **55**(2017), 135–142. DOI: 10.1109/MCOM.2017.1700030
- [7] W.L.Chan, K.Charan, D.Takhar, K.F.Kelly, R.G.Baraniuk, D.M.Mittleman, A Single-Pixel Terahertz Imaging System Based on Compressed Sensing, *Applied Physics Letters*, **93**(2008), no. 12. DOI: 10.1063/1.2989126
- [8] L.Leibov, A.Ismagilov, V.Zalipaev, B.Nasedkin, Y.Grachev, N.Petrov, A.Tcypkin, Speckle Patterns Formed by Broadband Terahertz Radiation and Their Applications for Ghost Imaging, *Scientific Reports* **11**(2021), no. 1, 20071. DOI: 10.21203/rs.3.rs-742925/v1
- [9] J.Greenberg, K.Krishnamurthy, D.Brady, Compressive Single-Pixel Snapshot X-Ray Diffraction Imaging, *Optics Letters*, **39**(2014), no. 1, 111–114. DOI: 10.1364/OL.39.000111
- [10] J.Ma, Single-Pixel Remote Sensing, *IEEE Geoscience and Remote Sensing Letters*, **6**(2009), no. 2, 199–203. DOI: 10.1109/LGRS.2008.2010959
- [11] V.Studer, J.Bobin, M.Chahid, H.S.Mousavi, E.Candes, M.Dahan, Compressive Fluorescence Microscopy for Biological and Hyperspectral Imaging, *Proceedings of the National Academy of Sciences*, **109**(2012), no. 26, E1679–E1687. DOI: 10.1073/pnas.1119511109
- [12] P.A.Morris, R.S.Aspsden, J.E.C.Bell, R.W.Boyd, M.J.Padgett, Imaging with a Small Number of Photons, *Nature Communications*, **6**(2015), no. 1, 5913. DOI: 10.1038/ncomms6913
- [13] J Cheng, Ghost Imaging through Turbulent Atmosphere, *Optics Express*, **17**(2009), no. 10, 7916–7921. DOI:10.1364/OE.17.007916

-
- [14] Y.Bromberg, O.Katz, Y.Silberberg, Ghost Imaging with a Single Detector, *Phys. Rev. A*, **79**(2009), no. 5, 053840. DOI:10.1103/PHYSREVA.79.053840
- [15] Z.Yang, Y.-M.Bai, K.-X.Huang, Y.-X.Liu, J.Liu, D. Ruan, J.-L.Li, Single-Pixel Full-Field Simultaneous Spatial and Velocity Imaging, *Optics and Lasers in Engineering*, **169**(2023), 107691.
- [16] W.Zhang, Z.Cao, H.Zhang, H.Xie, Z.Ye, L.Xu, Distribution Retrieval of Both Depth and Reflectivity in 3-D Objects via Using Modulated Single Pixel Imaging, *IEEE Transactions on Instrumentation and Measurement*, **72**(2022), 1–11. DOI: 10.1109/TIM.2022.3224515
- [17] X.Li, Y.Hu, Y.Jie, C.Zhao, Z.Zhang, Dual-Frequency Lidar for Compressed Sensing 3D Imaging Based on All-Phase Fast Fourier Transform, *Journal of Optics and Photonics Research*, **1**(2023). DOI: 10.47852/bonviewJOPR32021565
- [18] G.M.Gibson, S.D.Johnson, M.J.Padgett, Single-Pixel Imaging 12 Years On: A Review, *Optics Express*, **28**(2020), no. 19, 28190–28208. DOI: 10.1364/OE.403195
- [19] W.Gong, Performance comparison of computational ghost imaging versus single-pixel camera in light disturbance environment, *Optics & Laser Technology*, **152**(2022), 108140.
- [20] B.Liu, P.Song, Y.Zhai, X.Wang, W.Zhang, Modeling and Simulations of a Three-Dimensional Ghost Imaging Method with Differential Correlation Sampling, *Optics Express*, **29**(2021), no. 23, 38879–38893. DOI:10.1364/OE.442889
- [21] J.D.Schmidt, Numerical Simulation of Optical Wave Propagation with Examples in MATLAB, SPIE, 2010.
- [22] B.Sun, M.Edgar, R.Bowman, L.Vitert, S.Welsh, A.Bowman, M.Padgett, 3D Computational Imaging with Single-Pixel Detectors, *Science (New York, N. Y.)*, **340**(2013), 844–847. DOI: 10.1126/science.1234454.
- [23] Z.Zhang, X.Ma, J.Zhong, Single-Pixel Imaging by Means of Fourier Spectrum Acquisition, *Nature Communications*, **6**(2015), no. 1, 6225. DOI: 10.1038/ncomms7225
- [24] W.-K.Yu, Super Sub-Nyquist Single-Pixel Imaging by Means of Cake-Cutting Hadamard Basis Sort, *Sensors*, **19**(2019), no. 19, 4122. DOI: 10.3390/s19194122
- [25] M.-J.Sun, L.-T.Meng, M.P.Edgar, M.J.Padgett, N.Radwell, A Russian Dolls Ordering of the Hadamard Basis for Compressive Single-Pixel Imaging, *Scientific Reports*, **7**(2017), no. 1, 3464. DOI: 10.1038/s41598-017-03725-6
- [26] X.Yang, Y.Zhang, C.Yang, L.Xu, Q.Wang, Y.Zhao, Heterodyne 3D Ghost Imaging, *Optics Communications*, **368**(2016), 1–6.
- [27] D.J.Lum, S.H.Knarr, J.C.Howell, Frequency-Modulated Continuous-Wave LiDAR Compressive Depth-Mapping, *Optics Express*, **26**(2018), no. 12, 15420–15435. DOI: 10.1364/OE.26.015420

Моделирование метода однопиксельной визуализации для получения пространственного распределения объектов в ЛИДАР технологиях

Анастасия К. Лаппо-Данилевская

Азат О. Исмагилов

Университет ИТМО

Санкт-Петербург, Российская Федерация

Алексей А. Калинин

Санкт-Петербургский государственный университет

Российская Федерация

Антон Н. Цыпкин

Университет ИТМО

Санкт-Петербург, Российская Федерация

Аннотация. В данной работе представлены результаты моделирования, демонстрирующие успешное применение однопиксельной визуализации для реконструкции трехмерных изображений объектов в сочетании с технологиями лазерных дальнометров. В частности, рассматривается интеграция методов лазерного дальнометра с импульсным излучением на основе времени пролета (ToF) и частотно-модулированного непрерывного излучения (FMCW). В случае ToF моделирование показывает повышенную точность в различении расстояний между объектами, которые меньше расстояния, которое свет проходит за половину длительности сканирующего импульса. Эти результаты подчеркивают потенциал однопиксельной визуализации в современных приложениях трехмерной визуализации.

Ключевые слова: однопиксельная визуализация, трехмерная визуализация, лидары.

EDN: NUMFOQ
 УДК 517.55+517.51

$m - cv$ measure $\omega^*(x, E, D)$ and condenser capacity $C(E, D)$ in the class m -convex functions

Azimbay Sadullaev*

National University of Uzbekistan
 V. I. Romanovsky Institute of Mathematics
 of the Academy of Sciences of Uzbekistan
 Tashkent, Uzbekistan

Rasulbek Sharipov†

Urgench State University
 Urgench, Uzbekistan

Mukhiddin Ismoilov‡

National University of Uzbekistan
 Tashkent, Uzbekistan

Received 10.08.2024, received in revised form 15.09.2024, accepted 24.10.2024

Abstract. In this work we study very basic concepts of potential theory: polar sets and $m - cv$ measures in the class of m -convex functions in real space \mathbb{R}^n . We also study capacity of condenser $C(E, D)$ in the class m -convex functions and will prove a number of its potential properties.

Keywords: m -subharmonic function, convex function, m -convex function, $m - cv$ polar set, $m - cv$ measure, Borel measures, Hessians.

Citation: A. Sadullaev, R. Sharipov, M. Ismoilov, $m - cv$ measure $\omega^*(x, E, D)$ and condenser capacity $C(E, D)$ in the class m -convex functions, J. Sib. Fed. Univ. Math. Phys., 2025, 18(3), 387–401. EDN: NUMFOQ.



1. Introduction and preliminaries

Let $u(x) \in C^2(D)$ be a twice smooth function in the domain $D \subset \mathbb{R}^n$. Then the matrix $\left(\frac{\partial^2 u}{\partial x_j \partial x_k}\right)$ is symmetric, $\frac{\partial^2 u}{\partial x_j \partial x_k} = \frac{\partial^2 u}{\partial x_k \partial x_j}$. Therefore, after a suitable orthonormal transformation, it can be transformed into a diagonal form

$$\left(\frac{\partial^2 u}{\partial x_j \partial x_k}\right) \rightarrow \begin{pmatrix} \lambda_1 & 0 & \dots & 0 \\ 0 & \lambda_2 & \dots & 0 \\ \dots & \dots & \dots & \dots \\ 0 & 0 & \dots & \lambda_n \end{pmatrix},$$

where $\lambda_j = \lambda_j(x) \in \mathbb{R}$ are the eigenvalues of the matrix $\left(\frac{\partial^2 u}{\partial x_j \partial x_k}\right)$. Let

$$H^k(u) = H^k(\lambda) = \sum_{1 \leq j_1 < \dots < j_k \leq n} \lambda_{j_1} \dots \lambda_{j_k}$$

*sadullaev@mail.ru

†sharipovr80@mail.ru <https://orcid.org/0000-0002-3033-3047>

‡mukhiddin4449@gmail.com <https://orcid.org/0009-0005-9339-0582>

© Siberian Federal University. All rights reserved

be the Hessian of dimension k of the vector $\lambda = (\lambda_1, \lambda_2, \dots, \lambda_n)$.

Definition 1.1. A twice smooth function $u(x) \in C^2(D)$ is called m -convex in $D \subset \mathbb{R}^n$, $u \in m - cv(D)$, if its eigenvalue vector $\lambda = \lambda(x) = (\lambda_1(x), \lambda_2(x), \dots, \lambda_n(x))$ satisfies the conditions

$$m - cv \cap C^2(D) = \{H^k(u) = H^k(\lambda(x)) \geq 0, \forall x \in D, k = 1, \dots, n - m + 1\}.$$

When $m = n$ the class $n - cv$ coincides with the class of subharmonic functions $sh = \{\lambda_1 + \lambda_2 + \dots + \lambda_n \geq 0\}$, when $m = 1$ it coincides with the class of convex functions $cv = \{\lambda_1 \geq 0, \lambda_2 \geq 0, \dots, \lambda_n \geq 0\}$, moreover $cv = 1 - cv \subset 2 - cv \subset \dots \subset n - cv = sh$. The theory of subharmonic functions is a developed and important part of theory functions and mathematical physics. The theory of convex functions is well studied and reflected in the works of A. Aleksandrov, I. Bakelman, A. Pozdnyak and others (see [2–5]). When $m > 1$ this class was studied in the series of works by N. Ivochkina, N. Trudinger, X. Wang et al. [11, 19–21] (see also [8]).

If we want to construct a good theory of $m - cv$ functions, then the class of functions $C^2(D)$ is not enough. For example, if we want to solve the equation

$$\begin{aligned} H^{n-m+1}(u) &= f(u, x), \\ u|_{\partial D} &= \varphi \end{aligned}$$

or want to work with extreme $m - cv$ functions, such as maximal $m - cv$ functions, we need to extend the definition of $m - cv$ functions to a wider class of upper semi-continuous functions. In the work of N. Trudinger, X. Wang [21] $m - cv$ functions are introduced in the class of upper semi-continuous functions $u(x)$ in the domain $D \subset \mathbb{R}^n$, using the so-called "viscous" definition, that is $H^k(q) \geq 0$, $k = 1, 2, \dots, n - m + 1$, for any quadratic polynomial $q(x)$, such that the difference $u(x) - q(x)$ has only a finite number of local maximum in the domain D . In addition, in this work $H^{n-m+1}(u)$ (maximum degree operator) is defined as a Borel measure and with the help of this operator the capacity of condenser $C(E, D)$ was introduced, a number of potential properties of this capacity was proved.

To expand the domain of definition of $m - cv$ functions from $C^2(D)$ to a wider class of semi-continuous functions, we have proposed a completely new approach, the connection of $m - cv$ functions with m -subharmonic (sh_m) functions in complex space \mathbb{C}^n . The theory of sh_m -functions is well developed and is currently subject of study by many mathematicians (Z. Błocki [6], S. Dinew and S. Kolodziej [9, 10], S. Y. Li [13], H. C. Lu [14, 15] and etc). Quite a complete overview of this theory is available in the survey article by A. Sadullaev and B. Abdullaev [1] in proceedings of Mathematical Institute of the RAS.

Let us recall that the theory of the sh_m -functions is based on differential forms and currents $(dd^c u)^k \wedge \beta^{n-k} \geq 0$, $k = 1, 2, \dots, n - m + 1$, where $\beta = dd^c \|z\|^2$ is a standard volume form in \mathbb{C}^n . A twice smooth function $u(z) \in C^2(D)$, $D \subset \mathbb{C}^n$ is called strongly m -subharmonic $u \in sh_m(D)$, if at each point of the domain D

$$\begin{aligned} sh_m(D) &= \left\{ u \in C^2 : (dd^c u)^k \wedge \beta^{n-k} \geq 0, k = 1, 2, \dots, n - m + 1 \right\} = \\ &= \left\{ u \in C^2 : dd^c u \wedge \beta^{n-1} \geq 0, (dd^c u)^2 \wedge \beta^{n-2} \geq 0, \dots, (dd^c u)^{n-m+1} \wedge \beta^{m-1} \geq 0 \right\}, \end{aligned} \tag{1}$$

where $\beta = dd^c \|z\|^2$ is a standard volume form in \mathbb{C}^n .

Operators $(dd^c u)^k \wedge \beta^{n-k}$ are closely related to the Hessians. For a twice smooth function $u \in C^2(D)$, the second-order differential $dd^c u = \frac{i}{2} \sum_{j,k} \frac{\partial^2 u}{\partial z_j \partial \bar{z}_k} dz_j \wedge d\bar{z}_k$ (at a fixed point $o \in D$) is

a Hermitian quadratic form. After a suitable unitary coordinate transformation, it is reduced to a diagonal form $dd^c u = \frac{i}{2} [\lambda_1 dz_1 \wedge d\bar{z}_1 + \dots + \lambda_n dz_n \wedge d\bar{z}_n]$, where $\lambda_1, \dots, \lambda_n$ are eigenvalues of the Hermitian matrix $\left(\frac{\partial^2 u}{\partial z_j \partial \bar{z}_k} \right)$, which are real: $\lambda = (\lambda_1, \dots, \lambda_n) \in \mathbb{R}^n$. Note that the unitary transformation does not change the differential form $\beta = dd^c \|z\|^2$. It is easy to see that

$$(dd^c u)^k \wedge \beta^{n-k} = k!(n-k)! H^k(u) \beta^n, \quad (2)$$

where $H^k(u) = \sum_{1 \leq j_1 < \dots < j_k \leq n} \lambda_{j_1} \dots \lambda_{j_k}$ is the Hessian of dimension k of the vector $\lambda = \lambda(u) \in \mathbb{R}^n$.

Hence, the twice smooth function $u(z) \in C^2(D)$, $D \subset \mathbb{C}^n$ is strongly m -subharmonic if at each point $o \in D$ it satisfies the following inequalities

$$H^k(u) = H_o^k(u) \geq 0, \quad k = 1, 2, \dots, n - m + 1. \quad (3)$$

Note that, the concept of the strongly m -subharmonic functions in a generalized sense is also defined for upper-semicontinuous functions.

Definition 1.2. *The function $u(z)$ defined in a domain $D \subset \mathbb{C}^n$ is called sh_m , if it is upper semi-continuous and for any twice smooth sh_m functions $v_1, \dots, v_{n-m} \in C^2(D) \cap sh_m(D)$ the current $dd^c u \wedge dd^c v_1 \wedge \dots \wedge dd^c v_{n-m} \wedge \beta^{m-1}$ defined as*

$$\begin{aligned} & [dd^c u \wedge dd^c v_1 \wedge \dots \wedge dd^c v_{n-m} \wedge \beta^{m-1}] (\omega) = \\ & = \int u dd^c v_1 \wedge \dots \wedge dd^c v_{n-m} \wedge \beta^{m-1} \wedge dd^c \omega, \quad \omega \in F^{0,0}. \end{aligned} \quad (4)$$

is positive, $\int u dd^c v_1 \wedge \dots \wedge dd^c v_{n-m} \wedge \beta^{m-1} \wedge dd^c \omega \geq 0 \quad \forall \omega \in F^{0,0}, \omega \geq 0$. Here $F^{0,0}(D)$ is a family of infinitely smooth finite in D functions.

In the Blocki's work [6] it was proved that, this definition is correct, that for $u \in C^2(D)$ functions this definition coincides with the initial definition of sh_m -functions.

2. Relation between $m - cv$ and sh_m functions

To establish a connection between $m - cv$ functions and sh_m functions, we embed a real space \mathbb{R}_x^n into a complex space \mathbb{C}_z^n , $\mathbb{R}_x^n \subset \mathbb{C}_z^n = \mathbb{R}_x^n + i\mathbb{R}_y^n$ ($z = x + iy$), as a real n -dimensional subspace. Then, we extend the function $u(x)$, given in the domain $D \subset \mathbb{R}_x^n$ into domain $\Omega = D \times i\mathbb{R}_y^n \subset \mathbb{C}_z^n$ as $u^c(z) = u^c(x + iy) = u(x)$, by assuming it is a constant on parallel planes $\Pi_{x^0} = \{z \in \mathbb{C}^n : x = x^0, y \in \mathbb{R}^n\}$.

Theorem 2.1 (see [16, 18]). *A twice smooth function $u(x) \in C^2(D)$, $D \subset \mathbb{R}_x^n$, is $m - cv$ in D , if and only if a function $u^c(z) = u^c(x + iy) = u(x)$, that does not depend on variables $y \in \mathbb{R}_y^n$, is sh_m in the domain Ω .*

Theorem 2.1 allows us to define a m -convex function in the class of semi-continuous functions.

Definition 2.1. *An upper semi-continuous function $u(x)$ in a domain $D \subset \mathbb{R}_x^n$ is called m -convex in D , if the function $u^c(z)$ is strongly m -subharmonic, i.e. $u^c(z) \in sh_m(\Omega)$.*

This definition is convenient in the study of m -convex functions, by transferring well-known properties of sh_m -functions to the class $m - cv$. We present some non-trivial ones:

- (Approximation). We take a standard kernel $K_\delta(x) = \frac{1}{\delta^n} K\left(\frac{x}{\delta}\right)$, $\delta > 0$, where
- $K(x) = K(|x|)$;
- $K(x) \in C^\infty(\mathbb{R}^n)$;
- $\text{supp}K = B(0, 1)$;
- $\int_{\mathbb{R}^n} K(x)dx = \int_{B(0,1)} K(x)dx = 1$.

Then the convolution

$$u_\delta(y) = \int_D u(x)K_\delta(x-y)dx = \int_{\mathbb{R}^n} u(x+y)K_\delta(x)dx \quad (5)$$

has the property, that $u_\delta(x) \in m - cv(D_\delta)$, where $D_\delta = \{x \in D : \text{dist}(x, \partial D) > \delta\}$, $u_\delta(x)$ decreases as $\delta \downarrow 0$ and converges point wise to the function $u(x) \in m - cv(D)$.

- the limit of a uniformly convergent or decreasing sequence of $m - cv$ functions is $m - cv$;
- the maximum of a finite number of $m - cv$ functions is an $m - cv$ function;
- for an arbitrary locally uniformly bounded family, $\{u_\theta\} \subset m - cv$ the regularization $u^*(x)$ of the supremum $u(x) = \left\{ \sup_\theta u_\theta(x) \right\}$ will also be an $m - cv$ function. Since $m - cv \subset sh$, then the set $\{u(x) < u^*(x)\}$ is polar in $\mathbb{C}^n \approx \mathbb{R}^{2n}$. In particular, it has Lebesgue measure zero.

Similarly, for a locally uniformly bounded sequence, $\{u_j\} \subset m - cv$ the regularization $u^*(x)$ of the limit $u(x) = \overline{\lim}_{j \rightarrow \infty} u_j(x)$ will also be an $m - cv$ function, and the set $\{u(x) < u^*(x)\}$ is polar;

- if $u(x) \in m - cv(D)$, then for any hyperplane $\Pi \subset \mathbb{R}^n$ the restriction $u|_\Pi \in m - cv(D \cap \Pi)$.

From this property it easily follows that if $u(x) \in m - cv(D)$, then for any plane $\Pi \subset \mathbb{R}^n$, $\dim \Pi = m$, the restriction $u|_\Pi \in sh(D \cap \Pi)$.

For $m = 1$ it is not difficult to prove that a convex function $u(x) \in 1 - cv(D)$ belongs to Lipschitz class, i.e. $u(x) \in Lip(D)$. In the work [20] N.Trudinger and X.Wang proved a generalization of this remarkable result, that any m -convex function $u(x) \in m - cv$ at $m < \frac{n}{2} + 1$ is Hölder with exponent $\alpha = 2 - \frac{n}{n - m + 1}$, $u(x) \in Lip_\alpha(D)$.

Example 2.1. (fundamental $m - cv$ function).

$$\chi_m(x, 0) = \begin{cases} |x|^{2 - \frac{n}{n-m+1}} & \text{if } m < \frac{n}{2} + 1 \\ \ln|x| & \text{if } m = \frac{n}{2} + 1 \\ -|x|^{2 - \frac{n}{n-m+1}} & \text{if } m > \frac{n}{2} + 1 \end{cases} \quad (6)$$

Thus, for $m < \frac{n}{2} + 1$ the fundamental function is bounded and Lipschitz, and for $m \geq \frac{n}{2} + 1$ it is equal to $-\infty$ at the point $x = 0$. Note that for $m = n$, i.e. for the subharmonic case it coincides with the fundamental solution $-\frac{1}{|x|^{n-2}}$ of the Laplace operator Δ .

3. $m - cv$ polar sets and $m - cv$ measure

Definition 3.1. By analogy with polar sets in classical potential theory, a set $E \subset D \subset \mathbb{R}^n$ is called $m - cv$ polar in D , if there exists a function $u(x) \in m - cv(D)$, $u(x) \not\equiv -\infty$, such that $u|_E = -\infty$.

From the embedding $m - cv(D) \subset sh(D)$ it follows that every $m - cv$ polar set is polar in the sense of classical potential theory. In particular, for a $m - cv$ polar set E it is true $\mathcal{H}_{2n-2+\varepsilon}(E) = 0$, $\forall \varepsilon > 0$: and, therefore, the Lebesgue measure of a $m - cv$ polar set E is equal to zero.

$m - cv$ polar sets have another unexpected phenomenon, that when $m < \frac{n}{2} + 1$ they are empty, i.e. if the set $E \subset D$ is $m - cv$ polar, $m < \frac{n}{2} + 1$, then $E = \emptyset$. This follows from the fact that for $m < \frac{n}{2} + 1$ any $m - cv$ function is Hölder continuous (see section 2). However, for $m \geq \frac{n}{2} + 1$ there are non-empty $m - cv$ polar sets. Therefore, the properties of $m - cv$ polar sets proved below are meaningful only for the cases $m \geq \frac{n}{2} + 1$.

Theorem 3.1. *The countable union of $m - cv$ polar sets is $m - cv$ polar, i.e. if $E_j \subset D$ is $m - cv$ polar, then $E = \bigcup_{j=1}^{\infty} E_j$ is also $m - cv$ polar.*

The proof is identical to a similar proof for polar sets and we omit it.

Potential theory is usually constructed in regular domains with respect to one or another class of functions.

Definition 3.2. *A domain $D \subset \mathbb{R}^n$ is called $m - cv$ regular if there exists $\rho(x) \in m - cv(D)$ such that $\rho(x) < 0$, $\lim_{x \rightarrow \partial D} \rho(x) = 0$. It is called strictly $m - cv$ regular if there exists a twice smooth strictly $m - cv$ function in some neighborhood of the closure $D^+ \supset \bar{D}$ such that $D = \{\rho(x) < 0\}$. Strictly m -convexity of the function $\rho(x)$ in D^+ means that for some $\delta > 0$ the difference $\rho(x) - \delta \|x\|^2$ is an $m - cv$ function in D^+ .*

In the theory of m -convex functions, $m - cv$ measure plays the same role as the harmonic measure in classical potential theory. To exclude trivial cases, $m - cv$ regular or even strictly $m - cv$ regular domains are usually taken as a fixed domain $D \subset \mathbb{R}^n$.

Let $E \subset D$ be some subset of a strictly $m - cv$ regular domain $D \subset \mathbb{R}^n$.

Definition 3.3. *Consider the class of functions*

$$\mathcal{U}(E, D) = \{u(x) \in m - cv(D) : u|_D \leq 0, u|_E \leq -1\} \quad (7)$$

and put $\omega(x, E, D) = \sup \{u(x) : u \in \mathcal{U}(E, D)\}$. Then the regularization $\omega^*(x, E, D)$ is called $m - cv$ measure of the set E with respect to the domain D .

From the property of the upper envelope of $m - cv$ functions it follows that $\omega^*(x, E, D) \in m - cv(D)$. By Choquet's lemma (see [12, 17]) there is a countable subfamily $\mathcal{U}' \subset \mathcal{U}(E, D)$ such that $\{\sup \{u(x) : u \in \mathcal{U}'(E, D)\}^* \equiv \omega^*(x, E, D)$. It follows that an $m - cv$ measure $\omega^*(x, E, D)$ can be represented as a limit of a monotonically increasing sequence $\{u_j(x)\} \subset \mathcal{U}(E, D) : \left[\lim_{j \rightarrow \infty} u_j(x) \right]^* \equiv \omega^*(x, E, D)$.

In the particular case when $E \subset\subset D$ is compact, the functions $u_j(x) \in \mathcal{U}(E, D)$ can be chosen to be continuous in D , which can be easily verified by continuing $u_j(x) \in \mathcal{U}(E, D)$ into some fixed neighborhood $D^+ \supset \bar{D}$ and then approximating them with smooth functions $u_{jk} = u_j \circ K_k(x - y) \in m - cv(D^+) \cap C^\infty(D^+)$, $j, k = 1, 2, \dots$, we can find a sequence $u_{jk_j} \in m - cv(D^+) \cap C^\infty(D^+)$ monotonically increasing and $\{u_{jk_j}(x)\} \subset \mathcal{U}(E, D) : \left[\lim_{j \rightarrow \infty} u_{jk_j}(x) \right]^* \equiv \omega^*(x, E, D)$.

Properties of $m - cv$ measures:

1) (*monotonicity*) if $E_1 \subset E_2$, then $\omega^*(x, E_1, D) \geq \omega^*(x, E_2, D)$; if $E \subset D_1 \subset D_2$, then $\omega^*(x, E, D_1) \geq \omega^*(x, E, D_2)$.

2) $\omega^*(x, U, D) \in \mathcal{U}(U, D)$ for open sets $U \subset D$ and, therefore $\omega^*(x, U, D) \equiv \omega(x, U, D)$;

This property follows from the fact that for concentric balls $B(x^0, r) \subset B(x^0, R) \subset\subset U$, $0 < r < R$, an $m - cv$ measure

$$\omega^*(x, B(x^0, r), B(x^0, R)) = \max \left\{ -1, \frac{\chi_m(x, x^0) - \chi_m(R, x^0)}{\chi_m(R, x^0) - \chi_m(r, x^0)} \right\}$$

and therefore in both cases $m < \frac{n}{2} + 1$ or $m \geq \frac{n}{2} + 1$ we have $\omega^*(x^0, U, D) = -1$. Here $\chi_m(x, x^0)$ is a fundamental $m - cv$ function (see (6)).

3) If $U \subset D$ is an open set, $U = \bigcup_{j=1}^{\infty} K_j$, where $K_j \subset \overset{\circ}{K}_{j+1}$, then $\omega^*(x, K_j, D) \downarrow \omega(x, U, D)$ (easily follows from property 2).

4) If $E \subset D$ an arbitrary set, then there is a decreasing sequence of open sets $U_j \supset E$, $U_j \supset U_{j+1}$ ($j = 1, 2, \dots$), such that $\omega^*(x, E, D) = \left[\lim_{j \rightarrow \infty} \omega(x, U_j, D) \right]^*$.

In fact, if $\{u_j(x)\} \subset \mathcal{U}(E, D)$ is monotonically increasing such that $\left[\lim_{j \rightarrow \infty} u_j(x) \right]^* \equiv \omega^*(x, E, D)$, then an open set $U_j = \left\{ u_j < -1 + \frac{1}{j} \right\}$ has the property as $U_j \supset E$, $U_j \supset U_{j+1}$ ($j = 1, 2, \dots$) and

$$\omega^*(x, E, D) \leq \omega(x, U_j, D) \leq u_j(x) + \frac{1}{j}.$$

Hence $\omega^*(x, E, D) = \left[\lim_{j \rightarrow \infty} \omega(x, U_j, D) \right]^*$.

5) a $m - cv$ measure $\omega^*(x, E, D)$ is either nowhere equal to zero or identically equal to zero. $\omega^*(x, E, D) \equiv 0$ if and only if E is $m - cv$ polar in D .

Remark 3.1. Property 5 is meaningful only if $m \geq \frac{n}{2} + 1$. At $m < \frac{n}{2} + 1$ non-empty $m - cv$ polar set does not exist, so the trivial $m - cv$ measure $\omega^*(x, E, D) \equiv 0$ does not exist.

Example 3.1. Consider $m = 1$, a ball $B = B(0, 1)$ and a set in it $E = \{0\}$, consisting of one point. Consider a $1 - cv$ measure $\nu = \omega^*(x, E, B)$, $x \in \mathbb{R}^n$, $\nu \in \mathbb{R}$ as a function in $\mathbb{R}_{(x, \nu)}^{n+1}$. Then it is easy to see that the convex function $\nu = \omega^*(x, E, B)$, $x \in \mathbb{R}^n$, $\nu \in \mathbb{R}$ will be a cone, with a vertex at point $(0, -1)$ and a base at $\{x \in \partial B, \nu = 0\}$. Thus, $1 - cv$ measure $\omega^*(x, E, B) \not\equiv 0$.

Definition 3.4. A point $x^0 \in K$ is called $m - cv$ regular of a compact set K (relatively to D), if $\omega^*(x^0, K, D) = -1$. A compact set $K \subset D$ is called $m - cv$ regular compact if each of its points $x^0 \in K$ is $m - cv$ regular.

Since $m - cv(D) \subset sh(D)$, then $m - cv$ measure of a pair (K, D) is always no greater than the harmonic measure of this pair. Consequently, regular compacts in the sense of classical potential theory are always $m - cv$ regular. Therefore, the closure of the domain $G \subset\subset D$, with a twice smooth boundary ∂G is a $m - cv$ regular compact. It follows that for any compact $K \subset U \subset D$, where U is an open set, there is always a $m - cv$ regular compact $F : K \subset F \subset\subset U \subset D$. All this shows that the family $m - cv$ regular compact is quite rich.

6) If the set E lies compactly in a strictly $m - cv$ regular domain $D = \{\rho(x) < 0\}$, $E \subset\subset D$, then $m - cv$ measure $\omega^*(x, E, D)$ continues as $m - cv$ function to a neighborhood $\rho(x) < \delta$, $\delta > 0$, of the closure \bar{D} .

Actually, since $E \subset\subset D$ is a compact set, then there is a constant $C > 0$ such that $C\rho(x) < -1$, $\forall x \in E$. It follows that $C\rho(x) \in \mathcal{U}(E, D)$ and $C\rho(x) \leq \omega^*(x, E, D)$. Therefore, the function

$$w(x) = \begin{cases} \max\{C\rho(x), \omega^*(x, E, D)\} & \text{if } x \in D \\ C\rho(x) & \text{if } x \notin D \end{cases}$$

is $m - cv$ in some neighborhood $D^+ \supset \bar{D}$, $w(x) = \omega^*(x, E, D)$, $\forall x \in D$.

The following theorem plays an important role in the introducing condenser capacity and further studying the potential properties of m -convex functions.

Theorem 3.2. *If a compact set $E \subset D$ is $m - cv$ regular, then a $m - cv$ measure $\omega^*(x, E, D) \equiv \omega(x, E, D)$ and is a continuous function in D , $\omega^*(x, E, D) \in C(D)$.*

Proof. According to property 6) a $m - cv$ measure $\omega^*(x, E, D)$ continues to the neighborhood $\rho(x) < \delta$, $\delta > 0$, of the closure \bar{D} and approximating $\omega^*(x, E, D)$ in some neighborhood $D^+ \supset \bar{D}$ we find $u_j(x) \in C^\infty(D^+) \cap m - cv(D^+) : u_j(x) \downarrow \omega^*(x, E, D)$.

We fix a number $\varepsilon > 0$ and two neighborhoods $U = \{\omega^*(x, E, D) < -1 + \varepsilon\} \supset E$, $\check{D} = \{\omega^*(x, E, D) < \varepsilon\} \supset \bar{D}$. Applying Hartogs' lemma twice to the sequence $u_j(x) \downarrow \omega^*(x, E, D)$ and $U \supset E$, $\check{D} \supset \bar{D}$ find the number $j_0 \in \mathbb{N} : u_j(x) < -1 + 2\varepsilon$, $\forall x \in K$, $u_j(x) < 2\varepsilon$, $\forall x \in \bar{D}$, $j \geq j_0$. Then $u_j(x) - 2\varepsilon < -1$, $\forall x \in E$, $u_j(x) - 2\varepsilon < 0$, $\forall x \in D$, $j \geq j_0$, i.e. $u_j(x) - 2\varepsilon \in \mathcal{U}(E, D)$. From here, $\omega^*(x, E, D) - 2\varepsilon \leq u_j(x) - 2\varepsilon \leq \omega^*(x, E, D)$. This means that the sequence of smooth functions $u_j(x) \downarrow \omega^*(x, E, D)$ converges uniformly and $\omega^*(x, E, D) \in C(D)$. \square

4. Capacity value of a pair (E, D)

We fix a set $E \subset D$, considering, as above, the domain $D \subset \mathbb{R}^n$ to be strongly m -convex. Let $\omega^*(x, E, D)$ be a $m - cv$ measure of $E \subset D$. Then the integral

$$\mathcal{P}_{m-cv}(E, D) = - \int_D \omega^*(x, E, D) dV$$

is called $m - cv$ capacity of the set E with relation to D .

$m - cv$ capacity expresses the capacity value of a pair (E, D) . It has the following obvious properties: $\mathcal{P}_{m-cv}(E, D) \geq 0$ and $\mathcal{P}_{m-cv}(E, D) = 0$ if and only if E is a polar set in D .

Theorem 4.1. *The value $\mathcal{P}_{m-cv}(E, D)$ is an increasing and countably subadditive function of the set: $\mathcal{P}_{m-cv}(E_1, D) \leq \mathcal{P}_{m-cv}(E_2, D)$ for $E_1 \subset E_2$ and*

$$\mathcal{P}_{m-cv} \left(\bigcup_{j=1}^{\infty} E_j, D \right) \leq \sum_{j=1}^{\infty} \mathcal{P}_{m-cv}(E_j, D). \quad (8)$$

Moreover, $\mathcal{P}_{m-cv}(E, D)$ is continuous on the right, i.e. for any set $E \subset D$ and for any $\varepsilon > 0$ there is an open set $U \supset E$ such that $\mathcal{P}_{m-cv}(U, D) - \mathcal{P}_{m-cv}(E, D) < \varepsilon$.

Proof. Monotonicity of $\mathcal{P}_{m-cv}(E, D)$ obviously follows from the monotonicity of the $m - cv$ measure. Proof of (8) follows from a similar inequality $-\omega \left(x, \bigcup_{j=1}^{\infty} E_j, D \right) \leq - \sum_{j=1}^{\infty} \omega(x, E_j, D)$

for $m - cv$ measures: for any sets $E_j \subset D$ and $u_j(x) \in \mathcal{U}(E_j, D)$ the sum $\sum_{j=1}^{\infty} u_j(x)$ is $m - cv$ function in the broad sense (i.e., it can also equal $-\infty$). Besides $\sum_{j=1}^{\infty} u_j(x) \in \mathcal{U}\left(\bigcup_{j=1}^{\infty} E_j, D\right)$ and therefore, $\sum_{j=1}^{\infty} u_j(x) \leq \omega\left(x, \bigcup_{j=1}^{\infty} E_j, D\right)$. On the other side,

$$\begin{aligned} & \sup \left\{ \sum_{j=1}^{\infty} u_j(x) : u_j(x) \in \mathcal{U}(E_j, D) \right\} = \\ & = \sum_{j=1}^{\infty} \sup \{u_j(x) : u_j(x) \in \mathcal{U}(E_j, D)\} = \sum_{j=1}^{\infty} \omega(x, E_j, D), \end{aligned}$$

i.e.

$$\sum_{j=1}^{\infty} \omega(x, E_j, D) \leq \omega\left(x, \bigcup_{j=1}^{\infty} E_j, D\right).$$

Integrating this inequality and using Levy's theorem, we get

$$- \int \omega\left(x, \bigcup_{j=1}^{\infty} E_j, D\right) dV \leq - \sum_{j=1}^{\infty} \int \omega(x, E_j, D) dV,$$

so that (8) is true.

It remains to show the right continuity of the set function $\mathcal{P}_{m-cv}(E, D)$. We fix a set $E \subset D$ and according to the $m - cv$ measure property, construct a sequence of open sets $U_j \supset E$, $U_j \supset U_{j+1}$: $\left[\lim_{j \rightarrow \infty} \omega(x, U_j, D)\right]^* \equiv \omega^*(x, E, D)$. So, as $\omega(x, U_j, D)$ increasing, then again by Levy's theorem

$$\begin{aligned} \lim_{j \rightarrow \infty} \mathcal{P}_{m-cv}(U_j, D) &= - \lim_{j \rightarrow \infty} \int \omega(x, U_j, D) dV = - \int \lim_{j \rightarrow \infty} \omega(x, U_j, D) = \\ &= - \int \left[\lim_{j \rightarrow \infty} \omega(x, U_j, D)\right]^* dV = \mathcal{P}_{m-cv}(E, D). \end{aligned}$$

Hence, for any $\varepsilon > 0$, there is a number j_0 such that for $j \geq j_0$ the inequality $\mathcal{P}_{m-cv}(U_j, D) - \mathcal{P}_{m-cv}(E, D) < \varepsilon$ is true. The theorem is proved. \square

Corollary 4.1. For any decreasing sequence of compacts $K_1 \supset K_2 \supset \dots$ the following right continuity holds

$$\mathcal{P}_{m-cv}\left(\bigcap_{j=1}^{\infty} K_j, D\right) = \lim_{j \rightarrow \infty} \mathcal{P}_{m-cv}(K_j, D).$$

For arbitrary given sets $G_1 \subset G_2 \subset \dots$, $G = \bigcup_{j=1}^{\infty} G_j$, the left continuity holds

$$\mathcal{P}_{m-cv}\left(\bigcup_{j=1}^{\infty} G_j, D\right) = \lim_{j \rightarrow \infty} \mathcal{P}_{m-cv}(G_j, D).$$

From Corollary 4.1 it follows that the introduced capacity satisfies the Choquet axioms on the measurability of a capacity quantity $\mathcal{P}_{m-cv}(E, D)$ (see [12, 17]).

Theorem 4.2 (Choquet). *If a set function $C(E)$ satisfies the following Choquet conditions*

- a) $0 \leq C(E) < \infty, \forall E \subset \subset D$;
- b) if $E_1 \subset E_2$, then $C(E_1) \leq C(E_2)$;
- c) for any set $E \subset D$ and number $\varepsilon > 0$ there exists an open set $U \supset E$ such that $C(U) - C(E) < \varepsilon$;
- d) for any increasing sequence $E_j \subset E_{j+1}$ holds

$$C\left(\bigcup_{j=1}^{\infty} E_j\right) = \lim_{j \rightarrow \infty} C(E_j),$$

then any Borel set $E \in \mathcal{B}$ is measurable, i.e. if $E \in \mathcal{B}$, then

$$C(E) = C_*(E) = \sup \{C(K) : K \subset E - \text{compact}\}.$$

Thus, we have obtained that the capacity value $\mathcal{P}_{mcv}(E, D)$ we introduced above is a measurable function of the sets $E \subset D$, $\mathcal{P}_{mcv}(E, D) = \sup \{\mathcal{P}_{mcv}(K, D) : K \subset E - \text{compact}\}$.

5. Hessians H^k and condenser capacity

Although the $\mathcal{P}_{mcv}(E, D)$ -capacity of sets is simpler to define, measurable and has many properties of capacities, the concept of a condenser capacity is more natural, which is defined using the Hessians H^k as total mass of the measure.

Let us first recall the definition of Hessians H^k for a bounded semi-continuous function $u(x) \in m - cv(D) \cap L^\infty(D)$ as positive Borel measures (see [16]). We embed \mathbb{R}_x^n in \mathbb{C}_z^n , $\mathbb{R}_x^n \subset \mathbb{C}_z^n = \mathbb{R}_x^n + i\mathbb{R}_y^n$ ($z = x + iy$), as a real n -dimensional subspace of the complex space \mathbb{C}_z^n . Then an upper semi-continuous function $u(x)$ in the domain $D \subset \mathbb{R}_x^n$ will be m -convex in D , if the function $u^c(z) = u^c(x + iy) = u(x)$ which does not depend on the variables $y \in \mathbb{R}_y^n$, is strongly m -subharmonic, $u^c(z) \in sh_m(D \times i\mathbb{R}_y^n)$ in the domain $D \times i\mathbb{R}_y^n$ (Theorem 2.1).

If an m -convex function $u(x) \in m - cv(D)$ is locally bounded in the domain $D \subset \mathbb{R}_x^n$, then $u^c(z)$ will also be a locally bounded, strongly m -subharmonic function in the domain $D \times i\mathbb{R}_y^n \subset \mathbb{C}_z^n$. As it is known, the operators

$$(dd^c u^c)^k \wedge \beta^{n-k}, \quad k = 1, 2, \dots, n - m + 1$$

are defined for any bounded function $u \in sh_m(D \times i\mathbb{R}_y^n)$ as Borel measures in the domain $D \times i\mathbb{R}_y^n \subset \mathbb{C}_z^n$, $\mu_k = (dd^c u^c)^k \wedge \beta^{n-k}$, $k = 1, 2, \dots, n - m + 1$.

Since for a twice smooth function $(dd^c u^c)^k \wedge \beta^{n-k} = k!(n-k)!H^k(u^c)\beta^n$, then for a bounded, strongly m -subharmonic function $u^c(z)$ in the domain $D \times i\mathbb{R}_y^n \subset \mathbb{C}_z^n$, it is natural to determine its Hessians, equating to the measure

$$H^k(u^c) = \frac{\mu_k}{k!(n-k)!} = \frac{1}{k!(n-k)!} (dd^c u^c)^k \wedge \beta^{n-k}. \quad (9)$$

Since $u^c(z) \in sh_m(D \times i\mathbb{R}_y^n)$ does not depend on $y \in \mathbb{R}_y^n$, then for any Borel sets $E_x \subset D$, $E_y \subset \mathbb{R}_y^n$ the measures $\frac{1}{mes E_y} \mu_k(E_x \times E_y)$ do not depend on the set $E_y \subset \mathbb{R}_y^n$, i.e. $\frac{1}{mes E_y} \mu_k(E_x \times E_y) = \nu_k(E_x)$. Borel measures $\nu_k : \nu_k(E_x) = \frac{1}{mes E_y} \mu_k(E_x \times E_y)$, $k = 1, 2, \dots, n - m + 1$, we call Hessians H^k , $k = 1, 2, \dots, n - m + 1$ for bounded, m -convex function

$u(x) \in m - cv(D)$ in the domain $D \subset \mathbb{R}_x^n$. For a twice smooth function, $u(x) \in m - cv(D) \cap C^2(D)$ the Hessians are ordinary functions; however, for a non-twice smooth but bounded semi-continuous function, $u(x) \in m - cv(D) \cap L^\infty(D)$ the Hessians H^k , $k = 1, 2, \dots, n - m + 1$, are positive Borel measures.

Now we can define the concept of condenser capacity

Definition 5.1. Let K be a compact in the domain $D \subset \mathbb{R}^n$. Then the value

$$\begin{aligned} C_m(K) &= C_m(K, D) = \\ &= \inf \left\{ H_u^{n-m+1}(D) : u \in m - cv(D) \cap C(D), u|_K \leq -1, \liminf_{x \rightarrow \partial D} u(x) \geq 0 \right\} \end{aligned} \quad (10)$$

is called the condenser capacity (m -capacity of condenser) of (K, D) . For easiness of writing below, we omit the index "m" in the notation $C_m(K)$.

Let us prove the following properties of capacity $C(K) = C_m(K) = C_m(K, D)$

1) The capacity is monotonic, i.e. $C(E) \geq C(K) \forall E \supset K$ (obviously).

2) For any $m - cv$ regular compact $K \subset D$ holds $C(K) = H_{\omega^*}^{n-m+1}(K)$.

Actually, since compact $K \subset D$ is $m - cv$ regular, then $\omega^*(x, K, D) \equiv \omega(x, K, D) \in C(D)$ and $\omega^*(x, K, D) = -1 \forall x \in K$. Consequently,

$$C(K) = \inf \left\{ H_u^{n-m+1}(D) : u \in m - cv(D) \cap C(D), u|_K \leq -1, \liminf_{x \rightarrow \partial D} u(x) \geq 0 \right\} \leq H_{\omega^*}^{n-m+1}(K).$$

Conversely, for any fixed ε , $0 < \varepsilon < 1$ and for any $u \in m - cv(D) \cap C(D)$, $u|_K \leq -1$, $\liminf_{x \rightarrow \partial D} u(x) \geq 0$, an open set $F = \left\{ x \in D : u(x) + \frac{\varepsilon}{2} < (1 - \varepsilon)\omega^*(x, K, D) \right\} \subset\subset D$. Therefore, according to the comparison principle,

$$H_u^{n-m+1}(F) \geq (1 - \varepsilon)^{n-m+1} H_{\omega^*}^{n-m+1}(F).$$

In addition, $K \subset F$ and $H_{\omega^*}^{n-m+1}(D \setminus K) = 0$ in $D \setminus K$. So that

$$\begin{aligned} (1 - \varepsilon)^{n-m+1} H_{\omega^*}^{n-m+1}(D) &= (1 - \varepsilon)^{n-m+1} H_{\omega^*}^{n-m+1}(K) = (1 - \varepsilon)^{n-m+1} H_{\omega^*}^{n-m+1}(F) \leq \\ &\leq H_u^{n-m+1}(F) \leq H_u^{n-m+1}(D). \end{aligned}$$

Due to the arbitrariness ε , from here we get

$$H_{\omega^*}^{n-m+1}(D) \leq H_u^{n-m+1}(D),$$

i.e. inf on the right side of (10) reaches at $m - cv$ measure $\omega^*(x, K, D)$.

3) For any compact $K \subset D$

$$C(K) = \inf \{ C(E) : E \supset K, E \text{ } m - cv \text{ regular} \}. \quad (11)$$

In fact, from the monotonicity of capacity (property 1), the left side of (11) does not exceed the right side, i.e.

$$C(K) \leq \inf \{ C(E) : E \supset K, E \text{ } m - cv \text{ regular} \}. \quad (12)$$

Now, for any ε , $0 < \varepsilon < 1$ there exists $u \in m - cv(D) \cap C(D)$ such that $u|_K \leq -1$, $\liminf_{x \rightarrow \partial D} u(x) \geq 0$ and

$$H_u^{n-m+1}(D) - C(K) < \varepsilon. \quad (13)$$

Let $U = \{x \in D : u(x) < -1 + \varepsilon\}$ a neighborhood of a compact K and E is a $m - cv$ regular compact set, such that $K \subset E \subset\subset U$. Consider the open set

$$F = \left\{ x \in D : u(x) + \frac{\varepsilon}{2} < (1 - \varepsilon) \omega^*(x, E, D) \right\} \subset\subset D.$$

Since E is $m - cv$ regular compact, then $E \subset F \subset\subset D$. Therefore, according to the comparison principle and (13), we obtain

$$\begin{aligned} C(E) &= H_{\omega^*}^{n-m+1}(E) = H_{\omega^*}^{n-m+1}(F) \leq \frac{1}{(1-\varepsilon)^{n-m+1}} H_u^{n-m+1}(F) \leq \\ &\leq \frac{1}{(1-\varepsilon)^{n-m+1}} H_u^{n-m+1}(D) \leq \frac{1}{(1-\varepsilon)^{n-m+1}} (C(K) + \varepsilon). \end{aligned}$$

Hence, the right side of (11) does not exceed $\frac{1}{(1-\varepsilon)^{n-m+1}} (C(K) + \varepsilon)$. Since ε it is arbitrary, it does not exceed $C(K)$, i.e.

$$C(K) \geq \inf \{C(E) : E \supset K, E \text{ } m - cv \text{ regular}\}.$$

This inequality, together with (12), gives us the required statement.

4) If a compact $K \subset D$ is $m - cv$ regular, then

$$C(K) = \sup \{H_u^{n-m+1}(K) : u \in m - cv(D) \cap C(D), -1 \leq u < 0\}. \quad (14)$$

Proof. Since $C(K) = H_{\omega}^{n-m+1}(K)$, then

$$C(K) \leq \sup \{H_u^{n-m+1}(K) : u \in m - cv(D) \cap C(D), -1 \leq u < 0\}. \quad (15)$$

On the other hand, for any function $u \in m - cv(D) \cap C(D)$, we set $v(x) = \max \{(1 + \varepsilon)\omega(x, K, D), u(x)\}$, $0 < \varepsilon < 1$. Then $v \in m - cv(D) \cap C(D)$, $-1 \leq v < 0$ and $\lim_{x \rightarrow \partial D} v(x) = 0$. Therefore, according to the comparison principle

$$(1 + \varepsilon)^{n-m+1} H_{\omega}^{n-m+1}(D) \geq H_v^{n-m+1}(D) \geq H_v^{n-m+1}(K).$$

Since $H_{\omega}^{n-m+1}(D \setminus K) = 0$, then

$$H_v^{n-m+1}(K) = H_u^{n-m+1}(K).$$

From here,

$$(1 + \varepsilon)^{n-m+1} H_{\omega}^{n-m+1}(D) \geq H_v^{n-m+1}(K) \geq H_u^{n-m+1}(K)$$

and tending $\varepsilon \rightarrow 0$ we will receive

$$C(K) = H_{\omega}^{n-m+1}(K) \geq H_u^{n-m+1}(K).$$

Due to the arbitrariness of the function u

$$C(K) \geq \sup \{H_u^{n-m+1}(K) : u \in m - cv(D) \cap C(D), -1 \leq u < 0\},$$

which together with (15) gives us (14).

We define the external capacity in a standard way by assuming

$$C^*(E) = \inf \{C(U) : U \supset E - \text{open}\},$$

where the capacity of an open set is

$$C(U) = \sup \{C(K) : K \subset U\} = \sup \{C(K) : K \subset U, K \text{ } m - cv \text{ regular}\}.$$

Let us note the following properties of the external capacity

5) For any compact, $K \subset D$ its external capacity $C^*(K) = C(K)$.

This follows from property 3).

The following property of capacity is very important in practice.

Theorem 5.1. *If a set $U \subset D$ is open, then*

$$\begin{aligned} C(U) &= \sup \{H_u^{n-m+1}(U) : u \in m - cv(D) \cap C(D), -1 \leq u < 0\} = \\ &= \sup \{H_u^{n-m+1}(U) : u \in m - cv(D) \cap C^\infty(D), -1 \leq u < 0\}. \end{aligned} \quad (16)$$

Proof. For any $m - cv$ regular compact set $K \subset U$ we have

$$C(K) = \sup \{H_u^{n-m+1}(K) : u \in m - cv(D) \cap C(D), -1 \leq u < 0\}.$$

Therefore, $C(U) \geq C(K) \geq H_u^{n-m+1}(K)$ for any fixed $u \in m - cv(D) \cap C(D)$, $-1 \leq u < 0$. Since $K \subset U$ is an arbitrary $m - cv$ regular compact, then $C(U) \geq H_u^{n-m+1}(U)$. From here,

$$\begin{aligned} C(U) &\geq \sup \{H_u^{n-m+1}(U) : u \in m - cv(D) \cap C(D), -1 \leq u < 0\} \geq \\ &\geq \sup \{H_u^{n-m+1}(U) : u \in m - cv(D) \cap C^\infty(D), -1 \leq u < 0\}. \end{aligned} \quad (17)$$

On the other hand, we fix an arbitrary $m - cv$ regular compact set $K \subset U$. According to property 7) of the $m - cv$ measure, the $\mathcal{P}_{m-cv}(E, D)$ -measure $\omega(x, K, D)$ $m - cv$ continues into a certain neighborhood $G \supset \bar{D}$. It follows, that $\omega(x, K, D)$ can be approximated in some neighborhood of \bar{D} by infinitely smooth $m - cv$ convex functions $u_j(x) \downarrow \omega(x, K, D)$. Since the compact $K \subset U$ is $m - cv$ regular, then $\omega(x, K, D)$ is continuous in D . From this the convergence $u_j(x) \downarrow \omega(x, K, D)$ will be uniform and the sequence of Borel measures $H_{u_j}^{n-m+1}$ weakly converges to the measure H_ω^{n-m+1} , $H_{u_j}^{n-m+1} \mapsto H_\omega^{n-m+1}$.

From the properties of convergent Borel measures we have

$$C(K) = H_\omega^{n-m+1}(K) = H_\omega^{n-m+1}(U) \leq \liminf_{j \rightarrow \infty} H_{u_j}^{n-m+1}(U). \quad (18)$$

Let's us now fix a $\varepsilon > 0$ and put it down $v_j = \frac{u_j - \varepsilon}{1 + \varepsilon}$. Then $-1 \leq v_j < 0$, for large $j \geq j_0$ and therefore,

$$\begin{aligned} H_{u_j}^{n-m+1}(U) &= (1 + \varepsilon)^{n-m+1} H_{v_j}^{n-m+1}(U) \leq \\ &\leq (1 + \varepsilon)^{n-m+1} \sup \{H_w^{n-m+1}(U) : w \in m - cv(D) \cap C^\infty(D), -1 \leq w < 0\}. \end{aligned}$$

From here and according to (18) we have

$$\begin{aligned} C(K) &\leq \liminf_{j \rightarrow \infty} H_{u_j}^{n-m+1}(U) \leq \\ &\leq (1 + \varepsilon) \sup \{H_w^{n-m+1}(U) : w \in m - cv(D) \cap C^\infty(D), -1 \leq w < 0\}. \end{aligned}$$

Due to the arbitrariness of the number $\varepsilon > 0$

$$C(K) \leq \sup \{H_w^{n-m+1}(U) : w \in m - cv(D) \cap C^\infty(D), -1 \leq w < 0\}$$

and taking here the supremum over all $m - cv$ regular compacts $K \subset U$ we get

$$C(U) \leq \sup \left\{ \int_U (dd^c w)^n : w \in m - cv(D) \cap C^\infty(D), -1 \leq w < 0 \right\},$$

which together with (17) proves the theorem completely. \square

Remark 5.1. If $U \subset\subset D$ and $K \subset U$ is an arbitrary fixed compact, then $m - cv$ measure $\omega^*(x, K, D)$ $m - cv$ continues into a fixed neighborhood $D^+ \supset \bar{D}$ such that the extended function does not exceed 1 in D^+ . According to properties 2) and 4) we have

$$\begin{aligned} C(K) &\leq \sup \{ H_u^{n-m+1}(K) : u \in m - cv(G) \cap C(G), -1 \leq u < 0 \text{ in } D \text{ and } |u| < 1 \text{ in } D^+ \} \leq \\ &\leq \sup \{ H_u^{n-m+1}(U) : u \in m - cv(D) \cap C(D), -1 \leq u < 0 \} = C(K). \end{aligned}$$

So that

$$C(K) = \sup \{ H_u^{n-m+1}(K) : u \in m - cv(G) \cap C(G), -1 \leq u < 0 \text{ in } D \text{ and } |u| < 1 \text{ in } D^+ \}.$$

Using $C(U) = \sup \{ C(K) : K \subset U, K \text{ } m - cv \text{ regular} \}$, for an open set $U \subset\subset D$ we get

$$C(U) = \sup \{ H_u^{n-m+1}(U) : u \in m - cv(D) \cap C(D), -1 \leq u < 0 \text{ in } D \text{ and } |u| < 1 \text{ in } G \}.$$

Moreover, approximating $\omega^*(x, K, D)$ in the neighborhood \bar{D} by infinitely smooth functions, just as in the proof of Theorem 2.1, we obtain

Corollary 5.1. If $U \subset\subset D$ – an open set lying compactly in D , then

$$C(U) = \sup \{ H_u^{n-m+1}(U) : u \in m - cv(D) \cap C^\infty(D), -1 \leq u < 0 \text{ in } D \text{ and } |u| < 1 \text{ in } G \supset\supset D \}.$$

This relation is useful in practice because the Hessian H_u^{n-m+1} here is an ordinary function, defined in the neighborhood of \bar{D} .

6) The external capacity of condenser $C^*(E)$ is monotonic, i.e. if $E_1 \subset E_2$, then $C^*(E_1) \leq C^*(E_2)$; it is countably subadditive, i.e. $C^*\left(\bigcup_j E_j\right) \leq \sum_j C^*(E_j)$.

In fact, monotonicity C^* follows from monotonicity $C(K)$ in the class of pluriregular compacts. Let us show countably subadditivity: firstly let $E_j \subset D$ are open sets and $E = \bigcup_j E_j$.

According to Theorem 5.1

$$\begin{aligned} C(E) &= \sup \{ H_u^{n-m+1}(E) : u \in m - cv(D) \cap C^\infty(D), -1 \leq u < 0 \} \leq \\ &\leq \sup \left\{ \sum_j H_u^{n-m+1}(E_j) : u \in m - cv(D) \cap C^\infty(D), -1 \leq u < 0 \right\} \leq \\ &\leq \sum_j \sup \{ H_u^{n-m+1}(E_j) : u \in m - cv(D) \cap C^\infty(D), -1 \leq u < 0 \} \leq \sum_j C(E_j). \end{aligned}$$

For arbitrary sets $E_j \subset D$, for a fixed $\varepsilon > 0$ we will construct open sets $U_j \supset E_j$ such that $C(U_j) - C^*(E_j) < \frac{\varepsilon}{2^j}$. Then

$$\sum_j C^*(E_j) \geq \sum_j C(U_j) - \varepsilon \geq C\left(\bigcup_j U_j\right) - \varepsilon \geq C^*(E) - \varepsilon$$

and from here, at $\varepsilon \rightarrow 0$ we obtain the required statement.

7) For any increasing sequence of open sets $U_j \subset U_{j+1}$, $C\left(\bigcup_j U_j\right) = \lim_{j \rightarrow \infty} C(U_j)$.

It obviously follows from the fact that any compact space $K \subset \bigcup_j U_j$ belongs to U_j , starting from some $j \geq j_0$.

We prove that the introduced outer condenser capacity $C^*(E)$ satisfies the Choquet axioms on the measurability (see Theorem 4.2).

Theorem 5.2. *Any Borel set $E \in \mathcal{B}$ is measurable, i.e. if $E \in \mathcal{B}$, then*

$$C^*(E) = C_*(E) = \sup \{C(K) : K \subset E - \text{compact}\}.$$

References

- [1] B.Abdullaev, A.Sadullaev, Potential theory in the class of m -subharmonic functions. Analytic and geometric issues of complex analysis, *Trudy Mat. Inst. Steklova, MAIK Nauka/Interperiodica, Moscow*, **279**(2012), 155–180. DOI: 10.1134/S0081543812080111
- [2] A.D.Aleksandrov, Intrinsic geometry of convex surfaces. OGIZ, Moscow, 1948 (in Russian); German transl., Akademie Verlag, Berlin, 1955.
- [3] A.D.Aleksandrov, Dirichlet's problem for the equation $\det(z_{ij}) = \varphi$, *Vestnic Leningrad University*, **13**(1958), 5–24 (in Russian).
- [4] I.J.Bakelman, Variational problems and elliptic Monge-Ampere equations, *J. Diff. Geo.*, **18**(1983), 669–999.
- [5] I.J.Bakelman, Convex Analysis and Nonlinear Geometric Elliptic Equations, *Springer-Verlag, Berlin*, 1994. DOI: 10.1007/978-3-642-69881-1
- [6] Z.Łocki, Weak solutions to the complex Hessian equation, *Ann.Inst. Fourier, Grenoble*, **5**(2005), 1735–1756. DOI: 10.5802/aif.2137
- [7] M.Brelot, Éléments de la théorie classique du potentiel, Les Cours de Sorbonne. 3e cycle, Centre de Documentation Universitaire, Paris, 1959.
- [8] K.S.Chou, X.J.Wang, Variational theory for Hessian equations, *Comm. Pure Appl. Math.*, **54**(2001), 1029–1064. DOI: 10.1002/CPA.1016
- [9] S.Dinew, S.Kolodziej, A priori estimates for the complex Hessian equation, *Anal. PDE*, **7**(2014), 227–244. DOI: 10.2140/apde.2014.7.227
- [10] S. Dinew, S.Kolodziej, Non standard properties of m -subharmonic functions, *Dolom. Res. Not. Approx.*, **11**(2018), 35–50.
- [11] N.Ivochkina, N.S.Trudinger, X.J.Wang, The Dirichlet problem for degenerate Hessian equations, *Comm. Partial Diff. Equations*, **29**(2004), 219–235. DOI: 10.1081/PDE-120028851
- [12] N.S.Landkof, Foundations of Modern Potential Theory, Springer Berlin Heidelberg, 1972.
- [13] S.Y.Li, On the Dirichlet problems for symmetric function equations of the eigenvalues of the complex Hessian, *Asian J.Math.*, **8**(2004), 87–106. DOI: 10.4310/AJM.2004.v8.n1.a8

- [14] C.H.Lu, A variational approach to complex Hessian equations in \mathbb{C}^n , *Journal of Mathematical Analysis and Applications*, **431**(2015), no. 1, 228–259. DOI: 10.1016/j.jmaa.2015.05.067
- [15] H.Ch.Lu, Solutions to degenerate Hessian equations, *Journal de Mathematique Pures et Appliques*, **100**(2013), no. 6, 785–805. DOI: 10.1016/j.matpur.2013.03.002
- [16] A.Sadullaev, Definition of Hessians for m -convex functions as Borel measures, *Analysis and Applied Mathematics. AAM 2022. Trends in Mathematics, Birkhauser, Cham*, **6**(2024), 13–19. DOI: 10.1007/978-3-031-62668-5_2
- [17] A.Sadullaev, Potential theory, Universitet, Tashkent, 2022 (in Russian).
- [18] R.A.Sharipov, M.B.Ismoilov, m -convex ($m - cv$) functions, *Azerbaijan Journal of Mathematics*, **13**(2023), no. 2, 237-247. DOI: 10.59849/2218-6816.2023.2.237
- [19] N.S.Trudinger, X.J.Wang, Hessian measures I, *Topological Methods in Nonlinear Analysis, Topol. Methods Nonlinear Anal.*, **10**(1997), no. 2, 225–239.
- [20] N.S.Trudinger, X.J.Wang, Hessian measures II, *Anal. Math.*, **150**(1999), 579–604.
- [21] N.S.Trudinger, X.J.Wang, Hessian measures III, *J. Funct. Anal.*, **193**(2002), 1–23.

$m - cv$ мера $\omega^*(x, E, D)$ и емкость конденсатора $C(E, D)$ в классе m -выпуклых функций

Азимбай Садуллаев

Национальный университет Узбекистана
Институт математики им. В. И. Романовского Академии наук Узбекистана
Ташкент, Узбекистан

Расулбек Шарипов

Ургенчский государственный университет
Ургенч, Узбекистан

Муриддин Исмоилов

Национальный университет Узбекистана
Ташкент, Узбекистан

Аннотация. В данной работе изучаются самые начальные понятия теории потенциала: полярные множества и $m - cv$ меры в классе m -выпуклых функций в вещественном пространстве \mathbb{R}^n . Мы также изучаем емкость конденсатора $C(E, D)$ в классе m -выпуклых функций и будем доказывать некоторые ее потенциальные свойства.

Ключевые слова: m -субгармонические функции, выпуклые функции, m -выпуклые функции, $m - cv$ полярное множество, $m - cv$ мера, борелевские меры, гессианы.

EDN: WQGPWG

УДК 515.124

Some Remarks and Corrections of Recent Results from the Framework of S -metric Spaces

Nora Fetouci*

LMPA Laboratory
Department of Mathematics
Jijel University
Jijel, Algeria

Stojan Radenović†

Faculty of Mechanical Engineering
University of Belgrade
Belgrad, Serbia

Received 09.10.2024, received in revised form 23.12.2024, accepted 24.02.2025

Abstract. The content of this paper consists of results on Wardowski's F -contraction within S -metric spaces. Namely, in it we present corrections to some recent results by using only the property F1 of strict increasing of the function F . In our results, we combine β -admissible functions with F -contractions. Finally, we give an example that shows that F -contraction in the framework of S -metric spaces is a true generalization of Banach's contraction principle in the same framework.

Keywords: S -metric space, b -metric space, fixed point, F -contraction, β -admissible.

Citation: N.Fetouci, S.Radenović, Some Remarks and Corrections of Recent Results from the Framework of S -metric Spaces, J. Sib. Fed. Univ. Math. Phys., 2025, 18(3), 402–411.
EDN: WQGPWG.



1. Introduction and preliminaries

After Banach's result in 1922, many researchers in mathematics tried to somehow generalize his famous result. They did this either by breaking the metric space axioms or by generalizing the right-hand side " $\lambda d(x, y)$ " of the Banach's contractive condition $d(fx, fy) \leq \lambda d(x, y)$ of the mapping f from the metric space (X, d) to itself, where the scalar $\lambda \in [0, 1)$. Using the first case, new classes of spaces called generalized metric spaces such as partial metric spaces, metric-like spaces, b -metric spaces, partial b -metric and b -metric like spaces were created. In the last 20-30 years, these kinds of spaces have been studied a lot. According to the second case, many contractive conditions arose within metric spaces, such as Kannan, Chatterjea, Reich, Hardy-Rogers, Boyd-Wong, Meir-Keeler, Ćirić and many others. For more details on the various types of contractions see [3]. In addition to the aforementioned generalizations of the famous Banach result from 1922, in 2012 the Polish mathematician D. Wardowski [26] introduced a new type of contraction called F -contraction. And by using it, he gives a result that in the true sense generalizes Banach's contraction principle from 1922. After that, many works appeared on F -contractions that were applied to almost all the mentioned general metric spaces. Wardowski

*n.fetouci@univ-jijel.dz <https://orcid.org/0000-0002-1474-6554>

†sradenovic@mas.bg.ac.rs <https://orcid.org/0000-0001-8254-6688>

© Siberian Federal University. All rights reserved

introduces a strictly increasing function F defined on $(0, +\infty)$ with values in \mathbb{R} and denotes this property by **F1**. In addition to it, it adds two more properties **F2** (For each sequence $\{c_n\}$ of positive numbers, the following holds: $\lim_{n \rightarrow +\infty} c_n = 0$ if and only if $\lim_{n \rightarrow +\infty} F(c_n) = -\infty$) and **F3** (There exist $k \in (0, 1)$ such that $\lim_{\alpha \rightarrow 0^+} \alpha^k F(\alpha) = 0$). The set of all functions F that map $(0, +\infty)$ to \mathbb{R} and that satisfy **F1**, **F2** and **F3** in the literature is denoted by \mathcal{F} . For these and more details, the reader can see the papers [9, 10, 25, 26] and references therein. Particularly useful is the paper [9] in which all known results are proved using only the property **F1**. In works such as [2, 13, 14, 18] some authors consider Wardowski's approach but within the framework of S -metric spaces. In doing so, they use all three properties of mapping F and the so-called β -admissible mapping T from the given space (X, S) to itself. We will substantially improve these results in our discussion by using only the strictly increasing mapping F . We will also take an β -admissible mapping which is of transitive type (Definition 1.3., 1.4. and Lemma 1.3.). Also, see [19]. In both previous cases, the "distance" between two points was considered as a function with two variables, i.e., we had a mapping from X^2 to $[0, +\infty)$ i.e. metric d , partial metric p , b -metric b etc. Later, some researchers instead of two-variable functions went to three-variable functions, i.e., the mappings from X^3 to $[0, +\infty)$ and thus arrived at the following four classes of spaces: G -metric, G_b -metric spaces, S -metric and S_b -metric, The aim of this paper is to give an overview of the results on the last two classes of space as well as to present some new observations about them. We begin with definitions of basic terms in the class of S -metric spaces.

Definition 1.1 ([20]). *Let X be a non-empty set and denote by S the mapping from X^3 to $[0, +\infty)$ that satisfies the following axioms:*

(S1): $S(x, y, z) = 0$ if and only if $x = y = z$;

(S2): $S(x, y, z) \leq S(x, x, a) + S(y, y, a) + S(z, z, a)$ for all x, y, z, a from X .

Then the pair (X, S) is called an S -metric space and the mapping S is called a S -metric on X .

Some examples of S -metric spaces:

Example 1.1. *Let $\|\cdot\|$ a norm on the vector space V , then $S(x, y, z) = \|y + z - 2x\| + \|y - z\|$ is an S -metric on V .*

Example 1.2. *Let $\|\cdot\|$ a norm on the vector space V , then $S(x, y, z) = \|x - z\| + \|y - z\|$ is an S -metric on vector space V .*

Properties such as convergence of a sequence, Cauchyness of a sequence, complete of the space and continuity of a function, all within S -metric spaces are given by the following definition:

Definition 1.2 ([20]). *Let (X, S) be an S -metric space.*

(1) *A sequence $\{x_n\}$ in X converges to x if and only if $S(x_n, x_n, x) \rightarrow 0$ as $n \rightarrow +\infty$.*

(2) *A sequence $\{x_n\}$ in X is called a Cauchy sequence if $S(x_n, x_n, x_m) \rightarrow 0$ as $n, m \rightarrow +\infty$.*

(3) *The S -metric space (X, S) is said to be complete if every Cauchy sequence is convergent.*

(4) *A mapping $T : X \rightarrow X$ is said to be S -continuous if $\{Tx_n\}$ is S -convergent to Tx , where $\{x_n\}$ is an S -convergent sequence converging to x .*

For still details reader can see the following papers: [1, 2, 4–8, 11–14, 17, 18, 20–23, 27].

Similar to metric and G -metric spaces, open and closed balls are defined and the corresponding topology is based on them. For details, see the papers on S -metric spaces in the reference list. Here, the sequence converges on the S -metric if and only if it converges on that resulting topology. It is well known that such equivalence does not hold for b -metric, G_b -metric and S_b -metric spaces.

This is because the open sphere defined in them does not have to be open in the generated topology.

In this paper, we will discuss several recent results established by several authors and published recently in [2,13,14,18]. All these results connect F -contractions to β -admissible mappings of both within S -metric spaces. Using the connection of S -metric and b -metric spaces that is given and explained in the following Proposition, we will in one of the next papers provide a substantial correction of the result from [5]. Now we state the position on the relationship between S -metric and b -metric spaces:

Proposition 1.1. *Let (X, S) be an S -metric space. Then with $b(x, y) = S(x, x, y)$ a b -metric on the set X is given.*

The following applies:

- a)** (X, S) is complete S -metric space if and only if (X, b) is a complete b -metric space;
- b)** A Sequence x_n converges in S -metric space (X, S) if and only if it converges in b -metric space (X, b) ;
- c)** The same applies when the sequence x_n is a Cauchy sequence. Namely, it is Cauchy in (X, S) if and only if it is Cauchy in the b -metric space (X, b) ;
- d)** The mapping T from X to itself is continuous in (X, S) if and only if it is continuous in (X, b) ;
- e)** Since S is a continuous function with three variables, then the newly defined b -metric b is also such, i.e., a continuous function with two variables.

Remark 1.1. *For a proof of the mentioned properties, see the recent interesting paper [21].*

Thus, the coefficient s in the obtained b -metric space is equal to $\frac{3}{2}$. Let us also mention one error from the work of G. S. Saluja [18]: If (X, S) is a given S -metric space, then with $d_G(x, y) = S(x, x, y) + S(y, y, x)$ a metric on the set X is defined. According to Proposition 1.1, it is false. Indeed, if the above equality were possible, then we would have that the metric d_G is equal to the $2 \cdot b$ from Proposition 1.1. But since the coefficient s of the b -metric b is equal to $\frac{3}{2} > 1$, it means that b is not a metric. It follows from the assertion of the author in [18] that $b = \frac{1}{2}d_G$, i.e., that b is a metric, because obviously $\frac{1}{2}d_G$ is a metric.

In the continuation of the work, we significantly improve the results from several works ([2, 13, 14, 18]). We will only use the property **F1**, i.e. strict increasing of mapping F . In addition to the two lemmas that will be listed, we will use the following important property of the strictly increasing function F from $(0, +\infty)$ to \mathbb{R} . It reads: For each strictly increasing function F from $(0, +\infty)$ to \mathbb{R} the following applies: $F(a-0) \leq F(a) \leq F(a+0)$ where $F(a-0)$ and $F(a+0)$ are respectively the left and right limits of the function F at point a . Note that the following also applies: either $F(0+0) = -\infty$ or $F(0+0) = A$ where A is a real number.

In some works on F -contractions in S -metric spaces, it is assumed that the contractive condition

$$\tau + F(S(Tx, Ty, Tz)) \leq F(S(x, y, z))$$

holds whenever $S(Tx, Ty, Tz) > 0$. In this case, in the proofs, instead of x , i.e., y and z , the authors take $x = y = x_{n-1}$ and $z = x_n$, respectively. Namely, in some papers they assume that $\tau + F(Tx, Tx, Ty) \leq F(S(x, x, y))$ is fulfilled whenever $S(Tx, Tx, Ty) > 0$.

As in the case of considering F -contractions within metric spaces ([9, 24]), the following two Lemmas occupy an important place.

Lemma 1.1. *Let (X, S) be an S -metric space and $\{x_n\}$ be a Picard's sequence in it. If $S(x_{n+1}, x_{n+1}, x_n) < S(x_n, x_n, x_{n-1})$ for all $n \in \mathbb{N}$ then $x_n \neq x_m$ whenever $n \neq m$.*

Proof. Suppose the opposite, i.e., let $x_n = x_m$ for some n, m from \mathbb{N} with $n < m$. Due to the fact that $x_{n+1} = Tx_n = Tx_m = x_{m+1}$ we have

$$S(x_{n+1}, x_{n+1}, x_n) = S(x_{m+1}, x_{m+1}, x_m) < S(x_m, x_m, x_{m-1}) < \dots$$

$$\dots < S(x_{n+2}, x_{n+2}, x_{n+1}) < S(x_{n+1}, x_{n+1}, x_n) < \dots,$$

which is a contradiction. □

Lemma 1.2 ([22]). *Let (X, S) be an S -metric space and let $\{x_n\}$ be a Picard's sequence in it such that*

$$\lim_{n \rightarrow +\infty} S(x_{n+1}, x_{n+1}, x_n) = 0.$$

If $\{x_n\}$ is not a Cauchy sequence, then there exist an $\varepsilon > 0$ and two sequences $\{m_k\}$ and $\{n_k\}$, $n_k > m_k > k$ of positive integers such that the following sequences tend to ε^+ when $k \rightarrow +\infty$:

$$\{S(x_{m_k}, x_{m_k}, x_{n_k})\}, \{S(x_{m_k}, x_{m_k}, x_{n_k+1})\}, \{S(x_{m_k-1}, x_{m_k-1}, x_{n_k})\},$$

$$\{S(x_{m_k-1}, x_{m_k-1}, x_{n_k+1})\}, \{S(x_{m_k+1}, x_{m_k+1}, x_{n_k+1})\}, \dots$$

For the all details of the proof see [22] as well as [16].

The following two concepts and the result that connects them will be useful to us in the continuation of our work.

Definition 1.3 ([27]). *Let $T : X \rightarrow X$ and $\beta : X^3 \rightarrow [0, +\infty)$. Then we say that T is β -admissible if for all $x, y, z \in X$ we have*

$$\beta(x, y, z) \geq 1 \text{ implies } \beta(Tx, Ty, Tz) \geq 1.$$

Definition 1.4 ([27]). *Let $\beta : X^3 \rightarrow [0, +\infty)$. We say that β is transitive if*

$$\beta(x, y, y) \geq 1 \text{ and } \beta(y, z, z) \geq 1 \text{ implies } \beta(x, z, z) \geq 1,$$

for all $x, y, z \in X$.

The next result is the key to our further consideration and correction of already published results on F -contractions in S -metric spaces.

Lemma 1.3 ([27]). *Let $T : X \rightarrow X$ and $\beta : X^3 \rightarrow [0, +\infty)$ be β -admissible and transitive, respectively. Assume that there exists $x_0 \in X$ such that $\beta(x_0, Tx_0, Tx_0) \geq 1$. Define a sequence $\{x_n\}$ by $x_n = T^n x_0$. Then $\beta(x_m, x_n, x_n) \geq 1$, for all $m, n \in \mathbb{N}$ with $m < n$.*

We end this part of the paper with a list of all known $F - \beta$ contractive conditions, where F is a mapping from $(0, +\infty)$ to \mathbb{R} with all three known properties, while β is a mapping from X^3 to $[0, +\infty)$ β -admissible or β -admissible and transitive. We list all those contractive conditions:

- 1) $S(Tx, Ty, Tz) > 0$ implies $\tau + \beta(x, y, z) \cdot F(S(Tx, Ty, Tz)) \leq F(S(x, y, z))$;
- 2) $S(Tx, Ty, Tz) > 0$ implies $\tau + F(\beta(x, y, z) \cdot S(Tx, Ty, Tz)) \leq F(S(x, y, z))$;
- 3) $S(Tx, Tx, Ty) > 0$ implies $\tau + \beta(x, x, y) \cdot (F(S(Tx, Tx, Ty)) \leq F(S(x, x, y)))$;
- 4) $S(Tx, Tx, Ty) > 0$ implies $\tau + F(\beta(x, x, y) \cdot S(Tx, Tx, Ty)) \leq F(S(x, x, y))$.

If in 3)-4) on the right sides if $S(x, x, y)$ is replaced with

$$M(x, x, y) = \max \{S(x, x, y), S(x, x, Tx), S(y, y, Ty), (S(x, x, Tx) + S(x, x, Ty) + S(y, y, Tx))\},$$

then we have the so-called $\beta - F$ -weak contractions. In some papers from the reference list, theorems about the existence of a fixed point for $\beta - F$ contractions have been proven, but only if the mapping F satisfies all 3 listed properties. In the continuation of the work, we will significantly improve such results in the sense that we add the property of transitivity to the mapping β and remove the properties **F2** and **F3** from the mapping F .

Remark 1.2. *According to Proposition 1.1, we have that relations 3) and 4) give an F -contraction within b -metric spaces.*

We now state one of the first results stated and proved in ([14], Theorem 1).

Theorem 1.1. *Let (X, S) be a complete S -metric space and $T : X \rightarrow X$ be a $\beta - F$ -weak contraction satisfying the following conditions:*

(T1) *T is β -admissible,*

(T2) *there exists $u_0 \in X$ such that $\beta(u_0, u_0, Tu_0) \geq 1$,*

(T3) *T is S -continuous.*

Then T has a fixed point.

Remark 1.3. *For several results of this type the reader can see ([14], Theorem 2, [18], Theorem 3.2, [23], Theorem 5, [15], Theorems 2, 3 and 4).*

2. Main results

Our first new general result is given by the following Theorem:

Theorem 2.1. *If (X, S) is a complete S -metric spaces and if there exists $\tau > 0$ such that*

$$\tau + F(S(Tx, Ty, Tz)) \leq F(S(x, y, z)),$$

whenever $S(Tx, Ty, Tz) > 0$, where $F : [0, +\infty) \rightarrow \mathbb{R}$ is a strictly increasing function, then the mapping T has a unique fixed point in X . Moreover, if x is an arbitrary point in X , then the Picard's sequence $T^n x$ converges to this fixed point.

Proof. If u and v are two different fixed points of the mapping T , then

$S(u, u, v) = S(Tu, Tu, Tv) > 0$, because $Tu \neq Tv$. In this case, according to the given contractive condition we get $\tau + F(S(u, u, v)) \leq F(S(u, u, v))$ which is a contradiction with $\tau > 0$. So, if T has a fixed point it is unique. Also, from the given contractive condition the continuity of the mapping T follows. Indeed, the given contractive condition gives $S(Tx, Ty, Tz) < S(x, y, z)$ which means that the mapping $T : X \rightarrow X$ is S -continuous.

Now, we will prove the existence of the fixed point for the mapping T . Let x_0 be an arbitrary point in X and let $x_n = T^n x_0$ be the corresponding Picard's sequence. If $x_{n-1} = x_n$ for some $n \in \mathbb{N}$, then obviously x_{n-1} is a unique fixed point of the mapping T . And hence Theorem is proved. Let us now in the following prove that x_{n-1} is different from x_n for each $n \in \mathbb{N}$. Putting in the given contractive condition $x = y = x_{n-1}$ and $z = x_n$, we get that $S(Tx, Ty, Tz) = S(x_n, x_n, x_{n+1})$ which further means that:

$$\tau + F(S(x_n, x_n, x_{n+1})) \leq F(S(x_{n-1}, x_{n-1}, x_n)).$$

Since $\tau > 0$ and F is a strictly increasing function, we get that the sequence $\{S(x_n, x_n, x_{n+1})\}$ is strictly decreasing and therefore its limit $S^* \geq 0$ exists when $n \rightarrow +\infty$. Let us prove that $S^* = 0$. Indeed, by switching to the limit when $n \rightarrow +\infty$ in the last relation

and using the property of the function F about left and right limits we get $\tau + F(S^* + 0) \leq F(S^* + 0)$, which is a contradiction since $\tau > 0$. Note that according to Lemma 1.1 obtained that all members of the sequence x_n are mutually different, i.e., that $x_n \neq x_m$ whenever $n \neq m$. We need this when we prove the Cauchyness of the sequence $\{x_n\}$ because we will need the area of definition of the function F .

In order to prove that $\{x_n\}$ is a Cauchy sequence, we apply Lemma 1.2, i.e. We put $x = y = x_{n_k}$, $z = x_{m_k}$ in the given contractive condition, and so we get the following

$$\tau + F(S(x_{n_k+1}, x_{n_k+1}, x_{m_k+1})) \leq F(S(x_{n_k}, x_{n_k}, x_{n_k})).$$

If, in the last relation, we let k tends to $+\infty$ and use the property on the left and right limits of the function F , we get: $\tau + F(\varepsilon^+) \leq F(\varepsilon^+)$, which is obviously a contradiction with $\tau > 0$. Therefore, the sequence $\{x_n\}$ is a Cauchy sequence and since (X, S) is a complete S -metric space, it converges to some point, say u from X . By definition, this is written as $S(x_n, x_n, u) \rightarrow 0$ when $n \rightarrow +\infty$. From the continuity of the mapping T we have that $Tx_n \rightarrow Tu$ as $n \rightarrow +\infty$, which is written as $S(Tx_n, Tx_n, Tu) \rightarrow 0$ when $n \rightarrow +\infty$ or in the equivalent form $S(x_{n+1}, x_{n+1}, Tu) \rightarrow 0$ when $n \rightarrow +\infty$. The latter means that the sequence $\{x_{n+1}\} \rightarrow Tu$ when $n \rightarrow +\infty$. Due to the uniqueness of the limit within S -metric spaces, we have that $Tu = u$ is a unique fixed point of the F -contraction T on S -metric space. The proof of the Theorem is completed. \square

The following theorem is a mild generalization of Theorem 2.1 and its proof is the same as the proof of Theorem 2.1.

Theorem 2.2. *If (X, S) is a complete S -metric spaces and if there exists $\tau > 0$ such that*

$$\tau + F(S(Tx, Tx, Ty)) \leq F(S(x, x, y)),$$

whenever $S(Tx, Tx, Ty) > 0$, where $F : [0, +\infty) \rightarrow \mathbb{R}$ is a strictly increasing function, then the mapping T has a unique fixed point in X . Moreover, if x is an arbitrary point in X , then the Picard's sequence $T^n x$ converges to this fixed point.

Corollary 2.1. *By putting $F = \ln$ in the Theorems 2.1 and 2.2 we get one type of Banach contraction principle within S -metric spaces. It reads*

$$0 < S(Tx, Ty, Tz) \leq e^{-\tau} S(x, y, z) \quad \text{and} \quad 0 < S(Tx, Tx, Ty) \leq e^{-\tau} S(x, x, y),$$

respectively, where $\tau > 0$.

The previous Corollary shows that by choosing the function F , it is obtained that the F -contraction within S -metric spaces is also a Banach's contraction in the same framework. While the following example shows that there is an F -contraction that is not a Banach's contraction, i.e., that Wardowski's approach is also a true generalization of the Banach's contraction in this class of spaces within S -metric spaces. It is inspired by Wardowski's example from the paper [26].

Example 2.1. *Consider the sequence $\{x_n\}_{n \in \mathbb{N}}$ as follows: $x_n = \frac{n(n+1)}{2}$. Let $X = \{x_n : n \in \mathbb{N}\}$ and $S(x, y, z) = |x - z| + |y - z|$. Then (X, S) is a complete S -metric space. Define the mapping $T : X \rightarrow X$ by the formulae: $T(x_n) = x_{n-1}$ for $n > 1$ and $T(x_1) = x_1 = 1$, that is, x_1 is a fixed point of T . The mapping T with the F -contractive condition as in Theorem 2.1. is not an F -contraction with $F = \ln$ (which means that T is not the*

Banach's contraction). Indeed, we check it. Since, $x_n \neq x_m$ whenever $n \neq m$, we have for that case $S(Tx_n, Tx_n, Tx_1) > 0$. Therefore, for $n > 1$ we get

$$\begin{aligned} \lim_{n \rightarrow +\infty} \frac{S(Tx_n, Tx_n, Tx_1)}{S(x_n, x_n, x_1)} &= \lim_{n \rightarrow +\infty} \frac{|x_{n-1} - 1| + |x_{n-1} - 1|}{|x_n - x_1| + |x_n - x_1|} = \\ &= \lim_{n \rightarrow +\infty} \frac{|x_{n-1} - 1|}{|x_n - 1|} = \lim_{n \rightarrow +\infty} \frac{\frac{(n-1)n}{2} - 1}{\frac{n(n+1)}{2} - 1} = 1. \end{aligned}$$

This means that the condition

$$\tau + \ln(S(Tx_n, Tx_n, Tx_1)) \leq \ln(S(x_n, x_n, x_1)),$$

that is, the condition

$$\ln \frac{S(Tx_n, Tx_n, Tx_1)}{S(x_n, x_n, x_1)} \leq e^{-\tau}$$

is not possible for sufficient large n and any positive τ

Assuming now that $F(\alpha) = \alpha + \ln \alpha$, we obtain, according to Theorem 2.1 that Wardowski F -contraction in the framework of S -metric spaces is a true generalization of Banach contraction principle in the same framework. And in this case we have that $x_n \neq x_m$ whenever $n \neq m$, that is, $S(Tx_n, Tx_n, Tx_m) > 0$. Therefore, if $\tau = e^{-1}$ we check the following relation

$$e^{-1} + S(Tx_n, Tx_n, Tx_m) + \ln(S(Tx_n, Tx_n, Tx_m)) \leq S(x_n, x_n, x_m) + \ln(S(x_n, x_n, x_m)),$$

or equivalently,

$$\ln \frac{S(Tx_n, Tx_n, Tx_m)}{S(x_n, x_n, x_m)} \leq S(x_n, x_n, x_m) - S(Tx_n, Tx_n, Tx_m) - e^{-1},$$

that is,

$$\frac{S(Tx_n, Tx_n, Tx_m)}{S(x_n, x_n, x_m)} e^{S(Tx_n, Tx_n, Tx_m) - S(x_n, x_n, x_m)} \leq e^{-1}.$$

Since $Tx_n = x_{n-1}$, $Tx_m = x_{m-1}$ whenever both $n > m > 1$ and $Tx_1 = x_1$ the last inequality become

$$\frac{|x_{n-1} - x_{m-1}|}{|x_n - x_m|} e^{|x_{n-1} - x_{m-1}| - |x_n - x_m|} \leq e^{-1}.$$

We further get

$$\begin{aligned} \frac{\frac{(n-1)n}{2} - \frac{(m-1)m}{2}}{\frac{n(n+1)}{2} - \frac{m(m+1)}{2}} e^{|\frac{(n-1)n - (m-1)m}{2}| - |\frac{n(n+1) - m(m+1)}{2}|} &= \\ &= \frac{n+m-1}{n+m+1} e^{-(n-m)} \leq e^{-1}, \end{aligned}$$

which is true, because $\frac{n+m-1}{n+m+1} < 1$ as well as from $n > m$ we get $n-m \geq 1$, i.e., $e^{-(n-m)} \leq e^{-1}$.

About corrected results. Just as in Theorems 2.1 and 2.2, using Lemmas 1.1 and 1.2, we managed to get rid of the application of the properties **F2** and **F3** in the proofs, so in the rest of this paper we will describe (state) the steps of the proof of Theorem 1.1 using only the property **F1**. The price that for what we pay for is adding transitivity to the mapping $\beta : X^3 \rightarrow [0, +\infty)$. The same procedure applies to the correction of the evidence of the results mentioned in **Remark 1.1**. It is well known that in the presence of a β -admissible mapping, a

possible fixed point is not necessarily unique. That is why we only approach proving its existence. The first step in this proof would be to prove, starting from a given point x_0 with properties **(T2)** and **(T1)**, the existence of a sequence $\{x_n\}$ such that $\beta(x_n, x_n, x_{n+1}) \geq 1$ for each n from \mathbb{N} .

Using this obtained relation from the given contractive condition, it is obtained for the sequence x_n that the sequence $S(x_n, x_n, x_{n+1})$ is strictly decreasing. From there, according to the property about the left and right limits of the strictly increasing function F , it is obtained that $S(x_n, x_n, x_{n+1})$ tends to zero when n tends to $+\infty$. According to Lemma 1.1, it follows from the strictly decreasing sequence $S(x_n, x_n, x_{n+1})$ that all members of the sequence x_n are mutually different. Therefore, the conditions have been met to apply Lemma 1.2. to prove that the sequence $\{x_n\}$ is Cauchy. Of course, to eliminate the sequence $\beta(x_n, x_n, x_{n+1})$ the Lemma 1.3 is used. And then, in the last step, by letting k tends to $+\infty$, as in the proof of Theorems 2.1 and 2.2, we get a contradiction with $\tau > 0$. The rest of the proof is further as in Theorems 2.1. This method can therefore be used to improve (shorten) all the proofs of the results mentioned in the works from the list of references. To conclude: if any β -admissible function does not participate in the contractive condition, the fixed point is unique and it is sufficient only for the function **F** to assume the property **F1**. If a β -admissible function is present, with the addition that it is transitive, it is again sufficient to assume only the property **F1**, but then the fixed point does not have to be unique. \square

References

- [1] J.M.Afra, M.Sabbaghan, F.Taleghani, Some new fixed point theorems for expansive map on S -metric spaces, *Theory Approx. Appl.*, **14**(2020), no, 2, 57–64.
- [2] S.Chaipornjareansri, Fixed point theorems for F_w -contractions in complete S -metric spaces, *Thai J. Math.*, (2016), 98–109.
- [3] Lj.Ćirić, Some recent results in metrical fixed point theory, University of Belgrade, Beograd 2003, Serbia.
- [4] K.M.Devi, Y.Rohen, K.A.Singh, Fixed points of modified F -contractions in S -metric spaces, *J. Math. Comput. Sci.*, **12**(2022), 197. DOI: 10.28919/jmcs/7716
- [5] M.Din, U.Ishtiaq, M.Mukhtar, S.Sessa, H.A.Ghazwani, On generalized Sehgal-Guseman-like contractions and their fixed-point results with applications to nonlinear fractional differential equations and boundary value problems for homogeneous transverse bars, *Mathematics*, **12**(2024), 541. DOI: 10.3390/math12040541
- [6] T.Došenović, S.Radenović, S.Sedghi, Generalized metric spaces: Survey, *TWMS. J. Pure Appl. Math*, **9**(2018), no, 1, 3–17.
- [7] T.Došenović, S.Radenović, A comment on "Fixed point theorems of JS-quasi-contractions", *Indian J. Math. Dharma Prakash Gupta Memorial*, **60**(2018), no, 1, 141–152.
- [8] T.Došenović, M.Pavlović, S.Radenović, Contractive conditions in b -metric spaces, *Vojno tehnički glasnik/Mil. Tech. Cour.*, **65**(2017), no, 4, 851–865. DOI:10.5937/vojtehg65-14817
- [9] N.Fabiano, Z.Kadelburg, N.Mirkov, Vesna Šešum Čavić, S. Radenović, On F -contractions: A Survey, *Contemp. Math.*, **3**(2022), no, 3, 327. <http://ojs.wiserpub.com/index.php/CM/>

- [10] D.Gopal, M.Abbas, D.K.Patel, C.Vetro, Fixed points of \acute{a} -type F -contractive mappings with an application to nonlinear fractional differential equation, *Acta Math. Sci.*, **36**(2016), no. B3, 957–970. DOI:10.1016/S0252-9602(16)30052-2
- [11] A.Gupta, Cyclic contraction on S -metric space, *Int. J. Anal. Appl.*, **3**(2013), no. 2, 119–130.
- [12] N.T.Hieu, N.T.Ly, N.V.Dung, A generalization of Ćirić quasi-contractions for maps on S -metric spaces, *Thai J. Math.*, **13**(2015), no. 2, 369–380.
- [13] K.Javed, F.Uddin, F.Adeel, M.Arshad, H.Alaeidizaji, V.Parvaneh, Fixed point results for generalized contractions in S -metric spaces, *Mathematical Analysis and its Contemporary Applications*, **3**(2021), no. 2, 27-39.
- [14] B.Khomdram, Y.Rohen, M.S.Khan, N.Fabiano, Fixed point results for $\beta - F$ - weak contraction mappings in complete S -metric spaces, *Mil. Tech. Cour.*, (2024), 3–24.
- [15] K.M.Devi, Y.Rohen, K.A.Singh, Fixed points of modified F -contractions in S -metric spaces, *J. Math. Comput. Sci.*, **12**(2022), 197.
- [16] S.Radenović, Z.Kadelburg, D.Jandrlić, A.Jandrlić, Some results on weakly contractive maps, *Bull. Iranian Math. Soc.*, **38**(2012), no. 3, 625–645.
- [17] Y.Rohen, T.Došenović, S.Radenović, A note on the paper "A fixed point theorems in S_b -metric spaces", *Filomat*, **31**(2017), 3335–3346. DOI: 10.2298/FIL1711335R
- [18] G.S.Saluja, Fixed point results for generalized F_σ - contraction in complete S -metric spaces, *Annals of Mathematics and Computer Science*, **20**(2024) 25–40. DOI: 10.56947/amcs.v20.229
- [19] B.Samet, C.Vetro, P.Vetro, Fixed point theorems for $(\alpha - \psi)$ - contractive type mappings, *Nonlinear Anal.*, **75**(2012), 2154–2165.
- [20] S.Sedghi, N.Shobe, A.Aliouche, A generalization of fixed point theorems in S -metric spaces, *Matematički vesnik*, **64**(2012), no. 3, 258-266.
- [21] S.Sedghi, N.V.Dung, Fixed point theorems on S -metric spaces, *Matematički vesnik*, **66**(2014), no. 1, 113-124.
- [22] S.Sedghi, M.M.Rezaee, T.Došenović, S.Radenović, Common fixed point theorems for contractive mappings satisfying Φ -maps in S -metric spaces, *Acta Univ. Sapientiae, Mathematica*, **8**(2016), no. 2 298–311. DOI: 10.1515/ausm-2016-0020
- [23] T.Thai'bema, Y.Rohen, T.Stephen, O.Budhichandra, Fixed point of rational F -contractions in S -metric spaces, *J. Math. Comput. Sci.*, **12**(2022), 153. DOI: 10.12691/ajams-10-3-1
- [24] J.Vujaković, N.Kontrec, M.Tošić, N.Fabiano, S. Radenović, New Results on F -Contractions in Complete Metric Spaces, *Mathematics*, **10**(2022), 12. DOI:10.3390/math10010012
- [25] J.Vujaković, S.Radenović, On some F -contraction of Piri-Kumam-Dung-type mappings in metric spaces, *Vojnotehnički glasnik/Mil. Tech. Cour.*, **68**(2020), no. 4, 697–714. DOI: 10.5937/vojtahg68-27385

- [26] D.Wardowski, Fixed points of a new type of contractive mappings in complete metric spaces, *Fixed Point Theory Appl.*, **2012:94**(2012). DOI: 10.1186/1687-1812-2012-94
- [27] M.Zhoua, X.-l.Liu, S.Radenović, S - γ - ϕ - φ -contractive type mappings in S -metric spaces, *J. Nonlinear Sci. Appl.*, **10**(2017), 1613–1639. DOI: 10.22436/jnsa.010.04.27

Некоторые замечания и исправления недавних результатов из теории S -метрических пространств

Нора Фетуси

Лаборатория LMRA
Кафедра математики
Университет Джиджел
Джиджел, Алжир

Стоян Раденович

Факультет машиностроения
Белградский университет
Белград, Сербия

Аннотация. Содержание этой статьи состоит из результатов по F -сжатию Вардовского в S -метрических пространствах. В ней мы представляем поправки к некоторым недавним результатам, используя только свойство F1 строгого возрастания функции F . В наших результатах мы объединяем β -допустимые функции с F -сжатиями. Наконец, мы приводим пример, показывающий, что F -сжатие в рамках S -метрических пространств является истинным обобщением принципа сжатия Банаха в тех же рамках.

Ключевые слова: S -метрическое пространство, b -метрическое пространство, неподвижная точка, F -сокращение, β -допустимо.

EDN: XPPAYA

УДК 543.424

Application of Optical Methods in Standardization of Collagen-containing Hydrogen for 3D Bioprinting of Supporting and Connective Tissues

Elena V. Timchenko*

Institute of Informatics and Cybernetics
Samara University
Samara, Russian Federation

Nikolai A. Ryabov†

Samara State Medical University
Samara, Russian Federation

Oleg O. Frolov‡

Pavel E. Timchenko§

Institute of Informatics and Cybernetics
Samara University
Samara, Russian Federation

Larisa T. Volova¶

Samara State Medical University
Samara, Russian Federation

Sergej S. Ivanov||

Institute of Informatics and Cybernetics
Samara University
Samara, Russian Federation

Received 18.10.2024, received in revised form 23.11.2024, accepted 10.02.2025

Abstract. The paper presents the results of the application of optical methods in the standardization of collagen-containing allogeneic hydrogel produced at the Biotech Research Institute (Samara, Russia) from bioimplants of the Lioplast® trademark in comparison with the hydrogels available on the market from Rokit and Cellink companies. The Raman spectroscopy method was used as the main research method. An additional research method was the method of IR Fourier spectroscopy.

As a result of the conducted research using optical methods, it was found that the collagen structure is completely preserved in the composition of the allogeneic hydrogel produced at the Biotech Research Institute (Samara, Russia). Hydrogels of imported Rokit and Cellink companies also have a similar spectral composition. The obtained results can be further used as a rapid assessment and standardization of collagen-containing hydrogel with the addition of various components for personalized 3D bioprinting of human supporting and connective tissues.

As part of the current import substitution task, the developed collagen-containing allogeneic hydrogel may in the future represent a competitive analogue to foreign commercial products — hydrogels in bioprinting.

Keywords: Raman spectroscopy, infrared Fourier spectroscopy, collagen-containing hydrogel, supporting and connective tissues, 3D bioprinting.

*lazer-optics.timchenko@mail.ru <https://orcid.org/0000-0002-0539-7989>

†info@samsmu.ru <https://orcid.org/0000-0002-1332-953X>

‡frolov679@mail.ru <https://orcid.org/0000-0002-3225-8511>

§timpavel@mail.ru <https://orcid.org/0000-0003-3089-7966>

¶l.t.volova@samsmu.ru <https://orcid.org/0000-0002-8510-3118>

||koditek00@yandex.ru

Citation: E.V. Timchenko, N.A. Ryabov, O.O. Frolov, P.E. Timchenko, L.T. Volova, S.S. Ivanov, Application of Optical Methods in Standardization of Collagen-containing Hydrogen for 3D Bioprinting of Supporting and Connective Tissues, J. Sib. Fed. Univ. Math. Phys., 2025, 18(3), 412–419. EDN: XPPAYA.



Introduction

To date, 3D bioprinting of tissues and organs is one of the promising methods of biofabrication and is of great interest in the direction of creating complex cellular and tissue constructs for tissue regeneration, which allows for the manufacture of personalized implants taking into account the anatomy, pathology and biomechanical properties of organs and body parts of the patient's body [1]. The bioprinting process is carried out using bioinks, which include two main components — cells and hydrogel. Hydrogels are three-dimensional polymer meshes that, due to The properties of hydrophilicity are capable of retaining large amounts of water. Various natural polymers are used to produce hydrogels, among them biopolymers of allogeneic origin have predominant characteristics, including good biocompatibility and biodegradability, as well as low antigenicity and high regenerative potential. Commercial bioinks presented on the market today are characterized by a fairly high cost, which makes it necessary to develop our own domestic competitive analogues of such bioinks within the framework of the direction import substitution [2, 3].

Among the large number of biogenic hydrogels available on the market today, the hydrogels of PureColo "Cellink" (Sweden) and hydrogel can be distinguished INVIVO-GEL-ESSENTIAL (Korea), which have already successfully proven themselves as products for bioprinting and perfectly combined with various types of cells. The presented products are mainly used in scientific research tasks. Today, the Russian Federation is actively working on the development of domestic hydrogels, the creation of which will solve the problem of import substitution of foreign bioinks.

An important step in the bioprinting process of various constructs is their standardization, both at the stage of obtaining the initial material for bioprinting - hydrogels, and the final printed product. Therefore, it is necessary to evaluate the quality of hydrogels and bioinks in order to obtain data on the structure of the components contained in them. Among the physical research methods, optical methods such as Raman spectroscopy and IR Fourier spectroscopy are widely used, which They are non-destructive and operational methods of analysis, as well as widely used for solving biomedical problems [4-9]. Thus, in the work of the authors [4-5], studies on the use of Raman spectroscopy to assess the composition of tissues with a detailed interpretation of the main lines of Raman are presented.

The authors of the work [6], using the method of Raman spectroscopy, investigated the composition of biomaterials and extracellular matrix, including bone marrow. In the work of the authors [7] it is shown that using this method it is possible to determine the composition of the cell. So in The work of the authors [8] shows that non-destructive analysis of various biomaterials can be carried out using IR spectroscopy (FTIR).

Therefore, the aim of the work was to evaluate the possibility of using optical methods in the standardization of collagen-containing hydrogel for 3D bioprinting of human supporting and connective tissues.

Materials and methods of research

The objects of the study were: group 1 — allogeneic collagen-containing hydrogel (obtained from human bone tissue), Samara, Russia, Biotech Research Institute, Lioplast ©; group 2 — PureCol hydrogel © "Cellink" (Sweden); group 3 — INVIVO-GEL-ESSENTIAL hydrogel (Korea); group 4 — type I collagen sample "Cellink" (Sweden). The collagen-containing hydrogel was

obtained from an allogeneic material of demineralized bone tissue, pretreated using the original technology for obtaining bioimplants of the trademark "Lyoplast"© (TU- 9398-001 -01963143-2004, patent R+ No. 2366173 dated 05/15/2008; Certificate of conformity ISO 13485:2016, reg. No. RU CMS-RU.PT02.00115; ISO 9001:2015 certificate, per TIC 15 100 159171) [9].

Raman spectroscopy and IR Fourier spectroscopy were used as research methods. The Raman spectroscopy (Raman) method was implemented using an experimental stand consisting of a semiconductor laser (LML-785.ORB-04.450 MW), a spectrograph (Andor Sharmrock SR-303i) with an integrated digital camera cooled to -60°C , an optical raman module (PBL785) and a computer. The use of this spectrograph provided a resolution of 0.15 nm in wavelength at a low level of intrinsic noise. In this work, the Raman spectra were analyzed in the range $700\text{--}1800\text{ cm}^{-1}$. The Raman spectra were recorded using an optical probe, which was located above the object at a distance of 7 mm. Further processing of the Raman spectra consisted in filtering autofluorescence in the Raman spectra using the method of subtracting the fluorescent component by polynomial approximation I-ModPoly with polynomial degree 11 [10].

Normalization and smoothing of Raman spectra were performed using the SNV and Maximum Likely good Estimation Savitzky–Golay filter (ME-SG) (=4) methods. Infrared spectra were obtained using a Fourier spectrometer FT modification 801 (factory number 465; manufacturer Limited Liability Company Scientific and production company "SIMEX" (LLC NPF "SIMEX"), Novosibirsk). Transmission spectra were recorded using the prefix of multiple disturbed total internal reflection (hereinafter referred to as the prefix MNPVO) at the following parameter values:

- spectrum resolution of 8 cm^{-1} ;
- the number of scans (accumulations) for obtaining spectra is 36.

The results of the study

Fig. 1 shows the averaged Raman spectra of the samples.



Fig. 1. Research materials

It can be seen from Fig. 1 that lines are present in all three studied groups 1-3 of hydrogels CR, which are characteristic of type I collagen "Cellink": $1242\text{--}1265\text{ cm}^{-1}$ (AmideIII/ α -helix), 1412 cm^{-1} (CH_2 bending and scissoring modes of collagen and phospholipids), 1560 cm^{-1} (Amid II Parallel/Antiparallel α -sheet structure). At the same time, it can be seen that in the hydrogel of Korean production in the Raman spectra there are lines $1003\text{--}1075\text{ cm}^{-1}$ (Phenylalanine,

Breathingmode (collagen assignment)), 1650 cm^{-1} (Amide I/ α -helix), which also correspond to type I collagen "CELLINK" and determine the elasticity of tissues. Spectra of allogeneic collagen-containing hydrogel and hydrogel PureCol0 "Cellink" have similar spectral characteristics and, unlike the Korean-made hydrogel, have a Raman line at 832 cm^{-1} (C-C stretching, proline and hydroxyproline (collagen assignment)), which determines the properties of collagen fibrils such as elasticity and elasticity, which is important for tissue bioprinting. Further, a detailed analysis of the studied objects was carried out, the results of which are presented in Tab. 1 and in Figs. 2 and 3.

Table 1. Metric values for each sample group.

–	Precision	Recall	f1-score	support
Hydrogel	0.00	0.00	0.00	2
Purecol	0.00	0.00	0.00	1
ESSENTIAL	0.40	1.00	0.57	2

As can be seen from Tab. 1, the value of the F1-Score model is at the level of 40 percent, the ROC AUC is within 60 percent, and the rest of the metrics have low indicators, which indicates that groups 1–3 are difficult to distinguish between each other, which indicates the spectral similarity of their composition.

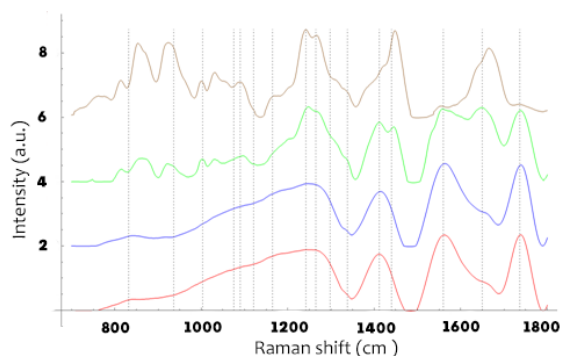


Fig. 2. Averaged Raman spectra of the samples: 1 (red line) — allogeneic collagen-containing hydrogel, 2 (blue line) — PureCol° "Cellink" hydrogel, 3 (green line) — INVIVO-GEL-ESSENTIAL hydrogel, 4 (brown line) — type I collagen sample "Cellink")

According to the decision matrix, it is clear that all test spectra are correctly classified (5). According to the ROCAUC and Precision-Recall graphs, the low classifying ability of the resulting classifier is also visible.

The value of ROC AUC (Receiver Operating Characteristic Area Under Curve) equal to 0.5 indicates that the model is not able to identify differences between the studied groups, which also indicates their spectral similarity.

Thus, the results obtained using Raman spectroscopy showed spectral similarities of the three studied hydrogels.

Fig. 4 shows the Fourier-infrared spectra of the three types of hydrogels studied from different manufacturers, as well as type I collagen "Cellink".

In the infrared spectra of all samples in the range of $3310\text{--}3291\text{ cm}^{-1}$, a wide peak of high intensity is observed, characteristic of valence vibrations of O-H, N-H ("Amide A") bound by intermolecular interaction (hydrogen bonds). In the region of $3078\text{--}3074\text{ cm}^{-1}$, both valence vibrations of the C-H (sp³) bond of heterocyclic fragments of amino acids that make up collagen (proline, oxyproline) and the "Amide B" band (stretching vibrations of C-N bonds) can

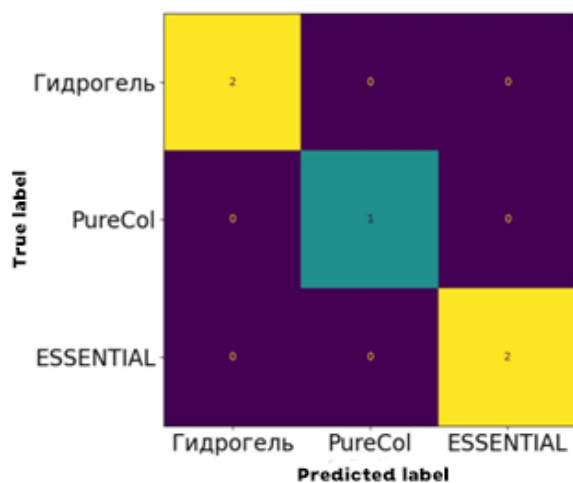


Fig. 3. Results matrix

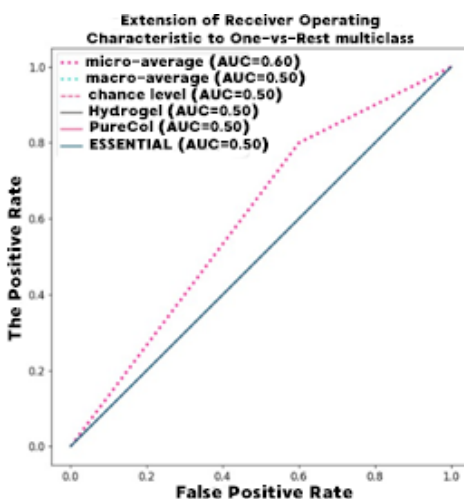


Fig. 4. Obtaining operating characteristics

manifest themselves. Absorption bands in the region of wave numbers $2958\text{--}2932\text{ cm}^{-1}$ and $2875\text{--}2874\text{ cm}^{-1}$ correspond to valence bands fluctuations in the C-H (sp^3) bond of alkyl groups. The most significant and widely used band for the characterization of biological materials is the peak "Amide 1", located near the range of $1700\text{--}1580\text{ cm}^{-1}$. It corresponds to the valence fluctuations of the C=O bond of the peptide group. In this case, high intensity bands at $1657\text{--}1631\text{ cm}^{-1}$ are present on the infrared spectra of all samples See^{-1} . These bands are characteristic of valence vibrations of C=O and N-H bonds (peak "Amide 1"). In the region of $1555\text{--}1536\text{ cm}^{-1}$ on the infrared spectra of the standard collagen type 1 "Cellink" and samples of all bands of high intensity corresponding to stretching vibrations of C-N and planar vibrations of N-H bonds (peak "Amide 2") are observed in the analyzed hydrogels.

In the region of $1453\text{--}1447\text{ cm}^{-1}$ and $1405\text{--}1404\text{ cm}^{-1}$, bands of medium and low intensity are present on all spectra, characteristic of both deformation vibrations of C-H and N-H bonds, and valence vibrations of C-N, C-C bonds. Further, in the region of $1340\text{--}1332\text{ cm}^{-1}$, maxima are observed, most likely associated with deformation fluctuations of the CH_2 groups of the proline

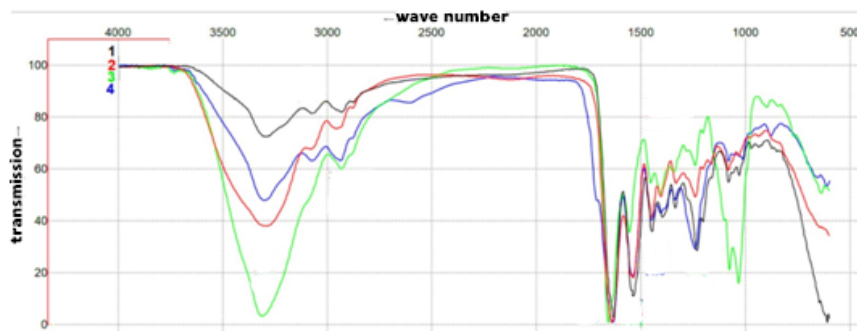


Fig. 5. Averaged IR spectra of the samples: 1 (black line) — type I collagen sample "Cellink"; 2 (red line) — INVIVO-GEL-ESSENTIAL hydrogel; 3 (green line) — PureCol® "Cellink" hydrogel; 4 (blue line) — allogeneic collagen-containing hydrogel

residue in the collagen polypeptide chain.

Absorption bands in the area of $1240\text{--}1232\text{ cm}^{-1}$ are caused by characteristic fluctuations of the amide group, deformation fluctuations of the carbon skeleton of amino acids that are part of the polypeptide chain of the material under study ("Amide 3"). Based on the spectral analysis carried out, it can be concluded that the main absorption bands in the infrared spectrum of the allogeneic hydrogel developed at the Biotech Research Institute are associated with characteristic fluctuations of specific groups in polypeptides. The IR spectrum of the allogeneic hydrogel is identical to the IR spectrum of the standard type 1 collagen "Cellink", which reflects their qualitative composition. The transmission spectrum of the Biotech Research Institute hydrogel has similar absorption bands with commercial hydrogels from "Rokit" and "Cellink" companies.

Taking into account the spectral similarities of the hydrogel developed by Vinni Biotech and the PureCol Cellink hydrogel, it can be concluded that the allogeneic hydrogel developed at the Biotech Research Institute can subsequently be applied to 3D bioprinting of human supporting and connective tissues using commercially available 3D bioprinters in the framework of import substitution.

Results

As a result of the conducted studies using the Raman spectroscopy method, it was found that the composition of the studied hydrogels of imported production, as well as the manufactured collagen-containing hydrogel, revealed AMIDII (Raman Spectroscopy lines $1200\text{--}1300\text{ cm}^{-1}$), Amide II (Raman Spectroscopy line 1554 cm^{-1}), CH_2 bending and scissoring modes of collagen and phospholipids 1450 cm^{-1} and Amide I (KP line $1650\text{--}1665\text{ cm}^{-1}$). These CD lines indicate the presence and preservation of the collagen structure in the composition of the studied hydrogels. The spectral composition of the developed at the Research Institute Biotech (Russia, Samara, Biotech Research Institute, Lioplast8) of allogeneic hydrogel has a similar composition to hydrogels of imported production. Additionally, using IR Fourier spectroscopy, it was found that the main absorption bands on the infrared spectrum of the allogeneic collagen hydrogel of the Biotech Research Institute are associated with characteristic fluctuations of specific groups in They are identical to the IR spectrum of the human type 1 collagen standard "Cellink", which reflects their qualitative composition and confirms the preservation of the collagen structure, and also has similar absorption bands with commercial hydrogels of Rokit and Cellink companies, which indicates the possibility of using the proposed allogeneic hydrogel of the Biotech Research

Institute in the future as an alternative to analogues available on the market as part of the import substitution program. The obtained research results can be further used as an express assessment and standardization of collagen-containing hydrogel with addition for personalized 3D bioprinting in the restoration of human supporting and connective tissues.

References

- [1] N.A.Tuneca, N.V.Bogacheva, U.O.Tunecva, Problems of dental implantation, *Vyatka medical Bulletin*, **62**(2019), no. 2, 86–93.
- [2] A.I.Nikolaev, L.M.Tsepov, Practical therapeutic dentistry, Medpress-inform, 2019.
- [3] L.Y.Orekhova, Periodontal diseases, Poly Media Press, 2004, 218–220.
- [4] I.V.Bazhutova, D.D.Ismatullin, A.V.Lyamin, D.A.Trunin, Species diversity of streptococci in periodontal diseases, *Immunopathology, allergology, infectology*, (2023), no. 1, 81–86. DOI: 10.14427/jipai.2023.1.81
- [5] D.D.Ismatullin, P.V.Bochkareva, I.V.,Bazhutova A.V.Lyamin, Galieva R.R., Zhestkov A.V., Zolotov M.O., Species diversity of streptococci in local and systemic infections, *Russian Clinical Laboratory Diagnostics*, **68**(2023), no. 10, 597–603 (in Russian). DOI: 10.51620/0869-2084-2023-68-10-597-603
- [6] N.A.Tuneca, N.V.Bogacheva, Comparative assessment of microbial contamination in periodontitis and peri-implantitis, *Bulletin of the Perm University. Ser. Biology*, (2021), no. 2, 101–109 (in Russian). DOI: 10.17072/1994-9952-2021-2-101-109
- [7] Xiaodan Ren, Qingshan Liu, Hui Feng, Xiaoying Yin The Characterization of Chitosan Nanoparticles by Raman Spectroscopy, *Applied Mechanics and Materials*, **665**(2014), 367–370. DOI: 10.4028/www.scientific.net/AMM.665.367
- [8] A.Carden, R.M.Rajachar, M.D.Morris, D.H.Kohn, Ultrastructural Changes Accompanying the Mechanical Deformation of Bone Tissue: A Raman Imaging Study, *Calcif. Tissue Int.*, **72**(2003), 166–175. DOI: 10.1007/s00223-002-1039-0
- [9] S.Berus, E.Witkowska, K.Niciski, E.Sadowy, W.Puzia, P.Ronkiewicz, A.Kamiska, Surface-enhanced Raman scattering as a discrimination method of Streptococcus spp. And alternative approach for identifying capsular types of S. Pneumonia isolates, *Spectrochimica Acta Part A: Molecular and Biomolecular Spectroscopy*, **233**(2020), 1–17. DOI: 10.1016/j.saa.2020.118088
- [10] P.E.Timchenko, E.V.Timchenko, L.T.Volova, O.O.Frolov, Use of Raman spectroscopy for the assessment of dentin materials during their fabrication, *Journal of Optical Technology*, **88**(2021), no. 9, 485–488.
- [11] P.E.Timchenko, E.V.Timchenko, L.T.Volova, O.O.Frolov, Spectral Analysis of Organic Components of Demineralized Bone Biografts, *Optics and Spectroscopy*, **126**(2019), no. 6, 769–775. DOI: 10.1134/S0030400X19060262
- [12] P.E.Timchenko, E.V.Timchenko, L.T.Volova, M.A.Zybin, O.O.Frolov, G.G.Dolgushov, Optical Assessment of Dentin Materials, *Optical Memory and Neural Networks*, **29**(2020), no. 4, 354–357. DOI: 10.3103/S1060992X20040116

Применение оптических методов в стандартизации коллагенсодержащего гидрогеля для 3D-биопечати опорных и соединительных тканей

Елена В. Тимченко

Институт информатики и кибернетики
Самарский университет
Самара, Российская Федерация

Николай А. Рябов

Самарский государственный медицинский университет
Самара, Российская Федерация

Олег О. Фролов

Павел Е. Тимченко

Институт информатики и кибернетики
Самарский университет
Самара, Российская Федерация

Лариса Т. Волова

Самарский государственный медицинский университет
Самара, Российская Федерация

Сергей С. Иванов

Институт информатики и кибернетики
Самарский университет
Самара, Российская Федерация

Аннотация. В работе представлены результаты применения оптических методов в стандартизации коллагенсодержащего аллогенного гидрогеля, произведенного в НИИ "Биотех" (г. Самара, Россия) из биоимплантатов торговой марки Lioplast® в сравнении с имеющимися на рынке гидрогелями компаний "Rokit" и "Cellink". В качестве основного метода исследования был использован метод спектроскопии комбинационного рассеяния. Дополнительным методом исследования являлся метод ИК-Фурье-спектроскопии.

В результате проведенных исследований с помощью оптических методов установлено, что в составе аллогенного гидрогеля, произведенного в НИИ "Биотех" (г. Самара, Россия), полностью сохранена коллагеновая структура. Подобный спектральный состав также имеют гидрогели импортного производства компаний Rokit и Cellink. Полученные результаты могут быть в дальнейшем использованы в качестве экспресс-оценки и стандартизации коллагенсодержащего гидрогеля с добавлением различных компонентов для персонализированного 3D-биопринтинга опорных и соединительных тканей человека.

В рамках актуальной на сегодняшний день задачи импортозамещения разработанный коллагенсодержащий аллогенный гидрогель в дальнейшем может представлять собой конкурентоспособный аналог зарубежным коммерческим продуктам — гидрогелям в биопечати.

Ключевые слова: инфракрасная Фурье-спектроскопия, метод спектроскопии комбинационного рассеяния, коллагенсодержащий гидрогель, опорные и соединительные ткани, 3D-биопечать.

EDN: ZMWLUA

УДК 512.546.8 + 512.548.77 + 517.986.6 + 517.987.1

Measures on Smashed Products of Quasigroups and their Algebras

Sergey V. Ludkowski*

Russian Technological University
Moscow, Russian Federation

Received 01.08.2024, received in revised form 13.12.2024, accepted 14.02.2025

Abstract. We study quasiinvariant measures on smashed and twisted wreath products of quasigroups. The quasiinvariance of measures is investigated relative to isotopies. Specific features are found for quasigroups in comparison with groups. Spaces of measures are scrutinized. Convolution algebras appear to be in general nonassociative because of the nonassociativity of the quasigroup. Ideals of topological convolution algebras are studied.

Keywords: quasigroup, measure, algebra, convolution, topology, invariance.

Citation: S.V. Ludkowski, Measures on Smashed Products of Quasigroups and their Algebras, *J. Sib. Fed. Univ. Math. Phys.*, 2025, 18(3), 420–429. EDN: ZMWLUA.



Introduction

Harmonic analysis on topological groups plays an important role in mathematics and its applications (see, for example, [1–8] and references therein). New directions of research are related with nonassociative algebra, noncommutative geometry, nonassociative mathematical physics, where quasigroups and loops appear frequently. They are nonassociative group analogs (see [9–11] and references therein). Moreover, quasigroups are frequently and actively used in informatics databases, since they open new possibilities in comparison with groups [18].

Harmonic analysis on nonassociative quasigroups and loops remains a little elaborated. There is very little known about relations between topologies and algebraic structures of quasigroups in comparison with groups. An existence of left- or right-invariant measure was studied earlier on topological groups in [19]. There was obtained a result, that from an existence of a left- or right-invariant nontrivial measure on the topological loop, it follows that it is everywhere dense in a locally compact loop. In particular, on locally compact core quasigroups left-invariant measures were constructed in [20]. Core quasigroups are particular cases of quasigroups. General topological quasigroups are studied in this article, as well as left or right quasigroups and loops. It is worth to emphasize, that the class of left (or right) quasigroups is wider than the class of quasigroups. Therefore this article contains new aspects in this area.

There are specific features of topological quasigroups in comparison with groups. This is caused by a reason, that in the associative case for the topological group G , there exists either left- or right-invariant uniformity on G compatible with its topology [3, 5, 21]. For the topological quasigroup generally the uniformity need not be neither symmetric, nor left-, nor right-invariant because of its nonassociativity.

*ludkowski@mail.ru

In abstract harmonic analysis on groups a large role is played by invariant and quasiinvariant measures. There is very little known about them in the nonassociative case. Therefore their investigations on quasigroups is important for the development of abstract harmonic analysis in the nonassociative case. The first section is devoted to this for smashed and twisted wreath products of quasigroups. On the other hand, it permits to construct quasiinvariant or invariant measures on a wide class of quasigroups. Moreover, the quasiinvariance of measures relative to isotopies is investigated. Specific features are found for quasigroups in comparison with groups. The second section deals with studies of ideals in the convolution algebra on a space of measures with the help of invariant and quasiinvariant measures on the quasigroup. The convolution algebra appears to be in general nonassociative because of the quasigroup nonassociativity. Minimal ideals of the topological convolution algebra are investigated.

All main results of this article are obtained for the first time. Their applications are discussed in the conclusion section.

We recall a definition in order to avoid any misunderstanding.

Definition 1. Let G be a set with multiplication (that is a single-valued binary operation) $G^2 \ni (a, b) \mapsto ab \in G$ defined on G such that

(i) for each a and b in G a unique $x \in G$ exists with $ax = b$.

The set G with multiplication satisfying condition (i) is called a left quasigroup. Symmetrically is considered the case:

(ii) a unique $y \in G$ exists satisfying $ya = b$.

The set G with multiplication satisfying condition (ii) is called a right quasigroup. Mappings in (i) and (ii) are denoted by $x = a \setminus b = Div_l(a, b)$ and $y = b / a = Div_r(a, b)$ correspondingly. If G is the left and right quasigroup, then it is called a quasigroup. If in addition

(iii) a neutral (that is unit) element exists $e_G = e \in G$: $eg = ge = g$ for each $g \in G$, then

the left (or right) quasigroup G with the unit element is called a left (or right correspondingly) loop. If G is the left and right loop, then it called a loop (or a unital quasigroup). Assume that G is the loop, $\mathcal{C}(G)$ is a center of the loop, $\mathcal{C}_m(G) \subseteq \mathcal{C}(G)$, $\mathcal{C}_m(G)$ is a commutative group such that $(ab)c = t_3(a, b, c)a(bc)$ for each a, b, c belonging to G , where $t_3(a, b, c) \in \mathcal{C}_m(G)$. Then G is called a metagroup.

Let \mathcal{T} be a topology on a left (or right) quasigroup (or loop) G such that multiplication $G \times G \ni (a, b) \mapsto ab \in G$ and the mapping $Div_l(a, b)$ (or $Div_r(a, b)$ correspondingly) are jointly continuous relative to \mathcal{T} , then (G, \mathcal{T}) is called a left (or right correspondingly) topological quasigroup (or loop correspondingly). If G is the left and right topological quasigroup (loop), then it is called a topological quasigroup (loop correspondingly).

It is supposed in this article that \mathcal{T} is the $T_1 \cap T_{3,5}$ topology, if something other will not be specified. For subsets A and B in G by means of $A - B$ is denoted their difference $A - B = \{a \in A : a \notin B\}$.

Remark 1. The notation $\mathcal{B}(X)$ is used in this article for the Borel σ -algebra on a topological space X , $\mathcal{F}_\mu(X)$ denotes a completion of $\mathcal{B}(X)$ by means of $|\mu|$, where μ is a measure on $\mathcal{B}(X)$ with values in $\bar{\mathbf{R}} = [-\infty, \infty]$ or \mathbf{C} , $|\mu|$ is a variation of the measure μ . Henceforth it assumed that $\mathcal{F}_\mu(X) \supseteq \mathcal{B}(X)$, σ -additive measures are considered on σ -algebras, on locally compact spaces Radon measures are investigated, if something other will not be specified. The measure $\lambda : \mathcal{F}_\lambda(G) \rightarrow \bar{\mathbf{R}}$ or $\lambda : \mathcal{F}_\lambda(G) \rightarrow \mathbf{C}$ is called left-quasiinvariant (or left-invariant) relative to H , if λ^{L_x} is equivalent to λ (or $\lambda^{L_x} = \lambda$ correspondingly) for each $x \in H$, where $H \subseteq G$, $\lambda^{L_x}(\Omega) = \lambda(x\Omega)$ for each $\Omega \in \mathcal{F}_\lambda(G)$. For $H = G$ "relative to G " is frequently omitted for short.

Definitions of smashed products and twisted wreath products are given in the appendix.

1. Quasiinvariant measures on smashed products of quasigroups

Theorem 1. *Assume that A and B are locally compact left T_1 quasigroups with nontrivial left-quasiinvariant measures λ_A and λ_B both taking values either in $\bar{\mathbf{R}} = [-\infty, +\infty]$ or in \mathbf{C} such that λ_B is also quasiinvariant relative to $\phi_1(a_1)$ for each $a_1 \in A$; $C = A \circledast^{\xi_1, \xi_2, \phi_1, \phi_2, \phi_3} B$ is a smashed product of A and B , with (jointly) continuous smashing mappings ξ_i, ϕ_j for each $i \in \{1, 2\}$ and $j \in \{1, 2, 3\}$. Then a nontrivial left-quasiinvariant measure λ_C exists on C induced by λ_A and λ_B .*

Proof. In view of Theorem 5.3 in [17] C as the topological space $A \times B$ is supplied with the Tychonoff product topology \mathcal{T}_C , consequently, C is locally compact, since A and B are locally compact. Multiplication on C is given by the formula

$\mu((a_1, b_1), (a_2, b_2)) = ((a_1 a_2), [(\xi_1(a_1, b_1, a_2) b_1^{(a_2)}) \xi_2(a_1, b_1, a_2)]^{\{a_1\}} b_2^{a_1})$ for each a_1, a_2 in A ; b_1, b_2 in B , where

$b_2^{a_1} := \phi_1(a_1) b_2, b_1^{(a_2)} := \phi_2(a_2) b_1, b_2^{\{a_1\}} := \phi_3(a_1) b_2, \phi_j : A \rightarrow \mathcal{A}(B)$, where $\mathcal{A}(B)$ denotes a family of all homeomorphisms from B on B , $\xi_i : A \times B \times A \rightarrow B$ and $A \times B \ni (a, b) \mapsto \phi_j(a) b \in B$ are (jointly) continuous mappings for each $i \in \{1, 2\}$ and $j \in \{1, 2, 3\}$, $(a_1, b_1) \in C$, a product on C is shortly denoted by $(a_1, b_1)(a_2, b_2)$ instead of $\mu((a_1, b_1), (a_2, b_2))$. From the Radon–Nikodym and the conditions of this theorem it follows that there exist factors of a quasiinvariance (that is

Radon–Nikodym derivatives) $d_{\lambda_A}(L_a, w_1) := \frac{\lambda_A^{L_a}(dw_1)}{\lambda_A(dw_1)}, d_{\lambda_B}(\phi_1(a_1), w_2) := \frac{\lambda_B^{\phi_1(a_1)}(dw_2)}{\lambda_B(dw_2)}$, and

$d_{\lambda_B}(L_{b_1}, w_2) := \frac{\lambda_B^{L_{b_1}}(dw_2)}{\lambda_B(dw_2)}$, where $\lambda_B^g(W_2) = \lambda_B(g(W_2))$ for a mapping $g : B \rightarrow B$ such that

$g : \mathcal{F}_{\lambda_B}(B) \rightarrow \mathcal{F}_{\lambda_B}(B), d_{\lambda_B}(g, w_2) := \frac{\lambda_B^g(dw_2)}{\lambda_B(dw_2)}, L_{b_1} b_2 = b_1 b_2$ for each b_1 and b_2 belonging

to $B, W_2 \in \mathcal{F}_{\lambda_B}(B)$, where $\mathcal{F}_{\lambda_B}(B)$ denotes a completion of the Borel σ -algebra $\mathcal{B}(B)$ relative to the variation $|\lambda_B|$ of the measure λ_B . Then it is possible to provide the product measure $\lambda_C = \lambda_A \times \lambda_B$ on C by virtue of theorem 1 in Ch. 3, Sect. 5 in [14], since $\mathcal{B}(C) \supset \mathcal{B}(A) \times \mathcal{B}(B)$. For each $f \in \mathcal{K}(C, \mathbf{F})$ according to the Fubini theorem

$$\int_C f(L_{(a_1, b_1)}^{-1} x) \lambda_C(dx) = \int_A \left(\int_B f((w_1, w_2)) \lambda_B^{L_{\beta(a_1, b_1, w_1)}}(dw_2^{a_1}) \right) \lambda_A^{L_{a_1}}(dw_1),$$

where $L_c^{-1} x = c \setminus x, x \in C, c \in C, w_1 \in A, w_2 \in B$,

$\beta = \beta(a_1, b_1, w_1) = [(\xi_1(a_1, b_1, w_1) b_1^{(w_1)}) \xi_2(a_1, b_1, w_1)]^{\{a_1\}}, \mathcal{K}(C, \mathbf{F})$ denotes the space of all continuous functions $h : C \rightarrow \mathbf{F}$ with a compact support, either $\mathbf{F} = \mathbf{R}$ or $\mathbf{F} = \mathbf{C}$ correspondingly. Since $\lambda_A^{L_{a_1}}$ is equivalent to λ_A , also $\lambda_B^{L_b}$ and $\lambda_B^{\phi_1(a_1)}$ are equivalent λ_B for each $a_1 \in A, b \in B$, then $\lambda_C^{L_{(a_1, b_1)}}$ is equivalent to λ_C . Moreover

$$d_{\lambda_C}(L_{(a_1, b_1)}, w) = d_{\lambda_A}(L_{a_1}, w_1) d_{\lambda_B}(L_{\beta}, w_2^{a_1}) d_{\lambda_B}(\phi_1(a_1), w_2),$$

where $w = (w_1, w_2) \in C, w_1 \in A, w_2 \in B, \beta = \beta(a_1, b_1, w_1)$. \square

Corollary 1. *If the conditions of theorem 1 are satisfied and in addition λ_A and λ_B are left-invariant, $\lambda_B^{\phi_1(a_1)} = \lambda_B$ for each $a_1 \in A$, then λ_C is left-invariant.*

Example 1. In particular, $\phi_1(a_1)$ may be in theorem 1 compositions of left shift operators of the form $L_{c_1} L_{\pi(a_1)}^n L_{c_2}$ with fixed c_1 and c_2 , where $\pi : A \rightarrow B$ is a continuous mapping,

$L_c L_b x = L_c(L_b x)$, $L_b x = bx$, $L_b^{-1} x = b \setminus x$, $L_b^{n+1} = L_b L_b^n$ for each $a_1 \in A$, for each b, b_1, c_1, c_2, x belonging to B . From the left quasiinvariance of the λ_B it follows in this case, that it is quasiinvariant relative to the transformations $\phi_1(a_1)$.

Theorem 2. *Assume that a left topological loop $C = D\Delta_A^{\phi, \eta, \kappa, \xi} F$ is smashed twisted wreath product of D with F and (jointly) continuous smashed mappings $\xi : A \times F \times A \rightarrow \mathcal{C}_1$ and ϕ, η, κ , where $F = B^V$, D and B are locally compact T_1 metagroups, A is a submetagroup in D with a finite discrete transversal set V for A in D with a continuous transversal mapping $\tau : D \rightarrow V$, $\mathcal{C}_1 \hookrightarrow \mathcal{C}(D) \cap \mathcal{C}(B)$. Let λ_D and λ_B be nontrivial left-quasiinvariant measures taking values both either in \mathbf{R} or in \mathbf{C} , such that λ_B is also quasiinvariant relative to $\phi(a_1)$ for each $a_1 \in A$. Then there exists a nontrivial left-quasiinvariant measure λ_C on C induced by λ_D and λ_B .*

Proof. Since V is finite, then F is a locally compact T_1 metagroup by Theorem 4 and Corollary 3 in [15]. From the continuity of $\tau : D \rightarrow V$ it follows that the mapping $\psi : D \rightarrow A$ is continuous by remark 1 in [16], since $q = q^\psi q^\tau$, $q^\psi = \psi(q)$, $q^\tau = \tau(q)$ for each $q \in D$, the mapping $D^2 \ni (q, r) \mapsto q/r \in D$ is (jointly) continuous. By virtue of theorem 3 in [16] C is the locally compact $T_1 \cap T_3$ loop, since D and F locally compact, since V is finite and discrete. Moreover, the local compactness and regularity imply that C Tychonoff $T_1 \cap T_{3\frac{1}{2}}$ by Theorems 3.3.11 and 3.2.6 in [21].

On the metagroup F the measure $\lambda_F = \prod_{v \in V} (\lambda_B)_v$ exists, where $(\lambda_B)_v = \lambda_B$ for each $v \in V$ by theorem 1 in Chapter 3, Section 5 in [14], since the set V is finite. Evidently the measure λ_F is F left-quasiinvariant and also quasiinvariant relative to $\phi(a_1)$ for each $a_1 \in A$. Then $d_{\lambda_F}(L_x, y) = \prod_{v \in V} d_{\lambda_B}(L_{x_v}, y_v)$, where $y = \{y_v \in B : v \in V\} \in F$.

Multiplication on C has the form:

$(d_1, f_1)(d_2, f_2) = (d_1 d_2, \xi((d_1^\psi, f_1), d_2^\psi) f_1 f_2^{\{d_1\}})$,
 where $\xi((d_1^\psi, f_1), d_2^\psi)(v) = \xi((d_1^\psi, f_1(v)), d_2^\psi) \in \mathcal{C}_1$ for each d_1 and d_2 in D , f_1 and f_2 in F , $v \in V$, $\mathcal{C}_1 \hookrightarrow \mathcal{C}(D) \cap \mathcal{C}(B)$, $\mathcal{C}(B) = \text{Com}(B) \cap N(B)$ is the center of the metagroup B , $(d_1, f_1) \in C$ (see remark 3 and theorem 3 in [16]), since by the conditions of this theorem $\xi : A \times F \times A \rightarrow \mathcal{C}_1$, in the considered case ξ is independent of f_2 . Moreover, $f_2^{\{d_1\}}(v) = f_2^{s(d_1, v)}(v^{[d_1 \setminus e]})$, $s(d_1, v) = e/(v/d_1)^\psi$, $(a^\tau)^{[c]} = (a^\tau c)^\tau$ for each a and c in D , $v \in V$, $b^{a_1} = \phi(a_1)b$ for each $b \in B$ and $a_1 \in A$, $\mathcal{A}(B)$ denotes a family of all homeomorphisms from B onto B , $\phi : A \rightarrow \mathcal{A}(B)$; η, κ, ξ and $A \times B \ni (a_1, b) \mapsto \phi(a_1)b \in B$ are the (jointly) continuous mappings.

As a measure on C it is possible to take the product measure $\lambda_C = \lambda_D \times \lambda_F$, consequently, $\lambda_C(W) = \lambda_D(W_1)\lambda_F(W_2)$ for each $W = W_1 \times W_2$, $W_1 \in \mathcal{B}(D)$, $W_2 \in \mathcal{B}(F)$. Therefore $\lambda_C^{L(d_1, f_1)}(dw) = \lambda_D^{L d_1}(dw_1)\lambda_F^{L \beta}(dw_2^{\{d_1\}})$ for each $w = (w_1, w_2) \in C$, $w_1 \in D$, $w_2 \in F$, $(d_1, f_1) \in C$, where $\beta = \beta(d_1, f_1, w_1) = \xi((d_1^\psi, f_1), w_1^\psi) f_1$. Hence for each $f \in \mathcal{K}(C, \mathbf{F})$ by virtue of the Fubini theorem

$$\int_C f(L_{(d_1, f_1)}^{-1} x) \lambda_C(dx) = \int_D \left(\int_F f((w_1, w_2)) \lambda_D^{L \beta(d_1, f_1, w_1)}(dw_2^{\{d_1\}}) \right) \lambda_D^{L d_1}(dw_1)$$

On the other hand, $w_2^{\{d_1\}}(v) = \phi(e/(v/d_1)^\psi)(w_2((v(d_1 \setminus e))^\tau))$ for each $v \in V$.

Therefore $\lambda_F(U_1 \times \cdots \times U_m) = \lambda_F(U_{g(1)} \times \cdots \times U_{g(m)})$ for each U_1, \dots, U_m belonging to $\mathcal{B}(B)$ and each bijection g of the set $\{1, \dots, m\}$, where $m = \text{card}(V)$. Then $d_{\lambda_F}(\phi_4(d_1), w_2) = \prod_{v \in V} d_{\lambda_B}(\phi_5(v, d_1), w_2(v))$ for $\phi_4(d_1)w_2 = w_2^{\{d_1\}}$, $\phi_5(v, d_1)(w_2(v)) = \phi(e/((\phi_6(d_1)v)/d_1)^\psi)(w_2(v))$, where $\phi_6(d_1)(v^{[d_1 \setminus e]}) = v$ for each $v \in V$. Thus the measure $\lambda_C^{L(d_1, f_1)}(dw)$ is equivalent to $\lambda_C(dw)$ and $d_{\lambda_C}(L_{(d_1, f_1)}, w) = d_{\lambda_D}(L_{d_1}, w_1) d_{\lambda_F}(L_{\beta(d_1, f_1, w_1)}, w_2^{\{d_1\}}) d_{\lambda_F}(\phi_4(d_1), w_2)$. \square

Corollary 2. *If the conditions of theorem 2 are satisfied and λ_D and λ_B are left-invariant, $\lambda_B^{\phi(a_1)} = \lambda_B$ for each $a_1 \in A$, then λ_C is left-invariant.*

Remark 2. Examples of metagroups, satisfying the conditions of Theorem 2, are provided in [15, 16] and with the help of theorems given there. Examples of left quasigroups are in [17]. For their construction it is possible to use not only topological quasigroups, but also topological groups and subsequently construct topological left (and symmetrically right) quasigroups, loops and metagroups with the help of smashed and twisted wreath products. In their turn, with the help of Theorems 1, 2 and Corollaries 1, 2 this provides abundant families of locally compact left (or right) quasigroups and loops with left- (or right-) quasiinvariant or invariant measures. It also is possible to use topological isotopies according to the theorem given below.

Theorem 3. *Assume that $G = Q(A)$ and $H = Q_1(B)$ are topological left T_1 quasigroups, which are topologically isotopic: $\gamma A(x_1, x_2) = B(\alpha_1 x_1, \alpha_2 x_2)$ for each x_1 and x_2 in Q , where α_1, α_2 are γ homeomorphisms of topological spaces Q and Q_1 . Assume also that λ_G is a measure left relative to $\alpha_2^{-1}\gamma$ quasiinvariant on G . Then λ_G and isotopy $(\alpha_1, \alpha_2, \gamma)$ induces a left- quasiinvariant measure on H .*

Proof. The measure λ_G and γ induce the measure $\lambda_H(W) = \lambda_G(\gamma^{-1}W)$ for each $W \in \mathcal{B}(Q_1)$. Then $\lambda_H(\gamma U) = \lambda_G(U)$ and $\lambda_H^{L_b}(\gamma U) = \lambda_G^{L_{\alpha_1^{-1}b}}(\alpha_2^{-1}\gamma U)$ for each $U \in \mathcal{B}(Q)$ and $b \in Q_1$, where $\alpha_2^{-1}\gamma U = \alpha_2^{-1}(\gamma(U))$. By the conditions of this theorem the measures $\lambda_G(du)$, $\lambda_G^{L_a}(du)$ and $\lambda_G^{\alpha_2^{-1}\gamma}(du)$ are equivalent for each $a \in Q$, where $u \in Q$. Therefore the measures $\lambda_H(dw)$ and $\lambda_H^{L_b}(dw)$ are equivalent for each $b \in Q_1$, since $a = \alpha_1^{-1}b \in Q$, where $w \in Q_1$. Moreover $d\lambda_H(L_b, w) = d\lambda_G(L_{\alpha_1^{-1}b}, \alpha_2^{-1}w)d\lambda_G(\alpha_2^{-1}\gamma, \gamma^{-1}w)$. \square

2. Applications of invariant measures and ideals in convolution algebras

Definition 2. Let G be a topological (left) T_1 quasigroup, $\mathbf{M}(G, \mathbf{F})$ be a space of σ -additive measures $\mu : \mathcal{F}_\mu(G) \rightarrow \mathbf{F}$ with a finite norm $\|\mu\| = |\mu|(G) < \infty$, where $\mathbf{F} = \mathbf{R}$ or $\mathbf{F} = \mathbf{C}$. For μ_1 and μ_2 belonging to $\mathbf{M}(G, \mathbf{F})$ the convolution is provided by the formula

$$(\mu_1 * \mu_2)(\Omega) = \int_G \int_G \chi_\Omega(xy) \mu_1(dx) \mu_2(dy),$$

where $\chi_\Omega(z)$ is the characteristic function of the subset Ω in G , $\chi_\Omega(z) = 1$ for each $z \in \Omega$, $\chi_\Omega(z) = 0$ for each $z \in G - \Omega$, $\Omega \in \mathcal{F}_\mu(G)$.

Theorem 4. *Assume that G is a topological left T_1 quasigroup, $\mu_j \in \mathbf{M}(G, \mathbf{F})$, $j \in \{1, 2\}$. Then $\|\mu_1 * \mu_2\| \leq \|\mu_1\| \|\mu_2\|$ and $\mu_1 * \mu_2 \in \mathbf{M}(G, \mathbf{F})$.*

Proof. For each $\Omega \in \mathcal{B}(G)$ by virtue of the Fubini theorem

$$\begin{aligned} \left| \int_G \int_G \chi_\Omega(xy) \mu_1(dx) \mu_2(dy) \right| &\leq \int_G \left| \int_G \chi_\Omega(xy) \mu_1(dx) \right| |\mu_2|(dy) \leq \\ &\leq \int_G \left(\int_G \chi_\Omega(xy) |\mu_1|(dx) \right) |\mu_2|(dy) = (|\mu_1| * |\mu_2|)(\Omega) \leq \|\mu_1\| \|\mu_2\|, \end{aligned}$$

since $x \setminus \Omega \in \mathcal{B}(G)$ for each $x \in G$. Therefore

$$(\mu_1 * \mu_2)(\bigcup_{j=1}^{\infty} \Omega_j) = \sum_{j=1}^{\infty} (\mu_1 * \mu_2)(\Omega_j)$$

for each disjoint Ω_j in $\mathcal{B}(G)$, $\Omega_{j_1} \cap \Omega_{j_2} = \emptyset$ for each $j_1 \neq j_2$ in \mathbf{N} , with $\bigcup_{j=1}^{\infty} \Omega_j = \Omega$, since $\chi_\Omega(z) = \sum_{j=1}^{\infty} \chi_{\Omega_j}(z)$ for each $z \in G$. Then $\mu_1 * \mu_2$ has an extension on $\mathcal{F}_{\mu_1 * \mu_2}(G) \supset \mathcal{B}(G)$. \square

Proposition 1. *Assume that G is a compact left T_1 quasigroup, $\lambda : \mathcal{F}_\lambda(G) \rightarrow [0, 1]$ is a left-invariant measure, $\lambda(G) = 1$. Then $\mathbf{F}\lambda$ is a one-dimensional left ideal in the algebra $(\mathbf{M}(G, \mathbf{F}), +, *)$.*

Proof. For each $\Omega \in \mathcal{F}_\lambda(G)$ and $\mu \in \mathbf{M}(G, \mathbf{F})$ there is the equality $\mu * \lambda(\Omega) = \lambda(\Omega)\mu(G)$, since $\mu * \lambda(\Omega) = \int_G \lambda(x \setminus \Omega)\mu(dx)$. \square

Theorem 5. *Let G be a locally compact T_1 quasigroup, $\lambda : \mathcal{F}_\lambda(G) \rightarrow [0, \infty]$ (and $\lambda_1 : \mathcal{F}_{\lambda_1}(G) \rightarrow [0, \infty]$) be a nontrivial left- (or right- correspondingly) invariant measure, $\mu \in \mathbf{M}(G, \mathbf{F})$; the measure μ generates an one-dimensional left (or right) ideal in the algebra $(\mathbf{M}(G, \mathbf{F}), +, *)$. Then G is compact, the measure μ generates the one-dimensional (two-sided) ideal, $\mu(dx) = \frac{\gamma}{\alpha(x)}\lambda(dx)$ with a constant $\gamma \neq 0$ in \mathbf{F} , $\alpha : G \rightarrow \mathbf{F}$ is a continuous bounded function, $\alpha(xy) = \alpha(x)\alpha(y)$ for each x and y in G , $\lambda(dx) = \beta\lambda_1(dx)$ with a positive constant β .*

Proof. If $\mathbf{F}\mu$ is the one-dimensional left ideal in $\mathbf{M}(G, \mathbf{F})$, then $\nu * \mu = \alpha_\nu\mu$ with $\alpha_\nu \in \mathbf{F}$ for each $\nu \in \mathbf{M}(G, \mathbf{F})$. In particular, $\delta_a * \mu = \alpha(a)\mu$ with $\alpha(a) \in \mathbf{F}$ for each $a \in G$. Moreover

$\|\delta_a * \mu\| = |\alpha(a)|\|\mu\| \leq \|\delta_a\|\|\mu\| = \|\mu\|$ by Theorem 4, consequently, $\alpha(a)$ is the bounded function. For each $a \in G$ and $f \in C_0(G, \mathbf{F})$ there is the equality

$$\int_G {}_a f(x)\mu(dx) = \alpha(a) \int_G f(z)\mu(dz),$$

since $\delta_a * \mu(\Omega) = \mu^{L_a^{-1}}(\Omega) = \alpha(a)\mu(\Omega)$ for each $\Omega \in \mathcal{F}_\mu(G)$, where $C_0(G, \mathbf{F})$ denotes the set of all continuous functions $f : G \rightarrow \mathbf{F}$ such that for each $0 < \epsilon < \infty$ there exists a compact subset K in G with $|f(x)| < \epsilon$ for each $x \in G - K$, where $\mathbf{F} = \mathbf{R}$ or $\mathbf{F} = \mathbf{C}$, ${}_a f(x) := f(ax)$. From Theorem 5.2 in [17] it follows that $\alpha(a)$ is the continuous function, since

$$\int_G ({}_a f(x) - {}_b f(x))\mu(dx) = (\alpha(a) - \alpha(b)) \int_G f(x)\mu(dx)$$

for each a and b in G . Since $\mathbf{F}\mu$ is the one-dimensional left ideal, then $\exists \Omega \in \mathcal{F}_\lambda(G), \mu(\Omega) \neq 0$, consequently, α is the nonzero function.

From the proof above it follows that $\mu^{L_a^{-1}}(dx)/\mu(dx) = \alpha(a)$, consequently, μ is the left-quasiinvariant measure. In view of the Riesz Theorem 7.2.8 in [4] and Remark 4.4 the measures $|\mu|$, λ and λ_1 are regular. In view of Theorem 4 in [17] $\mu \ll \lambda$ a function exists $h \in \mathbf{L}^1(G, \lambda, \mathbf{F})$ such that $\mu(dx) = h(x)\lambda(dx)$. Therefore $h(a \setminus x) = \alpha(a)h(x)$, since λ is left-invariant. Since $a(a \setminus x) = x$ is the quasigroup G , then $\mu(dx) = \frac{\gamma}{\alpha(x)}\lambda(dx)$, where $\gamma \neq 0$ is the constant in \mathbf{F} . Therefore $\alpha(az) = \alpha(a)\alpha(z)$ for each a and z in G . Thus the measure $\alpha(x)\mu(dx)$ is left-invariant. The function $\alpha(x)$ is bounded, consequently, $\lambda(G) < \infty$. Then $M(f) := \int_G f(x)\lambda(dx)$ is the left-invariant mean on $\mathbf{L}^1(G, \lambda, \mathbf{F})$, since λ is left-invariant. Moreover $M(\mathbf{L}^1(G, \lambda, \mathbf{F})) \neq 0$.

It remains to prove that G is compact. Assume the contrary, that G is locally compact noncompact left T_1 quasigroup, M is the left-invariant mean on $\mathbf{L}^1(G, \lambda, \mathbf{F})$. We take an open subset V in G such that its closure $cl_G V$ is compact. We choose $b_1 \in G$, $b_2 \in G - b_1V$ with $b_2V \subset G - b_1V$, further by induction $b_n \in G - \bigcup_{j=1}^{n-1} b_jV$ with $b_nV \subset G - \bigcup_{j=1}^{n-1} b_jV$, since G is noncompact. The function $f_n = \sum_{j=1}^n \hat{L}_{b_j}^{-1}\chi_V$ belongs to $\mathbf{L}^1(G, \lambda, \mathbf{F})$, since $cl_G V$ is compact, $n \in \mathbf{N}$, where $\hat{L}_b f(x) = f(bx)$, $\hat{L}_b^{-1} f(x) = f(b \setminus x)$ for each $x \in G$. Then for $x \in G$ the condition $b_j \setminus x \in V$ is equivalent to $x \in b_jV$. On the other hand, $(b_jV) \cap (b_kV) = \emptyset$ for each $j \neq k$ according to the choice of b_1, \dots, b_n in G . Therefore either $f_n(x) = 1$ or $f_n(x) = 0$, consequently, $\|\frac{1}{n}f_n\| = \frac{1}{n}$ and $M(\chi_V) = 0$, since $M(\hat{L}_b f) = M(f)$ is equivalent to $M(\hat{L}_b^{-1} f) = M(f)$ for each

$b \in G$, $f \in \mathbf{L}^1(G, \lambda, \mathbf{F})$. Thus, $M(\mathbf{L}^1(G, \lambda, \mathbf{F})) = \{0\}$. This gives the contradiction, consequently, G is compact.

In view of proposition 1 $\mathbf{F}\lambda$ is the left ideal, and symmetrically $\mathbf{F}\lambda_1$ is the right ideal in $(\mathbf{M}(G, \mathbf{F}), +, *)$. Therefore $\lambda_1 * \lambda = p\lambda_1 = q\lambda$, where p and q are positive constants, consequently, a positive constant exists β such that $\lambda(dx) = \beta\lambda_1(dx)$. \square

Conclusion

The results of this article can be used for the subsequent studies of the topological quasigroups and loops structure, homogeneous spaces and noncommutative manifolds related with quasigroups and loops [11, 12]. Besides applications of left- (or right-)invariant or quasiinvariant measures on quasigroups and loops mentioned in the introduction it is interesting to mention possible applications to the mathematical control of ruling simultaneously functioning programmed robots [18, 22], since they frequently are based on topologically-algebraic binary systems and measures. Other very important applications are: representation theory of quasigroups and loops, harmonic analysis on quasigroups and loops [1–3, 5–8], mathematical physics, etc.

Smashed products of topological left quasigroups and smashed twisted wreath products of topological metagroups were use in this article. On the other side, smooth quasigroups were constructed in [23] with the help of a generalization of the Lie group construction method such that a composition law was dependent on transformation parameters and on transformed variables. In particular, this was used on hypersurfaces described in the first class restrictions in a phase space.

It is possible to formulate a question for subsequent studies. Whether will coincide an extended measure from the loop on an enveloping (by Sabinin) group with the Haar measure of the enveloping loop? There different extension may be, while transformations of measures on the loop and on the group are different, since loops are nonassociative.

3. Appendix

For convenience of readers definitions and a notation are recalled in this appendix from works [15–17].

Definition 3. A topological left quasigroup prescribed by the conditions given below is denoted by $A^{\xi_1, \xi_2, \phi_1, \phi_2, \phi_3} B$ and it is called a smashed product of topological left quasigroups (with smashing mappings $\xi_1, \xi_2, \phi_1, \phi_2, \phi_3$).

Conditions. Let

- (i) (A, τ_A) and (B, τ_B) be topological left quasigroups,
- (ii) $\xi_i : A \times B \times A \rightarrow B$ and $A \times B \ni (a, b) \mapsto \phi_j(a)b \in B$ be (jointly) continuous mappings for each $i \in \{1, 2\}$ and $j \in \{1, 2, 3\}$,
- (iii) $\mu : (A \times B)^2 \rightarrow A \times B$ be a mapping such that
- (iv) $\mu((a_1, b_1), (a_2, b_2)) = ((a_1 a_2), [(\xi_1(a_1, b_1, a_2) b_1^{(a_2)}) \xi_2(a_1, b_1, a_2)]^{\{a_1\}} b_2^{a_1})$ for each a_1, a_2 in A ; b_1, b_2 in B , where
- (v) $b_2^{a_1} := \phi_1(a_1) b_2$,
- (vi) $b_1^{(a_2)} := \phi_2(a_2) b_1$,
- (vii) $b_2^{\{a_1\}} := \phi_3(a_1) b_2$,
- $\phi_j : A \rightarrow \mathcal{A}(B)$, where $\mathcal{A}(B)$ denotes a family of all homeomorphisms from B onto B ,

(viii) the Cartesian product $C = A \times B$ is supplied with the Tychonoff product topology τ_C and the mapping μ .

Remark 3. Let A and B be topological metagroups, \mathcal{C} be a commutative group such that

$$(i) \mathcal{C}_m(A) \hookrightarrow \mathcal{C}, \mathcal{C}_m(B) \hookrightarrow \mathcal{C}, \mathcal{C} \hookrightarrow \mathcal{C}(A) \text{ and } \mathcal{C} \hookrightarrow \mathcal{C}(B),$$

where $\mathcal{C}_m(A)$ denotes a minimal closed subgroup in $\mathcal{C}(A)$ containing $t_A(a, b, c)$ for each a, b and c in A .

An equivalence relation Ξ is considered on $A \times B$:

$$(ii) (\gamma v, b)\Xi(v, \gamma b) \text{ and } (\gamma v, b)\Xi\gamma(v, b) \text{ and } (\gamma v, b)\Xi(v, b)\gamma$$

for each v in A , b in B , γ in \mathcal{C} .

Let (iii) $\phi : A \rightarrow \mathcal{A}(B)$ be (jointly) continuous (single valued) mappings,

where $\mathcal{A}(B)$ denotes a family of all homeomorphisms from B onto B , satisfying conditions (iv)–(viii) given below. If $a \in A$ and $b \in B$, then it will be shortly written b^a instead of $\phi(a)b$, where $\phi(a) : B \rightarrow B$. Let also

$$\eta_{A,B,\phi} : A \times A \times B \rightarrow \mathcal{C}, \kappa_{A,B,\phi} : A \times B \times B \rightarrow \mathcal{C}$$

$$\text{and } \xi_{A,B,\phi} : ((A \times B)/\Xi) \times ((A \times B)/\Xi) \rightarrow \mathcal{C}$$

are (single valued jointly) continuous mappings shortly written by η , κ and ξ such that

$$(iv) (b^u)^v = b^{vu}\eta(v, u, b), \quad e^u = e, \quad b^e = b;$$

$$(v) \eta(v, u, \gamma b) = \eta(v, u, b);$$

$$(vi) (cb)^u = c^u b^u \kappa(u, c, b);$$

$$(vii) \kappa(u, \gamma c, b) = \kappa(u, c, \gamma b) = \kappa(u, c, b);$$

$$(viii) \kappa(u, \gamma, b) = \kappa(u, b, \gamma) = e;$$

$$\xi((\gamma u, c), (v, b)) = \xi((u, c), (\gamma v, b)) = \xi((u, c), (v, b))$$

$$\xi((\gamma, e), (v, b)) = e \text{ and } \xi((u, c), (\gamma, e)) = e$$

for each u and v in A , b, c in B , γ in \mathcal{C} , where e denotes the unit element in \mathcal{C} , A and B .

Let D be a topological metagroup, A be a submetagroup in D , V be a transversal set for A in D . Then, as it is known,

$$(ix) \forall a \in D, \exists_1 s \in A, \exists_1 b \in V, a = sb.$$

Then b in the decomposition (ix) is denoted by $b = \tau(a) = a^\tau$ and $s = \psi(a) = a^\psi$, where τ and ψ are shortened notations for $\tau_{A,D,V}$ and $\psi_{A,D,V}$. Thus (single-valued) mappings exist

$$(x) \tau : D \rightarrow V \text{ and } \psi : D \rightarrow A.$$

Assume that mappings τ and ψ are continuous.

$$(xi) \text{ If } b = a^\tau, \text{ then } e/b \text{ is also denoted by } a^{e/\tau}, \text{ and } b \setminus e \text{ is also denoted by } a^{\tau \setminus e}.$$

We put

$$(xii) (a^\tau)^{[e]} := (a^\tau c)^\tau \text{ for each } a \text{ and } c \text{ in } D.$$

Remark 4. Let B and D be topological metagroups, A be a submetagroup in D , V be the transversal set for A in D . Assume also that conditions (i)–(viii) are satisfied in remark3 for A and B . Then a topological metagroup exists

$$(i) F = B^V, \text{ where } B^V = \prod_{v \in V} B_v, \quad B_v = B \text{ for each } v \in V.$$

We put $T_h f = f^h$ for each $f \in F$ in $h : V \rightarrow A$. Then we define

$$\hat{S}_d(T_h f J) = T_{h S_d^{-1}} f S_d J,$$

where $J : V \times F \rightarrow B$, $J(f, v) = f J v$, $S_d J v = J v^{[d \setminus e]}$ for each $d \in D$, $f \in F$ and $v \in V$. Let also for each $f \in F$, $d \in D$

$$(ii) f^{\{d\}} = \hat{S}_d(T_{g_d} f E),$$

where

(iii) $s(d, v) = e/(v/d)^\psi$, $g_d(v) = s(d, v)$,
 $fEv = f(v)$ for each $v \in V$
 (see also (ix) and (xii) in Remark 3).

Definition 4. Assume that the conditions of Remarks 3 and 4 are satisfied, and on $C = D \times F$ a binary operation is provided by the formula:

(i) $(d_1, f_1)(d, f) = (d_1d, \xi((d_1^\psi, f_1), (d^\psi, f))f_1f^{\{d_1\}})$,
 where $\xi((d_1^\psi, f_1), (d^\psi, f))(v) = \xi((d_1^\psi, f_1(v)), (d^\psi, f(v)))$ for each d and d_1 in D , f in f_1 in F ,
 $v \in V$, where $C = D \times F$ is supplied with the Tychonoff product topology. Then the topological loop C supplied with this multiplication is called a smashed twisted wreath product of D with F . It is denoted by $C = D\Delta^{\phi, \eta, \kappa, \xi}F$.

References

- [1] A.A.Adhikari, M.R.Adhikari, Basic Topology, **1–3**, Springer, Singapore, 2022.
DOI: 10.1007/978-981-16-6509-7
- [2] C.Arhanacet, C. Kriegler, Projections, multipliers and decomposable maps on noncommutative L_p -spaces, *Mémoires de la Société Mathématique de France*, **177**(2023), 1–185.
DOI: 10.24033/msmf.485
- [3] A.Arangel'skii, M.Tkachenko, Topological Groups and Related Structures, World Sci., Atlantis Press, Amsterdam, 2008.
- [4] D.L.Cohn, Measure Theory, Birkhäuser, New York, 2013.
- [5] J.M.G.Fell, R.S.Doran, Representations of *-Algebras, Locally Compact Groups, and Banach *-Algebraic Bundles, **1, 2**, Acad. Press, Boston, 1988.
- [6] A.G.Farashahi, Classical harmonic analysis over spaces of complex measures on coset spaces of compact subgroups, *Analysis Math.*, **43**(2017), 461–473.
DOI: 10.1007/s10476-017-0205-6
- [7] V.Losert, The derivation problem for group algebras, *Annals of Mathem.*, **168**(2008), 221–246. DOI: 10.4007/annals.2008.168.221
- [8] S.V.Ludkovsky, Topological transformation groups of manifolds over non-Archimedean fields; representations and quasi-invariant measures, I; II, *J. Mathem. Sci.; N.Y. (Springer)*, **147**(2008), 6703–6846; **150**(2008), 2123–2223. DOI: 10.1007/s10958-007-0507-5,
DOI: 10.1007/s10958-008-0127-8
- [9] W.Herforth, P.Plaumann, Boolean and profinite loops, *Topology Proceedings*, **37**(2011), 233–237.
- [10] V.Kakkar, Boolean loops with compact left inner mapping groups are profinite, *Topology and Its Appl.*, **244**(2018), 51–54. DOI: 10.1016/j.topol.2018.06.002
- [11] J.D.H.Smith, An Introduction to Quasigroups and Their Representations, Chapman and Hall/CRC, Taylor and Francis Group, Boca Raton, 2007. DOI: 10.1201/9781420010633
- [12] L.V.Sabinin, Smooth Quasigroups and Loops, Kluwer, Dordrecht, 1999.
DOI: 10.1007/978-94-011-4491-9

-
- [13] F.Gürsey, C.-H.Tze, On the Role of Division, Jordan and Related Algebras in Particle Physics, World Scientific Publ. Co., Singapore, 1996. DOI: 10.1142/3282
- [14] N.Bourbaki, Integration. Measure, integration of measures. Nauks, Moscow, 1967.
- [15] S.V.Ludkowski, Structure and functions of topological metagroups, *Axioms*, **9**(2020), 1–11. DOI: 10.3390/axioms9020066
- [16] S.V.Ludkowski, Topologies on smashed twisted wreath products of metagroups, *Axioms*, **12**(2023), 1–12. DOI: 10.3390/axioms12030240
- [17] S.V.Ludkovsky, Quasi-invariant and invariant functionals and measures on systems of topological loops and quasigroups, *Siberian Math. J.*, **64**(2023), 1186–1199. DOI: 10.1134/S0037446623050117
- [18] B.Plotkin, Universal Algebra, Algebraic Logic, and Databases, Kluwer, New York, 1994.
- [19] S.V.Ludkovsky, Existence of an invariant measure on a topological quasigroup, *Topology and Its Appl.*, **275**(2020), 1–11. DOI: 10.1016/j.topol.2020.107147
- [20] S.V.Ludkowski, Left invariant measures on locally compact nonassociative core quasigroups, *Southeast Asian Bull. of Mathem.*, **46**(2022), 365–404.
- [21] R.Engelking, General Topology, Sigma Series in Pure Mathem. **6**, Heldermann Verlag, Berlin, 1989.
- [22] A.S.Zuev, D.A.Leonov, About managing the number of simultaneously functioning software robots of different types, *Russ. Technol. J.*, **12**(2024), no. 4, 7–22. DOI: 10.32362/2500-316X-2024-12-4-7-22
- [23] I.A.Batalin, Quasigroup construction and first class constraints, *J. Math. Phys.*, **22**(1981), 1837–1850. DOI: 10.1063/1.525155

Меры на сокрушающих произведениях квазигрупп и их алгебры

Сергей В. Людковский

Российский технологический университет
Москва, Российская Федерация

Аннотация. Исследуются квазиинвариантные и инвариантные меры на сокрушающих и скрученных вечных произведениях квазигрупп. Также изучается квазиинвариантность мер относительно изотопий. Найдены специфические особенности для квазигрупп по сравнению с группами. Изучаются пространства мер. Алгебры сверток в общем случае оказываются неассоциативными из-за неассоциативности квазигрупп. Исследуются идеалы топологических алгебр сверток.

Ключевые слова: квазигруппа, мера, алгебра, свертка, топология, инвариантность.